Digital Frequency Domain Multiplexing readout

Design and performance of the SPT-3G instrument and LiteBIRD satellite readout

JOSHUA MONTGOMERY

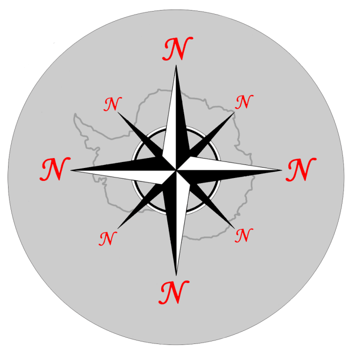

PhD
Physics
McGill University
Montreal, Quebec

A thesis submitted to McGill University
in partial fulfillment of the requirements of the degree of
Philosophy of Science in Physics

November 2020

Supervisor: Professor Matt Dobbs

ABSTRACT

Inflationary ΛCDM is the leading cosmological model used to describe the dynamics and evolution of our universe. Still, one of the core precepts of this model, *inflation*, remains only indirectly probed. A unique signature of inflation may be observable via polarization-sensitive measurements of the cosmic microwave background (CMB). Instruments designed to survey the CMB are now reaching the sensitivity required to either detect this signature or rule out the most likely models for inflation. These measurements benefit from combinations of ground-based instruments with high angular resolution, and space-based instruments with wide frequency coverage. This thesis presents my work on the SPT-3G ground-based instrument, and planned LiteBIRD satellite mission. The readout and operation of detectors in these instruments is critical to achieving sufficient sensitivity to detect the inflationary signal in the CMB. This work focuses on the interactions, related to readout, that determine instrument noise performance, detector stability, and crosstalk. I build up a theory of modern high-density and large-bandwidth frequency domain multiplexed readout, and validate that theory using SPT-3G instrument data. Finally, I apply an instrument noise model to forecast LiteBIRD readout performance and recommend specific detector and readout design properties.

ABRÉGÉ

Le modèle inflationniste ΛCDM est reconnu comme le modèle cosmologique principal pour décrire les dynamiques et l'évolution de notre univers. Toutefois, l'un des postulats principaux du modèle, *l'inflation*, n'a été sondé que de façon indirecte. Il est possible de détecter la signature distincte de l'inflation en mesurant avec précision la polarisation du rayonnement du fond cosmologique (CMB). Les instruments conçus pour étudier le CMB atteignent aujourd'hui la sensibilité nécessaire pour détecter cette signature ou, au contraire, infirmer les modèles les plus probables d'inflation. L'utilisation conjointe d'instruments au sol à haute résolution angulaire et de plateformes spatiales à grande couverture en fréquence permet d'améliorer la qualité des mesures. Cette thèse présente mon travail sur l'instrument au sol SPT-3G et le projet de mission satellitaire LiteBIRD. Le système de lecture de données et l'utilisation des détecteurs dans ces instruments jouent un rôle crucial dans l'obtention des sensibilités requises pour détecter le signal caractérisant l'inflation du CMB. Cet ouvrage analyse les interactions internes au sein du système de lecture de données qui déterminent la performance du bruit de l'instrument, la stabilité des détecteurs, et les couplages réciproques. Il présente également une théorie moderne pour la lecture de données via le multiplexage en fréquence à large bande et à haute densité. Le modèle de lecture de données que j'ai élaboré sur la base sur cette théorie est validé par les données instrumentales du SPT-3G. Ce modèle permet aussi d'estimer la performance en lecture de données du futur satellite LiteBIRD et générer les critères de configuration pour ses détecteurs et son système de lecture de données.

ACKNOWLEDGMENTS

Early on as a graduate student, my supervisor Matt Dobbs would joke that not knowing how to do something rarely slowed me down. I want to thank Matt for continuing to give me the opportunity to break increasingly larger things, while ensuring it happens with considerably less frequency. The ethos of the Winterland Lab has been one of the most inspiring elements of graduate school, and for that I thank everybody I've had the fortune of working alongside here, in particular: Amy Bender, Tijmen de Haan, Gavin Noble, Adam Gilbert, Graeme Smecher, JF Cliche, Kevin Bandura, and Maclean Rouble.

I am deeply indebted to the entire SPT-3G collaboration for their support, patience, and guidance – especially throughout the 2018 winter season that I spent at the South Pole. Thanks to John Carlstrom, Brad Benson, Tom Crawford, and Dan Marrone for allowing me drive the telescope(s) for a year; and to the operations team who put thousands of hours into ironing out every detail of the repair process following the "stopping event" that winter. Separately, I want to thank my fellow polies, who made that repair possible and also made Antarctica a much less harsh continent – Adam Jones, Sabrina Shemet, Johannes Werthebach, Robert Schwarz, and Hans Boenish. If it weren't for the late Steele Diggles, South Pole Machinist Extraordinaire, both the telescope and I would have spent 2018 sitting on our haunches; it was a privilege to have worked with Steele, and an honor to have spent the winter with him, I miss him dearly.

This thesis benefited considerably from conversations with, and access to specific work from, my colleagues on SPT-3G, Polarbear-2, and LiteBIRD: Graeme Smecher, for countless hours talking through DAN, firmware, electronics, and ~~terrible~~ excellent music; JF Cliche, for teaching me how to project manage; Daniel Dutcher, for providing his code for the initial SPICE template of the cryogenic circuit, and advice about parasitic capacitances; Amy Bender for, well, too much to list here, including memos I've drawn on for the noise analysis, efforts in her own cryogenic setups to validate crazy ideas, and as a steady and skeptical hand at the wheel of the operations group; Zhaodi Pan, for his FTS and time constant analysis data products and code; Adam Anderson, for help with crosschecks with processed data quality metrics; Amy Lowitz, for help understanding mK SQUID setups and a crucial late-night conversation about lithography defects; Jessica Avva, for her optical crosstalk analysis data products; John Groh, for conversations about SQUID dynamic impedance and wire-harness capacitances; Tucker Elleflot, for a ton of work over the last year to implement many of the theories surrounding SQUID performance and current sharing noise; Tijmen de Haan, for technical advice and invaluable discussions about LiteBIRD design; and Sasha Rahlin, for an enormous amount of `pydfmux` development work and GCP support, especially over 2018.

Fundamentally, graduate school is a selfish pursuit whose sacrifices are often mostly borne by those around us. My parents may recognize this only as the natural continuation of a history of love and support to give me the opportunity to be here in the first place, but it is more than that; and I continue to be grateful to them. Whatever challenges or difficulties are contained in the work below pale in comparison to the patience, support, and kindness of my partner, Marina Malkova.

ABOUT THE MANUSCRIPT

This thesis was typeset using LaTeX, and formatted based on the `classicthesis` style developed by André Miede.[1] The cover illustration is from the 2018 South Pole Winterover patch, designed by Robert Schwarz[2] and used with permission. Many of the figures were made using `matplotlib` [48] and PGF/Ti*k*Z [95]. Analyses were performed using `python` scientific packages [70, 98, 99].

1 http://www.miede.de
2 http://www.antarctic-adventures.de

*Dedicated to TYPE VIII errors,
and the gradual acceptance that even
very simple mazes have infinite possible paths.*

AUTHOR CONTRIBUTION

This thesis presents my work in areas critical to the development and success of the South Pole Telescope (SPT-3G) and Polarbear-2 instruments, and to the design of the LiteBIRD telescope. These efforts cannot be contextualized without the work of others within these collaborations, nor do they exist in a vacuum independent of that labour. Where it may otherwise be ambiguous within the text I indicate work done solely or dominantly by myself using the first person; work done in collaboration with others in the third person; and work done primarily by others through citations or by directly referencing those people. This section provides a general guide to my specific contributions in each chapter, and highlights work from others that I have drawn from or built off of.

Chapter 1 provides the scientific and theoretical background and context, and largely invokes historical work cited in the text.

Chapter 2 describes the SPT-3G and LiteBIRD instruments. Sections 2.1.3 and 2.2.2 are devoted specifically to detailing the scope and content of my contributions to both collaborations.

Chapter 3 describes well-established TES detector theory, although I introduce some new formalism to present results relevant to readout performance.

Chapter 4 presents the theoretical foundation for the present implementation of Digital Frequency Domain Multiplexing (DfMUX). Some of this theory is well-established, or has already been presented in papers I co-authored (specifically, [14]). Other elements are presented here for the first time, such as the theoretical description of Digital Active Nulling in the presence of digital latency (Section 4.6). This was a collaboration between myself and Graeme Smecher. I authored the resulting algorithm for operating the Digital Active Nulling feedback in this regime, which is used on SPT-3G and Polarbear-2, and is being developed for LiteBIRD.

Chapter 5 presents a detailed analytic description of crosstalk mechanisms in DfMUX systems. These derivations are my own, and improve upon the previous theoretical framework presented in Dobbs et al., 2012 [26]. This work distinguishes itself from Dobbs et al. in a number of ways that are now relevant in the higher multiplexing (and bandwidth) regime. Specifically, it addresses crosstalk cancellation mechanisms; consequences of non-ideal stray impedances; and incorporates projection effects from the complex demodulation. I also introduce a quantitative relationship between the crosstalk and scatter in the LC resonance fabrication, which will drive LC fabrication requirements for LiteBIRD. A key outcome of this study is that current efforts to reduce crosstalk by minimizing series stray inductance will spoil the cancellation between crosstalk mechanisms, and would lead to no-better or even worse crosstalk. Instead, I propose an alternative optimization strategy that can reduce crosstalk by a factor of three relative to present designs.

Chapter 6 presents an evaluation of SPT-3G instrument parameters and performance relative to theoretical expectations. It also presents a theory to explain LC resonance scatter and parasitic series resistance by edge effects due to lithographic defects. The analysis presented, and formulation of the edge effect theory, are my own work; though, I relied on critical resources for understanding the cryogenic lithography geometry provided by Amy Lowitz and Gavin Noble. There are a few sets of measurements in this chapter that are not my own – including the characterization of the focal plane detector time constants (led by Zhaodi Pan); measurements of SPT-3G crosstalk using optical sources (led by Jessica Avva and Amy Bender); and the initial theory for parasitic parallel capacitances in the LCs (by Daniel Dutcher). Any quantities such as those are credited to others directly in the text. Although I did not contributed directly to those analyses, the measurements were performed using tools I developed or co-developed as part of the `pydfmux` readout control software library. `pydfmux` is currently used to operate SQUIDs and tune detector arrays at dozens of laboratory test beds, as well as on the SPT-3G and POLARBEAR-2 telescopes, and will be adapted for the LITEBIRD system.

The `pydfmux` repository itself is approximately 65k lines of python and contains algorithms to perform the core functionality of detector and readout operation and provide a real-time interface to the electronics system and TES biases. It also tracks the book-keeping and performs the concurrency required to efficiently operate ∼15,000 detectors simultaneously. Within that repository are transfer functions calculated for the warm and cold electronics, and tools to track and evaluate instrument state and performance. Graeme Smecher developed the computing architecture, concurrency, and database models, while I wrote the algorithms that interface with cryogenic hardware, including those to operate and evaluate SQUIDs and TES detector arrays. In 2015 I hosted a summer-school style tutorial session over several weeks to introduce DfMUX users to the new ICE system and software, and traveled to support and teach users at national laboratories and universities throughout the next year. While I continue to be the primary author and manager of `pydfmux`, there have since been more than 30 individual contributors, with several dedicated developers who continue to modernize and improve the repository. The requirements of modern systems such as SPT-3G and POLARBEAR-2 mean that this algorithmic design is considerably more sophisticated than previous generations, however many of the algorithms I designed were informed by work done by my predecessors on the SPTPOL, POLARBEAR, and EBEX instruments. These instruments used the previous generation of readout electronics and software, written by Tijmen de Haan, James Kennedy, and Kevin MacDermid, among others. In addition to `pydfmux`, I devised and wrote substantial portions of the on-board (compiled C) firmware responsible for lower-level interactions between the control software, cryogenic hardware, and data products.

Chapter 7 evaluates the SPT-3G readout system noise performance, both in isolation and within the context of the SPT-3G detector parameters. This work, and in particular the three main findings of this study, are the product of my own analyses. These are (1), an additional source of readout noise due to a parasitic capacitive "current sharing" path (Section 7.2.5); (2), the relationship between the 220 GHz detector performance and boosted responsivity due to parasitic series impedance (Section 7.6), which resolves the question of why these detectors under-performed expectations; and (3), the quantitative relationship between readout noise and SQUID dynamic impedance. The primary output of this chapter is a full electronic circuit and noise model, which captures all relevant warm and cryogenic dynamics for predicting instrument readout noise. I have indicated in the text where the above work draws upon specific earlier work of others. The initial discovery of (a separate form of) current sharing noise was a collaborative effort between a large segment of the SPT-3G collaboration, and inspired my work to find different mechanisms [13]. Daniel

Dutcher provided invaluable early circuit models of capacitive parasitics in the LCs [31]. John Groh, while working on the Polarbear-2 instrument, first identified a relationship between SQUID output gain and SQUID dynamic impedance. In deriving the nuances in the amplifier noise contributions to the demodulation chain I benefited greatly from internal memos written by Amy Bender.

Chapter 8 applies the circuit and noise models validated on SPT-3G in Chapter 7 to forecast LiteBIRD readout noise performance and recommend specific detector and readout designs. This analysis is my own, but uses initial conditions provided by the LiteBIRD collaboration and calculated by others. In particular, the expected LiteBIRD photon noise, detector phonon noise, and radiative loading from the optical elements for each observing band are drawn from the LiteBIRD Sensitivity Calculation Version 28.0 document. This document is written primarily by Takashi Hasebe, Charles Hill, Tomotake Matsumura, Aritoki Suzuki, Kam Arnold, Johannes Hubmayr, Sophie Henrot-Versille and Yuki Sakurai.

I've made a number of contributions to the success of the SPT-3G project that aren't reflected directly in the topics discussed in this thesis. I was part of the team at FermiLab that conducted the integration and pre-deployment commissioning of the full receiver, where we found that deployed TES detectors were violating a crucial stability criterion (described in Sections 4.3 and 6.4.1). I took a primary role in showing this, and in developing strategies to sufficiently overcome this during the 2017 engineering run, in which we were able to perform initial sky observations and several critical noise and systematics studies. In 2017 I traveled to the South Pole for the decommissioning of SPTpol and deployment of SPT-3G, and to perform on-sky commissioning. In 2018 I returned to assist with the replacement of the problematic components and re-deployment of a new focal plane. During the 2018 season I was a "winterover," deployed for 10 months to the Amundsen-Scott Research Station at the South Pole in Antarctica to operate the South Pole Telescope, which included SPT-3G and the South Pole segment of the Event Horizon Telescope (EHT). During this time I developed techniques to improve SPT-3G observing efficiency by more than 10%. In March of that winter a telescope drive system fault resulted in destruction of the thermal standoffs supporting the sub-Kelvin stage of the SPT-3G focal plane. Over the course of four months I led what is likely the most extensive winter repair of a scientific instrument at the South Pole to date.[3] During that repair we were able to remove the focal plane and repair the telescope drive system in time to perform scheduled observations with EHT. The focal plane itself was repaired, reinstalled, and SPT-3G was observing again by mid-July.

Although this work focuses on the SPT-3G instrument, my contributions to the readout system architecture and design have been equivalently utilized within the Polarbear-2 collaboration, of which I am also a member, credited as a "builder," and co-author on Polarbear-2 instrument and science papers. I am also a co-author on post-2018 Event Horizon Telescope collaboration outputs that utilize data taken during the 2018 winter observing season.

3 This wouldn't have been possible without the extensive support and direction from the collaboration off-continent, and assistance from fellow "polies:" Steele Diggles, Adam Jones, Sabrina Shemet, Johannes Werthebach, Hans Boenish, and Robert Schwarz.

CONTENTS

Abstract ii

Abrégé ii

Acknowledgments iii

Author Contribution vi

List of Figures xiv

List of Tables xviii

1 PARAMETERIZING OUR UNIVERSE 1
- 1.1 Inflationary ΛCDM cosmology 3
- 1.2 The Cosmic Microwave Background 4
- 1.3 Cosmic Microwave Background polarization 8
  - 1.3.1 E-mode and B-mode polarization patterns 10
- 1.4 Primordial inflationary gravity waves 15
- 1.5 Foregrounds 19
- 1.6 Towards a measurement of inflationary gravity waves 21

2 THE SPT-3G INSTRUMENT AND LITEBIRD TELESCOPE 23
- 2.1 The South Pole Telescope 23
  - 2.1.1 The SPT-3G instrument 28
  - 2.1.2 SPT-3G science forecasts 31
  - 2.1.3 Contribution to SPT-3G 31
- 2.2 The LiteBIRD satellite 34
  - 2.2.1 LiteBIRD science 35
  - 2.2.2 Contribution to LiteBIRD 38

3 TRANSITION EDGE SENSORS 39
- 3.1 TES power balance 39

3.2 Electrothermal feedback 42
3.3 TES stability 43
3.3.1 Minimum DC stable R_{frac} 45
3.4 Responsivity 46
3.5 Phonon and photon noise 47
3.5.1 Detector phonon noise 47
3.5.2 Photon noise 47
3.5.3 TES Johnson noise 49
3.6 Multiplexing 49

4 READOUT THEORY 52
4.1 Frequency Domain Multiplexing 52
4.2 Cryogenic filter design 53
4.2.1 Ideal cryogenic filter parameters 54
4.2.2 Legacy cryogenic filter design 55
4.2.3 Current generation 68x cryogenic filter design 55
4.3 Modified dynamic stability criterion 57
4.3.1 Designing for stability 59
4.4 Cold amplification using SQUIDs 60
4.4.1 Basic SQUID theory 60
4.4.2 Non-linear SQUID response 61
4.4.3 SQUID tuning 62
4.4.4 Challenges in using SQUIDs for DfMUX 65
4.5 Static Nulling 65
4.6 Digital Active Nulling 67
4.6.1 DAN feedback 69
4.6.2 DAN phase 70
4.6.3 DAN gain 70
4.6.4 DAN Stability Criteria 71
4.6.5 Anti-Nulling 75
4.6.6 Satisfying the Stability Criteria 75
4.7 Network analysis and bias frequency selection 78
4.8 Warm electronics 82

5 CROSSTALK IN FREQUENCY DOMAIN MULTIPLEXING 85
5.1 Crosstalk circuit model and science signal 86
5.1.1 Science signal 87
5.2 Leakage current crosstalk 88
5.2.1 Instability due to leakage power 89
5.3 Leakage power crosstalk 89
5.4 "Tuning out" Z_{com} 90
5.5 Crosstalk cancellation 91
5.6 Crosstalk frequency scheduling 93
5.7 Low L_{stray} 94
5.8 Crosstalk removal 95
5.9 Crosstalk sensitivity to LC frequency scatter 97

6 SPT-3G PARAMETER CHARACTERIZATION 99
6.1 Built SQUID properties 99
6.1.1 SQUID dynamic impedance 101
6.2 Lithographic filter properties 103
6.2.1 Systematic LC frequency scatter 104
6.2.2 Statistical LC frequency scatter 104
6.2.3 Geometric susceptibility of LC resonators to defects 109
6.2.4 Missing frequencies in SPT-3G 113
6.2.5 Parasitic impedance of lithographic filters 113
6.3 Built TES detector properties 116
6.4 SPT-3G stability 119
6.4.1 DC stability 119
6.4.2 Dynamic stability 121
6.5 SPT-3G crosstalk performance 123
6.6 Crosstalk and stability performance summary 128

7 SPT-3G NOISE 129
7.1 Individual readout noise sources 130
7.2 Transfer functions 130
7.2.1 Cryogenic capacitances to ground 137
7.2.2 Demodulation chain transfer function 138

7.2.3 Carrier transfer function 141
7.2.4 Nuller transfer function 143
7.2.5 Current sharing transfer function 146
7.2.6 Modulation penalty 150
7.3 Full SPT-3G readout noise model in NEI 154
7.4 SPT-3G readout NEI 161
7.4.1 Low dynamic impedance operation 164
7.4.2 SPT-3G readout NEI when observing 166
7.5 Interpreting NEI in DfMUX systems 168
7.6 Excess responsivity 170
7.7 SPT-3G readout noise performance summary 170
7.8 Towards a higher-performing system 173

8 LITEBIRD NOISE FORECASTING 174
8.1 Baseline LiteBIRD DfMUX Configuration 175
8.2 NEI performance forecasting 177
8.3 NEI vs detector parameters 178
8.4 Forecasting responsivity 185
8.5 LiteBIRD noise performance vs detector parameters 187
8.6 LiteBIRD noise performance forecast by band 190
8.7 Speculative optimization: bandwidth compression 193

9 CONCLUDING REMARKS 195
9.1 Digital Active Nulling 195
9.2 Crosstalk 196
9.3 Lithography performance 196
9.4 SPT-3G readout noise 197
9.5 Responsivity 198
9.6 LiteBIRD forecasting 198
9.7 The path forward 199

A COMPARISONS BETWEEN DOBBS2012 AND THE PRESENT CROSSTALK MODEL 202

B DESIGNING FOR NON-LINEARITY 205

B.1 Third order intermodulation distortion 205
B.2 Base frequency 206

C BUCK REGULATOR NOISE 207

Bibliography 208

LIST OF FIGURES

Figure 1.1 The cosmic microwave background, as seen in temperature by the PLANCK satellite. 6
Figure 1.2 The CMB angular power spectrum. 7
Figure 1.3 Producing net polarization via Thomson scattering. 9
Figure 1.4 The CMB sky polarization vector field. 10
Figure 1.5 E- and B- mode decomposition of a polarization vector field 11
Figure 1.6 Quadrupolar temperature distributions from density perturbations and gravity waves. 13
Figure 1.7 Simulations of polarization vector fields from scalar and tensor Fourier modes. 14
Figure 1.8 Simulated angular power spectra for the auto-correlations and cross-correlations between T, E, and B mode CMB anisotropies. 16
Figure 1.9 Cosmic history through reionization. 17
Figure 1.10 Simulated B-mode lensing and primordial inflationary gravity wave (IGW) power spectra. 18
Figure 1.11 Temperature foregrounds to the primary CMB signal at 1 degree scales. 19
Figure 1.12 Polarization foregrounds for B-mode measurements of the reionization bump and recombination peak. 20
Figure 2.1 The SOUTH POLE TELESCOPE. 24
Figure 2.2 The Antarctic Plateau. 26
Figure 2.3 The 2018 South Pole winterover crew. 27
Figure 2.4 The SOUTH POLE TELESCOPE receiver and detector cutaway. 29
Figure 2.5 The SPT-3G survey field. 30
Figure 2.6 CMB temperature and polarization power spectra forecasts for SPT-3G. 32
Figure 2.7 Delensing forecasts for combinations of SPT-3G and BICEP/*Keck Array*. 33

Figure 2.8 LiteBIRD spacecraft overview. 35
Figure 2.9 Target LiteBIRD observing band sensitivity. 36
Figure 2.10 Projected LiteBIRD contribution to measurements of the BB spectrum. 37
Figure 3.1 TES resistance vs temperature curve. 40
Figure 3.2 TES power-balance graphic. 41
Figure 3.3 TES load curves. 42
Figure 3.4 Generalized TES bias circuit diagram. 44
Figure 4.1 Simplified DfMUX circuit. 53
Figure 4.2 General amplitude-modulation diagram. 54
Figure 4.3 Lithographic filter elements. 56
Figure 4.4 Cryogenic readout hardware. 57
Figure 4.5 Comparison between 16x and 68x multiplexing resonances. 58
Figure 4.6 SQUID biasing schematic. 61
Figure 4.7 SQUID response function. 62
Figure 4.8 SQUID tuning plots. 64
Figure 4.9 Simplified fMUX diagram that includes a nulling circuit. 66
Figure 4.10 DAN bandwidth demonstration. 68
Figure 4.11 Full DfMUX circuit diagram, including DAN. 69
Figure 4.12 DAN bandwidth as a function of DAN gain. 72
Figure 4.13 DAN feedback block diagram. 73
Figure 4.14 Numerical calculations of the DAN transfer functions as a function of gain and latency. 74
Figure 4.15 Anti-nulling regions of DAN feedback. 76
Figure 4.16 DAN tuning flowchart. 77
Figure 4.17 SPT-3G DAN gain and loopgain distributions. 79
Figure 4.18 Carrier and nuller network analyses and synthesized comb impedance. 81
Figure 4.19 ICE warm readout electronics. 83
Figure 5.1 Cryogenic filter circuit. 86
Figure 5.2 Crosstalk component phase and magnitude. 92
Figure 5.3 Fractional crosstalk contributions. 93
Figure 5.4 Crosstalk as a function of resonance spacing. 94
Figure 5.5 Crosstalk for a linear frequency scheduling. 95

Figure 5.6 Crosstalk for a minimized L_{stray}. 96
Figure 5.7 Crosstalk for a crosstalk-optimized system. 96
Figure 5.8 Crosstalk with LC frequency scatter. 98
Figure 6.1 SPT-3G SQUID parameter histograms. 100
Figure 6.2 SA13 SQUID $V(\phi)$ curves (high and low dynamic impedance). 102
Figure 6.3 Photos of LC Lithography defects. 106
Figure 6.4 Scatter in SPT-3G LC resonance frequencies (pooled standard deviation). 107
Figure 6.5 Scatter in SPT-3G LC resonance frequencies (by batch and mask version). 108
Figure 6.6 Lithographic capacitor geometry. 111
Figure 6.7 Lithography defect model for LC resonance scatter. 112
Figure 6.8 Missing resonances in the SPT-3G readout. 114
Figure 6.9 z_{lcr} as a function of bias frequency, with LC defect model. 115
Figure 6.10 SPT-3G focal plane detector normal resistance (R_n) as a function of bias frequency. 117
Figure 6.11 Effective detector time constants used on SPT-3G. 118
Figure 6.12 Thévenin equivalent series impedance for detectors in the SPT-3G receiver, binned by LC channel. 120
Figure 6.13 Histogram of the DC stability of SPT-3G detectors. 120
Figure 6.14 Histograms of the dynamic stability of SPT-3G detectors. 122
Figure 6.15 Histogram of the electrical term in SPT-3G detector dynamic stability. 123
Figure 6.16 Minimum stable R_{frac} for SPT-3G detectors. 124
Figure 6.17 The minimum stable τ_{eff} for SPT-3G detectors. 125
Figure 6.18 Zoom-in of the minimum stable τ_{eff}. 125
Figure 6.19 Comparison of measured and simulated crosstalk in SPT-3G. 127
Figure 7.1 Electrical circuit model schematic. 136
Figure 7.2 Capacitance to ground in the lithography. 137
Figure 7.3 2D layout of the LC Chip design used in SPT-3G. 139
Figure 7.4 Cryogenic circuit admittance simulations. 140
Figure 7.5 Demodulation signal path circuit diagram. 141
Figure 7.6 The output filter (χ_{output}) as a function of Z_{dyn}. 142

Figure 7.7 Measurements of χ_{output} in SPT-3G. 142
Figure 7.8 Analytic carrier transfer functions H_c^{Vcomb} and H_c^{Vtes}. 143
Figure 7.9 Analytic carrier transfer function H_c^{I}. 144
Figure 7.10 The analytic nuller transfer function. 145
Figure 7.11 Simplified current sharing circuit diagram. 147
Figure 7.12 Measured and simulated current sharing factor. 148
Figure 7.13 Simulated current sharing factor with parasitic current modifications. 149
Figure 7.14 Complete SPT-3G noise model and components. 155
Figure 7.15 SPT-3G noise component breakdown. 156
Figure 7.16 Measured SPT-3G readout noise in NEI 162
Figure 7.17 Measured SPT-3G noise alongside the SPT-3G noise model expectation. 163
Figure 7.18 SPT-3G readout noise with low Z_{dyn} SQUIDs. 165
Figure 7.19 Readout noise correction between saturated and in-transition operation. 167
Figure 7.20 A comparison between readout noise, non-readout noise, and total noise, in SPT-3G. 168
Figure 7.21 Percentage increase in noise due to SPT-3G readout. 169
Figure 7.22 Non-readout NEI at the TES vs boosted responsivity. 171
Figure 8.1 An inductive bias circuit design. 177
Figure 8.2 Projected NEI overview. 179
Figure 8.3 LiteBIRD NEI breakdown for the baseline configuration. 180
Figure 8.4 LiteBIRD NEI breakdown for the mK SQUID noise configuration. 181
Figure 8.5 LiteBIRD NEI breakdown for the 30nH SQUID input inductance configuration. 182
Figure 8.6 LiteBIRD NEI breakdown for the 10nH input inductance configuration. 183
Figure 8.7 LiteBIRD NEI projections as a function of $(R_{\mathrm{TES}} + R_s)$. 184
Figure 8.8 Responsivity in the 40 GHz band vs R_{TES} and R_s. 186
Figure 8.9 Projected noise increase in the 40 GHz and 402 GHz bands. 188

Figure 8.10 Δ% noise increase for the 40 GHz LiteBIRD band across R_{TES} and R_s parameter space. 189
Figure 8.11 Projected crosstalk in a LiteBIRD-like instrument with a compressed bandwidth of 1 MHz to 3 MHz. 194
Figure A.1 A crosstalk model comparison with Dobbs2012 (early SPT-3G design parameters). 203
Figure A.2 A crosstalk model comparison with Dobbs2012 (built SPT-3G parameters). 204

LIST OF TABLES

Table 1.1 Cosmological parameters derived from measurements of the CMB. 8
Table 2.1 The SPT-3G survey map depths. 30
Table 3.1 Detector parameters and properties summary table. 51
Table 7.1 Carrier-chain noise sources. 131
Table 7.2 Nuller-chain noise sources. 132
Table 7.3 Demodulation-chain noise sources. 133
Table 7.4 Cryogenic signal path noise sources. 134
Table 7.5 Carrier chain noise sources referred to NEI at the SQUID summing junction. 157
Table 7.6 Nuller chain noise sources referred to an NEI at the SQUID summing junction. 158
Table 7.7 Demodulation chain noise sources referred to NEI at the SQUID summing junction. 159
Table 7.8 Noise sourced from cryogenic system components referred to NEI at the SQUID summing junction. 160
Table 8.1 LiteBIRD readout noise projections by observing band assuming R_{TES}=600 mΩ and R_s=300 mΩ. 191
Table 8.2 LiteBIRD readout noise projections by observing band assuming R_{TES}=600 mΩ and R_s=200 mΩ. 192

1 PARAMETERIZING OUR UNIVERSE

Observations of the known universe indicate that it is homogeneous and globally isotropic, such that even causally separated regions appear to have the same underlying composition and structure. That structure is broadly composed of four classes of matter-energy:

ORDINARY BARYONIC MATTER that is non-relativistic, and interacts via the electromagnetic force. It is also often called "luminescent matter," because it is the basis of everything directly observable via the electromagnetic spectrum.

COLD DARK MATTER (CDM) that is also non-relativistic, but does not interact electromagnetically. Instead, CDM interacts primarily through the gravitational force. Evidence of CDM contributions to our universe come from observations at all scales, first hinted at in the 1930s with measurements of the rotational velocities of nearby galaxies, and later formalized and given the name CDM in the 1980s [7, 17, 18, 69].

RADIATION energy in the form of electromagnetic waves and relativistic neutrinos.

DARK ENERGY (Λ) a form of vacuum energy that is thought to drive the accelerating expansion of the universe. Dark energy presents as a constant energy per unit volume. Consequently, unlike other forms of matter-energy, dark energy density is not diluted by the expansion of the universe. There are a number of theoretical mechanisms through which dark energy can arise, including from the field equations of general relativity, but the first observational evidence came in 1998 with measurements of supernovae, which showed the expansion of our universe to be accelerating [71, 84].

Observations additionally indicate that the topology of our universe is consistent with euclidean space, implying no (or nearly no) global space-time curvature [20, 76]. Finally, our universe is expanding, such that the total size is increasing as a function of time: all non-gravitationally-bound objects are receding from one another as a function of their distance from each other, and this process is accelerating.

The dynamics of this universe, though not its initial conditions, are described by the ΛCDM model of Big Bang cosmology, which accounts for the accelerating expansion of the universe, the various forms of matter-energy, and the evolution of large scale structure. The size of the universe is parameterized by the scale factor $a(t)$, such that $a(t_0) = 1$ at present day. The relative energy densities of the constituent components have changed over time as the universe expands. These dynamics can be described by the Friedmann–Lemaître–Robertson–Walker (FLRW) equation:

$$H^2 = H_0^2 \left(\frac{(\Omega_{\mathrm{CDM},0} + \Omega_{\mathrm{bary},0})}{a^3} + \frac{\Omega_{r,0}}{a^4} + \Omega_{\Lambda,0} \right) , \tag{1.1}$$

where H is the Hubble parameter and H_0 is the Hubble constant,

$$H(t) = \frac{\dot{a}(t)}{a(t)} \tag{1.2}$$

$$H_0(t) = \frac{\dot{a}(t_0)}{a(t_0)} . \tag{1.3}$$

The parameters $\Omega_{x,0}$ characterize the relative energy density in the universe for each constituent component today. Cold dark matter is given by $\Omega_{\mathrm{CDM},0}$; baryonic matter by $\Omega_{\mathrm{bary},0}$; radiation by $\Omega_{r,0}$;[1] and dark energy by $\Omega_{\Lambda,0}$. These are dimensionless parameters, formulated by normalizing the energy densities of each component (ρ_x) by the present day total energy density ("critical density," ρ_{crit}):

$$\Omega_x \equiv \frac{\rho_x(t_0)}{\rho_{\mathrm{crit}}} = \left(\frac{8\pi G}{3H_0^2} \right) \rho_x(t_0) , \tag{1.4}$$

where G is the gravitational constant. In this formulation, the terms in the parenthesis of Equation 1.1 sum to 1 at present day.

Equation 1.1 is a deceptively simple model that describes the chronology of our universe. By drawing on observations to measure the components of this equation precisely we can learn about our cosmological past and future, and understand how structure evolved and collapsed to form complex features such as our galaxy. However, this model fails to describe our universe in a few important respects.

THE HORIZON PROBLEM: ΛCDM can allow us to "play the tape backwards" to understand structure *evolution* in the universe, but it does not offer an explanation for the initial conditions. In particular, why portions of our observable universe that are not in causal contact appear, nevertheless, to have the same local properties. In the expansion

1 Where for our purposes, in the early universe, neutrinos can be considered massless and highly relativistic, and so $\Omega_{r,0} = \Omega_{\gamma,0} + \Omega_{\nu,0}$ [94].

modeled by Equation 1.1, these portions of the universe would never have had a chance to reach equilibrium through interaction (to thermalize), so by what means do they acquire such global homogeneity?

THE FLATNESS PROBLEM: Similarly, the topological flatness of our universe is peculiar because it requires a specific energy density. Analogous to how local space-time topology is curved around objects with extremely high mass density, the global topology is also a function of the global energy density. It appears unlikely for our universe to be so topologically flat if there were no mechanism to force it so.

INITIAL ANISOTROPIES: Similar to the horizon problem – a *perfectly isotropic* universe would have thermalized as it expanded, and today would remain much more locally isotropic than observed, with much less large scale structure. One explanation is that initial structure was seeded by local perturbations larger than the horizon of thermal interaction, but simple ΛCDM cosmology doesn't explain the source of these initial anisotropies.

A modification to this theory, *inflationary* ΛCDM, posits a mechanism to provide global homogeneity, local anisotropy, and an explanation for the apparent flatness of our universe's topology.

1.1 INFLATIONARY ΛCDM COSMOLOGY

Cosmological Inflation is a theory of the very early universe, developed in the 1970s and 1980s, that resolves a number of cosmological puzzles; among them, the Horizon Problem, Flatness Problem, and the question of initial anisotropy [36, 55, 90]. The dominant inflationary model today is known as "slow-roll" inflation [3, 59]. This theory suggests that the universe was initially in thermal equilibrium and causally connected, but at a very early time ($\sim 10^{-36}$ seconds after the Big Bang singularity, from which our universe began) it underwent a period of *superluminal expansion*. Slow-roll inflation is theorized to have been driven by the decay of a scalar "inflaton field," present after the Big Bang singularity. The resulting exponential expansion flattened any initial curvature of the topology.[2] It also offers an explanation for the

2 Since the expansion of the space-time metric outpaced the expansion of the space-time *horizon*, any locally observable curvature was minimized. This is analogous to how measurements over the surface area of a stamp glued to a marble will readily reveal substantial curvature; but those same measurements conducted over a stamp glued to an earth-sized sphere will not.

initial anisotropy – quantum fluctuations in the inflaton field, which would otherwise have rapidly thermalized, were stretched beyond the thermalization horizon during the inflationary period [11, 37, 42, 91].

The inflationary period of exponential expansion eventually ceased, after which the universe continued to expand at a slower rate, but the original quantum fluctuations were locked-in as super-horizon scale anisotropies. Horizon scales eventually expanded to include these anisotropies, which generated local structure as they began to interact gravitationally.

1.2 THE COSMIC MICROWAVE BACKGROUND

Notice that, although we haven't yet specified the relative contributions of matter, radiation, or dark energy, Equation 1.1 indicates that the universe can be considered as taking place in three separate eras. At sufficiently early time, when the scale factor $a(t)$ is small, the energy density of the universe is dominated by radiation. As it expands, radiation energy is diluted: wavelengths of light propagating through the universe expand and are *redshifted* to lower frequencies. This redshift can be parameterized in terms of the scale factor,

$$z(t) = \frac{1}{a(t)} - 1\,, \tag{1.5}$$

and serves as a proxy to look-back time, such that light emitted at redshift $z(t)$ and observed now ($z = 0$) is shifted in wavelength by a factor of

$$\frac{\lambda_{\text{observed}}}{\lambda_{\text{emitted}}} = 1 + z(t) = \frac{1}{a(t)}\,. \tag{1.6}$$

At some time later the universe achieves matter-radiation energy equivalence, but it is still extremely energetic – too energetic for charged particles to form neutral atoms. Instead, the universe is a mixture of photons and baryons that form a tightly-coupled plasma, and gravitationally-interacting dark matter. The density of this medium is anisotropically distributed, with those initial anisotropies sourced by quantum fluctuations in the pre-inflationary era.

The density anisotropies propagate acoustically through the photo-baryonic plasma, undergoing a series of harmonic oscillations as over-densities collapse gravitationally, build pressure, and expand again due to radiation pressure. As the dark matter (which interacts gravitationally but is not susceptible to radiation pressure) clumps together, it alternately dampens some oscillations of the photo-baryonic plasma, and enhances others [46].[3]

The degree of pressure with which over-dense regions rebound is mediated by how well coupled the photons and baryons are by free electrons. As the plasma cools, it becomes progressively more optically thin: the mean free path of the photons grows, dampening each successive oscillation. At approximately z =1,100 the universe cools enough for the free electrons to form neutral hydrogen atoms, fully decoupling the photo-baryonic plasma. This period is known, for historical reasons, as "recombination."[4]

After recombination, photons stream freely through the electrically neutral universe from their last scattering from the surface of the photo-baryonic plasma. They are observed today as a cosmic microwave background (CMB), emanating from all directions, having been redshifted down from much higher frequencies in the intervening ∼13.5 billion years. Figure 1.1 shows an all-sky map of the CMB, as measured with the PLANCK satellite telescope in 2015. This is an image of the last surface from which photons scattered in the early universe, often just called the "last scattering surface." It shows that the medium of the early universe is nearly perfectly isotropic and homogeneous. It contains minute deviations of on the order of one in 10^4, which trace slight under- and over- densities of the plasma, corresponding to acoustic waves in the photon-baryonic plasma at the time of recombination.

The measurement of spatial anisotropies in the CMB can be decomposed into spherical harmonics

$$T(\theta, \varphi) = \sum_{\ell,m} a_{\ell m} Y_{\ell m}(\theta, \varphi) \,, \tag{1.7}$$

where $T(\theta, \varphi)$ is the temperature as a function of spherical coordinates, $Y_{\ell m}(\theta, \varphi)$ are Laplace's spherical harmonics, and the $a_{\ell m}$ coefficients describe the mean temperature of the CMB at each (ℓ,m) – multipole and azimuthal number. The multipole number is inversely related to angular size on the sky, such that $\ell = 100$ corresponds to approximately 1 degree scales. The amplitude and angular scale of spatial anisotropies are found by taking an angular power spectrum,

$$C_\ell = \frac{1}{2\ell + 1} \sum_{m=-\ell}^{\ell} a_{\ell m} a^*_{\ell m} \,, \tag{1.8}$$

3 During even-numbered harmonics of the primary oscillation, the photo-baryonic and dark matter densities are anticorrelated, reducing the amplitude of the oscillation; while the opposite is true for odd-numbered harmonics.

4 Despite the fact that it is the *first* combination of protons and electrons.

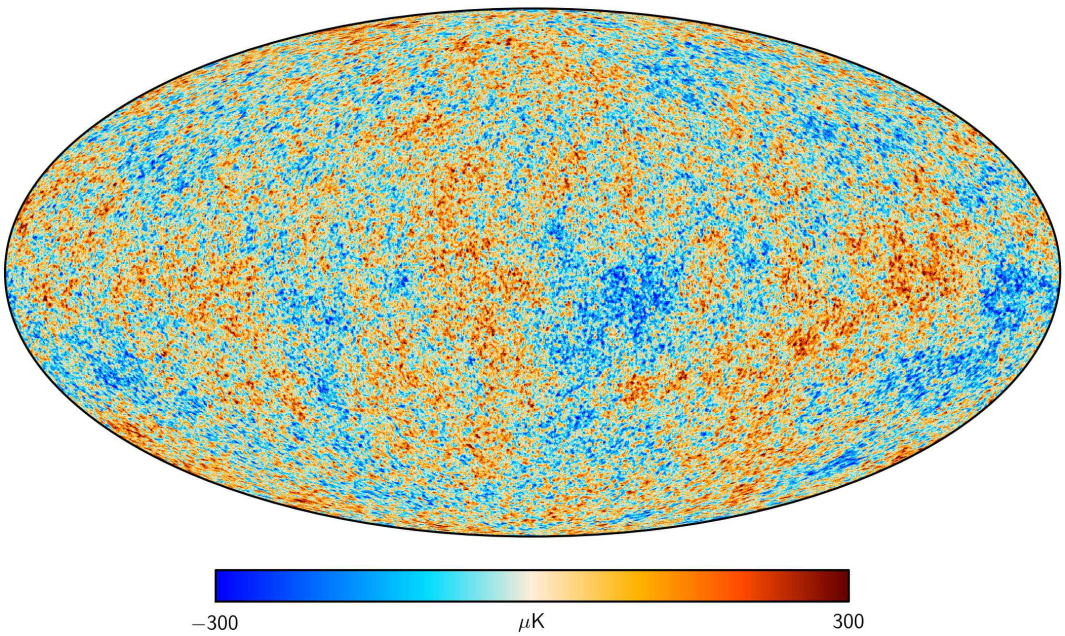

Figure 1.1: The cosmic microwave background, as seen in temperature by the PLANCK satellite. Cold and hot regions indicate slight over- and under- densities in the photo-baryonic plasma at the time of recombination. The colour scale indicates temperature variation from the mean value (a $\sim$2.7 K black-body, [64]). These are interpreted in the context of Inflationary ΛCDM as the acoustic oscillations from anisotropies, originally sourced by quantum fluctuations that were stretched to super-horizon scales during inflation. Image from ESA and the Planck Collaboration, Planck Collaboration et al., 2018 [77].

where C_ℓ is the amplitude of fluctuations at angular scales of ℓ. This is plotted in Figure 1.2; the *acoustic peaks* of the CMB are clearly discernible as local maxima.

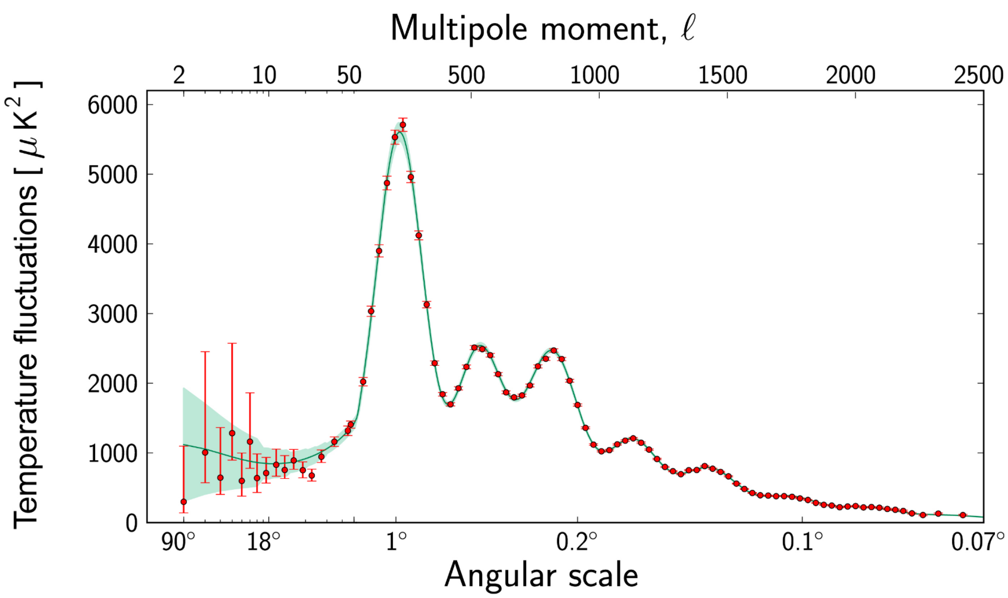

Figure 1.2: The angular power spectrum of CMB temperature anisotropies is a measurement of the amplitude and angular scale of acoustic oscillations in the photo-baryonic plasma at the time of recombination. These are the *acoustic peaks*, and they contain a wealth of information about the properties of the early universe. Image from ESA and the Planck Collaboration, Planck Collaboration et al., 2014 [74].

The primary peak is the horizon scale during recombination – corresponding to the perturbation mode on the sky that had time to fully compress before recombination. Each successive peak is an acoustic harmonic – indicating modes that had time to oscillate. These are dampened substantially by *Silk damping*, the diffusion of photons between modes as the mean free path grows and the photo-baryonic matter decouples at later times [46, 87]. Measurements of the CMB blackbody temperature, and the angular scale and amplitude of the acoustic peaks, can be used to precisely calculate a set of cosmological parameters that parameterize the ΛCDM model. Table 1.1 shows an excerpt of recently derived cosmological parameters from Planck Collaboration et al., 2018 [76].

Recent cosmological parameter constraints

Parameter	Description	Value (68% limits)
H_0 [km s^{-1}Mpc^{-1}]	Hubble constant	67.66 ± 0.42
$\Omega_{\mathrm{bary},0}$	Current baryon density	0.0493(6)
$\Omega_{\mathrm{CDM},0}$	Current cold dark matter density	0.265(7)
$\Omega_{\mathrm{r},0}$	Current radiation ($\Omega_{\gamma,0} + \Omega_{\nu,0}$) Density	$5.38(15)\times10^{-5}$
$\Omega_{\Lambda,0}$	Current dark energy density	0.6889 ± 0.0056
$\rho_{\mathrm{crit},0}$ [g cm^{-3}]	Critical density	$8.545(5)\times10^{-30}$
t_0 [Gyr]	Age of the universe	13.787 ± 0.02
z_{eq}	Redshift of matter/radiation equality	3387 ± 21

Table 1.1: Excerpt of cosmological parameters published by the Planck Collaboration. Includes derived parameters that use data from non-CMB experiments, and assumes a ΛCDM model. Values are 68% confidence interval limits unless otherwise noted [76].

1.3 COSMIC MICROWAVE BACKGROUND POLARIZATION

Recombination happens relatively rapidly, which is why the acoustic peaks are so visible. However, it is not instantaneous: there is a period during which the universe transitions from being optically thick to being optically thin. Because of this transition, some fraction of the photons detectable today will have been emitted when the universe was still optically thick, and simply avoided additional scattering. As the universe transitions through recombination that fraction increases. Temperature fluctuations of the CMB therefore record a weighted projection of the underlying density field over the duration of this transition, rather than a true snapshot, or slice in time.

Polarization of the CMB occurs via Thomson scattering between photons and free electrons. However, for photons in a locally isotropic area, this scattering produces no *net polarization*. Net polarization due to Thomson scattering can only occur if there is a spatial asymmetry in the intensity of the incoming photons. Such asymmetry can arise if the photons are being emitted from surfaces with a spatial temperature asymmetry (Figure 1.3).[5] Put another way – net polarization in the CMB is produced by quadrupole anisotropies in the photon

5 Or a spatial asymmetry in gravitational potential, as discussed in Section 1.3.1.

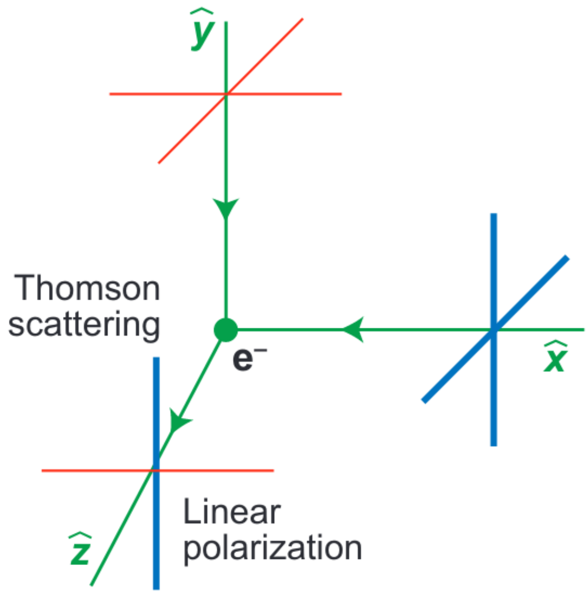

Figure 1.3: All Thomson scattering generates polarization, but a net linear polarization is only possible if there is a spatial asymmetry to the intensity of incoming photons. In the above figure, photons emitted from two different regions, one hot (red) and one cooler (blue), scatter from the same electron, generating two different linear polarizations. Because the sources are thermal there are more photons from the hot region that are scattered in this way, generating a net linear polarization. In general this net polarization can be achieved by quadrupolar temperature anisotropies in the medium emitting the source photons. Image from Hu and White, 1997 [47].

temperatures [47]. This happens when enough photons are able to diffuse from two different anisotropic regions to scatter from the same free electron. Such diffusion is only possible during the very end of recombination, when the universe is quite optically thin and the mean free paths of photons are large.

As such, the polarization anisotropies of the CMB capture the surface of last scattering in a much more narrow slice of time, and more faithfully render the density perturbations at the time of recombination. They are also sensitive to phenomena in the early universe that cannot be detected via temperature fluctuations alone, described next.

1.3.1 *E-mode and B-mode polarization patterns*

CMB polarization measurements produce a vector field built from individual measurements of Stokes Q and U parameters[6] using linearly polarized detectors (Figure 1.4). The vector

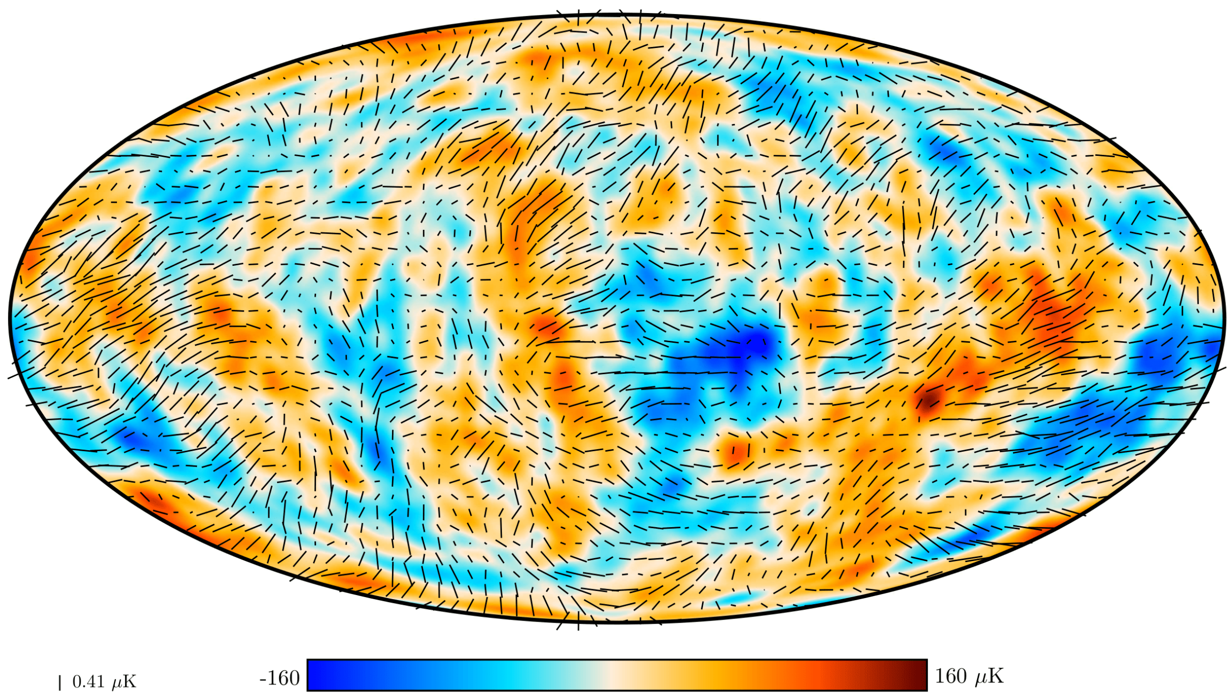

Figure 1.4: A representation of the CMB polarization as a vector field, produced from the Planck satellite. Image from ESA and the Planck Collaboration, Planck Collaboration et al., 2018 [77].

6 Stokes parameters, often defined in terms of a vector (I, Q, U, V), are used to describe the intensity and polarization of electromagnetic radiation, where I corresponds to total intensity, the Q and U vectors are a basis for the linear polarizations, and V parameterizes the circular polarization state.

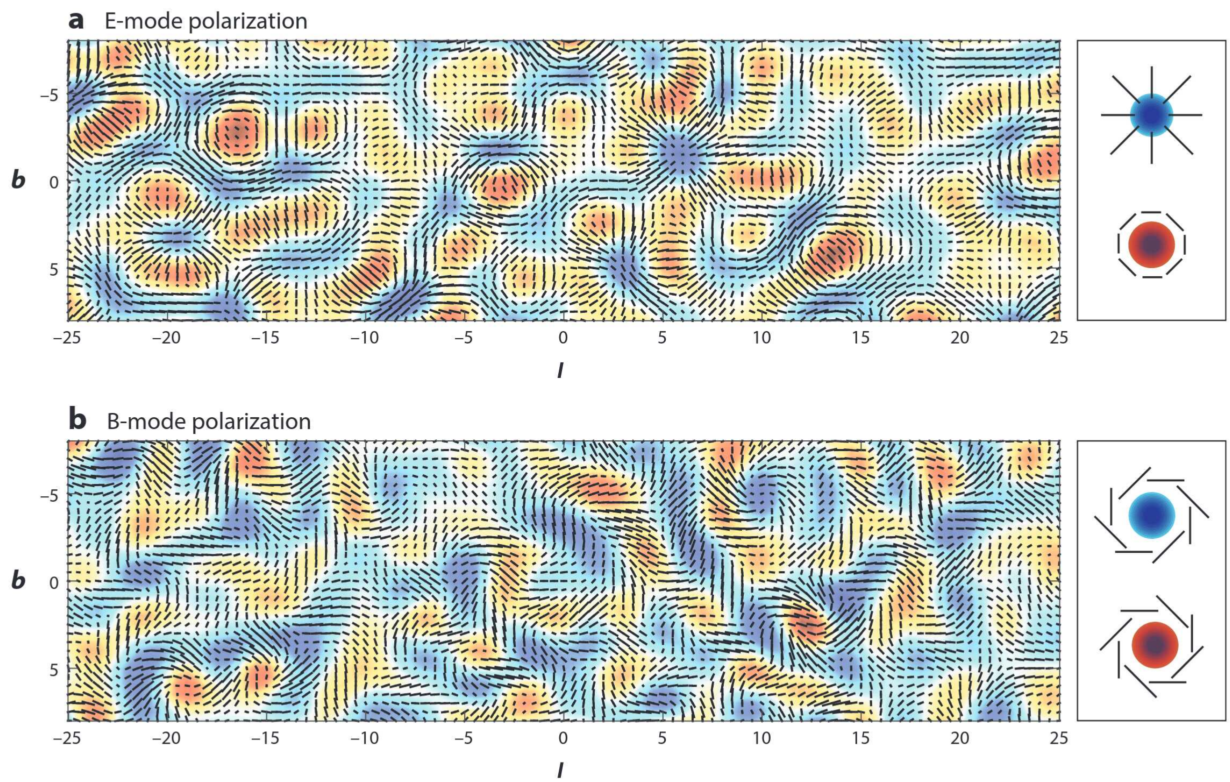

Figure 1.5: The E- and B- mode components are orthogonal, and form a basis for observed polarization fields: any CMB polarization measurement is a linear combination of E- and B- modes. Shown here is a simulated decomposition of a patch of polarized sky into the E- and B- mode components. Notice the handedness of B-modes. Image from Kamionkowski and Kovetz, 2016 [54].

field can be decomposed into a basis composed of curl-free (E-mode) and divergence-free (B-mode) components.[7] Example polarization fields composed of E-modes only and B-modes only are shown in Figure 1.5.

As discussed in the previous section, polarization of the CMB manifests from quadrupole anisotropies in the intensities of incoming photons to the last scattering surface. This can be generated in three ways:

SCALAR DENSITY PERTURBATIONS of the medium produce underlying hot-and-cold temperature variations of the blackbody emitter, and therefore quadrupole intensity anisotropies (Figure 1.6). These produce E-mode polarization patterns as well as the acoustic modes responsible for total intensity anisotropies (temperature spectrum, TT). Therefore the E-mode power spectrum (EE) is tightly correlated with the TT power spectrum.[8]

VECTOR-MODE PERTURBATIONS would be generated by vortical motions in the photo-baryonic plasma. Such perturbations would generate primarily B-mode polarization patterns *at small angular scales* [47]. An inflationary era would dampen these modes, but they are predicted by some alternative theories of the early universe, including those based on cosmic- or super- strings. While analysis of existing data has placed constraints on these modes [73], they have not been detected and won't be the focus here.

TENSOR-MODE PERTURBATIONS in the space-time metric arising from gravitational waves can also generate quadrupolar distributions in the observed photon temperatures. This happens because the stretching and compressing of space-time varies the energy of photons that propagate through it, in a process analogous to red- or blue- shifting (Figure 1.6). These quadropules need not be symmetric in the same way as a scalar density mode, and are uncorrelated with the underlying acoustic modes of the last scattering medium. Such tensor perturbations generate both E-mode and B-mode polarization patterns.

Figure 1.7 illustrates this by showing the polarization fields that result from (A) a single Fourier mode of a scalar metric perturbation and (B), a single Fourier mode of a tensor field perturbation.

7 In analogy to electric and magnetic fields.
8 Formally, this is a tight *anti-correlation*. Peaks in TT correspond to troughs in EE.

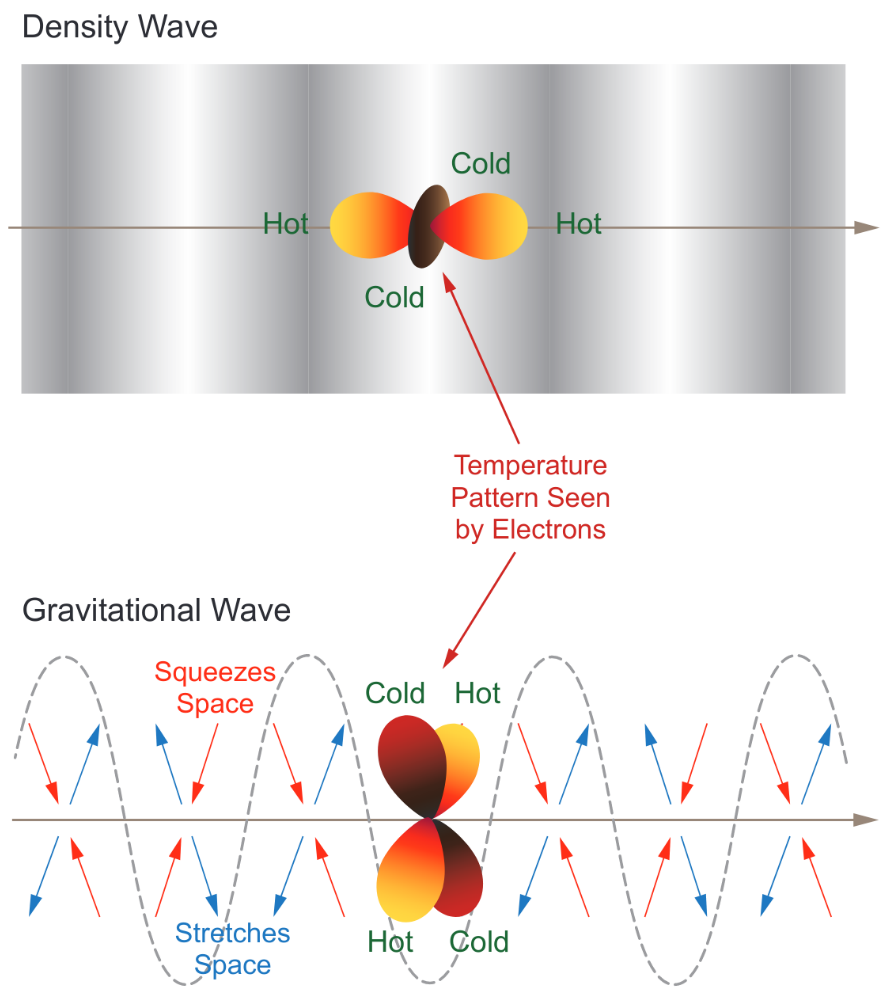

Figure 1.6: Both density perturbations (top) and gravitational waves (bottom) produce quadrupolar temperature distributions, from which Thomson scattering will produce net polarization. Image from The BICEP/Keck collaboration et al., 2018 [97].

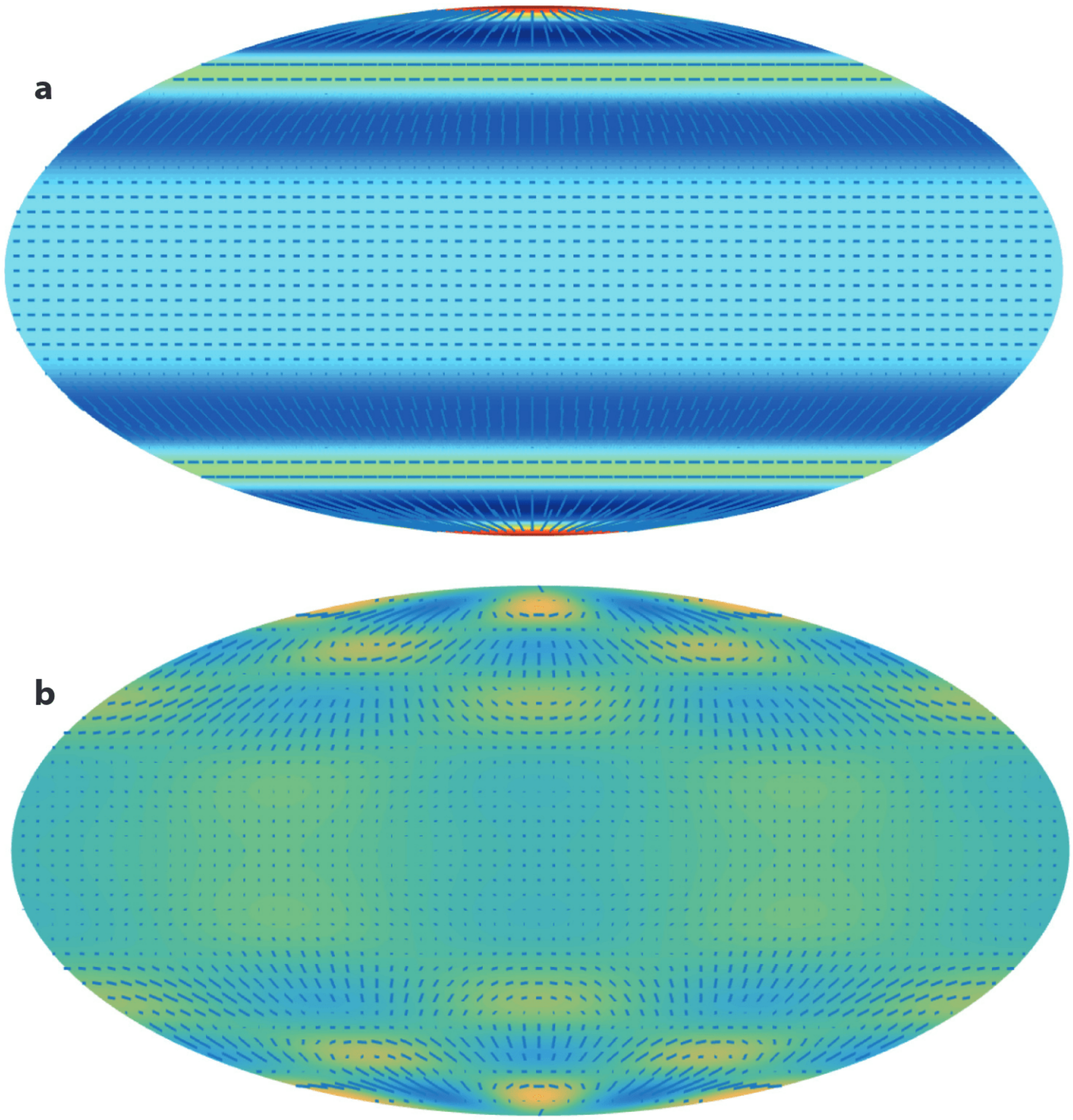

Figure 1.7: Simulations of the net observed polarization resulting from a single Fourier mode of a scalar density perturbation (top), and a tensor field perturbation (bottom). The scalar density mode in the top image clearly generates E-mode polarization components, but no B-modes. The tensor mode in the bottom image generates both E- and B- modes. Image from Kamionkowski and Kovetz, 2016 [54].

B-mode polarization patterns can also be generated from pure E-mode CMB emission as the photons are deflected by gravitational fields between the last scattering surface and us. The power spectrum of these B-modes is known as the *lensing B-mode power spectrum*.[9] Amplitudes of the EE and lensing BB power spectra are 2-5 orders of magnitude below the TT power spectrum, and we are only recently in an era of precision measurements of the polarized CMB sky. The first detection of the E-mode power spectrum was made in 2003 by the DASI experiment [58], and the lensing B-mode spectrum was first measured in 2013 with a cross-correlation between the CMB and cosmic infrared background [39] (using the SPTpol telescope in cross-correlation with data from the Herschel Space Observatory [72]), and in 2014 from the CMB alone [80] (with the Polarbear telescope).

Non-lensing B-modes have not yet been detected, but a measurement of them is considered a major test for inflationary theory.

1.4 PRIMORDIAL INFLATIONARY GRAVITY WAVES

Inflationary theory succeeds in resolving a number of problems in the ΛCDM model, and it makes testable predictions related to the characteristics of the CMB. However, critics of inflationary cosmology argue that inflation swaps some fine-tuning problems for others – due to the plethora of inflationary models that exist for the initial scalar field and its decay [32]. Moreover, the mechanism of superluminal expansion has never been directly probed via measurement. Non-lensing B-modes in the CMB polarization field may provide such a probe. Gravitational waves would have been generated during the period of superluminal expansion, and continued to propagate through the universe after inflation ceased. These *primordial inflationary gravity waves* would generate an extremely weak B-mode signature in the CMB polarization at large angular scales, with a power spectrum distinct from the lensing spectrum (Figure 1.8).

After recombination, the universe underwent a long period of structure evolution with electrically neutral hydrogen and helium baryonic matter (the "dark ages"). By $z \sim 7$ that matter collapsed sufficiently to begin powering the first stars and quasars. Emission from these compact objects converted the surrounding neutral gas into a plasma, rapidly *reionizing*

9 The lensing power spectrum can be used to reconstruct the "lensing field" – a remarkable method of counting the matter in the observable universe, and another data point with which to measure the cosmic history.

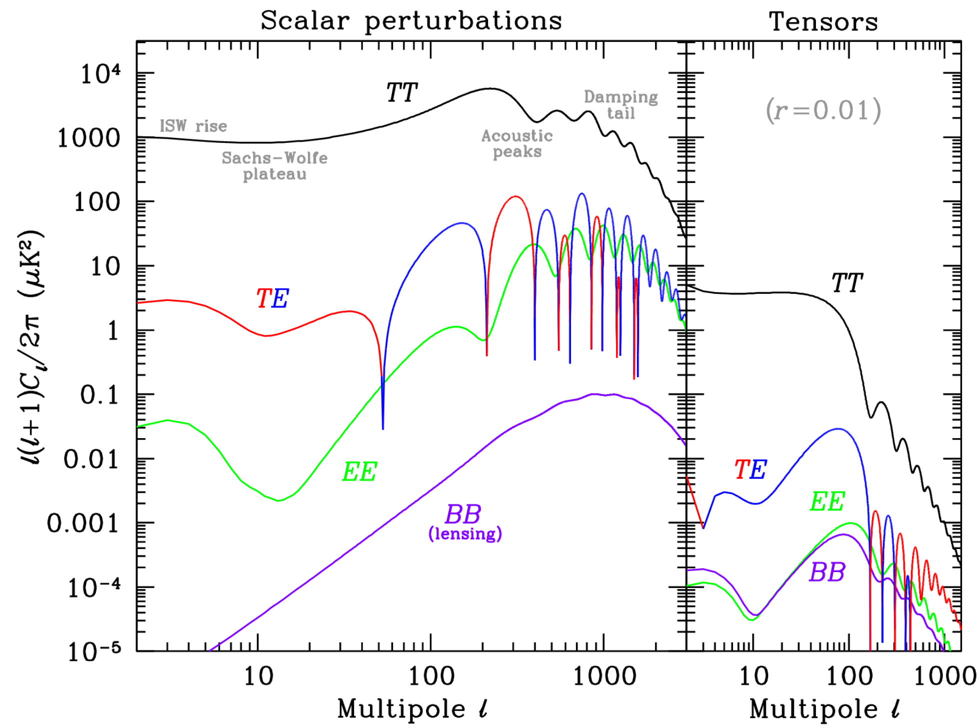

Figure 1.8: The above plot shows simulated angular power spectra for the auto-correlations and cross-correlations between T, E, and B mode CMB anisotropies. These are produced using a standard ΛCDM model with cosmological parameters from the Planck analysis, and separated into components generated by scalar fluctuations (left) and tensor fluctuations (right) in a scenario in which r=0.01. Notice that the primordial B-mode signature (Tensor BB) is nearly 8 orders of magnitude weaker than the first acoustic peak in the temperature (TT) spectrum. Image from Tanabashi et al., 2018 [94].

the universe. This cosmic history is shown in Figure 1.9. Reionization once again produced a

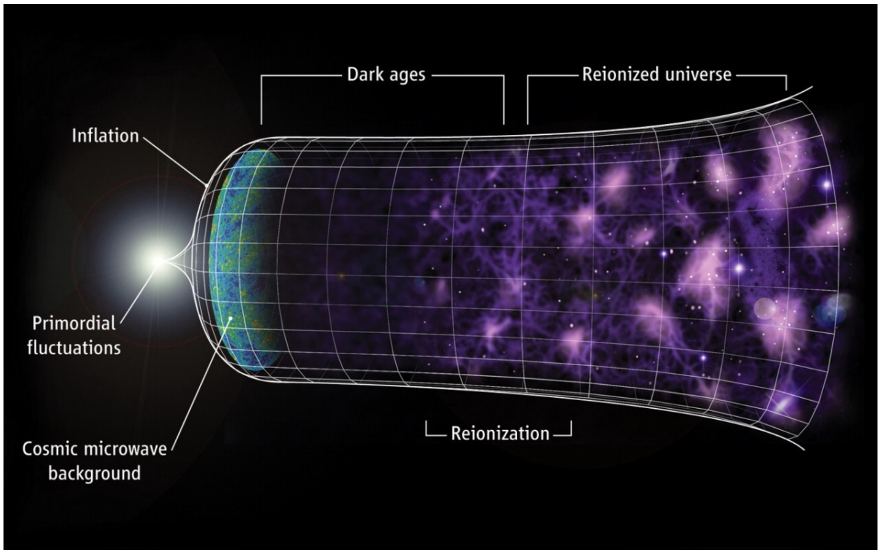

Figure 1.9: After recombination the baryonic material in the universe was almost entirely electrically neutral, and the CMB photons streamed freely without interacting much with the medium. Eventually, the first compact objects like stars and quasars began to form, and emission from these objects rapidly reionized the universe, generating plasma from what had been primarily neutral hydrogen and helium. CMB photons began to interact with the much larger density of free electrons now in the universe, generating reionization signatures in the CMB. Image from Faucher-Giguère et al., 2008 [35].

large number of free electrons in the universe,[10] with a spatial and temperature distribution determined by the structure of the universe at this later time. Residual CMB photons, having traveled through the neutral universe freely until this point, scattered with the new free electrons, producing distortions of the CMB field. These reionization features in the CMB trace much more recent density perturbations than those during recombination, and so appear at much larger angular scales. As in the epoch of recombination, primordial inflationary gravity waves would generate perturbations in the spatial intensity distribution of photons scattering with free electrons. The resulting polarization pattern would be detected in the CMB polarization as B-modes [54]. Inflationary models generate a prediction for the angular power spectrum of primordial B-modes, with two distinct peaks at $\ell < 10$ (the "reionization bump") and $\ell \approx 80$ (the "recombination peak"), shown in Figure 1.10.

The recombination peak presents at approximately ∼2 degree scales on sky, making it accessible to ground-based instruments without full-sky coverage. The reionization bump is

10 Though the density of free electrons was still much lower than before recombination, the ionization fraction is thought to have jumped four orders of magnitude following reionization, to ≈1% [54].

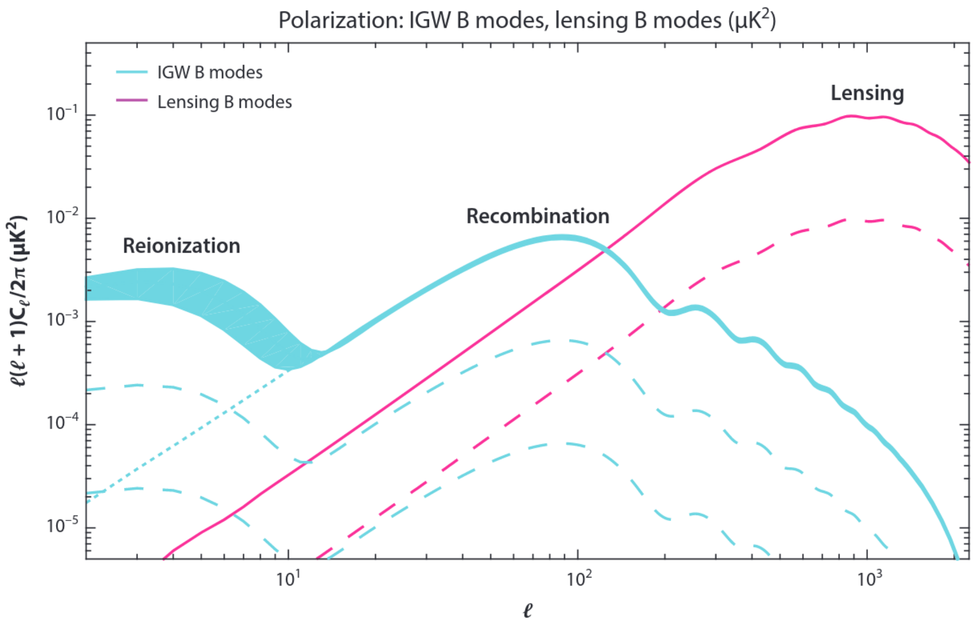

Figure 1.10: Simulations of the B-mode lensing and primordial inflationary gravity wave (IGW) power spectra are given above for various values of the tensor-to-scalar ratio r (0.1, 0.01, 0.001; cyan solid and dashed lines, with increasing amplitude corresponding to larger values of r). The shaded region indicates potential values for a $\pm 1\sigma$ uncertainty in the optical depth to reionization (the cyan dotted line shows the B-mode power spectrum with no epoch of reionization). The dashed magenta line shows the residual lensing power spectrum assuming a 90% effective removal of lensing B-mode power. Notice that the two peaks in the primordial IGW wave spectrum occur at ℓ <10 (the reionization bump) and $\ell \approx$80 (the recombination peak). Also that for models of inflation not already excluded, only the reionization bump can be observed without removing the lensing B-mode signal. Image from Kamionkowski and Kovetz, 2016 [54].

only accessible to space-based platforms with full-sky coverage, because it exists at much larger angular scales than are visible to any ground-based survey field. A robust detection of either would be evidence of primordial gravity waves generated by inflationary expansion of the universe. A measurement of the amplitude would constrain the *energy scale of inflation*, narrowing the potential inflationary models. This energy scale is parameterized by the relative power in scalar and tensor perturbations, the *tensor-to-scalar ratio, r*. Modern constraints made using a combination of data from the BICEP/*Keck Array* ground-based telescopes and PLANCK space-based observatory, have placed upper limits of $r < 0.06$ [78]. The most likely inflationary models predict an $r \sim 0.01$.

1.5 FOREGROUNDS

Anisotropies in the CMB *temperature* spectrum can be measured directly with a single appropriately-chosen observing band. This works because the primary CMB anisotropies are the dominant astrophysical signal at that observing frequency (Figure 1.11). Polarization

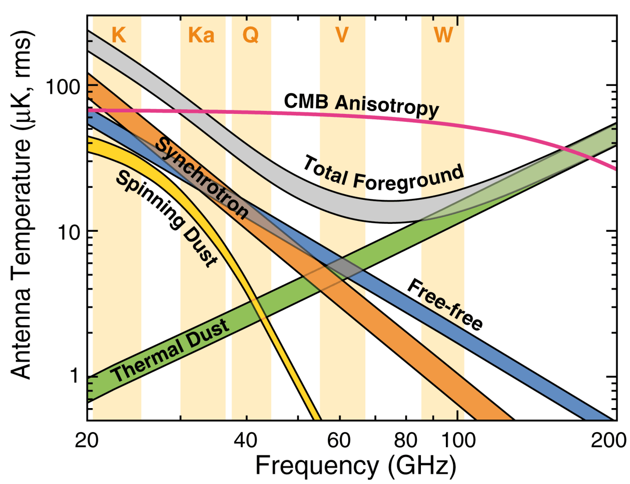

Figure 1.11: Shown here, as a function of observing frequency, is the relative amplitude of astrophysical foregrounds to primary CMB temperature anisotropies at approximately 1 degree scales. Notice the large region of frequency space in which the CMB temperature is the dominant source of power, relatively uncontaminated by synchrotron or galactic dust emission. Image from Bennett et al., 2013 [15].

anisotropies are much weaker, and the primordial B-mode spectrum even weaker still. In a single-band observation of the CMB, foreground contamination is indistinguishable from the polarized E- and B- modes of the CMB. This is shown in Figure 1.12, which calculates the relative B-mode power as a function of frequency, at the two scales where the primordial B-mode signature should be largest. For values of r that have not already been excluded, the dominant power at all frequencies comes from polarized dust emission. For some potential values of r it is further dominated by the lensing B-mode spectrum and synchroton radiation.

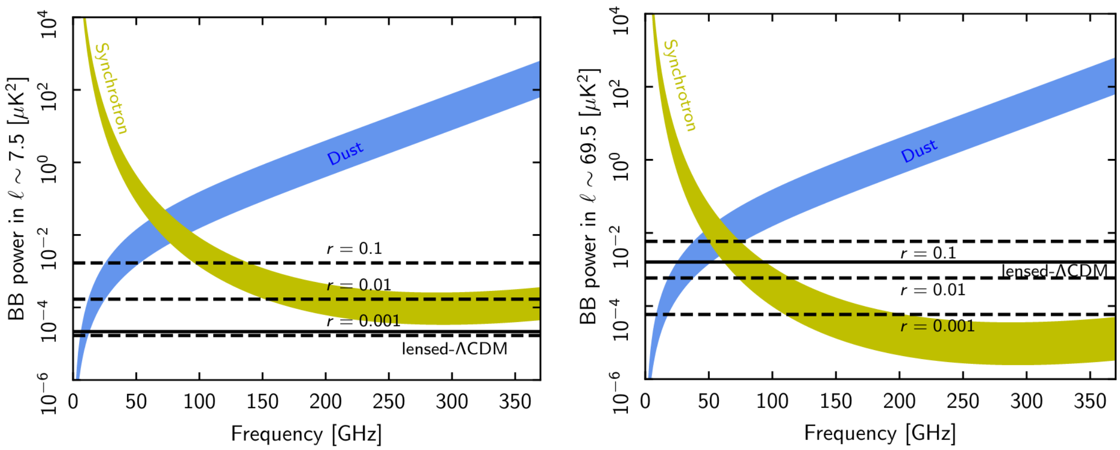

Figure 1.12: Projections of the relative B-mode power as a function of frequency from astrophysical sources. The left image is modeled for the ℓ-region containing the projected reionization bump. The right image is modeled for an ℓ region containing the expected recombination peak. Notice that in all cases the hypothesized primordial B-mode signal is contaminated by much larger foreground contributions from either galactic dust (blue), synchrotron emission (green), or lensing B-modes (solid line). These can only be separated using multiwavelength observations. Image from Planck Collaboration et al., 2018 [79].

The only asset we have to overcome the problem of foreground contamination is that these foregrounds have well-parameterized *frequency* and *angular* power spectra:

LOW FREQUENCY MEASUREMENTS are dominated by synchrotron emission, and so they constrain the synchrotron foreground model at all frequencies.

HIGHER FREQUENCY MEASUREMENTS constrain the model for polarized dust emission. Since the dust spectrum has a less dramatic frequency dependence it is important to have as many frequency bands as possible.

HIGH ℓ MEASUREMENTS in a similar way constrain the model for the lensed B-mode contribution.

Multi-wavelength observations can be used to subtract the contributions of dust and synchroton emission from the measured B-mode angular power spectrum, and high-ℓ B-mode measurements can be used to "de-lens" the lensing contribution, to reveal the primordial B-mode spectrum beneath the foregrounds.

This poses a unique challenge. A true multi-wavelength survey down to very low ℓ can only be conducted from space; where all angular scales on the sky are visible, and observing bands aren't limited by narrow windows of low atmospheric absorption. Meanwhile, measurements of high-ℓ scales require fine optical resolution that is difficult to achieve with space-based platforms due to size and weight limitations, but is essential for characterizing the lensing power spectrum. The most promising path towards a measurement of primordial inflationary gravity waves pairs high-resolution ground-based instruments with a space-based platform that can observe multi-wavelength polarized signals over the full sky.

1.6 TOWARDS A MEASUREMENT OF INFLATIONARY GRAVITY WAVES

This thesis presents my work on two experiments designed to meet this challenge –

THE SPT-3G INSTRUMENT: A ground-based experiment with one of the most promising de-lensing capabilities currently fielded. Together with the BICEP/*Keck Array*, it is projected to achieve $\sigma_r \lesssim 0.002$ via a de-lensed measurement of the recombination peak [97].

THE LITEBIRD TELESCOPE: An upcoming multi-wavelength space-based observatory, which will be sufficiently sensitive to achieve $\sigma_r \leq 0.001$, via a measurement of the reionization bump, and which will use a readout system based on the one deployed on SPT-3G [43].

Both of these instruments can only meet their goals with sufficiently low-noise operation, a constraint defined primarily by the size of the focal plane and performance of the readout system.[11] I begin in Chapters 3 and 4 by describing the relationship between detector sensitivity and the SPT-3G readout system, which I helped to design and wrote the control software for. In Chapters 5, 6, and 7 I present novel, and more complete, crosstalk and noise models for this readout architecture, and validate them against SPT-3G performance. This is particularly relevant because it identifies the cause of a previously unexplained loss of

11 These two are related, as the readout design plays a large role in the achievable focal plane size.

sensitivity in one observing band. These models are now being used to design the LiteBIRD readout system, and define the detector parameters and requirements. I conclude in Chapter 8 by forecasting the readout performance of the LiteBIRD design, including proposing specific changes with respect to the SPT-3G design it is based on, and verifying that the requirements for the instrument success can be met by such a design.

2 THE SPT-3G INSTRUMENT AND LITEBIRD TELESCOPE

The South Pole Telescope and LiteBIRD satellite are two CMB instruments well positioned to provide the sensitivity, angular resolution, and multi-wavelength data required in order to substantially improve constraints on the tensor-to-scalar ratio, r.

The South Pole Telescope has a 10-meter dish and is ideal for precision measurements of the polarized CMB at high-ℓ, such as those necessary to de-lens the B-mode spectrum. The current SPT-3G instrument is the third camera to be installed on the South Pole Telescope, and successor to the SPTpol instrument, which was used to perform the first measurement of the lensing B-mode power spectrum [39]. SPT-3G is a substantial upgrade to SPTpol, adding a third frequency band, an order of magnitude more detectors, and a roughly three-fold increase in survey area. We are currently in the middle of a planned 5-year survey, with science results from the first two years of data underway.

The LiteBIRD satellite is a proposed space-based CMB telescope led by the Japanese Space Agency (JAXA), and being designed and built in collaboration with the European Space Agency (ESA), the French National Centre for Space Studies (CNES), the Canadian Space Agency (CSA), and the American National Aeronautics And Space Administration (NASA). LiteBIRD plans to launch in 2028, and conduct a 3-year observing campaign of the CMB, with a sensitivity to the tensor-to-scalar ratio of $\sigma_r < 0.0006$ (statistical).

My graduate studies have focused on the development, integration, and deployment of the SPT-3G camera and readout, and the readout forecasting, design, and development of the LiteBIRD telescope.

2.1 THE SOUTH POLE TELESCOPE

The South Pole Telescope (Figure 2.1) is situated at the geographic South Pole on the Antarctic Plateau, as part of the Amundsen-Scott Research Station. The South Pole is one of the few sites where the CMB can be observed with precision, for which the mantra is "high and dry." Microwave radiation is readily absorbed by water vapor, and a thick atmosphere is bright relative to the dim CMB radiation. The extreme cold (-60 C) and high altitude (2,800 meters) at the South Pole limit the total precipitable water vapor in the atmosphere, through

Figure 2.1: The South Pole Telescope has a 10-meter primary mirror and off-axis gregorian optical configuration. The telescope cabin (rectangular box at the bottom of the ground-shield above) houses the secondary and tertiary mirrors, as well as the SPT-3G instrument. Photo by author, winter of 2018.

which the telescope must look.[1] The observing environment and weather is also exceptionally stable at the South Pole, where polar darkness reigns for 6 months of the year and its location within the polar vortex keeps maximum wind speeds and atmospheric turbulence low.

1 The leading alternative site for terrestrial CMB observations is the Atacama Plateau in Chile, which is less stable and dry, but at much higher altitude.

Figure 2.2: The geographic South Pole on the Antarctic Plateau is an extremely stable, but remote, observing environment. Pictured here are the three CMB telescopes at the South Pole, SPT (upper right, with the prominent 10 meter dish), Bicep (just below SPT, with an upward facing ground shield), and the *Keck Array* (left). Photo by author, sunrise of 2018.

The site is so remote that it is only accessible for ∼4 months during the austral summer season, after which a small contingent of "winterovers" manage the research station, and associated scientific experiments, in isolation throughout the austral winter (Figure 2.3). Two of these winterovers are there specifically to operate and maintain the South Pole Telescope.[2]

Figure 2.3: The Amundsen-Scott Research Station winterover crew for the 2018 austral winter. A group of approximately 40 people spend most of the year in isolation, supporting the ongoing environmental and astrophysical science missions at the South Pole. There has been a continuous scientific presence at the Amundsen-Scott Research Station since 1957. Photo by Robert Schwarz.

2 For the 2018 austral winter I was fortunate enough to be one of the SPT winterovers, along with my colleague, Adam Jones.

2.1.1 *The SPT-3G instrument*

The SPT-3G camera was installed on SPT in 2017 and began observing its primary CMB field in 2018. It observes the sky in three frequency bands, 95 GHz, 150 GHz, and 220 GHz at angular resolutions of 1.0, 1.2, and 1.6 arcmin respectively.[3] The instrument focal plane consists of approximately 2,500 tri-chroic pixels. Each pixel couples both linear polarizations, from each of the three frequency bands, to 6 individual background-noise limited detectors, for a total of ∼15,000 detectors [13]. The SPT-3G focal plane is shown in Figure 2.4. The detectors used are transition-edge sensors (TES), which are total- power bolometers. TES detectors are kept within their superconducting transition, and measure incident radiative power via changes in exhibited resistance; they must be cryogenically cooled to just 300 mK above absolute zero, which is accomplished with Helium-3 Pulse Tube Coolers (to 4 K) and a Helium-3 Sorption Fridge (for the mK stage). The detector technology itself is discussed in Chapter 3.

The SPT-3G survey area is a 1500 deg^2 patch of the southern sky around what is known as the "Southern Hole," where galactic dust emission is low (Figure 2.5). This area can be observed continuously during the 8-month observing season over the austral winter. The on-sky efficiency during this observing season is approximately 56%, dictated primarily by the duty cycle of the cryogenics, which halts observation for several hours a day [89].

Current and expected total survey depths are given in Table 2.1. Overall, the array noise performance is consistent with expectations based on the design specifications, with the exception of the 220 GHz detectors, which have a noise performance 1.5x-2x worse than expected [13]. This is thought to be partially due to poorer-than-expected transmission in the optical anti-reflective coatings, but I find that a substantial increase is also due to an interaction between between the readout and cryogenic hardware parameters, discussed in detail in Chapter 7. One outcome of the work presented in Chapter 7 is a set of recommendations that may improve the 220 GHz noise performance for the remainder of the observing campaign.

---

3 $\ell > 5000$, though in practice such high angular resolution is used for the detection of galaxy clusters and cluster cosmology analysis, rather than the power spectrum analysis described in Chapter 1. Power spectrum band-powers are usually evaluated for $\ell < 3500$.

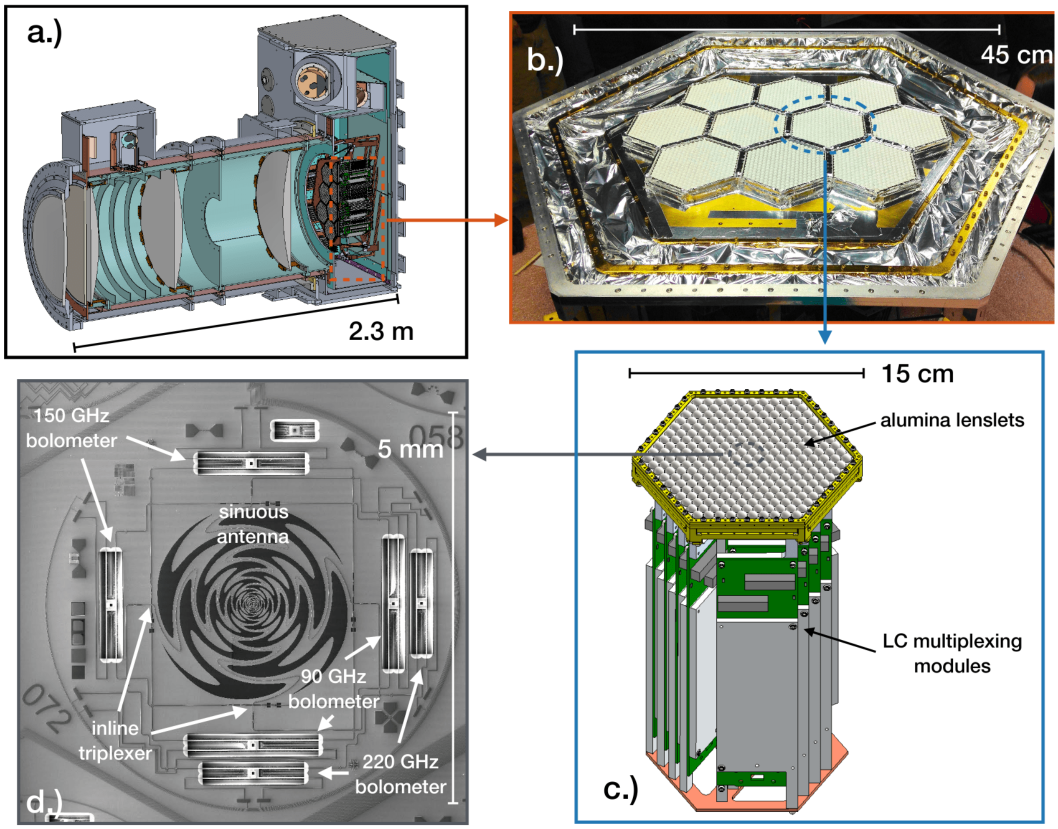

Figure 2.4: **a.)** The SPT-3G instrument cutaway. **b.)** The full SPT-3G focal plane, consisting of 10 6" wafers. **c.)** Each detector wafer uses alumina lenslets (described in [67]) to focus incoming light into pixels beneath them, and is read out using multiplexing modules (discussed in detail in Chapter 4). **d.)** An individual detector pixel. Both linear polarizations of incoming light are coupled electrically to a set of orthogonal sinuous antennae (described in [81]). The electrical signals are then separated using inline *triplexers* before being deposited as incident power on the six individual TES detectors, one for each of the three bands and two polarizations. Image from Anderson et al., 2018 [4].

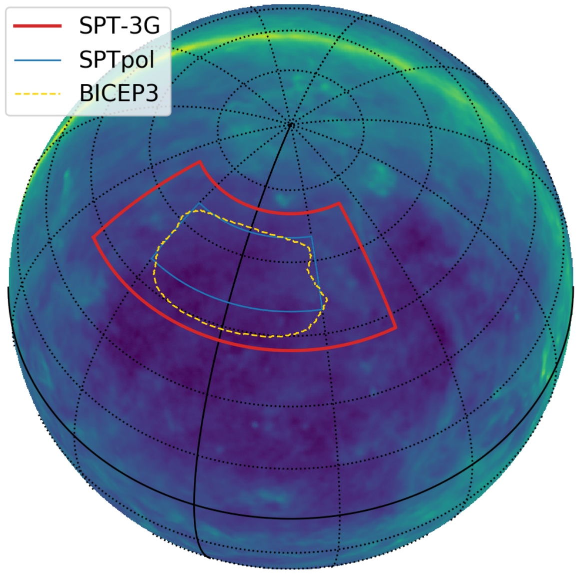

Figure 2.5: The celestial sphere (oriented with the south celestial pole at the top) with an overlay of the PLANCK thermal dust map [75] and outline of the 1,500 deg^2 SPT-3G survey area (solid red). This SPT-3G field is designed to have good overlap with previous SPT instruments (SPTPOL 500 deg^2 wide field, solid blue), as well as fully overlap with BICEP/*Keck Array* observing fields (dashed yellow) [2]. Survey footprint and overlay code by Adam Anderson.

	Map noise in Temperature (Polarization) [µK-arcmin]		
Band	SPTPOL	SPT-3G Current	SPT-3G Forecast
95 GHz	12 (17)	6 (8)	3 (4)
150 GHz	6 (9)	5 (7)	2 (3)
220 GHz	N/A	17 (24)	9 (13)

Table 2.1: Noise in the temperature and polarization maps shown here for the deepest SPTPOL field (100 deg^2) [16], and a forecast for the full 1500 deg^2 SPT-3G survey [13]. Also included is the current 1500 deg^2 SPT-3G map depths, approximately 2 years into the survey. The noise is expressed as the root-mean-square of an equivalent temperature fluctuation in µK (thermodynamical temperature, T_{CMB}) averaged in a pixel of one arcmin in linear size. The 220 GHz performance is about a factor of 1.5-2x worse than predicted. Part of this is due to difficulty achieving the targeted optical performance of the anti-reflective lens coatings at the higher frequencies [68], but it is also partially due to interactions between detector parameters and readout design described in Chapter 7.

2.1.2 *SPT-3G science forecasts*

The SPT-3G survey will improve cosmological constraints through: analyses of more sensitive power spectra measurements, similar to those described in Chapter 1; characterization of the lensing B-mode spectrum, and development of de-lensing methodology; and measurements of galaxy clusters.[4] I will focus here specifically on improvements to measurements of the CMB polarization power spectra. In particular, SPT-3G is expected to significantly improve measurements of the E- and B- mode polarization spectra at high ℓ, enabling de-lensing of the B-mode spectrum at the recombination peak by a factor of 4 in B-mode power [16]. Figure 2.6 summarizes the expected anisotropy sensitivity, in temperature and polarization, across the full multipole range. The projected r constraints through de-lensing with the Bicep/*Keck Array* experiments are given in Figure 2.7.

2.1.3 *Contribution to SPT-3G*

The Mcgill Cosmology Instrumentation Laboratory designed and built the room-temperature readout electronics, and co-designed the cryogenic readout electronics, used on SPT cameras, including SPT-3G. My contribution to SPT-3G is broadly linked to the readout system. I characterized the prototype electronics as a Masters student, and assisted in the design and conceptualization of the final versions. This process included the calculation and verification of the electronic transfer functions, crosstalk and noise properties, as well as the initial evaluation and operation of the hardware – from the benchtop through to an end-to-end cryogenic system. I also developed quality control procedures and metrics that have been used to validate hundreds of copies of these electronics deployed on several telescopes.

I am the primary author of `pydfmux`, the readout control software used to operate detectors, and while validating the readout electronics I developed many of the algorithms to tune, optimize, and characterize the instrument performance.[5] `pydfmux` is currently used at dozens

---

4 Galaxy clusters can be detected in a red-shift independent way by looking for local decrements and increments in the CMB, where hot gasses within galaxy clusters inverse-Compton-scatter incoming CMB photons up to different frequencies. This is known as the Sunyaev–Zeldovich effect [93]. In this way, the CMB is a back-light through which compact objects that make up the large scale structure of the universe can be detected out to very high redshift. This is another means to measure the evolution of structure in the universe, and constrain the physics that drives that evolution.

5 This was done in collaboration with Graeme Smecher, the engineer and architect behind the electronics firmware. Graeme developed the CS framework of `pydfmux` to communicate with the

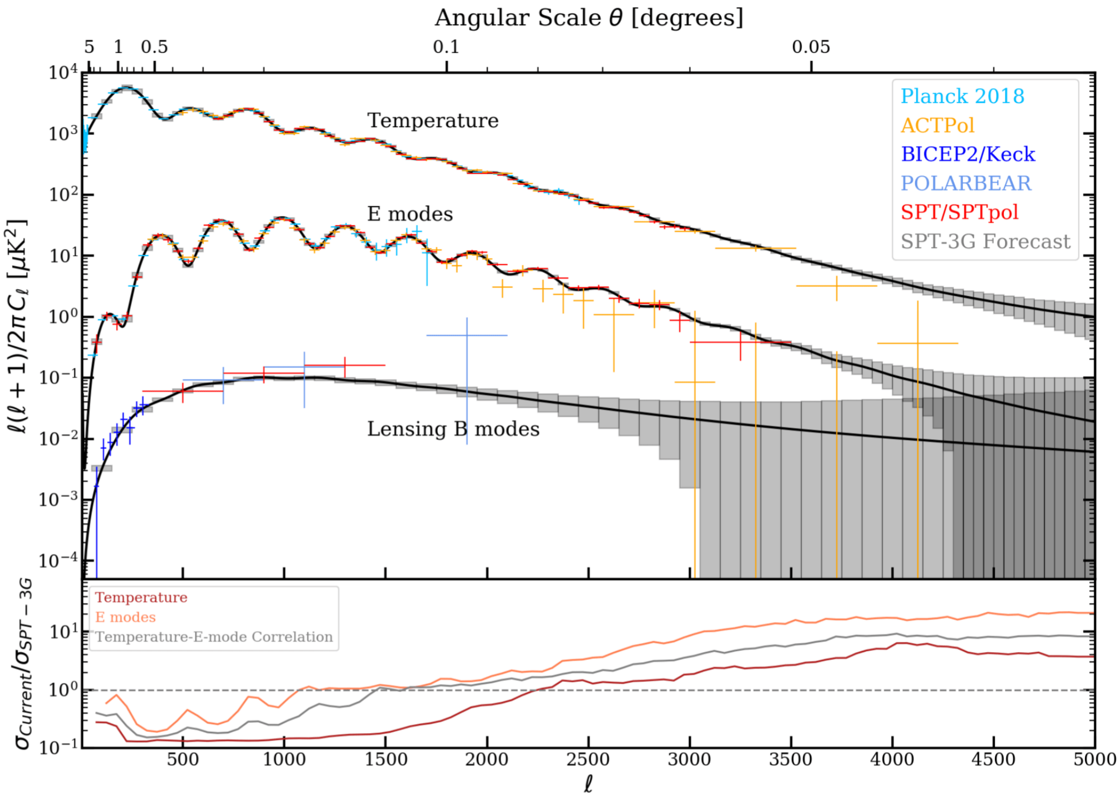

Figure 2.6: Projected improvements to measurements of the CMB temperature and polarization power spectrum, using data from the full SPT-3G observing campaign. **Top:** Individual power spectra with gray vertical bars representing expected SPT-3G data error-bars. Constraints from the PLANCK satellite [76], BICEP/*Keck Array* [96], ACTPOL [61], POLARBEAR [80], SPT-SZ [92], and SPTPOL [44, 56] experiments are also shown. **Bottom:** Expected improvement in each of the temperature and polarization auto- and cross- spectra compared to some of the most sensitive current measurements. This is indicating that SPT-3G is expected to significantly improve constraints on the temperature and polarization power spectra at small angular scales, where the lensing B-mode signal is largest. Note: data in the above compilation are current to 2018. Additional data has been published by the BICEP/*Keck Array* collaboration [97] and ADVACT [19] since this figure was compiled, and an updated compilation plot (without the SPT-3G forecast bars) can be found in Choi et al., 2020 [19]. The above image is from Bender et al., 2018 [13].

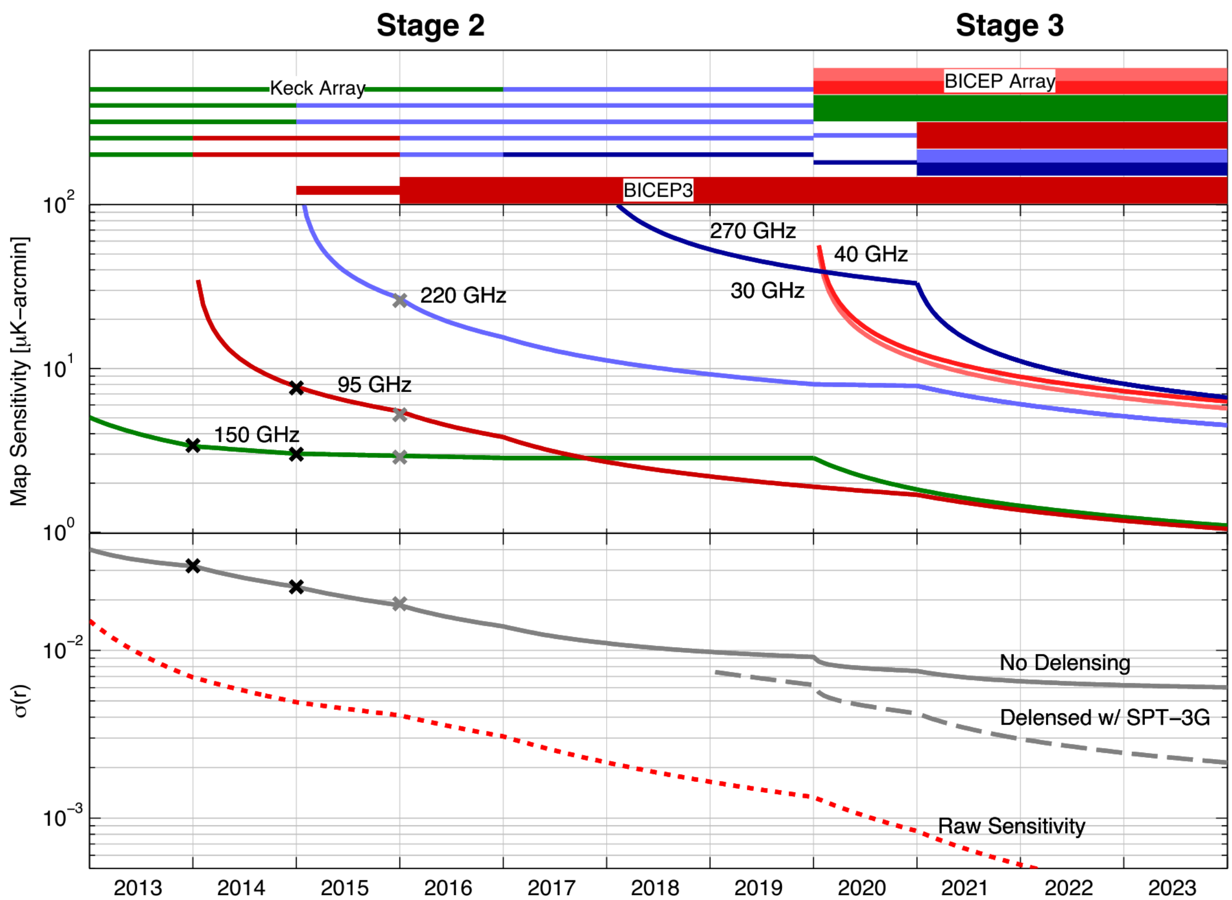

Figure 2.7: Shown above are projections of the sensitivity to gravitational B-modes achieved by the ground-based Bicep/*Keck Array* and SPT-3G instruments as a function of time, with year on the x-axis. Colors indicate different frequency modules deployed incrementally on each telescope. "Raw sensitivity" indicates the constraining power in the absence of foregrounds, while the grey solid line indicates the projected success of foreground removal from combinations of multi-wavelength data. The dashed gray line indicates the projected success of de-lensing using SPT-3G data. Sensitivity to r with $\sigma_r \lesssim 0.002$ may be possible by 2024 by combining these large aperture telescope measurements from the Bicep/*Keck Array* with de-lensing from the SPT-3G survey. Image from The BICEP/Keck collaboration et al., 2018 [97].

of laboratory test beds, as well as on the SPT-3G and POLARBEAR-2 telescopes, and will be adapted for the LITEBIRD system. As SPT-3G was being built I traveled to testbeds at Berkeley, the University of Chicago, FermiLab, and Argonne National Laboratory, hosting tutorials and assisting in the deployment of the readout hardware and integration with the early cryogenic hardware.

In 2015 I spent the summer at the South Pole working on the SPTPOL instrument in the final years of its survey. In 2017 I was a member of the team that integrated the readout with the full SPT-3G camera at Fermilab, before again traveling to the South Pole for the 2017 summer season, this time to deploy SPT-3G for the "Year-0" engineering run. In 2018, SPT-3G began the first year of its observing campaign and I wintered over at the South Pole for 10 months as part of the two-person team operating it.

Since then, my work on SPT-3G has primarily been focused on optimizing the telescope to improve observing efficiency and sensitivity. I've made novel contributions to the noise and crosstalk models that apply generally to the form of readout technology employed on the SPT-3G and POLARBEAR-2 instruments. These models are key to designing the future LITEBIRD satellite.

2.2 THE LITEBIRD SATELLITE

The LITEBIRD satellite is an in-development space-based CMB telescope, with an expected launch date of 2028, funded for development in Canada by the Canadian Space Agency (CSA). It will operate from the second Lagrangian point (L2) while conducting a 3-year full-sky survey. The LITEBIRD focal plane will consist of $\sim$5,000 polarization-sensitive detectors over 15 frequency bands, from 40 GHz to 402 GHz.[6] This will be a substantial technological leap relative to the most recent space-based CMB instrument, the PLANCK satellite, which used 74 total detectors over 9 frequency bands. LITEBIRD is lead by JAXA, the Japanese Space Agency, and was selected as a JAXA Strategic Large Mission in 2019.[7] It also has contributions from ESA member nations, Canada, and from the USA via NASA,

readout electronics firmware and signal processing, and I developed the programs that operate the cryogenic detector hardware, characterize the system, and interface with the users and General Telescope Control Program.

6 The rule of thumb for space-based detectors such as these is 1,000 detectors in space are as sensitive as 100,000 detectors on the ground. This is because noise is dominated by non-CMB photon fluctuations, and there are many more sources of additional loading when observing from the ground.

7 Historically, every JAXA mission selected as a Strategic Large Mission has flown.

where it has received technological development funding and is in the proposal process for a larger mission contribution.

The instrument consists of three separate telescopes, shown in Figure 2.8: the LFT (low frequency telescope), MFT (mid-frequency telescope), and HFT (high frequency telescope) and will have angular resolutions between 0.2° and 1.2°, with a typical angular resolution of 0.5° at 150 GHz.[8] The angular resolution and full-sky visibility tailor the instrument for measurements over the multiple range $2 < \ell < 200$. The projected survey depth in all bands

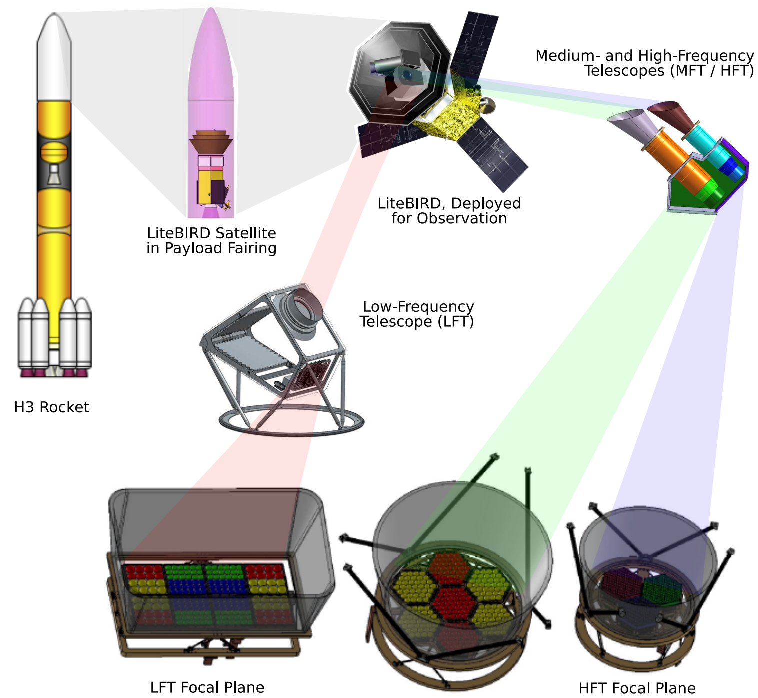

Figure 2.8: LiteBIRD spacecraft overview. Image from Graeme Smecher, image elements courtesy of NASA and JAXA.

is given is Figure 2.9, which shows how sensitivity is concentrated in the 100 GHz to 200 GHz range, where the CMB polarization signal is largest.

2.2.1 *LiteBIRD science*

LiteBIRD has three primary scientific objectives:

8 Many narrow-band observing frequencies allow for much better control of systematics than fewer broadband optics.

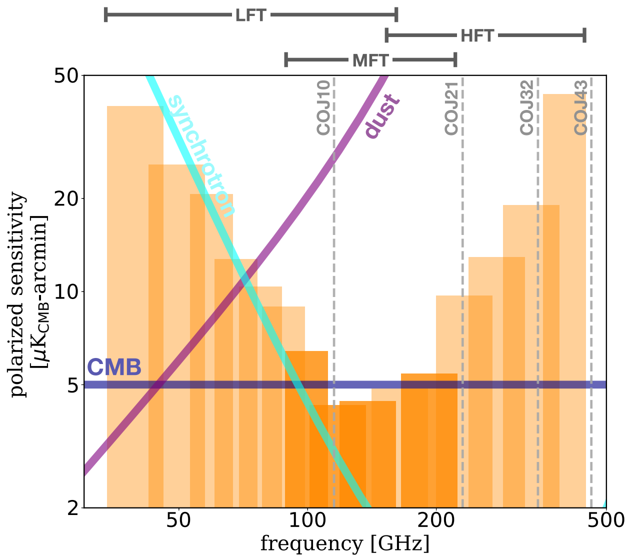

Figure 2.9: LiteBIRD sensitivity as a function of readout band. The broad and fine frequency coverage will allow for robust component separation and foreground removal, with the bulk of the sensitivity concentrated in the regime where the CMB signature will be strongest. Image courtesy of NASA.

1. To detect primordial B-modes and measure the tensor-to-scalar ratio with a precision of $\sigma_r < 0.0006$ (statistical), sufficient to exclude the best-motivated models of inflation if undetected ("large slow roll" models).[9]

2. To fully measure the low-ℓ reionization peak in the E-mode spectrum to the limit imposed by cosmic variance. This would (A) allow a measurement of the sum of the neutrino masses to sufficient precision to distinguish between the two possible mass hierarchies, and constrain the individual neutrino masses; and (B) be factor of two improvement over the Planck measurements of the reionization spectrum [43].

3. To produce all-sky maps of dust and synchrotron polarization. This would allow large-scale magnetic field studies of the Milky Way, and unlock foreground analysis and removal in a wide set of ground-based experiments.

In many ways, the measurements of r targeted by LiteBIRD are companion measurements to similar efforts by ground-based experiments. A hint of $r > 0$ from a ground-based Stage-3 instrument in the next few years (such as Bicep/*Keck Array* with SPT-3G de-lensing) would

9 "Full success" of the mission is defined by a total $\sigma_r < 0.001$, including all forms of systematics and biases. The value above is predicted based on the most recent sensitivity analyses.

strengthen the potential science benefit from LiteBIRD, which would be measuring the *reionization bump*, rather than the *recombination peak* visible to ground-based instruments (recall Figure 1.10). A hint of, or weak detection from the ground of the recombination peak may be controversial without a measurement of the reionization bump, which would be more statistically robust. Additionally, efforts to de-lens a ground-based observing campaign with SPT-3G will generate the expertise and methodologies to perform de-lensing with the LiteBIRD data set. Such a combination has the potential to further improve LiteBIRD σ_r by nearly a factor of 2.

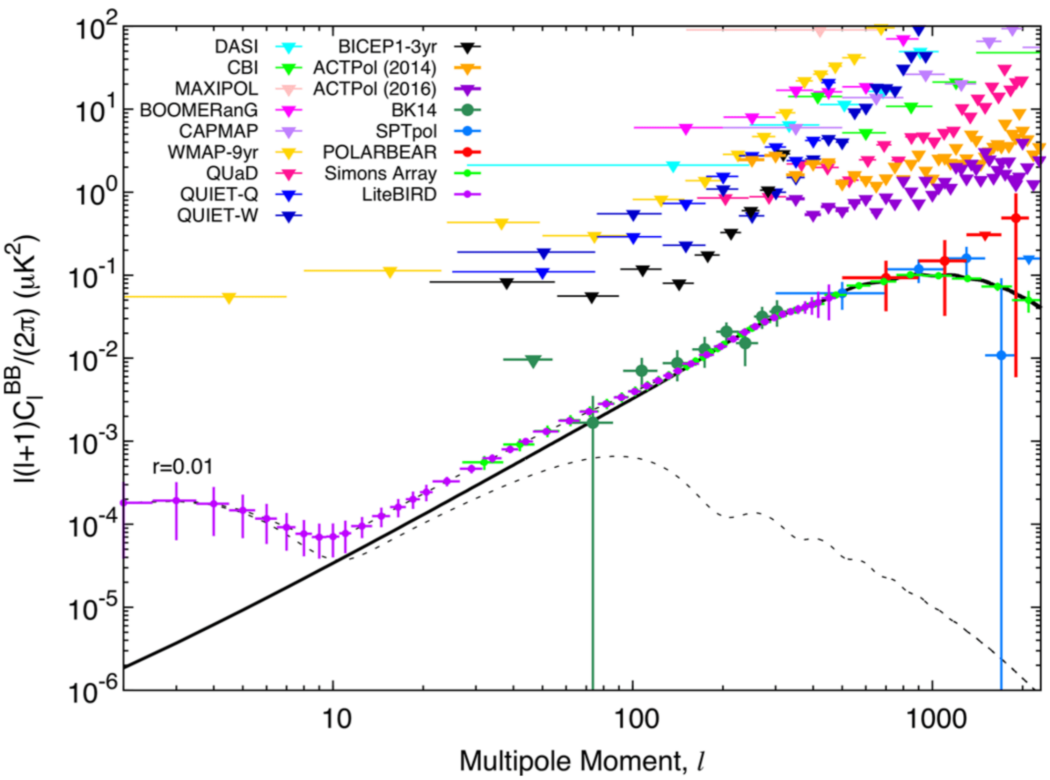

Figure 2.10: A compilation BB power spectrum showing previous and current instrument constraints alongside LiteBIRD measurement projections (purple) for a theoretical cosmology with $r = 0.01$. The dashed black line shows the inflationary gravity wave signal under such a cosmology, and the solid black line shows the lensing signal. Notice the advantages of observing the reionization bump at such low ℓ, where the lensing spectrum is weak and no delensing would be required for a detection. Image from Hazumi et al., 2019 [43].

2.2.2 *Contribution to LiteBIRD*

The Canadian contribution to LiteBIRD instrument hardware is the "Warm Electronics," a space-qualified version of the readout electronics adapted from the design currently in use on SPT-3G and Polarbear-2, and conceptual co-design of the cryogenic readout hardware. I'm involved in the LiteBIRD mission planning, space qualification and design of the readout hardware, and cryogenic electronics design. I currently manage the technology development and Phase-0 projects with the Canadian Space Agency. I've represented and advocated for the LiteBIRD satellite since 2015, including at the Canadian Astronomical Society (CASCA) Mid-Term Review, the Canadian Space Exploration Workshop, and to the Canadian Space Agency during LiteBIRD mission planning and technology development project reviews.

My work includes design and testing of prototype hardware, specifically to improve upon the SPT-3G readout in critical performance areas. My role in the broader LiteBIRD collaboration includes forecasting warm and cold readout performance; calculating system reliability and observing efficiency; making architectural design recommendations for detectors and cryogenic readout; and defining broader subsystem requirements.

3 TRANSITION EDGE SENSORS

Modern ("Stage-3") CMB survey instruments all detect incoming CMB photons using Transition-Edge Sensors (TES), which have been the standard for approximately 18 years. TES detectors are bolometric (total-power) sensors that are kept in the superconducting transition between a normal and zero resistance state. While in the transition, the TES resistance is a strong function of temperature. This is utilized by applying a voltage bias, such that deposited power raises the TES temperature and resistance, resulting in a change of current through the circuit. That change in current can then be sensed independently.

TES detectors have become the defacto standard because they achieve such a high responsivity ($S = \frac{\delta I}{\delta P}$) that instrument noise currents can be made to be small, relative to the induced noise current generated by statistical fluctuations of incoming CMB photons. In this sense they are *background noise limited*. This leads modern instruments to advance by operating more TES detectors simultaneously, in denser focal planes, rather than trying to improve the individual performance of the sensors themselves.

TES properties are strongly modified by interactions with the biasing and readout circuit (hereafter, the *readout* system). In this chapter I introduce just the fundamental TES properties, independent of the readout. These concepts will be elaborated on in Chapter 4, which describes the theory of multiplexed readout.

3.1 TES POWER BALANCE

The TES detectors used on SPT-3G are made of a stack of titanium and gold (described in [81]) with a superconducting transition temperature of ∼500 mK. The superconducting transition of a TES is characterized by the $R(T)$ curve (Figure 3.1). At temperatures above the critical temperature (T_c), the TES exhibits a normal resistance (R_n). When the TES temperature is below the critical temperature ($T < T_c$), the TES transitions into a superconducting state, such that $R << R_n$.

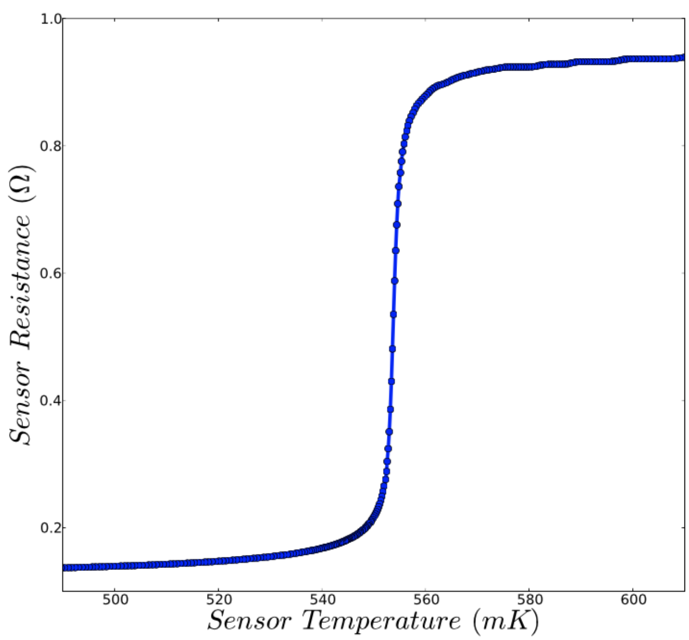

Figure 3.1: A typical measured $R(T)$ curve for a TES. Notice the steep transition where fractionally small changes in temperature result in large changes in resistance. This particular plot is of an SPTpol TES. SPT-3G detector transitions are somewhat cooler, and have a higher normal resistance. Image from Sayre, 2014 [86].

The TES thermal dynamics are described by the power-balance equation,[1]

$$C\frac{\delta T}{\delta t} = P_J - P_G + Q\,. \tag{3.1}$$

Where:

- The TES is characterized by its heat capacity (C), and the change in TES temperature as a function of time.
- Heat is *extracted* from the TES through a weak thermal link ($G(T)$), to a temperature bath ($T_{\text{bath}} < T_c$). This cooling power is defined as $P_G = G(T - T_{\text{bath}})$.
- Heat is *deposited* on the TES via Joule dissipation from the electrical bias, $P_J = IV$, and incident radiation, Q.
- The cooling power (P_G) when the system is at equilibrium ($P_J = Q = \frac{\delta T}{\delta t} = 0$) defines the *detector saturation power*. This saturation power, P_{sat}, is the minimum power required to keep the detector from entering the superconducting transition, such that $R = R_n$.

These are shown graphically in Figure 3.2.

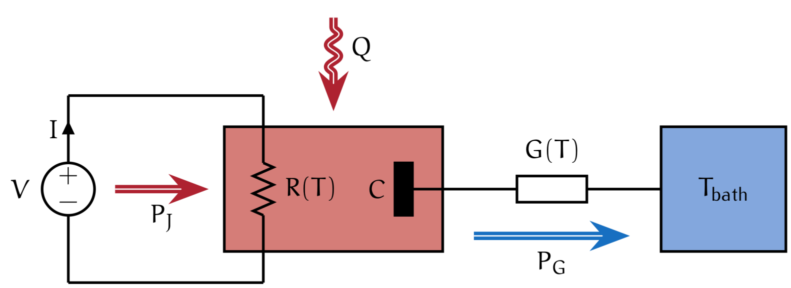

Figure 3.2: A graphical representation of the TES power-balance equation. The TES is described by its resistance as a function of temperature, $R(T)$, and heat capacity, C. $P_J = IV$ is the electrical (Joule) power delivered by the voltage bias; Q is incident power from the sky; and $P_G = G(T - T_{\text{bath}})$ is the power extracted through a thermal bath. Image from Rahlin, 2016 [82].

1 For a much more complete treatment of TES thermal dynamics, see Irwin and Hilton, 2005 [50].

3.2 ELECTROTHERMAL FEEDBACK

The TES location within the superconducting transition is a function of the total power on the TES,

$$P_{\text{TES}} = P_J + Q - P_G\,. \tag{3.2}$$

When $P_G > Q$, a TES may be *tuned* to an operating point in the transition by adjusting P_J (Figure 3.3). A TES will remain in the transition if the total power on the TES doesn't

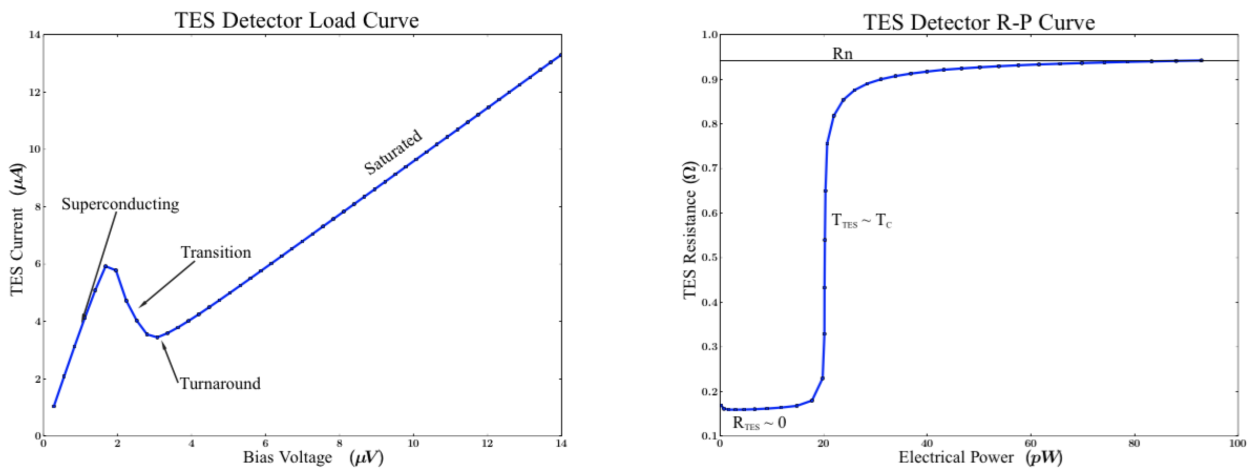

Figure 3.3: TES load curves describe the position of the TES within the superconducting transition as a function of bias voltage (left) and total power (right). By incrementally lowering the bias voltage, we can tune a detector to an operating point within the superconducting transition. Image from Sayre, 2014 [86].

diverge in response to fluctuations in Q. Due to the positive slope of the $R(T)$ curve, this is satisfied when $\dfrac{\delta P_{\text{TES}}}{\delta R} < 0$, or equivalently[2] $\dfrac{\delta P_J}{\delta R} < 0$. P_{TES} is therefore dynamically coupled to both the thermal properties of the TES ($R(T)$) and the electrical properties of the bias circuit (P_J). This coupling is known as *electrothermal feedback* (ETF); it is parameterized by the TES *logarithmic sensitivity*,

$$\alpha = \frac{\partial \log R}{\partial \log T} = \frac{T}{R}\frac{\partial R}{\partial T}\,, \tag{3.3}$$

and detector *loopgain*,

$$\mathcal{L} = \frac{\alpha P_J}{GT}\,. \tag{3.4}$$

2 Because Q is invariant to the detector resistance; and P_G is an extremely weak function of detector temperature, for the small variations in temperature within the transition.

For TES detectors, $\alpha > 0$; $\mathcal{L}$ is a dimensionless parameter that describes the strength of electrothermal feedback.[3]

Negative electrothermal feedback

The criterion $\frac{\delta P_J}{\delta R} < 0$ is guaranteed in the limit where electrical bias power is provided as a fixed voltage bias, $P_J = \frac{V_{\text{bias}}^2}{R}$. In this case, incident power Q will raise the detector resistance, which is countered by decrement in P_J, establishing a new equilibrium point within the transition. This scenario is known as *negative* electrothermal feedback. Notice, in particular, how loopgain is a function of detector resistance; operating a detector lower in the superconducting transition increases the loopgain $\underset{\sim}{\propto} \frac{1}{R}$.[4]

Positive electrothermal feedback

Any series resistance with the TES (R_s) will spoil the voltage bias, interfering with negative electrothermal feedback. In the limit where $R_s >> R_{\text{TES}}$, the fixed voltage bias becomes a stiff *current* bias, and $P_J \approx I_{\text{bias}}^2 R_{\text{TES}}$, such that $\frac{\delta P_J}{\delta R} > 0$. This generates *positive* electrothermal feedback and destabilizes the TES.

There is always some non-zero series impedance due to the biasing circuit, which can be generalized as a pure voltage bias delivered to the TES with some Thévenin equivalent complex series impedance, z_s (Figure 3.4).

3.3 TES STABILITY

A TES has a natural thermal response that acts as a damped harmonic oscillator [49], with a thermal time constant of

$$\tau_0 = \frac{C}{G}\,. \tag{3.5}$$

3 SPT-3G detectors typically operate in the range $7 \gtrsim \mathcal{L} \gtrsim 10$.
4 P_J changes fractionally much slower than R, see Figure 3.3.

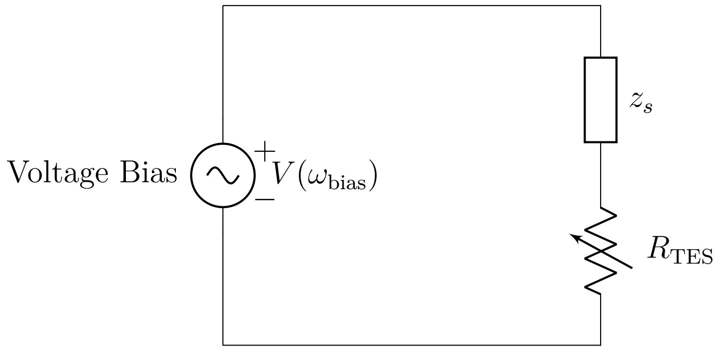

Figure 3.4: A generalized bias circuit with a voltage bias delivered to the TES through a complex Thévenin equivalent impedance. This voltage bias can be a DC bias, or a sinusoidal AC bias.

Electrothermal feedback modifies the thermal impulse response of a TES, such that the *effective* time constant is given by [34]

$$\tau_{\mathrm{eff}} = \frac{\tau_0}{\mathcal{L}\frac{R_{\mathrm{TES}}-|z_s|}{R_{\mathrm{TES}}+|z_s|}+1} \, . \tag{3.6}$$

The impulse response of a TES under various forms of electrical bias has been rigorously derived in Irwin et al., 1998 [49], and so here I will present only the relevant summaries for our usage cases.

Purely real series impedance

For a purely real Thévenin series impedance ($z_s = R_s$), the TES responds to thermal impulse by decaying monotonically to equilibrium (negative ETF), or diverging monotonically to either extrema state (superconducting or normal, due to positive ETF). The crossover point between these two scenarios occurs when ($\tau_{\mathrm{eff}} = 0$). Therefore, in this scenario the stability requirement is simply

$$R_{\mathrm{TES}} \geq R_s \left(\frac{\mathcal{L}-1}{\mathcal{L}+1} \right) \, . \tag{3.7}$$

This is the "DC stability criterion," and it limits the relative magnitude of R_s and R_{TES} to prevent a runaway positive feedback response.

Complex series impedance

In the presence of a *complex* Thévenin series impedance, the electrical bias circuit can have a non-trivial impulse response of its own, with a time constant τ_{elec}.[5] The resulting interaction can generate an *under-damped* impulse response in the electrothermal system. When under-damped, the TES will oscillate in response to perturbations. Although the response may eventually decay to an equilibrium point, those oscillations generate instability and non-linear output, making the TES unsuitable for our purposes. The general solution for a critically damped impulse response is given in Irwin et al., 1998 [49] as $\frac{\tau_{\text{eff}}}{\tau_{\text{elec}}} = 3 + 2\sqrt{2}$, such that the stability criterion to avoid under-damped TES behavior is

$$\frac{\tau_0}{\mathcal{L}\frac{R_{\text{TES}}-|z_s|}{R_{\text{TES}}+|z_s|} + 1} \geq \left(3 + 2\sqrt{2}\right)\tau_{\text{elec}}\,. \tag{3.8}$$

This is the "dynamic stability criterion;" it is a more strict extension of Equation 3.7, and further constrains the relationship between the electrical bias circuit and TES parameters, as seen later in Section 4.3.

3.3.1 *Minimum DC stable R_{frac}*

When tuning detectors we often parameterize depth in the superconducting transition with R_{frac},

$$R_{\text{frac}} \coloneqq \frac{|R_{\text{TES}} + z_s|}{|R_{\text{n}} + z_s|}\,. \tag{3.9}$$

The minimum stable R_{frac} can be inferred from the DC stability criterion (Equation 3.7) as

$$R_{\text{frac}} \gtrsim \frac{2|z_s|}{|R_n + z_s|}\,. \tag{3.10}$$

This is more a heuristic than a rule, as it does not account for dynamic instability or effects of very low loopgain. However, it is a reasonable gauge to use when estimating the usable range of the TES transition under typical conditions. For SPT-3G a typical $|z_s|$ is $\approx 300\,\text{m}\Omega$, and a typical $R_n \approx 2\,\Omega$. For these parameters Equation 3.10 predicts instability around $R_{\text{frac}} \approx 0.26$,

5 Irwin primarily derived this for systems with a series inductance in the bias circuit, such that $\tau_{\text{elec}} = \frac{L}{R}$. We will focus on bias circuits that use a series LCR filter, such that $\tau_{\text{elec}} = \frac{2L}{R}$. This is covered in more detail in Chapter 4.

which is consistent with laboratory measurements that achieved stable minimums down to $R_{\text{frac}} \approx 0.3$ [62].

3.4 RESPONSIVITY

The detector responsivity characterizes how well a detector converts a change in incident power to a change in current. Where the detector logarithmic *sensitivity*, α, is a property of the TES alone, the *responsivity*, S, is a function of both TES and electrical circuit properties. In an ideal DC-biased TES the fundamental responsivity is [50]

$$S_{\text{DC}} = \frac{\delta I}{\delta P} = \frac{-1}{V_{\text{TES bias}}} \,. \tag{3.11}$$

However, in a less idealized system, as in Figure 3.4, this is modified to [34]

$$S_{\text{DC}} = \left(\frac{-1}{V_{(\text{TES bias})}}\right) \frac{\mathcal{L} R_{\text{TES}}}{R_{\text{TES}} + z_s + \mathcal{L}(R_{\text{TES}} - z_s)} \,. \tag{3.12}$$

In the special case of a voltage bias that is delivered as a sinusoid,[6] $V_{(\text{TES bias, rms})}$ with frequency $\omega >> \frac{1}{\tau_{\text{eff}}}$, this responsivity is further modified by $\sqrt{2}$:

$$S = \left(\frac{-\sqrt{2}}{V_{(\text{TES bias, rms})}}\right) \frac{\mathcal{L} R_{\text{TES}}}{R_{\text{TES}} + z_s + \mathcal{L}(R_{\text{TES}} - z_s)} \,. \tag{3.13}$$

These modification terms are the product of several different mechanisms:

1. Sinusoidal biased systems exhibit an intrinsic responsivity advantage of $\sqrt{2}$ over DC-biased detectors [26].[7]
2. Finite loopgain. In the limit of $z_s = 0$ the second term simplifies to $\frac{\mathcal{L}}{\mathcal{L}+1}$.
3. Series impedance. In the limit of infinite loopgain the second term simplifies to $\frac{R_{\text{TES}}}{R_{\text{TES}} - z_s}$.

Finite loopgain and series impedance have a coupled effect on the overall responsivity, as both mediate the strength of electrothermal feedback. When z_s is complex, the relevant metric is

6 As is used in the SPT-3G readout.
7 This appears to give a performance advantage to sinusoidally biased systems over DC biased systems, but is offset by a $\sqrt{2}$ noise penalty discussed in Section 7.2.6. The intrinsic signal-to-noise of DC-biased and AC-biased systems are the same.

the magnitude $|S|$. For our parameters, only the real component of the Thévenin equivalent series impedance, $R_s = \mathrm{Re}(z_s)$, has much influence on S.

3.5 PHONON AND PHOTON NOISE

System noise sources are broadly defined as readout sources and non-readout sources. Readout noise sources will be covered in detail in Chapter 7, but the non-readout noise sources are more closely related to the bolometer or sky properties, and will be defined here. These are generated either by the random motions of thermal carriers between the TES and thermal bath (phonon noise), or by the photon arrival statistics (photon noise).

3.5.1 *Detector phonon noise*

In an isothermal system, random propagation of energy carriers generates a noise power with a spectral density

$$\mathrm{NEP}_{\mathrm{g,iso}} = \sqrt{4k_B T^2 G}\,, \tag{3.14}$$

but the thermal link between bolometer and T_{bath} is not an isothermal system. A correction factor for the temperature gradient between bolometer and heat sink is derived in Mather, 1982 [65] to be

$$\mathrm{NEP}_{\mathrm{g}} = \sqrt{\gamma_{NE} 4k_B T^2 G}\,, \tag{3.15}$$

where $\gamma_{NE} \approx 0.7$ for SPT-3G-like T_c and T_{bath}. Bolometer phonon noise is a leading source of noise, after photon noise, in modern systems such as SPT-3G. It can be improved by operating lower T_c detectors, or detectors with lower total saturation power.[8]

3.5.2 *Photon noise*

For the the regime where $h\nu >> k_B T_{\mathrm{source}}$ (as when observing CMB-like blackbody sources, T_{source} ~3 K, at frequencies much higher than the microwave), the photon arrival times can be considered random and independent, and are described by Poisson statistics

$$\mathrm{NEP}_{\gamma,\mathrm{shot}} = \sqrt{2h\nu P_{\mathrm{rad}}}\,, \tag{3.16}$$

8 This motivates the change from ~300 mK T_{bath} on SPT-3G to ~100 mK T_{bath} for LiteBIRD.

where h is the Planck constant, ν is the observing frequency, and P_{rad} is the total incoming radiation power from the CMB sky, but also from the atmosphere or emission from optical surfaces.

In the regime where $h\nu << k_B T_{\text{source}}$ (as when observing thermal sources at frequencies much lower than the microwave), photon arrival times are highly correlated due to photon bunching. This generates an additional photon noise correlation term, and the resulting noise is described by the Dicke radiometer equation, where $\text{NEP}_{\gamma,\text{Dicke-limit}} = \frac{P_{\text{rad}}}{\sqrt{\Delta\nu}}$.

Millimeter-wave CMB experiments operate in the crossover regime, between photon noise described by Poisson statistics and photon noise described by the Dicke equation. Moreover, the Dicke equation is strictly valid only for a detector that couples to a single spatial mode, through an idealized set of optics. Transmission through non-idealized optics involves scattering, reflection, and some degree of multimoded coupling. A more complete analysis of photon-correlation noise for millimeter-wave CMB experiments specifically is given in Zmuidzinas, 2003 [100]. That work demonstrates that corrections to the photon correlation noise term can be significant for our operating conditions. It also provides analytic means to calculate them, given precise scattering and coupling matrices. Unfortunately these are are poorly characterized for the built instruments, and so we leave this as a correction term $0 < \xi < 1$,[9]

$$\text{NEP}_{\gamma,\text{corr}} = \sqrt{\xi \frac{P_{\text{rad}}^2}{\Delta\nu}}\,, \tag{3.17}$$

such that the complete expression for photon noise is

$$\text{NEP}_{\gamma} = \sqrt{2h\nu P_{\text{rad}} + \xi \frac{P_{\text{rad}}^2}{\Delta\nu}}\,, \tag{3.18}$$

9 ξ is often estimated for a range of values when predicting the total photon noise. An estimate for SPTpol was given in [26] as ~ 0.3, while LiteBIRD sensitivity analyses conservatively assume $\xi = 1$.

3.5.3 *TES Johnson noise*

Bolometers are Ohmic devices with an instantaneous real resistance at all times, and generate Johnson noise power density equal to $\sqrt{4k_BTP_\mathrm{J}}$. However, when the detectors are in the superconducting transition this is suppressed by electrothermal feedback [63],

$$\mathrm{NEP}_{\mathrm{TES,Johnson}} \approx \frac{\sqrt{4k_BTP_\mathrm{J}}}{1+\mathcal{L}}\,. \tag{3.19}$$

The strong suppression by loopgain under typical operating conditions makes this a negligible source of noise.

3.6 MULTIPLEXING

Since at least 1997, with the BOOMERanG experiment, CMB instruments have operated in the photon noise limit, such that photon noise is the dominant noise source, followed by phonon noise [21]. In such a regime the most common way to improve instrument sensitivity is to observe the sky with more detectors, and develop focal planes with increasing detector densities.[10] CMB experiments at the turn of the millennium operated fewer than 50 detectors.[11] The current SPT-3G focal plane consists of ∼15,000 detectors, and future "Stage 4" instruments (such as CMB-S4) are planned with an additional order of magnitude increase [1]. Individually biasing each detector in sub-Kelvin arrays of this size would require prohibitively powerful cryogenic capabilities, since each bias line is an unbroken conductive element to room temperature.[12] This thermal limitation forced a paradigmatic shift away from direct biasing, and towards higher complexity in readout instrumentation. Two separate techniques emerged – Frequency Domain Multiplexing (FDM), the focus of this thesis; and

10 An alternative means to increase sensitivity is through massively *multi-moded* optics. However, historically the path taken by the field has been large-pixel arrays coupled to single-, or very nearly single-, moded optics. The recently proposed PIXIE satellite experiment uses a 4-detector focal plane that couples to 22,000 modes, but failed to secure funding for the Explorer class satellite missions [57].

11 MAXIMA and BOOMERanG both operated 16 detectors; ACBAR began with 4 detectors and grew to 16; and the PLANCK HFI operated 48 detectors.

12 The existing sub-Kelvin thermal budget for SPT-3G is 2 µW. A direct-biasing scheme in SPT-3G would require nearly a factor of 10 increase in cooling power.

Time Division Multiplexing (TDM, [24]). Both surmount the problem by allowing multiple detectors to share sets of wires.

The first version of what would become the SPT-3G FDM system was the Analog Frequency Domain Multiplexer (AfMUX), designed in 2005 for the APEX-SZ camera on the APEX telescope. The AfMUX system was capable of 7x multiplexing. In 2007, that AfMUX system was also deployed on the first South Pole Telescope camera, SPT-SZ. In 2011, at McGill, the concept was developed into a digital signal processing platform for the second South Pole Telescope camera, SPTpol. This became known as the McGill Digital Frequency Domain Multiplexing (DfMUX) system (hereafter the "Legacy" DfMUX). The Legacy DfMUX system was eventually capable of 16x multiplexing. It addition to SPTpol, it was deployed on the EBEX balloon-borne instrument, and the ground-based Polarbear telescope [26, 27].

My research efforts have been on the development of a third generation of this readout technology, which has enabled 68x (and is capable of 128x) multiplexing. This current DfMUX system is operating on the SPT-3G and Polarbear-2 experiments, and I am now involved in the design and development of a space-qualified version for the LiteBIRD satellite mission.

Summary of TES parameters

Parameter	Symbol	Equation	Note
TES normal resistance	R_n	$R(T >> T_c)$	
TES operating resistance	R_{TES}	$R(T \sim T_c)$	In-transition
Series impedance with the TES	z_s		Thevenin equivalent series impedance of bias circuit
Fractional resistance	R_{frac}	$\dfrac{\lvert R_{\text{TES}} + z_s\rvert}{\lvert R_{\text{n}} + z_s\rvert}$	
Thermal bath temperature	T_{bath}	$T_{\text{bath}} < T_c$	$\sim$300 mK (SPT-3G)
Thermal conductance to T_{bath}	$G(T)$		
Extracted bath power P_G	$G(T - T_{\text{bath}})$		
TES saturation power	P_{sat}	$G(T_c - T_{\text{bath}})$	Maximum power required to keep $R_{\text{TES}} = R_n$
Deposited joule power	P_J	$I_{\text{TES}}V_{\text{TES}}$	TES bias power
TES sensitivity	α	$\dfrac{T}{R}\dfrac{\partial R}{\partial T}$	Property of TES transition
Loopgain	$\mathcal{L}$	$\dfrac{\alpha P_J}{GT}$	$7 \gtrsim \mathcal{L} \gtrsim 10$ (SPT-3G)
Negative ETF (stable)		$\dfrac{\delta P_J}{\delta R} < 0$	Satisfied by fixed voltage bias $P_J = \dfrac{V_{\text{bias}}^2}{R}$
Positive ETF (unstable)		$\dfrac{\delta P_J}{\delta R} > 0$	Satisfied by stiff *current* bias $P_J = I_{\text{bias}}^2 R$
TES thermal time constant	τ_0	$\dfrac{C}{G}$	Where C is the TES heat capacity
TES effective time constant	τ_{eff}	$\dfrac{\tau_0}{\mathcal{L}\dfrac{R_{\text{TES}} - \lvert z_s\rvert}{R_{\text{TES}} + \lvert z_s\rvert} + 1}$	τ_0 is sped up by ETF
Bias circuit electrical time constant	τ_{elec}	$\dfrac{2L}{R}$	Time constant for a series LCR bias circuit
DC Stability Criterion		$R_{\text{TES}} \geq R_s\left(\dfrac{\mathcal{L}-1}{\mathcal{L}+1}\right)$	If z_s is purely real (R_s)
Dynamic Stability Criterion		$\dfrac{\tau_0}{\mathcal{L}\dfrac{R_{\text{TES}} - \lvert z_s\rvert}{R_{\text{TES}} + \lvert z_s\rvert} + 1} \geq \left(3 + 2\sqrt{2}\right)\tau_{\text{elec}}$	If z_s is complex.
Minimum stable R_{frac}		$R_{\text{frac}} \gtrsim \dfrac{2\lvert z_s\rvert}{\lvert R_n + z_s\rvert}$	A rule of thumb estimate
Responsivity	$S = \dfrac{\delta I}{\delta P}$	$\left(\dfrac{-\sqrt{2}}{V_{(\text{TES bias, rms})}}\right)\dfrac{\mathcal{L}R_{\text{TES}}}{R_{\text{TES}} + z_s + \mathcal{L}(R_{\text{TES}} - z_s)}$	For sinusoidally biased systems
TES phonon noise	NEP_{g}	$\sqrt{\gamma_{NE}4k_BT^2G}$	$\gamma_{NE} \approx 0.6$
TES photon noise	NEP_{γ}	$\sqrt{2h\nu P_{\text{rad}} + \xi\dfrac{P_{\text{rad}}^2}{\Delta\nu}}$	$0 < \xi < 1$
TES Johnson noise	$\text{NEP}_{\text{TES,Johnson}}$	$\approx \dfrac{\sqrt{4k_BTP_{\text{J}}}}{1+\mathcal{L}}$	Insignificant when $\mathcal{L} > 1$

Table 3.1: Detector parameters and relevant operating principals defined and derived in Chapter 3.

4
READOUT THEORY

This chapter introduces the required lexicon and operational principals of Frequency Domain Multiplexing (fMUX), as used on the SPT-3G instrument. I describe how the system design is shaped by specific fabrication limitations (Section 4.2); as well as the interactions between readout and detectors, which modify the TES stability (Section 4.3). Section 4.4 covers the basic operation of the cryogenic amplifiers (Superconducting Quantum Interference Devices, or "SQUIDs"), which require the application of a feedback strategy described in Sections 4.5 and 4.6. Section 4.7 introduces techniques used to evaluate the end-to-end readout system in-situ, and to choose detector bias parameters. Finally, Section 4.8 introduces the custom signal processing and readout electronics used on SPT-3G and Polarbear-2.

4.1 FREQUENCY DOMAIN MULTIPLEXING

Frequency Domain Multiplexing takes advantage of the fact that thermal (and electrothermal) time constants of TES detectors can be engineered to be relatively slow ($\mathcal{O}(1\text{ms})$). The voltage bias can therefore be provided as a sinusoid at MHz frequencies, rather than as a DC potential. At these frequencies the detector will not respond to the instantaneous variations in voltage bias, but will still receive a deposition of electrical power proportional to the root-mean-square of the sinusoid amplitude. In this way we substitute independent *bias wires* for independent *biasing sinusoids*, which are summed on a single set of wires. The TES elements are then embedded within parallel legs of a network of cryogenic LC filters, such that each cryogenic filter leg consists of an inductor (L), capacitor (C), and TES, in series. These series band-pass filters shield each TES from bias frequencies other than their own, allowing multiple TES detectors to be biased and read out using a single pair of transport wires (Figure 4.1).

As with direct-biasing, TES detectors in an FDM system respond to changes in incident sky power with variations in resistance. This amplitude-modulates the current waveform that is the result of the biasing sinusoid, in an operation analogous to AM-radio: sky signals are encoded in the sidebands of each bias sinusoid (Figure 4.2). The collection of modified sinusoids is summed together at a cryogenic amplifier, transmitted to room-temperature electronics, and digitally demodulated to recover the sky signal. The number of TES elements that may be operated in tandem this way is the multiplexing (MUX) factor.

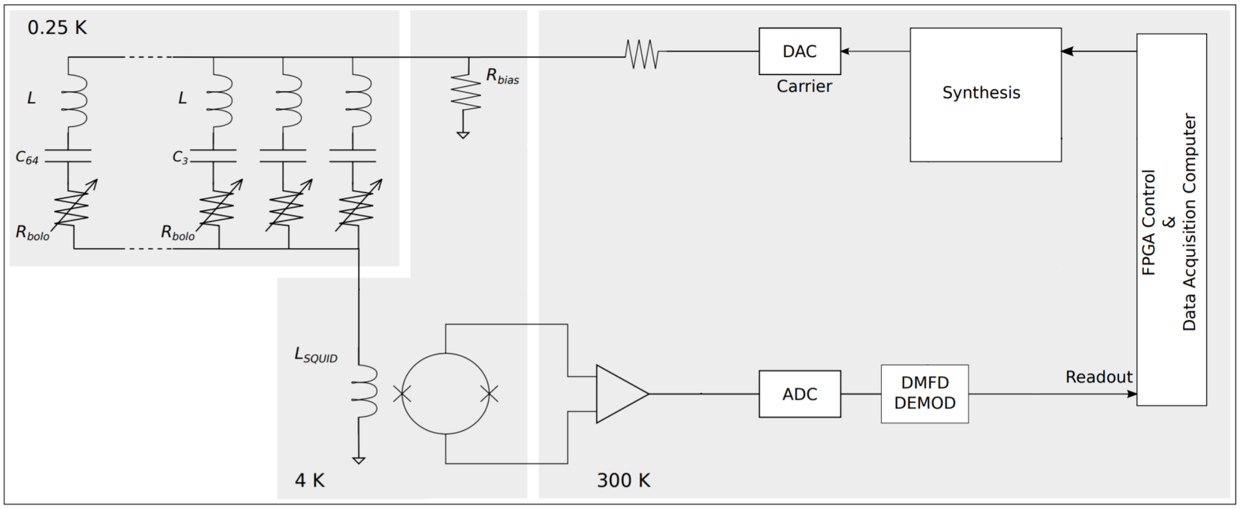

Figure 4.1: A simplified schematic diagram of the multiplexing scheme. A carrier DAC provides a current bias waveform that is converted to a voltage through $R_{\mathrm{bias}} << R_{\mathrm{TES}}$. This voltage bias is applied to a comb of LCR filters in which the TES detectors are embedded. The filters provide isolation between the TES detectors, which are individually biased by sinusoids at the LCR resonance frequencies. The resulting current is sensed through the SQUID, and then digitally demodulated. Image adapted from Bender et al., 2014 [14].

4.2 CRYOGENIC FILTER DESIGN

Higher multiplexing factors in FDM systems can be achieved by increasing the total bandwidth and/or increasing the density of resonant LC filters. There is an optimal combination of these based on how they effect performance metrics such as crosstalk and stability. However, realizing that optimal combination is difficult due to limitations in the fabrication technology and large-scale production. The different strategic compromises made between the Legacy and current DfMUX systems illustrate these points well, and point the way towards future design improvements.

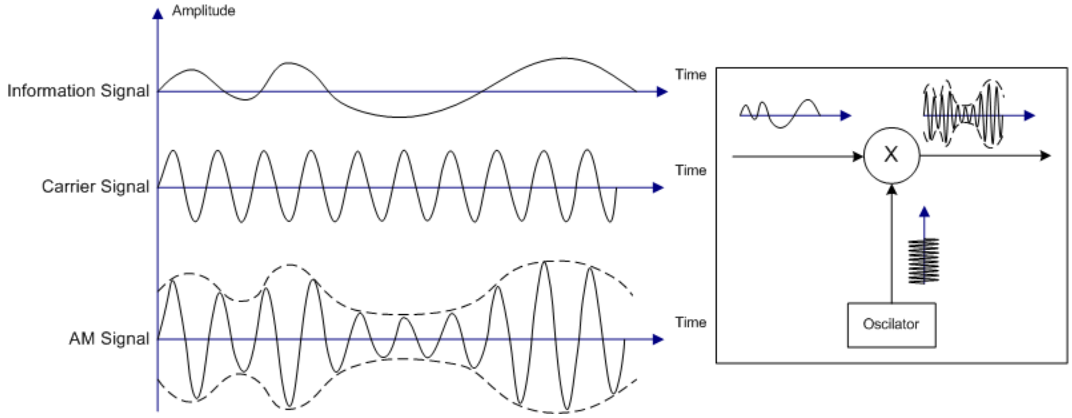

Figure 4.2: This diagram shows generically how amplitude modulation works to encode signal. In our case the information signal comes from the variation in TES resistance in response to changes in incident radiative power. The carrier signal is an individual sinusoidal bias; and the AM signal is the resulting amplitude-modulated current waveform at the cryogenic amplifier. Image from Ivan Akira, 2010 [51].

4.2.1 *Ideal cryogenic filter parameters*

An ideal cryogenic filter design for DfMUX would have densely populated filters that maintain strong isolation between TES detectors. Such density requires precision in the resonance fabrication, and isolation comes from narrow bandwidth (BW). For our single-pole filter design

$$BW = \frac{R}{2\pi L}\,, \tag{4.1}$$

where R is the total real series resistance within the cryogenic filter leg, and should be dominated by R_{TES}. POLARBEAR-2 and SPT-3G operate detectors at approximately 0.7 and $1.4\,\Omega$ respectively.[1]

For the typical TES detectors in DfMUX systems, the minimum bias frequency would theoretically be $\mathcal{O}(100\,\mathrm{kHz})$. Lower frequencies are preferred because they minimize any reactance in the cryogenic circuit due to stray complex impedances, which can compromise TES stability (Section 3.3, Equation 3.7). The resonant frequency of an LCR filter is defined by the filter inductance and capacitance as

$$\omega = \frac{1}{\sqrt{LC}}\,. \tag{4.2}$$

1 This is one property that favors lower bolometer impedances – as it leads to better isolation within the circuit and higher channel densities.

In DfMUX systems, the same inductance is used for every LC filter, and resonant frequencies are tuned by the choice of capacitance. This reduces complexity in the cryogenic fabrication and enforces a uniform bandwidth across the system.

4.2.2 *Legacy cryogenic filter design*

Legacy DfMUX systems follow the above design closely – populating a bandwidth between 300 kHz and 1.3 MHz with up to 16 cryogenic filter resonances, using inductors that are each 24 µH. Extending the success of that design to higher channel densities within this bandwidth would require better isolation between resonant frequencies: even larger inductors and even smaller capacitors. This is frustrated primarily by (1), the commercial availability of cryogenic-capable capacitors with sufficiently low capacitance; and (2), the imprecision in achieved capacitances of commercial devices. Extending to higher frequencies has an additional penalty in the form of growing equivalent series resistance (ESR). ESR is a property arising from interactions with the dielectric medium used in a capacitor. That interaction generates a series resistance, which threatens TES stability. Typical ESR from the commercial ceramic capacitors used in Legacy systems are ∼290 mΩ at frequencies below 1 MHz and scale approximately linearly with frequency [66]. Together, these constraints kept resonances in Legacy DfMUX systems broad, widely spaced, and low frequency.[2]

4.2.3 *Current generation 68x cryogenic filter design*

The non-cryogenic portion of the current generation DfMUX system supports up to 128x multiplexing. Full 128x operation has been demonstrated in the lab with 128x cryogenic filters and mock-detectors [38]; however, current deployed instruments are limited by bandwidth and fabrication tolerances to cryogenic circuitry capable of a maximum of 68x multiplexing. The 68x cryogenic filter design prioritizes greater control of capacitor properties over low resonant frequencies. Instead of using surface mounted ceramic capacitors, the LC filters are made up of custom 2D photo-lithographed structures, the geometries of which generate the

2 There was an additional reason why frequencies above 1.3 MHz were not utilized in Legacy DfMUX systems, related to the implementation of the SQUID devices. This is not relevant in the DfMUX system that is the focus here, but the details can be found in Dobbs et al., 2012 [26].

inductance and capacitance.[3] Figure 4.3 shows these individual structures, and Figure 4.4 shows how they are used within the context of the cryogenic electronics [85].

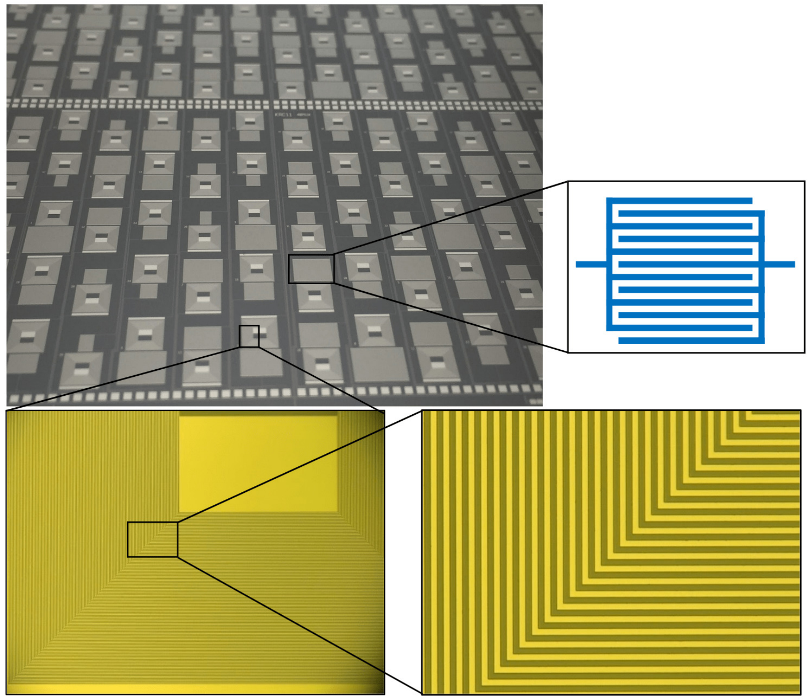

Figure 4.3: A lithographic wafer (upper left) which is made up of individual spiral inductors (lower), and inter-digitated capacitors (diagram, upper right). These are 2D structures that generate their electrical properties through the coupling between aluminum surface structures. Trace widths in the above images are 4 µm and the structures in the top left frame are each approximately 15 mm^2. Images provided by Aritoki Suzuki, more fabrication information available in Rotermund et al., 2016 [85].

The precision of photo-lithography allows greater control and uniformity in individual capacitance and inductance values. The process is also well-suited to mass fabrication. There is no additional dielectric material between the planar surface features that generate capacitance, meaning effectively zero ESR penalty at higher frequencies. A limitation of this method is that photo-lithographed capacitors achieve low capacitance values easily, but struggle to provide large capacitances. This favours the use of larger inductance values with tighter bandwidth and better isolation between channels, but it limits the usable bandwidth to above approximately 1.6 MHz. Figure 4.5 compares the resonances used in Legacy and current DfMUX systems.

3 Legacy DfMUX systems have used lithographic inductors, but never lithographic capacitors.

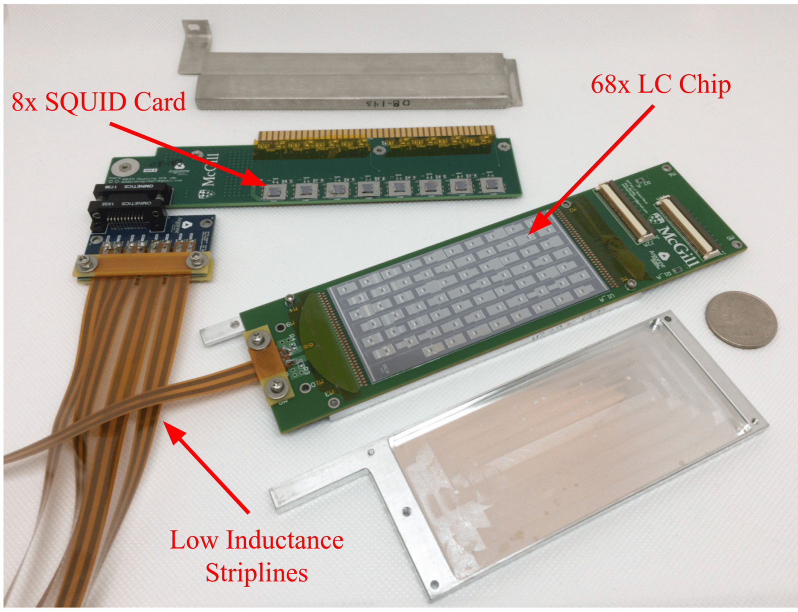

Figure 4.4: Lithographic planar resonances are fabricated in batches of 6" wafers before being diced down to 68x monolithic chips and mounted to "LC boards." This image also contains the low-inductance superconducting striplines that connect the LC boards (at sub-Kelvin) to the cryogenic SQUID amplifiers (at 4K). Image from Bender et al., 2018 [13].

4.3 MODIFIED DYNAMIC STABILITY CRITERION

The electrical time constant (τ_{elec}) of an LCR filter is well-defined and parameterized by the decay constant[4]

$$\tau_{\mathrm{elec}} = \frac{2L}{R}\,. \tag{4.3}$$

Together the general solution for the TES dynamic stability criteria (Section 3.3, Equation 3.8) gives the specific relevant form of the dynamic stability criteria:

$$\frac{\tau_0}{\mathcal{L}\frac{R_{\mathrm{TES}}-z_s}{R_{\mathrm{TES}}+z_s}+1} \geq \left[3+2\sqrt{2}\right]\left(\frac{2L}{z_s+R_{\mathrm{TES}}}\right)\,. \tag{4.4}$$

4 This is exactly true for a critically damped LCR circuit. However, the 68x circuit parameters yield an under-damped solution that includes a complex component. This complex component defines an oscillation frequency of around 20MHz. Note that this is distinct from the under-damped property of the *electrothermal system* itself. The consequence of using an under-damped filter is not an instability in the electrothermal feedback system. Rather, at frequencies near the oscillation frequency (around 20 MHz) the filter appears lower impedance than it would with a critically damped filter. In practice this is not relevant for us, as those frequencies are out of band and heavily filtered by other components in the system. I consider only the decay constant here.

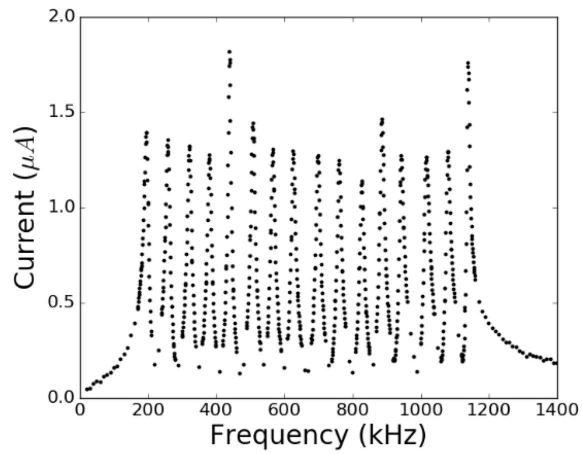

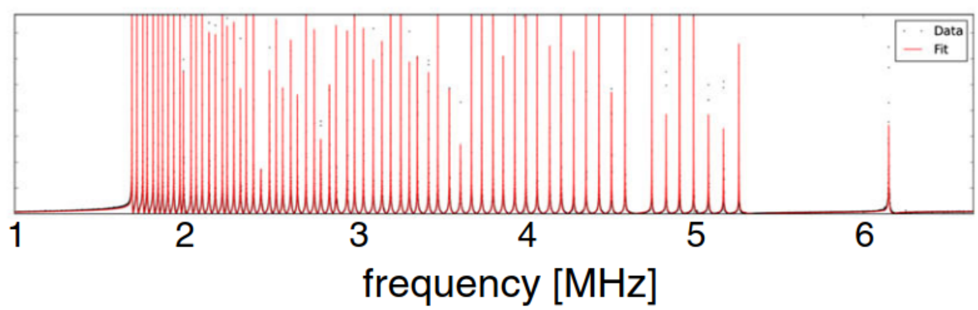

Figure 4.5: Top: A Legacy 16x DfMUX comb of resonances. These used 24 µH inductors with R_{TES} ≈0.7 Ω detectors. Image from EBEX Collaboration et al., 2018 [33]. **Bottom:** An SPT-3G comb of resonances that use 60 µH inductors and R_{TES} ≈1.4 Ω detectors, resulting in better resonance isolation and higher channel densities. Image from Anderson et al., 2018 [4].

In the limit of $R_{\text{TES}} >> z_s$ this reduces to the more commonly quoted form

$$\frac{\tau_0}{\mathcal{L}+1} \gtrsim 5.8 \frac{2L}{R_{\text{TES}}} \,. \tag{4.5}$$

4.3.1 *Designing for stability*

Equation 4.4 is most useful to constrain the relationship between allowable filter parameters (LC design) and detector thermal time constant (TES design). Notice that when designing for higher multiplexing we desired large inductance values to improve isolation between neighboring channels. However this same choice drives us to instability *unless we also use slower detectors*. This is a challenge because we prefer to modulate our desired signal relatively rapidly, either by scanning quickly over the sky or using a specific rotating signal modulator (in the case of POLARBEAR-2 and LITEBIRD). This shifts sky signals out to higher sideband frequencies, where intrinsic ("$1/f$") flicker noise is low, as are the effects of any slow systematics such as drifts of the mK stage temperature.[5] By increasing the filter inductance to enable higher multiplexing, SPT-3G requires detectors nearly four times slower than SPTPOL. Sufficiently slow detectors will generate an asymmetric beam on the sky as the telescope scans. We offset this partially by scanning slower,[6] and by performing a detailed campaign to measure the detector beam shapes with planet observations, in order to account for the effect during data analysis.

That these two motivations are at odds generates an optimization pressure to target detector τ_{eff} very near to the margin of stability. This is a difficult needle to thread, and depends on correct prediction of optimum parameters; accurate measurement of the achieved detector time constants; and precise control over the TES fabrication uniformity. SPT-3G was plagued by instability during its 2017 engineering run before better fabrication tolerances could be achieved and slower detectors were targeted.[7]

5 This technique is one reason why $1/f$ noise is addressed by design, and not a significant source of noise in DfMUX instruments.

6 This trades better resolution of the smallest features on the sky for slightly noisier measurements of the largest features.

7 The final results are covered in more detail in Chapter 6.

4.4 COLD AMPLIFICATION USING SQUIDS

TES detectors have sufficient responsivity to detect $\mathcal{O}(10\ \mathrm{aW})$ fluctuations in deposited power. Nevertheless, the resulting current modulations of interest can be as small as $\mathcal{O}(10\,\mathrm{pA})$, and require additional cryogenic amplification before they can be transmitted to room temperature electronics. The DC stability criterion (Equation 3.7) imposes the limitation that the input impedance to any cryogenic amplifier must be $<<R_{\mathrm{TES}}$. The combined requirements of low input impedance, low noise, and sufficient gain, has so far required the use of Superconducting Quantum Interference Devices (SQUIDs). SQUIDs are highly non-linear devices that operate as transimpedance magnetometers. A SQUID will sense small variations in current using a low-impedance inductive input coil, and produce an output voltage large enough to be amplified with conventional warm electronics.

Despite their widespread use in TES-based instruments, the combination of DfMUX and SQUID amplification seems to suffer from a set of prohibitive limitations. These limitations are only solved by a careful implementation of digital feedback, described in Section 4.5. In the sections below I introduce basic SQUID physics, how they are biased and operated, and the primary obstacles to SQUID use in a DfMUX system.

4.4.1 *Basic SQUID theory*

SQUIDs use the Josephson effect to generate an electrical potential in response to current through an inductor, which serves as the SQUID input coil. They are composed of two fundamental elements: the SQUID input coil, through which the current of our TES network flows; and a superconducting loop, broken by small insulating barriers (Josephson junctions), shown in Figure 4.6.[8]

Current at the SQUID input coil generates a magnetic flux through the superconducting loops. A consequence of the quantum mechanical nature of superconductivity is that total magnetic flux through superconducting loops is quantized [25, 28, 60]. This property is expressed in screening currents induced around the loops, which maintain fixed flux quanta by either opposing or contributing to the input flux. Those screening currents tunnel quantum

8 For DfMUX we actually use SQUID Series Arrays (SSAs), consisting of many of these loops in parallel and series.

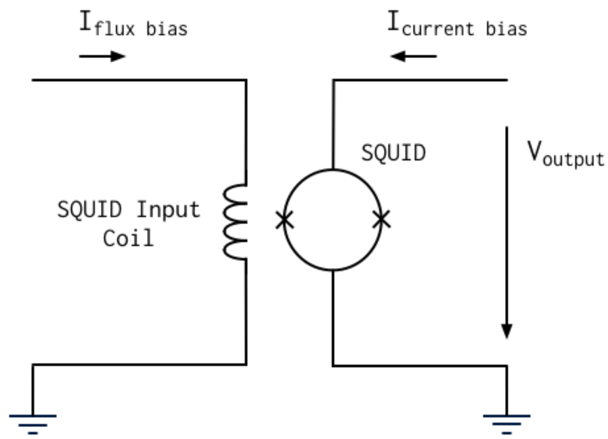

Figure 4.6: Schematic diagram showing the SQUID. On the right is the SQUID input coil, through which a current flows and generates flux. The flux through the superconducting loop generates screening currents through the loop. Those screening currents generate a voltage across the Josephson junctions, which is the SQUID output. The process acts like a transimpedance amplifier, with a transimpedance of $\mathcal{O}(100\,\Omega)$. Image from Montgomery, 2015 [66].

mechanically through the Josephson junctions, but produce a voltage across the junctions upon exceeding a critical current [53].

By providing that critical current with a separate fixed bias (the *SQUID junction current bias*) it is possible to measure *changes* in the screening currents (and therefore in the current through the SQUID input coil) by the variation in voltage across the Josephson junctions. That voltage (the *SQUID output*) is then further amplified using conventional electronic amplifiers.

SQUIDs deployed on SPT-3G exhibit a typical transimpedance of $Z_{\text{trans}} \approx 1000\ \frac{\text{V}}{\text{A}}$, converting pA input currents to nV output voltages. A detailed overview of the physics of SQUIDs is available in John Clarke's excellent SQUID Handbook, J. Clarke, 2004 [52].

4.4.2 *Non-linear SQUID response*

A traditional amplifier has a predominantly linear response, such that $V(I) = G \times I$, with gain G. By comparison, the SQUID response function is *periodic* and *non-single-valued*. It can only be usefully operated over the narrow range of input amplitudes where the output is single-valued and approximately linear. As the input amplitudes grow, so too does the non-linearity of the output response. Figure 4.7 shows the periodic response function of the SQUID, as well as the limited regime that can be considered approximately linear. For a

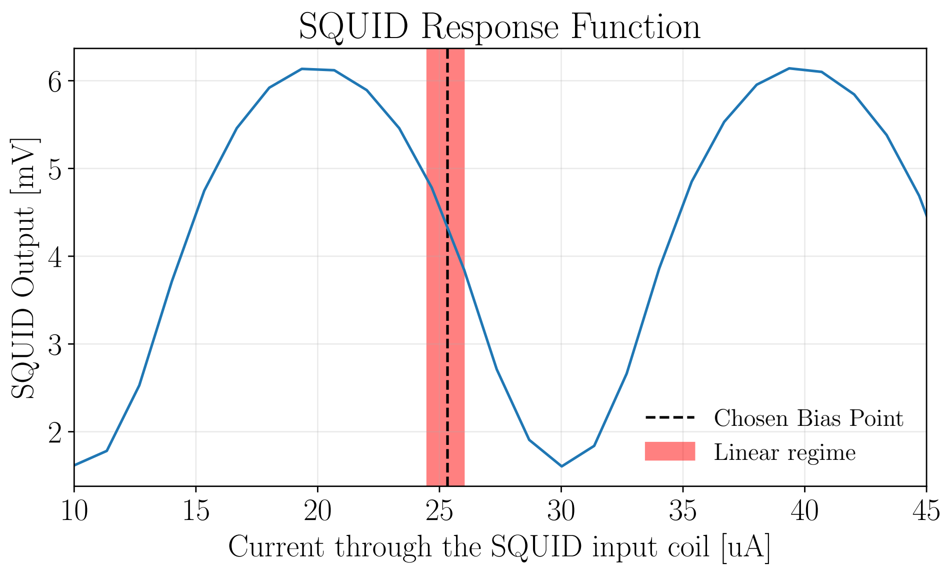

Figure 4.7: The SQUID output response is a periodic and non-single valued function of the input current, limiting the input amplitudes for which it can be usefully operated. Annotated above is the approximately linear response regime and the "bias point." We bias the SQUID using a DC current through the SQUID input coil to center the SQUID response in the linear regime.

SQUID to operate in a linear regime, and with a large transimpedance, it must be "tuned" to the proper operating point.

4.4.3 *SQUID tuning*

The SQUID response function is called the $V(\phi)$ ("v-phi") curve. A SQUID is tuned when:

1. The dynamic range (peak-to-peak amplitude of the $V(\phi)$) is maximized. A large dynamic range corresponds to a larger region of linearity within the $V(\phi)$, and a larger maximum transimpedance.

2. The transimpedance is large (corresponding to a region of the $V(\phi)$ curve with a large derivative).

3. Response to small variations in input current is linear (the local region of the $V(\phi)$ curve at the bias point is well approximated by a line).

There are two separate biases used to tune the SQUID:

THE SQUID JUNCTION CURRENT BIAS adjusts the current through the Josephson junctions relative to the critical current, and determines the dynamic range of the SQUID.

THE FLUX BIAS adjusts the baseline flux through the SQUID, selecting a local region of the $V(\phi)$ curve and, with it, the particular transimpedance and linearity of the device.

Each of these adjustments, and an example of a chosen tuning point, are given in Figure 4.8.

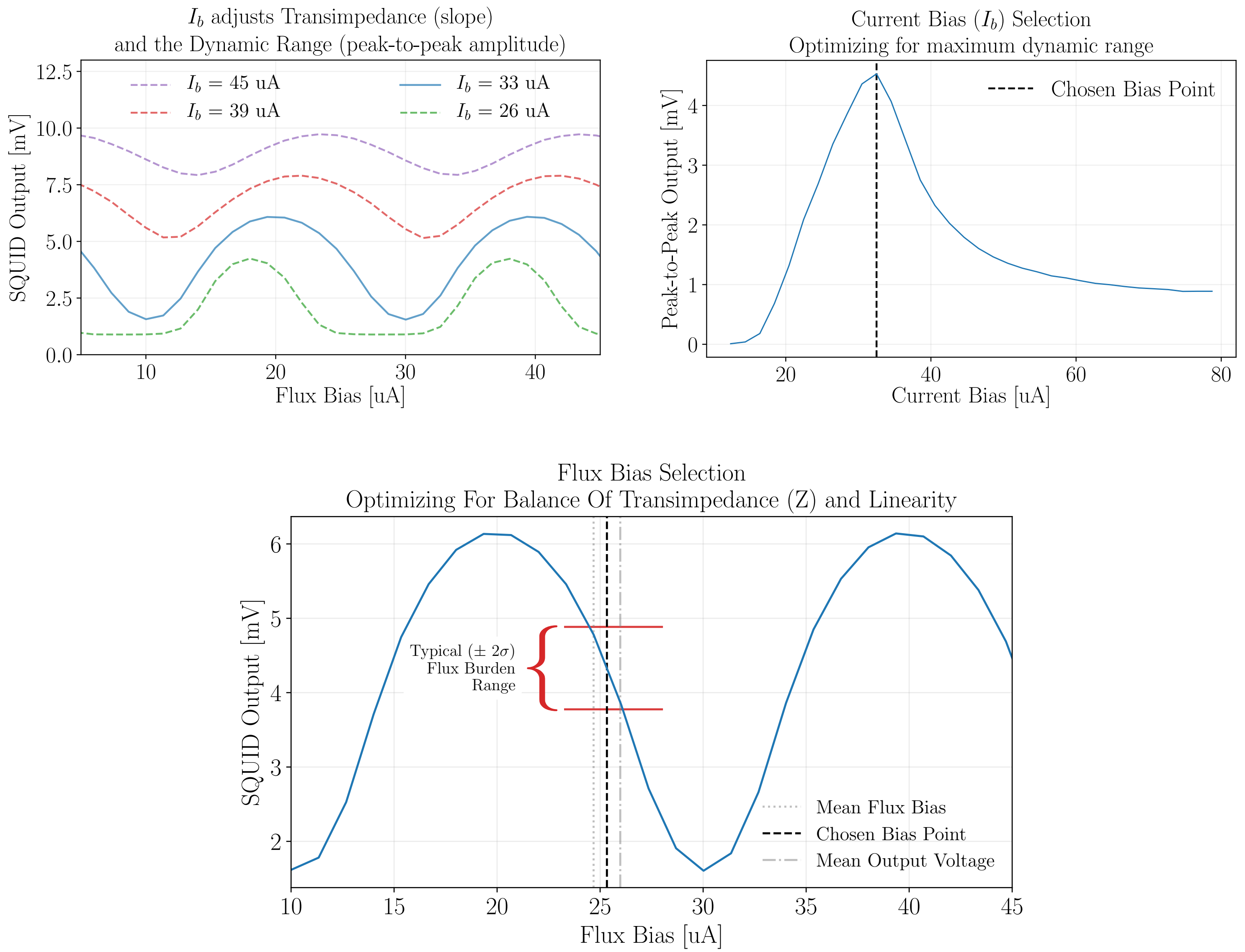

Figure 4.8: Top left: Successive SQUID $V(\phi)$ measurements are shown by plotting the SQUID voltage output as a function of both flux bias (along each curve) and SQUID junction current bias (the separate curves). The peak-to-peak amplitude of each curve on the left correspond to a single point in the right hand figure. **Top right:** SQUID dynamic range as a function of SQUID junction current bias (I_b). The value of I_b that maximizes the peak-to-peak amplitude of the $V(\phi)$ also maximizes the highest possible transimpedance. **Bottom:** $V(\phi)$ of a tuned SQUID with an optimal current bias of 33 µA, and flux bias chosen as the midpoint between the mean output voltage and mean flux bias between peak and trough.

4.4.4 *Challenges in using SQUIDs for DfMUX*

The biggest challenges to using SQUIDs as cryogenic amplifiers in DfMUX systems come from *flux burdening* and *series reactance*. SPT-3G uses SA13 SQUIDs, fabricated at the National Institute of Standards and Technology (NIST) [13]. For these devices, the maximum root-mean-square input current (flux burden) that still produces a single-valued output is approximately $I_{\text{input coil}}$=2.1 µA, and the linear regime is much smaller. Meanwhile, a single carrier sinusoid providing a typical voltage bias for a TES results in $I_{\text{input coil}}$=2.5 µA at the SQUID input coil. Without an additional mechanism to address this flux burden, even just a single TES bias is sufficient to saturate a SQUID.

The series reactance generated by the SQUID input coil is also problematic. Although SQUIDs have much lower input impedance than conventional cryogenic HEMT (high-electron-mobility transistor) amplifiers, it is still too large to stably operate detectors at high bias frequencies. Currently deployed SA13 SQUIDs have a 70 nH SQUID input coil, enough to violate the DC stability criterion at the upper ranges of the bias frequency bandwidth.[9] Both of these issues are solved using a form of feedback called "nulling."

4.5 STATIC NULLING

Limitations to the SQUID dynamic range and series reactance are overcome in fMUX systems using a technique pioneered on the AfMUX and Legacy DfMUX designs, described in Dobbs et al., 2012 [26], and Dobbs et al., 2008 [27]. The original version of this technique worked by injecting inverted copies of the carrier sinusoids ("nullers") across the SQUID input coil. The phase and amplitude of each nuller tone was adjusted to cancel current due to the bias frequencies at the *SQUID summing junction*. This is known as "static nulling," and it prevents current at the bias frequencies from flowing through the SQUID input coil. The additional nulling circuit is shown in Figure 4.9, using the simple circuit model introduced earlier.

9 Commercially produced SQUIDs have achieved SQUID input coil inductance as low as 10 nH, however they are noisier and more susceptible to nonlinear behavior, and haven't yet been viably demonstrated for DfMUX.

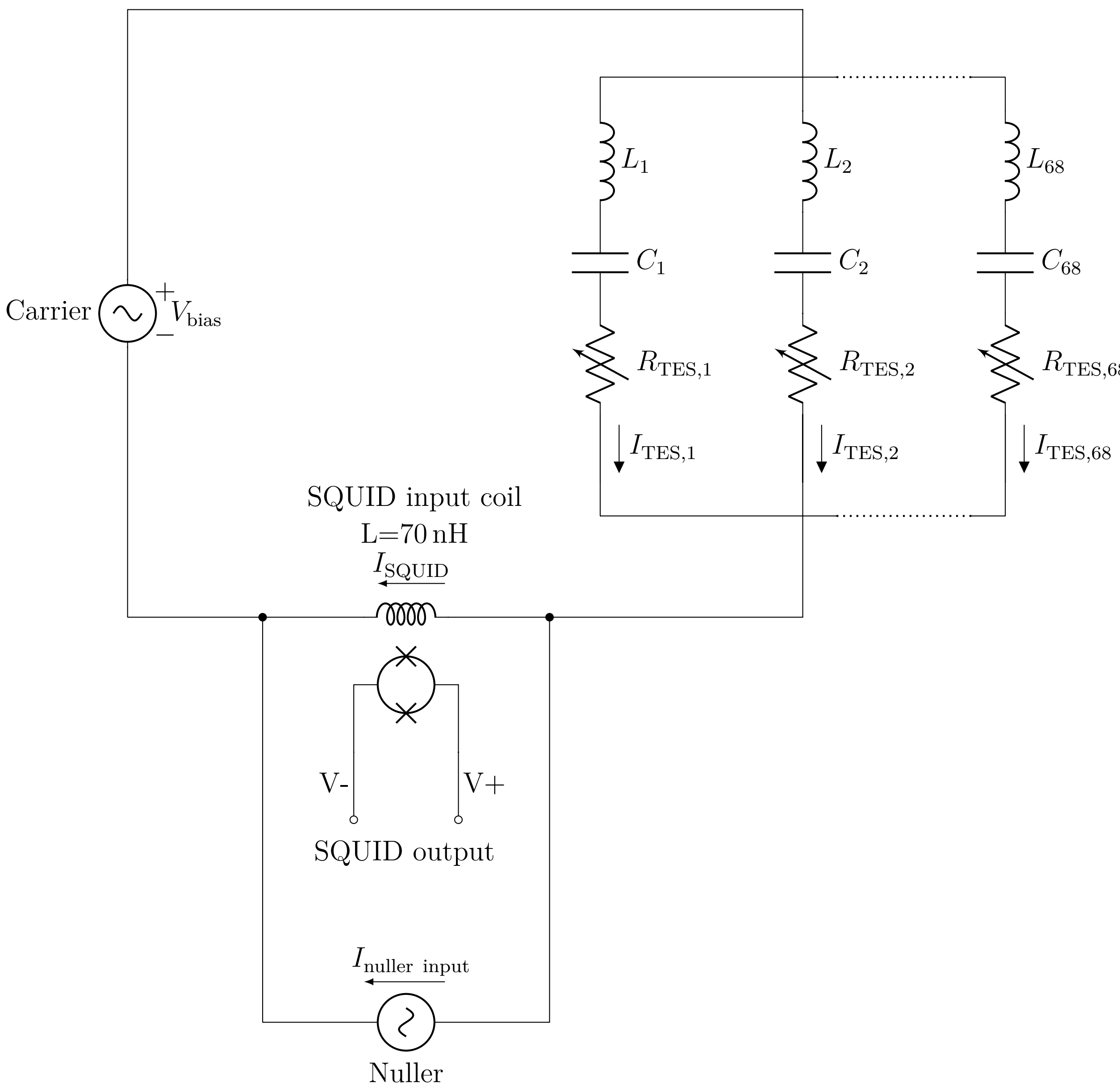

Figure 4.9: A simplified DfMUX circuit that includes both the SQUID amplifier and the nulling lines. The *SQUID summing junction* is indicated by the filled-in nodes on either side of the SQUID input coil. Static Nulling injects inverted copies of the carrier sinusoids via the nulling lines. Digital Active Nulling (DAN) injects current at the SQUID summing junction to force the voltage across the SQUID input coil to zero over the active bandwidth, generating a virtual ground and preventing any current from flowing through to flux burden the SQUID.

This addresses the dominant source of flux burden on the SQUID (current from the primary bias tones themselves). It also generates a “virtual ground” across the SQUID input coil at the bias frequencies,[10] nulling away the flux burden from carrier tones.

Static nulling only addresses the flux burden on the SQUID at the bias frequencies; it doesn’t prevent flux burdening sourced from side-band signals, or any environmental electromagnetic interference (EMI). However, these are much smaller amplitude signals, and could be addressed separately using a lower loop-gain broadband proportional feedback, in the form of an analog flux locked loop (FLL) [26].

This combination of static nulling and a Flux Lock Loop works well at bandwidths below $\sim$1.2 MHz, but the FLL is unstable at higher frequencies. This is a fundamental consequence of the analog form of broadband feedback used, and of the phase shift in that feedback incurred over long cable lengths. A different technique is required for the current generation DfMUX system, which reaches 128x multiplexing over 10 MHz of bandwidth. The new technique eliminates low-loopgain broadband proportional feedback, replacing it with narrow-band high-loopgain integral feedback. These narrow bands are centered at each bias frequency. This is known as Digital Active Nulling (DAN) [27].

4.6 DIGITAL ACTIVE NULLING

Whereas static nulling only nulls precisely at the bias frequency of the TES, and so cannot stabilize the TES by nulling away the series reactance, DAN extends that feedback to into a bandwidth several dozen kHz wide by *dynamically adjusting* each nuller tone in real-time (Figure 4.10). The effective DAN bandwidth is largely limited by the digital latency of the signal processing involved in updating nuller tone phases and amplitudes.

DAN as a methodology was developed in 2012 to support the Legacy DfMUX system, predating my involvement in the project, and the original DAN implementation is described in de Haan et al., 2012 [22]; while we first presented the 64x-capable DfMUX readout in [14]. The conceptual fundamentals for the 128x implementation are largely unchanged from the descriptions offered in those publications. However, the *structural* demands of 128x multiplexing, and associated digital latency, have imposed much more strict stability requirements on the feedback loop. These are described for the first time here.

10 A simple way to see this is just that it forces the voltage difference across the SQUID input coil to zero at those frequencies.

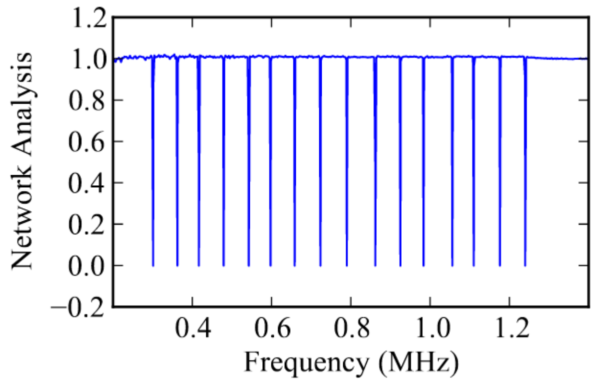

Figure 4.10: A network analysis taken by injecting current through the nuller lines at each frequency, while Digital Active Nulling is enabled. This is a way to probe the effectiveness of the DAN nulling bandwidth. Minima of the network analysis above indicate frequencies at which no current flows through the SQUID input coil. The DAN integrating feedback provides infinite loopgain at the central frequency, which falls off in a bandwidth around that central frequency. Image from de Haan et al., 2012 [22].

The digital signal processing required for DAN occurs in firmware on an FPGA motherboard. Limitations imposed by the FPGA force us to use more sophisticated techniques than before in order to generate and demodulate the required sinusoids. These techniques incur larger latency than the simpler, more resource hungry, versions. In earlier implementations, stable feedback loop parameters were universal, but in the 128x system they must be individually tailored to each detector channel. This required a more nuanced analysis of the DAN feedback behavior and stability.

Presented below is an analytic description of the DAN stability criterion, and a method of tailoring the feedback parameters in real-time for each detector based on that criterion. This is my original contribution to the DAN development and implementation, and so the sections that follow describe Digital Active Nulling only at the appropriate level of abstraction to present it. This work was a collaboration with Graeme Smecher, a firmware engineer who works with the McGill Cosmology Instrumentation Laboratory and implemented the DAN firmware.

4.6.1 *DAN feedback*

DAN modulates each nulling sinusoid in amplitude and phase using a digitally-implemented discrete-time integrating feedback loop. The output of a DAN channel is a sinusoid at frequencies up to 10 MHz. DAN feedback updates the amplitude and phase of that sinusoid at 625 kHz.[11] This is a baseband integral feedback system, which ensures infinite loopgain at baseband, and that the feedback bandwidth and loopgain is not a function of the primary mixing frequency (it works just as well at 1 MHz as it does at 6 MHz).[12]

The SQUID output signal (which is the sum of the carrier sinusoid, the amplitude modulations of that sinusoid from sky power, and the nulling tone) is mixed down using a complex demodulator and becomes the *DAN residual* at baseband. A digital gain is applied to that residual, before it is accumulated by a discrete-time integrator, mixed back up to the original frequency, and injected into the cryogenic summing node at the SQUID input coil. This process is shown graphically in Figure 4.11. The resulting amplitude-and-phase-modulated nulling tone cancels the carrier as well as any signal encoded in the carrier sidebands.

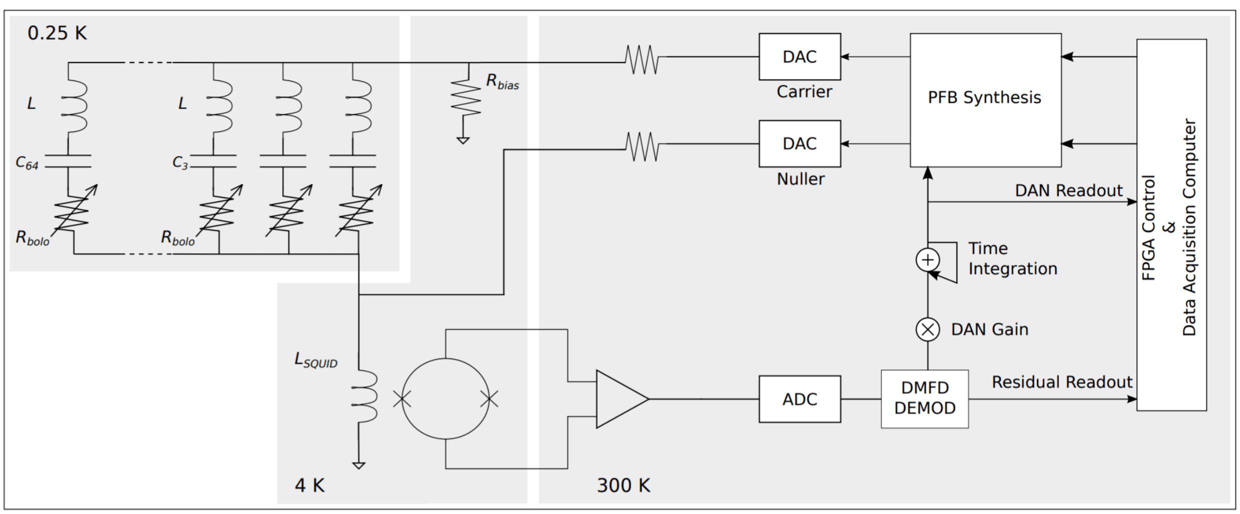

Figure 4.11: A schematic diagram of the 64x DAN implementation. In the 128x implementation both the demodulation and the synthesis are performed using polyphase filter banks (PFBs), instead of just the synthesis (as in this figure). A discussion of PFB techniques is beyond the scope of this document, but can be found in Bender et al., 2014 [14], Montgomery, 2015 [66], and more generally, Harris et al., 2003 [40]. Image adapted from Bender et al., 2014 [14].

11 Though the actual effective feedback bandwidth (with meaningful loopgain) is much narrower.
12 There are minor implementation caveats to this, but they are negligible.

The integrating feedback loop itself can be represented by:

$$DAN[k] = G_{\text{DAN}} \times SQUID[k] + DAN[k-1] \tag{4.6}$$

Where k indicates the discrete time sample, $DAN[k]$ is the output of the DAN integrator at discrete time k, G_{DAN} is the digital gain applied to the integration loop, and $SQUID[k]$ is the output of the SQUID at sample k. When DAN is operating successfully, $SQUID[k]$ is very small (indicating very low residual signal through the SQUID), and the science data stream becomes $DAN[k]$. The success of this feedback depends on two factors: proper *phase* of the DAN alignment ensures cancellation of the carrier tone, and proper *gain* of the feedback loop balances stability and bandwidth of the feedback around the carrier tone.

4.6.2 *DAN phase*

At the baseband frequencies, the relative phases between the SQUID output signal and the DAN input signal must be anti-aligned *at the SQUID summing junction* (ensuring perfect cancellation of a carrier tone and side-bands, and establishing negative feedback). This condition cannot be met until the relative phase shifts caused by any complex impedance in the circuit are dynamically measured and accounted for, a process called "DAN alignment." The phase alignment is performed by varying the amplitude of a series of tones injected into the SQUID input coil with the nuller lines and measuring the phase offset of the signal at the SQUID output. The procedure typically achieves a phase alignment error much better than our acceptable tolerance of 0.5°.

4.6.3 *DAN gain*

The DAN gain, G_{DAN}, mediates both the loopgain and the bandwidth of the DAN feedback. For successful operation, G_{DAN} must be high enough to ensure a bandwidth of negative feedback that encompasses the bolometer bandwidth and science signal modulations; but low enough that no regions of positive feedback exist and there are no frequencies for which the signal response is unbounded. The interval of successful DAN gain values is sensitive to the *total system loopgain* (including analog gains and SQUID transimpedance), and the digital latency of the feedback.

Both of these are simpler for the 16x and 64x systems. For low latencies, even very high DAN gains produce stable and bounded outputs, and at frequencies <1.3MHz the analog system passband is flat over the operating bandwidth. Consequently, the Legacy and 64x systems were only lightly sensitive to the choice of digital gain, allowing G_{DAN} to function approximately like a system constant, determined once and used universally.

The 128x implementation more than tripled the digital latency, from ~5 µs to ~15 µs. Moreover, the analog passband across the 10 MHz of bandwidth varies by factors of 3-5 due to parasitic impedances and filtering for RFI, anti-imaging, and anti-aliasing. Larger detector focal planes also mean there is a wider distribution of SQUID transimpedance and detector normal resistance, all of which affect the system loopgain.

4.6.4 *DAN Stability Criteria*

In de Haan et al., 2012 [22] the DAN stability is described with respect to the system loopgain ($\mathcal{L}_{\mathrm{sys}}$),[13] system latency ($L$), and the frequency separation from the bias (feedback) frequency (δf). The general relation for $\mathcal{L}_{\mathrm{sys}}$ is given by

$$\mathcal{L}_{\mathrm{sys}}(\delta f) \propto \frac{G_{\mathrm{analog}} \times G_{\mathrm{DAN}}}{\delta f} \,. \tag{4.7}$$

I have extended this formalism here to explicitly include the gain terms that were implicit in [22], such that G_{DAN} is the programmable digital gain applied to the feedback, and G_{analog} is the open-loop gain of the entire cryogenic circuit, including the gains of the digitizer path before the SQUID, and the demodulation path after the SQUID.

As G_{DAN} is increased, the envelope of effective negative feedback widens (Figure 4.12). For feedback to be stable, $\mathcal{L}_{\mathrm{sys}}$ must fall below unity at frequencies that incur a 180° or more phase shift due to latencies ($\delta f < \delta f_{\mathrm{max}}$, where $\delta f_{\mathrm{max}} = \frac{1}{2L}$).

We now depart from the derivation in [22] by first decomposing G_{analog} into components from the nuller chain (G_{N}, between the DAN output and the SQUID input) and the demodulation chain (G_{D}, between the SQUID output and the DAN input). We can then restate the above in terms of the total closed loop gain (K_0):

$$K_0 = G_{\mathrm{N}} \times G_{\mathrm{D}} \times G_{\mathrm{DAN}} \,. \tag{4.8}$$

13 This is not the same as the detector loopgain defined in Equation 3.4.

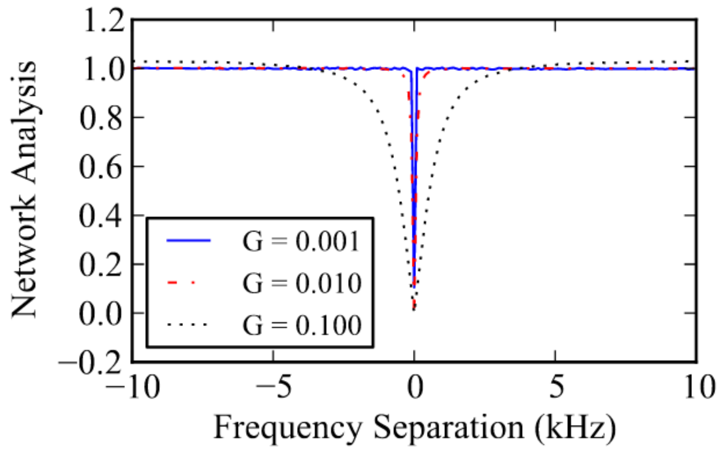

Figure 4.12: Once phase-aligned, the DAN digital gain parameter G_{DAN} (here G) is increased to widen the envelope of effective negative feedback. Typical operation of SPTpol, with Legacy 16x DfMUX, used a G of approximately 0.01 (the red dotted line), providing sufficient negative feedback over the TES bandwidth (<200Hz). Image from de Haan et al., 2012 [22].

For any system latency, there is some closed loop gain (K_{max}) such that the system stops being BIBO (bounded-input-bounded-output) stable – and a bounded input can result in an unbounded output. Our goal is to characterize this relationship between stability, latency, and gain, to find the optimum value of K_0 for any L.

First we construct a model of DAN feedback in z-space (the discrete-time-domain analogue to Laplace space), where a latency can be represented by z^{-L} with L in units of integer samples. The DAN integrating block from Equation 4.6 becomes:

$$Y(z) = G_{\mathrm{DAN}} \times X(z) + z^{-1} Y(z)\,. \tag{4.9}$$

The full DAN loop is shown visually in Figure 4.13.[14]

The *closed-loop transfer function* describes the ratio of input signal of the DAN feedback to the output of the DAN feedback, and can be represented as

$$H(z) = \frac{N(z)}{D(z)} = \frac{G_{\mathrm{D}}\, G_{\mathrm{DAN}}}{1 - z^{-1} + K_0 z^{-L}}\,. \tag{4.10}$$

14 Figures 4.13, 4.14, and 4.15 were produced by Graeme Smecher for a document we are co-authoring and which is in preparation.

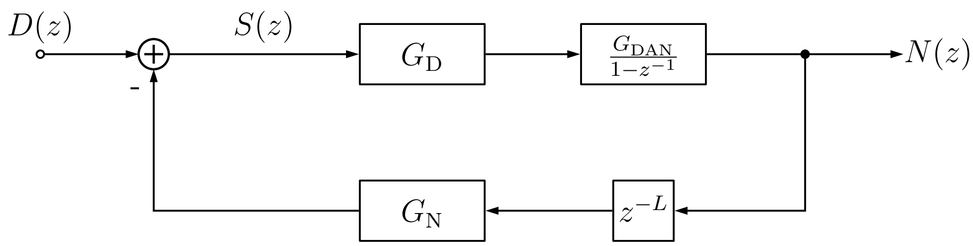

Figure 4.13: The DAN feedback can be expressed in z-space as an equation that takes as its input $D(z)$, produces a nulling output $N(z)$, and consists of a transformation that includes gains for each branch of the feedback (G_D and G_N), the accumulation of the discrete integral feedback ($\frac{G_\mathrm{DAN}}{1-z^{-1}}$), and latency ($z^{-L}$). Image from Graeme Smecher.

The output of the summing junction (ie, the signal at the SQUID output when DAN is enabled, and a measure of how much current is being driven through the SQUID) is given by

$$S(z) = D(z) - G_\mathrm{N} z^{-L} N(z)\,. \tag{4.11}$$

The transfer function that describes the ratio of SQUID loading to input signal of the DAN feedback loop is

$$E(z) = \frac{S(z)}{D(z)} = \frac{1 - z^{-1}}{1 - z^{-1} + K_0 z^{-L}}\,. \tag{4.12}$$

$H(z)$ describes how efficient the DAN feedback loop is at capturing the input (science) signal. $E(z)$ describes how efficient the DAN feedback loop is at zeroing the current through the SQUID input coil. For stable operation both must remain bounded for a finite input signal. We can investigate the behavior of these two transfer-functions by numerically solving these equations for varying values of gain (K_0) and latency (L). Note that in z-space, for our internal DAN loop sampling rate (625 kHz) and latency (~15 µs), the 128x system latency corresponds to L=9.

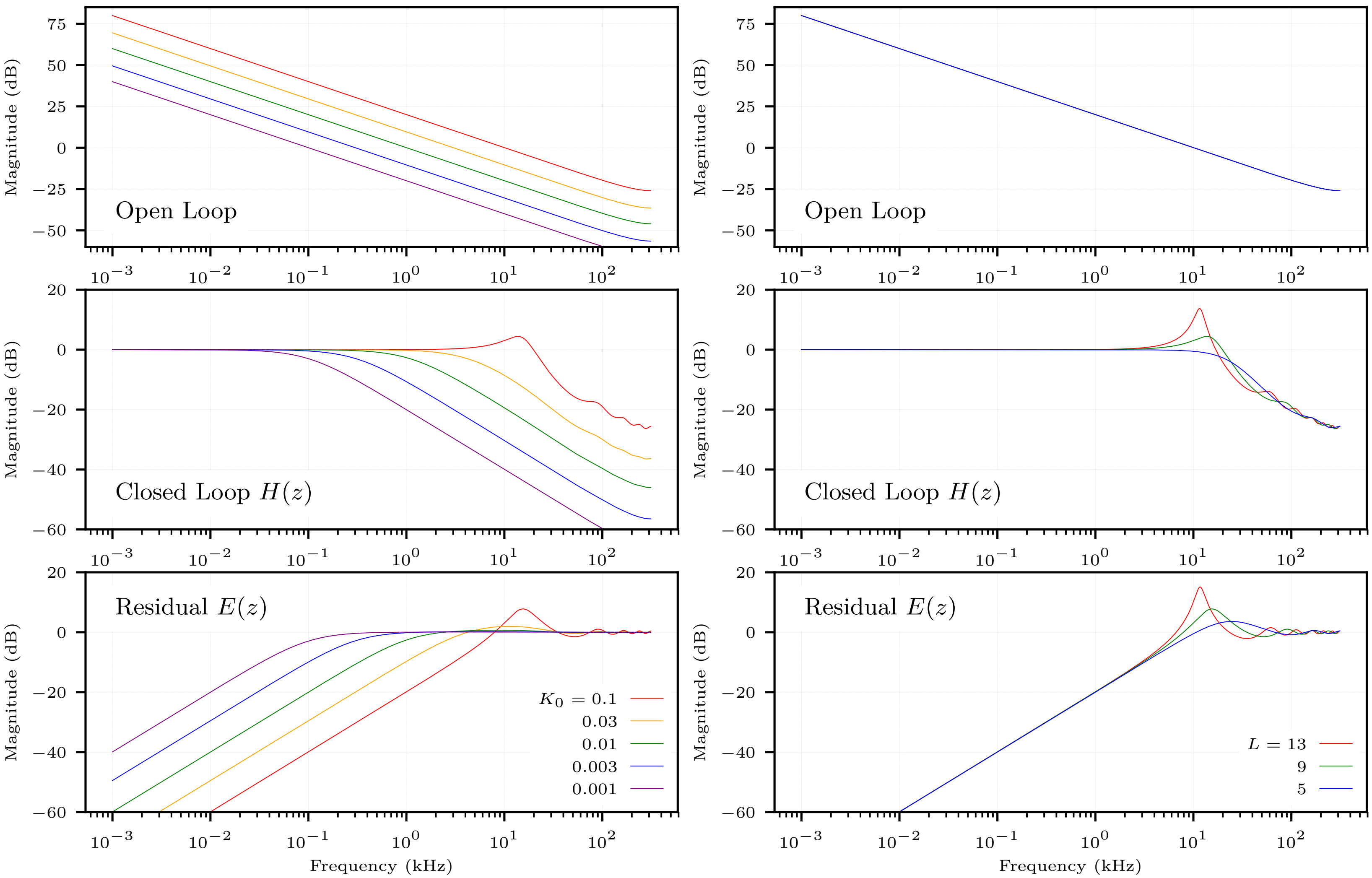

Figure 4.14: Numerical solutions of Equations 4.10 and 4.12 for a variety of system gains (K_0) and latency (L). The left column fixes L=9, and the right column fixes K_0=0.1. Note that this is showing the spectral character of the feedback transfer functions, and that regions in $H(z)$ and $E(z)$ that go positive in magnitude correspond to frequencies at which a stimulus tone results in an *amplification* by the DAN feedback, rather than a *suppression*. These are all still *stable* configurations, but they additionally flux burden the SQUID. Image from Graeme Smecher.

4.6.5 *Anti-Nulling*

The plots in Figure 4.14 all show combinations of gain and latency that still result in BIBO stable DAN feedback, but they reveal an additional subtlety: for some combinations of K_0 and L there are spectral features of the transfer functions that produce *amplification* in response to input stimulus, rather than suppression. This behavior hasn't been recognized or characterized previously, and indicates that for our system latency there are choices of G_{DAN} that result in stable feedback with strong negative loopgain in the narrow science band around the TES, but which actually amplify noise or EMI features in regions around $\delta f \sim 10\,\mathrm{kHz}$. This amplification is unlikely to compromise TES stability or contaminate science band signal, but will additionally flux burden the SQUID, degrading linearity and overall system noise performance. We term this behavior "anti-nulling," and for L=9 we begin anti-nulling at a critical gain of $K_{\mathrm{C}} = 0.05$ (Figure 4.15). As gain or latency increases this amplification eventually becomes unbounded and drives the loop unstable.

If we treat K_{C} as the upper bound for total closed-loop gain, the lower bound is defined by our nulling requirements for the science band. In de Haan et al., 2012 [22] that requirement was stated as $> 99\%$ nulling effectiveness ($H(z)$, in our formalism) at the highest δf used for science. For SPT-3G this corresponds to a minimum $K_0 = 0.0044$, ensuring -20dB in $H(z)$ at our maximum science bandwidth of 65 Hz. In practice we use $K_0 = 0.005$.

4.6.6 *Satisfying the Stability Criteria*

To satisfy the above DAN stability criteria, and ensure each detector has a closed loop gain of $K_0 = 0.005$, the open-loop gain for each detector ($G_{\mathrm{N}} \times G_{\mathrm{D}}$) must be measured, and the appropriate digital gain term $G_{\mathrm{DAN}} = \dfrac{0.005}{G_{\mathrm{N}} \times G_{\mathrm{D}}}$ can be custom programmed. This can be done efficiently by using data from the probe tones already employed during the phase-alignment procedure. By comparing the input and output tone amplitudes, we are able to measure the true open loop gain. Note that this can be done without a transformation into physical units (which is a difficult calibration that includes some additional uncertainty. Instead, the loopgain (a unitless quantity) is calculated in native digital counts at the DAC and ADC, which correspond exactly to $N(z)$ and $D(z)$ shown in Figure 4.13. The full algorithmic steps for DAN tuning are given in Figure 4.16.

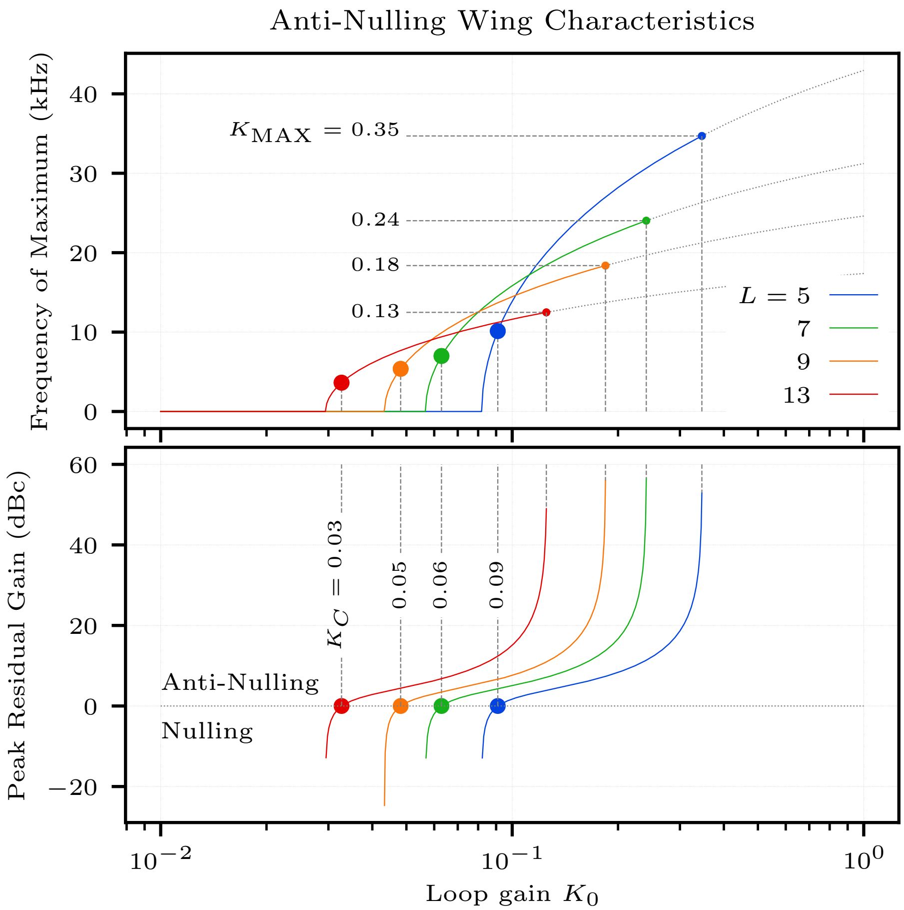

Figure 4.15: The maximum desirable K_0 is set by K_C, above which anti-nulling occurs, even if the loop remains BIBO-stable. Note that $\frac{K_{\mathrm{MAX}}}{K_{\mathrm{C}}}$ is largely independent of L, and typically ~ 3.8, which provides a convenient empirical way to characterize a system (it's easier to find the gain that causes instability than it is to measure anti-nulling directly). Image from Graeme Smecher.

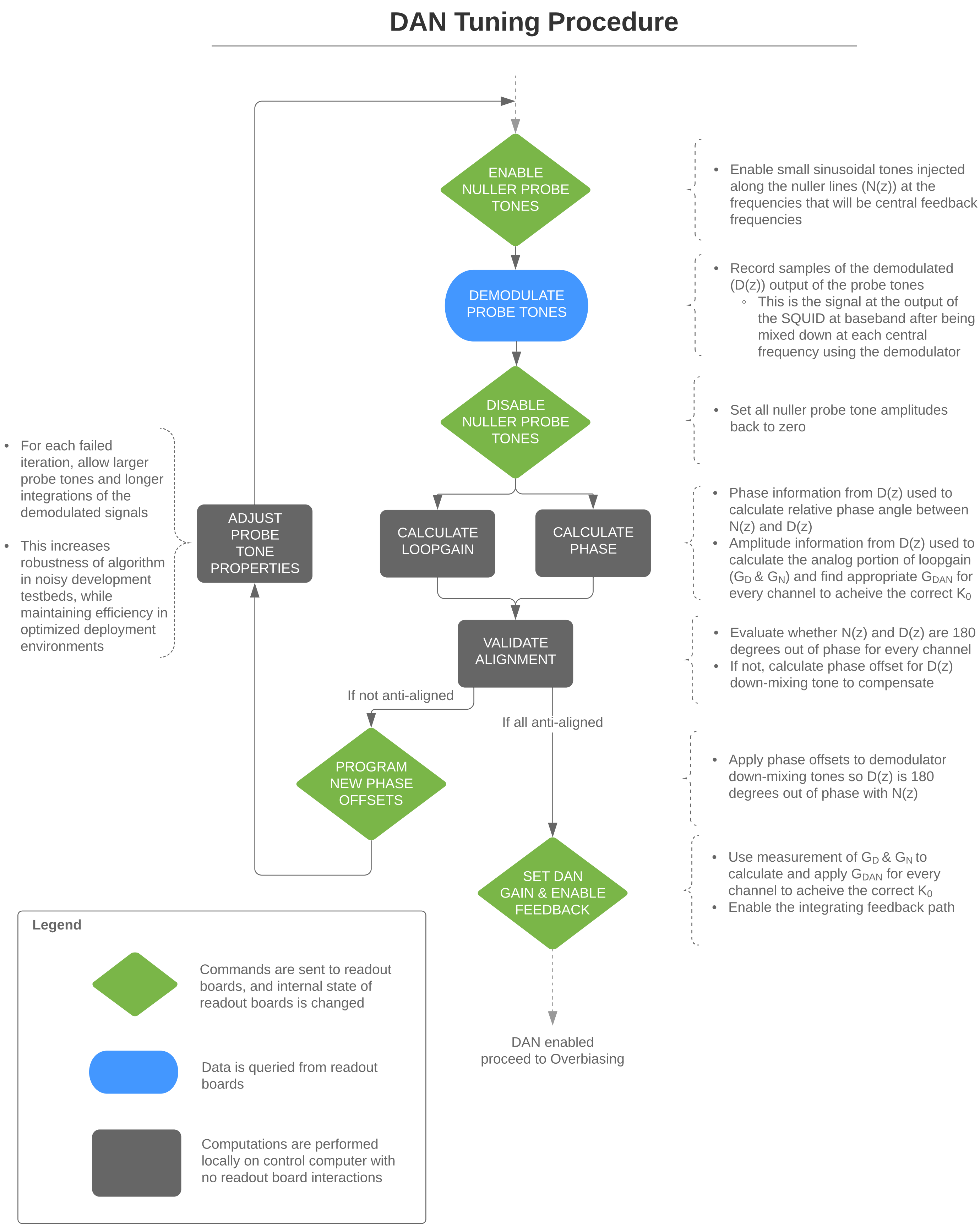

Figure 4.16: DAN is tuned by injecting tones from $N(z)$ and measuring the phase and amplitude response in $D(z)$. The phase is used to ensure the feedback is perfectly negative at baseband, and the amplitude information is used to ensure the closed loop gain K_0 is stable with sufficient nulling efficiency over the science band.

The resulting distribution of optimally calculated DAN gains for the SPT-3G array is shown in Figure 4.17. The development of the method described above for determining optimal DAN gains allowed us to relax constraints on latency in the DfMUX firmware. With these relaxed constraints we were able to increase the multiplexing factor supported by the firmware from 64x to 128x without any hardware changes. Presently, our algorithms, firmware, and warm electronics are ahead of what is implemented in the cold readout hardware (68x in SPT-3G), and provide a clear path toward the even higher multiplexing factors that will be needed to support future focal planes, like CMB-S4, which are planned to have $\mathcal{O}(100{,}000)$ detectors.

4.7 NETWORK ANALYSIS AND BIAS FREQUENCY SELECTION

DAN complicates the process of selecting bias frequencies because a measurement of the total circuit admittance is no longer representative of the effective comb admittance once DAN is enabled. In particular, the SQUID input coil acts as a series inductance that modifies the resonant frequencies of the LC filters. Any direct measurement of the circuit admittance that includes the SQUID input coil will exhibit modified resonance peak locations, which will not be consistent with the peak locations when operating DAN. There are two ways to address this: the first is by measuring the admittance at every frequency with DAN enabled, explicitly removing the effect of the SQUID on the measurements, but this is extraordinarily inefficient;[15] the second is by a linear combination of direct measurements from the carrier and nuller tones in the form of *network analyses*.

A network analysis is a method of probing an analog circuit and a common general tool for analog circuit analysis, where it is often performed with a dedicated network analyzer device. A complete network analysis in the traditional sense allows one to determine the effective circuit of any linear analog device. Our primary objective is less ambitious, and can be accomplished with a limited form of AC network analysis that can be performed in situ by the readout system. There are two types of network analyses measurements used in the DfMUX system:

15 Performing the DAN alignment and feedback enabling requires $\sim$20x the number of interactions with the electronics than simply enabling a carrier or nuller tone and measuring the resulting signal through the SQUID.

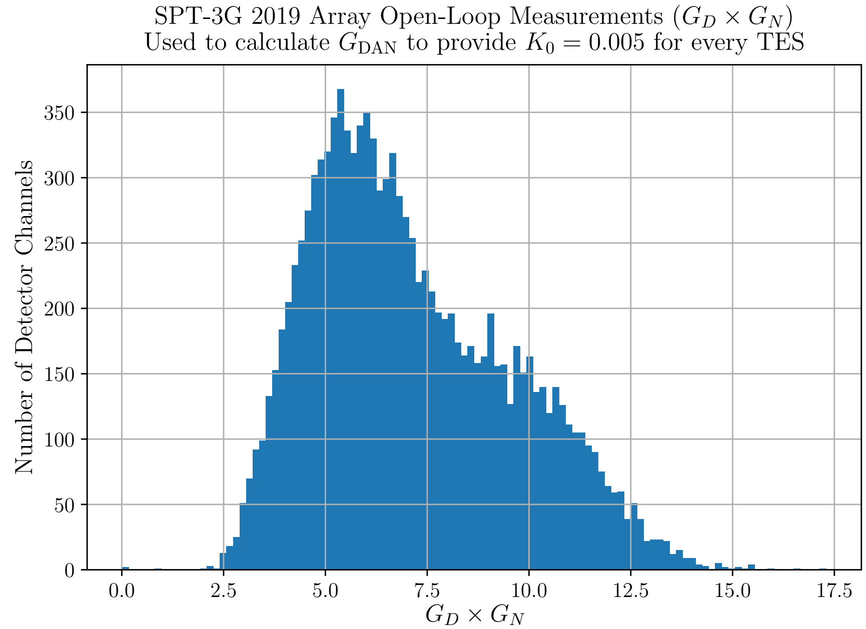

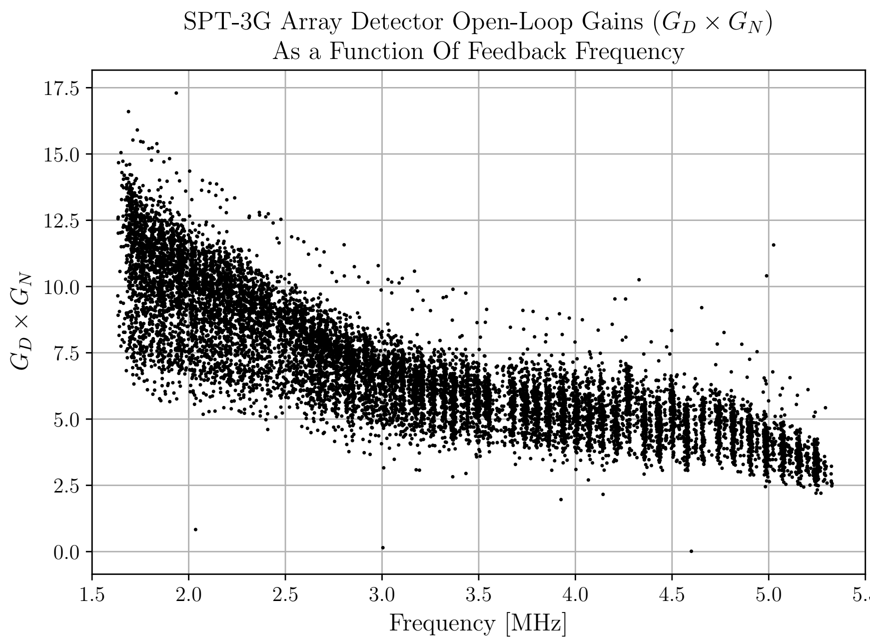

Figure 4.17: Top: The array distribution of measured open-loop gains ($G_D \times G_N$) used to calculate G_{DAN} for each TES such that $K_0 = 0.005$ for all channels. Note that the distribution spans a factor of ~ 7 in $G_D \times G_N$, which without using this methodology would correspond to a factor of ~ 7 variation in K_0 across the array, and have serious implications for stability. **Bottom:** The variation in open-loop gain ($G_D \times G_N$) depends strongly on the passband shape of the analog signal-path filtering and the SQUID input coil reactance, which are the dominant features seen here. The width of the distribution seen in any narrow slice of bandwidth is dominated by relative variation in R_n compared to the SQUID input coil reactance. The primary motivator driving custom G_{DAN} derivations for each channel is the increased bandwidth of the new readout system, together with the narrower stability region due to increased system latency.

CARRIER NETWORK ANALYSES are performed by sweeping a sinusoidal voltage of known amplitude (V_{bias}) across the bandwidth via the carrier lines, and measuring the SQUID output voltage ($V_{\text{SQUID Output}}$),[16] which can be converted to the current through the SQUID input coil using SQUID transimpedance ($I^{\text{carrier netanal}}_{\text{SQUID input coil}} = \frac{V_{\text{SQUID output}}}{Z_{\text{trans}}}$). This is a measurement of the total admittance of the cryogenic circuit, including the SQUID input coil:

$$I^{\text{carrier netanal}}_{\text{SQUID input coil}} = \left(\frac{1}{Z_{\text{com}} + Z_{\text{net}} + Z_{\text{SQUID}}}\right) \times V_{\text{bias}}\,. \tag{4.13}$$

NULLER NETWORK ANALYSES are performed by sweeping a sinusoidal current of known amplitude (I_{nuller}) across the bandwidth via the nuller lines, and measuring the SQUID output voltage ($V_{\text{SQUID output}}$), which can be converted to a current through the SQUID input coil using the SQUID transimpedance. A nuller network analysis is a measurement of the relative impedance of the SQUID input coil reactance and the rest of the circuit (the parallel legs of the SQUID summing junction, Figure 4.9).

$$I^{\text{nuller netanal}}_{\text{SQUID input coil}} = \left(\frac{Z_{\text{com}} + Z_{\text{net}}}{Z_{\text{comb}} + Z_{\text{net}} + Z_{\text{SQUID}}}\right) \times I_{\text{nuller}}\,. \tag{4.14}$$

The bias frequencies we wish to use are those in which the admittance $Y_{\text{DAN}} = \frac{1}{Z_{\text{net}}+Z_{\text{com}}}$ is maximized. By dividing the results of a carrier network analysis by the results of a nuller network analysis we can recover a measurement of Y_{DAN}

$$\frac{I^{\text{carrier netanal}}_{\text{SQUID input coil}}}{I^{\text{nuller netanal}}_{\text{SQUID input coil}}} \times \left(\frac{V_{\text{carrier input}}}{I_{\text{nuller input}}}\right) = \left(\frac{1}{Z_{\text{net}} + Z_{\text{com}}}\right) = Y_{\text{DAN}}\,. \tag{4.15}$$

This is shown for several resonances of an SPT-3G comb in Figure 4.18. Notice how the peaks in the DAN admittance (bottom panel) are offset from the peaks in a carrier network analysis, and more closely correspond to the nulls in a nuller network analysis (where the cryogenic comb appears much lower impedance than the SQUID). Bias frequencies are selected based on the peak locations of the derived comb admittance, using carrier and nuller network analyses.

16 Phase can also be measured, despite digital latencies, by using an internally re-routed signal as a calibration. Presently this functionality isn't used.

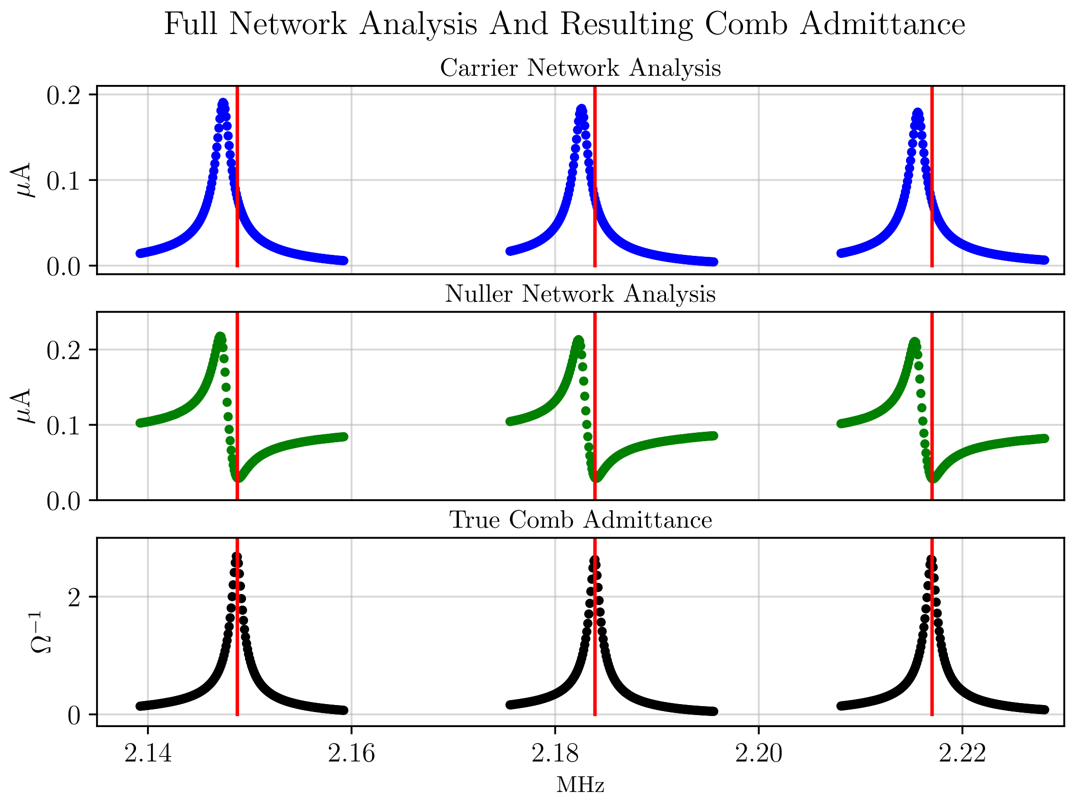

Figure 4.18: **Top:** the result of a carrier network analysis shown here for three resonances of an SPT-3G comb. Peaks indicate regions where the impedance of the entire circuit ($Z_{\mathrm{comb}} + Z_{\mathrm{net}} + Z_{\mathrm{SQUID}}$) is minimized. **Middle:** A nuller network analysis over the same frequency ranges shows minima where $Z_{\mathrm{comb}} + Z_{\mathrm{net}} << Z_{\mathrm{SQUID}}$ and current does not flow through the SQUID input coil. **Bottom:** A division of the carrier and nuller network analysis measurements can be used to construct the admittance of just $Z_{\mathrm{comb}} + Z_{\mathrm{net}}$, which reflects the circuit behavior when DAN is operating. This true comb admittance is used to determine bias frequencies that minimize series impedance with the TES.

4.8 WARM ELECTRONICS

The DfMUX system is operated using a set of electronics at room temperature that consists of:

AN FPGA MOTHERBOARD ("ICEBOARD") housing the Field Programmable Gate Array (FPGA) that performs the digital signal processing integral to the readout system. The ICEBoard also has an embedded ARM processor, which allows for sophisticated communication between the ICEBoards and control computers.

TWO FMC (FPGA MEZZANINE CARD) DIGITIZERS that are mounted to each ICEBoard, and perform the digital-to-analog and analog-to-digital conversion of the synthesizer and demodulator signals.

SQUID CONTROLLER BOARDS (SQCB) that have one-to-one mappings with the Digitizers. These house the SQUID bias DACs and the first pre-amplification stages for signals at the output of the SQUID.

Figure 4.19 shows each of these components. The ICEBoard and FMC mezzanine are mounted together and housed in an electronics crate several meters from the telescope, but the SQCB must be mounted directly against the cryogenic feedthrough harness and enclosed in a separate RF-tight box, which guarantees the integrity of the low signal amplitudes at the output of the SQUID.

Together this system is known as the ICE system, and it was designed in the McGill Cosmology Instrumentation Laboratory [8]. The ICEBoards are a multi-function cosmology readout electronics platform. They are used by SPT-3G and POLARBEAR-2 millimeter-wave CMB experiments; but also, with a separate mezzanine card, on the Canadian Hydrogen Intensity Mapping Experiment (CHIME): a radio interferometer that implements an N^2 correlator [9, 10]. We are currently also adapting the ICE system for microwave kinetic inductance (mKID) readout.

The ICE system is described in detail in Bandura et al., 2016 [8]. One novel element that hasn't been previously documented are the strategies we deploy in the hardware, firmware, and software design to overcome the consequences of 3rd order intermodulation distortion (IMD3) products. This harmonic distortion results from the non-linear elements of the TES and SQUID. If these distortion products aren't designed against they will hopelessly contaminate

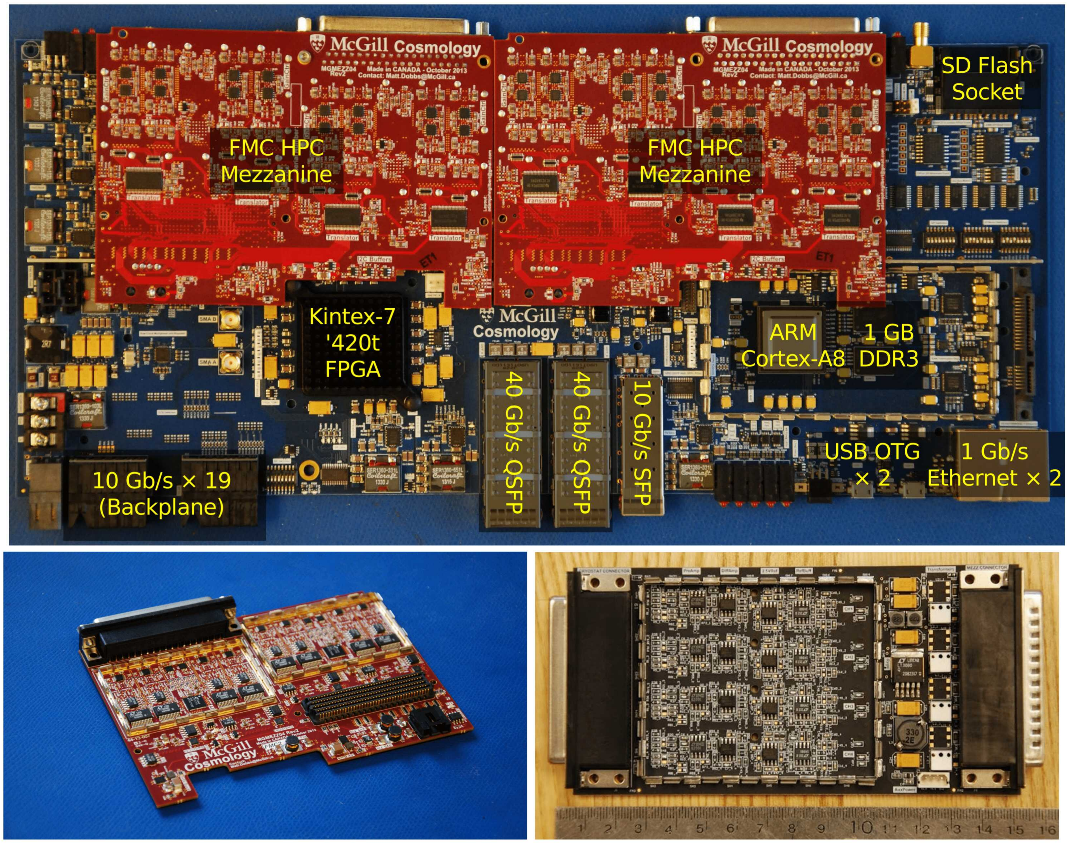

Figure 4.19: Top: The ICEBoard FPGA platform that performs the signal processing at the heart of the DfMUX system. The embedded ARM processor runs a limited linux and set of compiled C that interprets between high level algorithms (run on a control computer) and low level commands (executed by the FPGA). Each ICEBoard can operate 8 SQUID channels at 128x multiplexing each for a total of 1024 readout channels, although this is presently limited by the cryoelectronics, which has achieved 68x (544 readout channels total). **Bottom left:** The FMC digitizer mezzanine card that performs analog-to-digital and digital-to-analog conversion. **Bottom right:** The SQUID Controller Board, which performs the pre-amplification of the SQUID output and contains the electronics that drive the SQUID biases. More detail about this platform and the associated annotations are available in [8] and [14]. Images from Bender et al., 2014 [14].

the TES science data, and flux burden the SQUID elements. A closer look at IMD3, and the specific strategy I developed for SPT-3G and POLARBEAR-2 operation, is presented in Appendix B.

5 CROSSTALK IN FREQUENCY DOMAIN MULTIPLEXING

Crosstalk in an FDM system is dominated by electrical interactions within the cryogenic filters, not by optical crosstalk sourced by reflections in the optics, which are typically of much lower amplitude. These electrical interactions are generally presented as two conceptually distinct mechanisms: *leakage* ***current*** *crosstalk* due to imperfect isolation between LC filters, and *leakage* ***power*** *crosstalk* due to any series impedance common to the filtering network. These mechanisms have been analytically described before in Dobbs et al., 2012 [26]. However, those derivations make approximations that are no longer valid for 68x multiplexing filter topologies. In particular they:

1. Assume that biasing always occurs precisely at the resonant frequency of the LC filters, rather than at a frequency optimized for additional stray impedance.[1]

2. Assert that only the magnitude of the crosstalk terms matter, when in fact preserving the phase information in the derivations reveals that the two forms of crosstalk can cancel, and that the phase of the crosstalk signal is offset from that of the science signal.

3. Do not account for series impedances to the TES within the LCR network, or a common series impedance external to the LCR network.

The derivations below account for each of these effects. Section 5.1 presents the circuit model and defines the science signal against which crosstalk is measured. Section 5.2 covers leakage current crosstalk, and Section 5.3 covers leakage power crosstalk. In Section 5.5 I show how cancellation of the two terms can occur, and how crosstalk can be minimized through a choice of signal measurement basis. This chapter presents only my own work, but a comparison with Dobbs et al., 2012 [26] for a variety of parameters can be found in Appendix A.

1 A more detailed explanation of how bias frequencies are now chosen is given in Section 4.7.

5.1 CROSSTALK CIRCUIT MODEL AND SCIENCE SIGNAL

Consider a cryogenic network whose total impedance is given by

$$Z_{\text{tot}}(\omega) = Z_{\text{net}}(\omega) + Z_{\text{com}}(\omega)\,, \tag{5.1}$$

where Z_{net} is the effective impedance of all parallel LCR legs of the network, and Z_{com} is a common impedance in series with the full network, as illustrated in Figure 5.1.

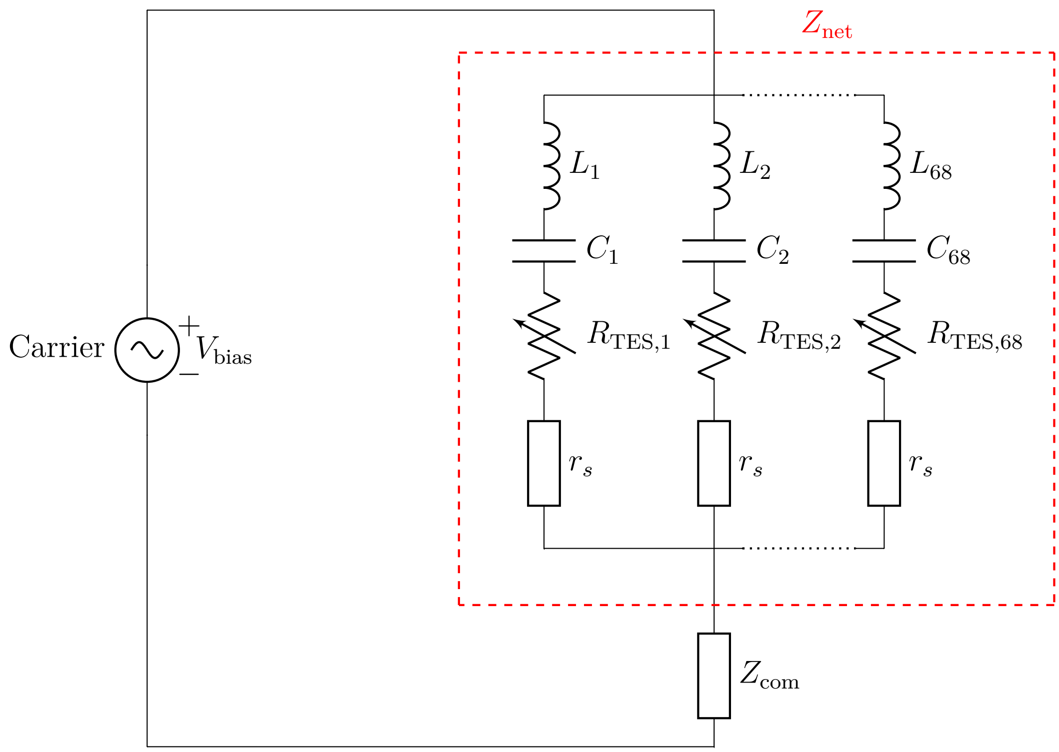

Figure 5.1: An example circuit diagram of the cryogenic network. This includes all relevant components used in the derivation of leakage current crosstalk and leakage power crosstalk. For simplicity in the notation I will keep the real parasitic series resistance within each cryogenic leg (r_s) the same (this does not effect the form of the final expressions).

For a given bias frequency ω_i, the impedance of any single cryogenic filter leg is

$$Z_{n,i} = R_{\text{TES},n} + r_s + j\omega_i L_n + \frac{1}{j\omega_i C_n}\,. \tag{5.2}$$

The *on-resonance* cryogenic leg is then $Z_{i,i}$, while $Z_{n\neq i,i}$ are the impedances of *off-resonance* cryogenic legs. The impedance of the parallel network as a whole is

$$Z_{\mathrm{net}}(\omega_i) = \left(\sum_{n=1}^{\mathrm{MUX\ factor}} \frac{1}{Z_{n,i}} \right)^{-1} . \tag{5.3}$$

Off-resonance cryogenic legs with the lowest impedance are the *nearest neighbours*, at frequencies adjacent to the on-resonance leg ($Z_{i\pm1,i}$). Nearest neighbors have a special significance because both crosstalk mechanisms are strong functions of the relative impedance between the on-resonance and off-resonance legs. Consequently, only crosstalk between nearest neighbors is significant.[2] For SPT-3G design parameters, the nearest neighbor impedances ($Z_{i\pm1,i}$) range from 20 to 80 Ω, while on-resonance impedances ($Z_{i,i}$) are typically <2 Ω. The impedance of the network at each bias frequency may therefore be approximated

$$Z_{\mathrm{net}}(\omega_i) \approx Z_{i,i} . \tag{5.4}$$

This approximation is accurate to >98.5% at the lowest frequencies of the SPT-3G schedule, and >99.5% through most of the band. It is the only approximation made in deriving the crosstalk model below.

5.1.1 *Science signal*

At each bias frequency ω_i there is a fixed sinusoidal voltage applied to the network. As we observe the sky, changes in incident radiative power on the i^{th} TES modulate that resistance ($R_{\mathrm{TES},i}$). This in turn modulates the amplitude of the current at ω_i, which is our output signal (I_i). The data we are interested in as our signal is therefore:

$$\left[\frac{\delta I_i}{\delta R_{\mathrm{TES},i}}\right]_{\mathrm{signal}} = \frac{\delta}{\delta R_{\mathrm{TES},i}} \left[\frac{V_{\mathrm{bias}}(\omega_i)}{(Z_{i,i} + Z_{\mathrm{com}}(\omega_i))}\right] \tag{5.5}$$

$$\delta I_{i,\mathrm{signal}} = \frac{-V_{\mathrm{bias}}(\omega_i) \cdot \delta R_{\mathrm{TES},i}}{(R_{\mathrm{TES},i} + r_s + j\omega_i L_i + \frac{1}{j\omega_i C_i} + Z_{\mathrm{com}}(\omega_i))^2} . \tag{5.6}$$

2 Nevertheless, the equations themselves are general, and can be used to calculate the full crosstalk matrix between any detector pair.

Crosstalk occurs when I_i is modulated by changes in the impedance of other detectors, $\left(\frac{\delta I_i}{\delta R_{\mathrm{TES},n\neq i}}\right) \neq 0$.

5.2 LEAKAGE CURRENT CROSSTALK

Most current induced through the filter by a bias voltage at ω_i flows through the lowest impedance (on-resonance) leg; but that bias also induces leakage current through the higher impedance (off-resonance) legs of the filter. When a TES within an off-resonance leg ($n \neq i$) fluctuates in resistance (such as in response to sky power) it modulates the amplitude of that leakage current. This is *leakage current crosstalk*, and it allows signal that originates in off-resonance TES detectors to appear as a modulation of the carrier frequencies of the on-resonance TES. This form of crosstalk is given by

$$\left[\frac{\delta I_i}{\delta R_{\mathrm{TES},n}}\right]_{\mathrm{LCX}} = \frac{\delta}{\delta R_{\mathrm{TES},n}}\left[\frac{V_{\mathrm{bias}}(\omega_i)}{(Z_{n,i} + Z_{\mathrm{com}}(\omega_i))}\right] \tag{5.7}$$

$$\delta I_{i,n,\mathrm{LCX}} = \frac{-V_{\mathrm{bias}}(\omega_i)\cdot\delta R_{\mathrm{TES},n}}{(R_{\mathrm{TES},n} + r_s + j\omega_i L_n + \frac{1}{j\omega_i C_n} + Z_{\mathrm{com}}(\omega_i))^2}\,. \tag{5.8}$$

The on-resonance bolometer encodes sky signal by amplitude-modulating its bias sinusoid (Equation 5.6) – but now the off-resonance bolometer is *also* encoding sky signal by amplitude modulating *the same bias sinusoid*. This may be expressed as a crosstalk fraction using Equation 5.6:

$$\left[\frac{\delta I_{i,n,\mathrm{LCX}}}{\delta I_{i,\mathrm{signal}}}\right] = \frac{\delta R_{\mathrm{TES},n}}{\delta R_{\mathrm{TES},i}}\left(\frac{R_{\mathrm{TES},i} + r_s + j\omega_i L_i + \frac{1}{j\omega_i C_i} + Z_{\mathrm{com}}(\omega_i)}{R_{\mathrm{TES},n} + r_s + j\omega_i L_n + \frac{1}{j\omega_i C_n} + Z_{\mathrm{com}}(\omega_i)}\right)^2 \tag{5.9}$$

$$= \frac{\delta R_{\mathrm{TES},n}}{\delta R_{\mathrm{TES},i}}\left(\frac{Z_{i,i} + Z_{\mathrm{com}}(\omega_i)}{Z_{n,i} + Z_{\mathrm{com}}(\omega_i)}\right)^2\,, \tag{5.10}$$

where $\delta R_{\mathrm{TES},n} \approx \delta R_{\mathrm{TES},i}$ for detectors with reasonably well controlled α, and similar readout impedances, observing the same sky.

Notice that although Z_{com} contributes to this effect, it is not required for it. Leakage current crosstalk occurs whether or not there is a common impedance in series with the network. Notice also that in Equation 5.8 there are no terms that include the on-resonance bolometer ($R_{\text{TES},i}$). Leakage current crosstalk from an off-resonance detector is independent of the on-resonance detector.[3]

5.2.1 *Instability due to leakage power*

Leakage current induced by neighboring bias voltages contributes to the electrical power dissipated across each TES; this is called *leakage power*. In the simple case when $Z_{\text{com}} = 0$, leakage power deposited across a TES is given by

$$P_{n,i} = \left(\frac{V_{\text{bias}}(\omega_i)}{Z_{n,i}}\right)^2 R_{\text{TES},n} \,. \tag{5.11}$$

For SPT-3G filter parameters the leakage power is typically less than 1% of on-resonance bias power; however, because $Z_{n,i} >> R_{\text{TES},n}$, leakage power is sourced by stiff current bias, generating *positive electrothermal feedback* (Table 3.1).

When a TES changes in resistance, that change will be countered strongly by the change in electrical power from its own bias (ω_i), but will be *reinforced* by the change in leakage power at neighboring bias frequencies (ω_n). Though a small effect, this does dilute the negative electrothermal feedback experienced by the TES and degrades its stability in a similar way to excess series impedance.

5.3 LEAKAGE POWER CROSSTALK

Under some conditions leakage power will introduce an additional crosstalk mechanism. When $Z_{\text{com}}(\omega_n) \neq 0$, it forms a voltage divider with the entire cryogenic network, $Z_{\text{net}}(\omega_n)$. The leakage power across the i^{th} TES is then a function of $Z_{\text{net}}(\omega_n)$, which is sensitive to $\delta R_{\text{TES},n}$ (Equation 5.4). This allows variations in $R_{\text{TES},n}$ to modulate the leakage power deposited on $R_{\text{TES},i}$. Depositions of leakage power are similar to depositions of radiative power – they

3 Though the *fraction of the total* δI_i that comes from leakage current does depend on $R_{\text{TES},i}$.

amplitude-modulate the TES bias sinusoid. As with leakage current crosstalk, the effect is most acute between nearest neighbors. The full expression is derived as

$$\begin{aligned}
\left[\frac{\delta I_i}{\delta R_{\mathrm{TES},n}}\right]_{\mathrm{LPX}} &= \frac{1}{V_{\mathrm{bias}}(\omega_i)}\left[\frac{\delta P_i}{\delta R_{\mathrm{TES},n}}\right] \\
&= \frac{1}{V_{\mathrm{bias}}(\omega_i)}\frac{\delta}{\delta R_{\mathrm{TES},n}}\left[\left(\frac{Z_{\mathrm{net}}(\omega_n)V_{\mathrm{bias}}(\omega_n)}{Z_{\mathrm{net}}(\omega_n)+Z_{\mathrm{com}}(\omega_n)}\right)^2\frac{R_{\mathrm{TES},i}}{(R_{\mathrm{TES},i}+r_s+j\omega_n L_i+\frac{1}{j\omega_n C_i})^2}\right] \\
&\approx \frac{(R_{\mathrm{TES},n}+r_s+j\omega_n L_n+\frac{1}{j\omega_n C_n})Z_{\mathrm{com}}(\omega_n)}{(R_{\mathrm{TES},n}+r_s+j\omega_n L_n+\frac{1}{j\omega_n C_n}+Z_{\mathrm{com}}(\omega_n))^3}\left(\frac{2\ V^2_{\mathrm{bias}}(\omega_n)R_{\mathrm{TES},i}}{V_{\mathrm{bias}}(\omega_i)(R_{\mathrm{TES},i}+r_s+j\omega_n L_i+\frac{1}{j\omega_n C_i})^2}\right)
\end{aligned} \tag{5.12}$$

where the approximation defined in Equation 5.4 has been made in the last term. Expressed as $\delta I_{i,n,\mathrm{LPX}}$ this becomes

$$\delta I_{i,n,\mathrm{LPX}} \approx \frac{V^2_{\mathrm{bias}}(\omega_n)}{V_{\mathrm{bias}}(\omega_i)}\left(\frac{Z_{n,n}\ Z_{\mathrm{com}}(\omega_n)}{(Z_{n,n}+Z_{\mathrm{com}}(\omega_n))^3}\right)\left(\frac{2\ R_{\mathrm{TES},i}\ \delta R_{\mathrm{TES},n}}{Z^2_{i,n}}\right). \tag{5.13}$$

Or, given as a crosstalk fraction:

$$\left[\frac{\delta I_{i,n,\mathrm{LPX}}}{\delta I_{i,\mathrm{signal}}}\right] \approx -\left(\frac{V^2_{\mathrm{bias}}(\omega_n)\delta R_{\mathrm{TES},n}}{V^2_{\mathrm{bias}}(\omega_i)\delta R_{\mathrm{TES},i}}\right)\frac{(Z_{i,i}+Z_{\mathrm{com}}(\omega_i))^2}{(Z_{n,n}+Z_{\mathrm{com}}(\omega_n))^3}\left(\frac{2\ R_{\mathrm{TES},i}\ Z_{n,n}\ Z_{\mathrm{com}}(\omega_n)}{Z^2_{i,n}}\right). \tag{5.14}$$

This is a more complicated expression than for the leakage current crosstalk, though it simplifies considerably under the assumption that the detectors are approximately uniform. The most notable difference is the *sign* of the crosstalk. Unlike leakage current crosstalk, which is positive, leakage *power* crosstalk is negative. There is therefore some cancellation that occurs between them in the total crosstalk.

5.4 "TUNING OUT" $Z_{\rm com}$

In the SPT-3G system, $Z_{\rm com}$ can be quite large, and comes from a stray inductance ($L_{\rm stray}$ ~45 nH) in the superconducting striplines that provide the voltage bias, such that $Z_{\rm com}(\omega_i) = j\omega_i L_{\rm stray}$. This contributes >1$j\Omega$ at the higher frequencies of our operating bandwidth. Such a large $Z_{\rm com}$ slightly decreases leakage current crosstalk, and increases leakage power crosstalk. However, this reactance "tunes out" with the proper choice of bias frequency, and so won't effect TES stability much. For every i^{th} TES it is possible to choose a bias frequency ω_i such that:

$$\omega_i \approx \frac{1}{\sqrt{(L_i + L_{\text{stray}})C_i}}\,. \tag{5.15}$$

Some residual variation in the Thévenin equivalent impedance of the system remains, which will be discussed in Section 6.2.5.

5.5 CROSSTALK CANCELLATION

Leakage current and leakage power crosstalk mechanisms have opposing signs: in the case of leakage current, a decrement in the resistance of a neighboring TES increases the amplitude of the carrier tone, generating a positive copy of the neighboring TES signal; in the case of leakage power, a decrement in the resistance of a neighboring TES increases the power deposition on the on-resonance TES, reducing the amplitude of the carrier tone and generating a negative copy of the neighboring TES signal. The cancellation between these two forms of crosstalk can be understood in terms of the vector addition of each component

$$\delta I_{i,n,\text{tot}} = \delta I_{\text{i,signal}} + \delta I_{i,n,\text{LCX}} + \delta I_{i,n,\text{LPX}}\,. \tag{5.16}$$

The current modulations due to signal (Equation 5.6), leakage current (Equation 5.8), and leakage power (Equation 5.13) are complex-valued. Each process generates a modulation in current at ω_i, but those modulations have different phases. The phases and magnitudes of each of these are plotted for typical SPT-3G parameters in Figure 5.2. *Any forecasting of crosstalk performance must sum the components through vector addition, and not by summing the individual magnitudes.*

The DfMUX data acquisition preserves the complex signature of δI_i when recording data, but we choose a rotation that maximizes $\frac{\delta I_i}{\delta P_{\text{rad}}}$ along a single axis, and discard the other.[4] The rotation angle is determined by varying total radiative power on the focal plane, accomplished by slewing the telescope up and down through a section of atmosphere. As can be seen in Figure 5.2, this rotation is very nearly optimal, owing to the relatively small crosstalk fractions. Additionally, the leakage current signals are nearly 180° out of phase, and so the

4 This is done to improve signal to noise, and is described more in Section 7.2.6.

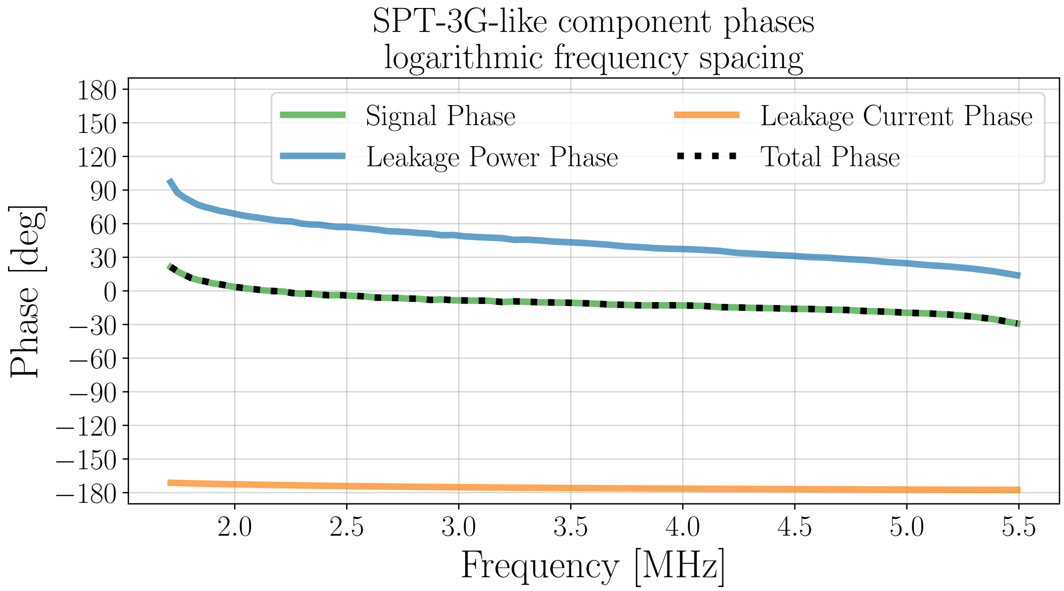

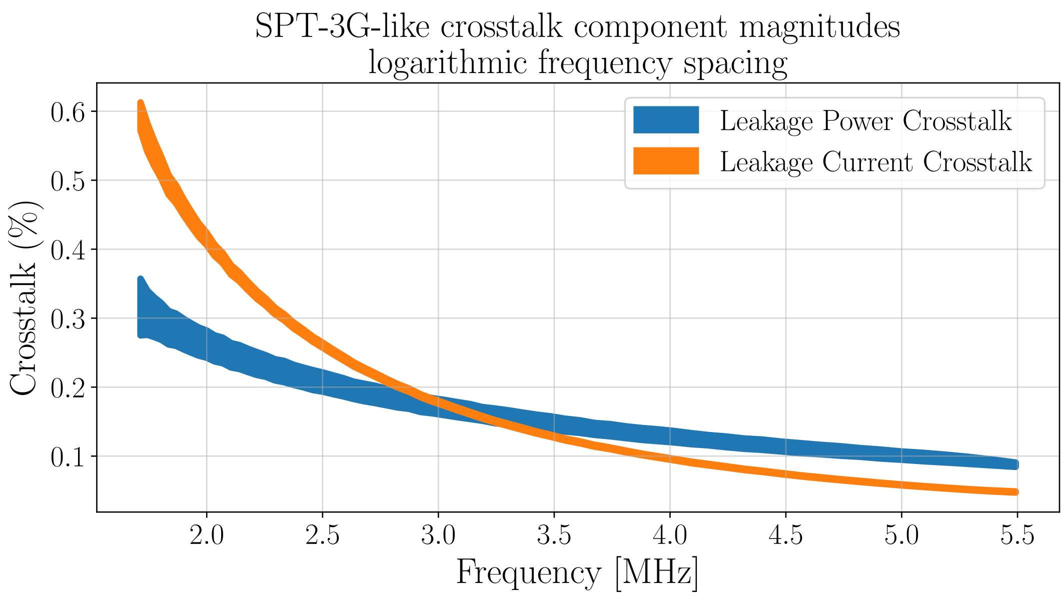

Figure 5.2: Top: The phase of each crosstalk component for a simulated SPT-3G comb. The signal phase is not perfectly zero throughout the band because of variations in the residual reactance in the degree to which L_{stray} can be tuned out. The phases $\delta I_{i,\mathrm{signal}}$ and δI_i are nearly identical because the total crosstalk fraction is very low. Most striking, the relative phase offset between the leakage power phase and the signal phase ranges from between approximately 45° and 90°. An accounting of the leakage power crosstalk that only considers the magnitude of the effect will significantly overestimate it. **Bottom:** The magnitudes of each crosstalk component for an SPT-3G-like system. Only the *projection* of these magnitudes aligned with the signal phase will contaminate the data. The widths of the shaded areas reflect differences between $(i, i+1)$ and $(i, i-1)$ crosstalk matrix elements for each i^{th} TES.

leakage current crosstalk is well approximated by taking its magnitude. However, the leakage power and signal phases are between approximately 45° and 90° offset from one another. A projection of the data along the signal phase will contain only a fraction of the total leakage power crosstalk, and any estimate that considers only the magnitude of leakage power crosstalk will dramatically overestimate it. For SPT-3G-like parameters the resulting crosstalk contributions along the projected axis are given in Figure 5.3, where the total crosstalk fraction is

$$\frac{\delta I_{i,n,\text{crosstalk}}}{\delta I_{i,\text{signal}}} = \frac{\delta I_{i,n,\text{LCX}} + \delta I_{i,n,\text{LPX}}}{\delta I_{i,\text{signal}}} \,. \tag{5.17}$$

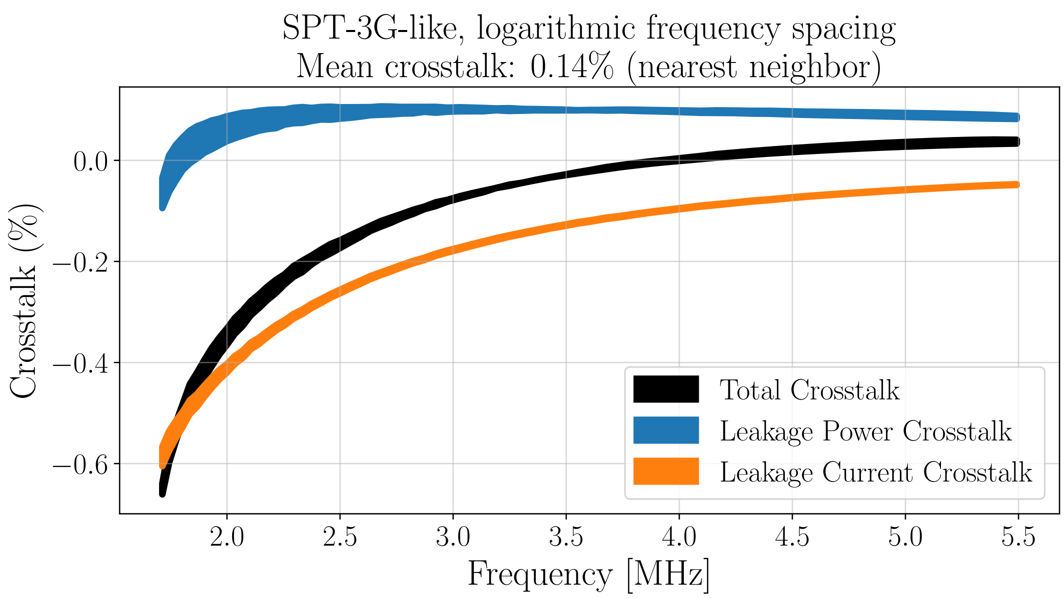

Figure 5.3: Fractional crosstalk contributions for an SPT-3G-like system are given above. Notice that total crosstalk undergoes some cancellation as the leakage power and leakage current terms oppose each other over most of the bandwidth. The widths of the shaded areas reflect differences between $(i, i+1)$ and $(i, i-1)$ crosstalk matrix elements for each i^{th} TES.

5.6 CROSSTALK FREQUENCY SCHEDULING

The relative phase offsets, and subsequent data rotation, were not considered in the original Dobbs et al., 2012 [26] crosstalk models used to design the SPT-3G frequency scheduling. This, along with an early design target of $1\,\Omega$ detectors and a higher L_{stray}=60 nH, led to an overestimate of the leakage power crosstalk contribution, especially at high frequency. A *logarithmic frequency spacing* was used to mitigate the expected higher crosstalk at high bias frequency by increasing the channel spacing (and therefore isolation). In a such a design, frequency separations grow logarithmically, with the closest spacing of ∼30 kHz at low frequency to largest spacing of ∼103 kHz at high frequency.

In the final configuration, and accounting for the phase differences and data projection, SPT-3G is *leakage current crosstalk dominated*. The result is that the total crosstalk fraction is very sensitive to frequency separation; because of the logarithmic frequency scheduling, lower bias frequencies incur larger fractional crosstalk than the high bias frequencies we initially worried about (Figure 5.4). An alternative frequency spacing that allocates detectors

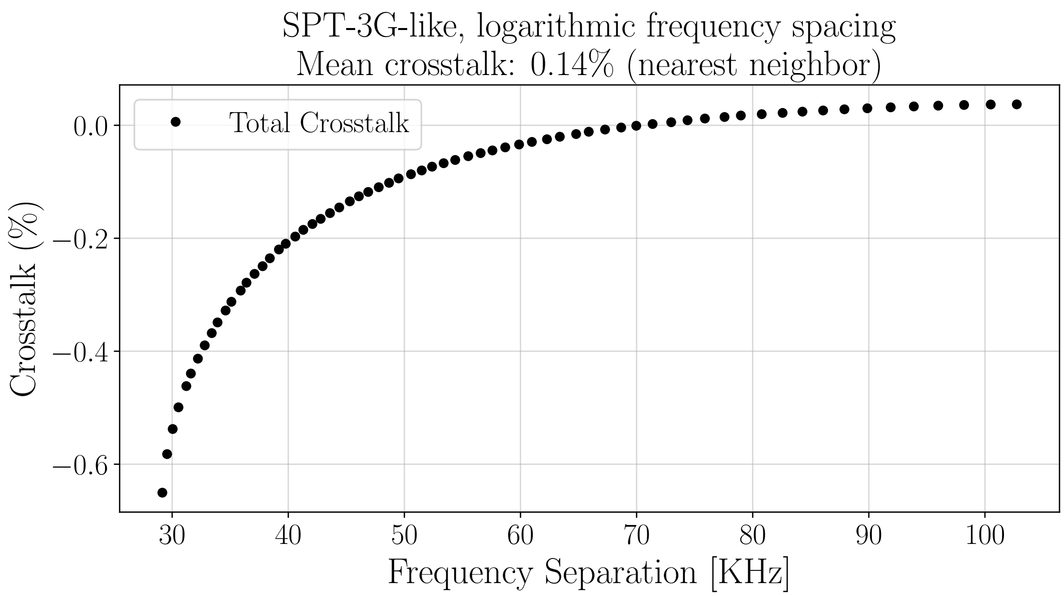

Figure 5.4: In the regime where the leakage power crosstalk is largely negligible, we are dominated by leakage current crosstalk, and inherit a frequency separation dependence that maps directly onto bias frequency.

linearly in bias frequency, would result in better overall crosstalk performance (Figure 5.5).

5.7 LOW L_{stray}

In part due to this misunderstanding of the leakage power crosstalk contribution, the path to better crosstalk performance is often thought to be through minimization of L_{stray}, such as the 10 nH targeted and achieved in Lowitz et al., 2020 [62]. This is accomplished by moving the SQUIDs to the mK stage and avoiding long stripline wiring to the cryogenic filters. Such a design has a number of other potential merits, but will actually spoil this crosstalk cancellation, and result in a higher total crosstalk (Figure 5.6). *In the designs being*

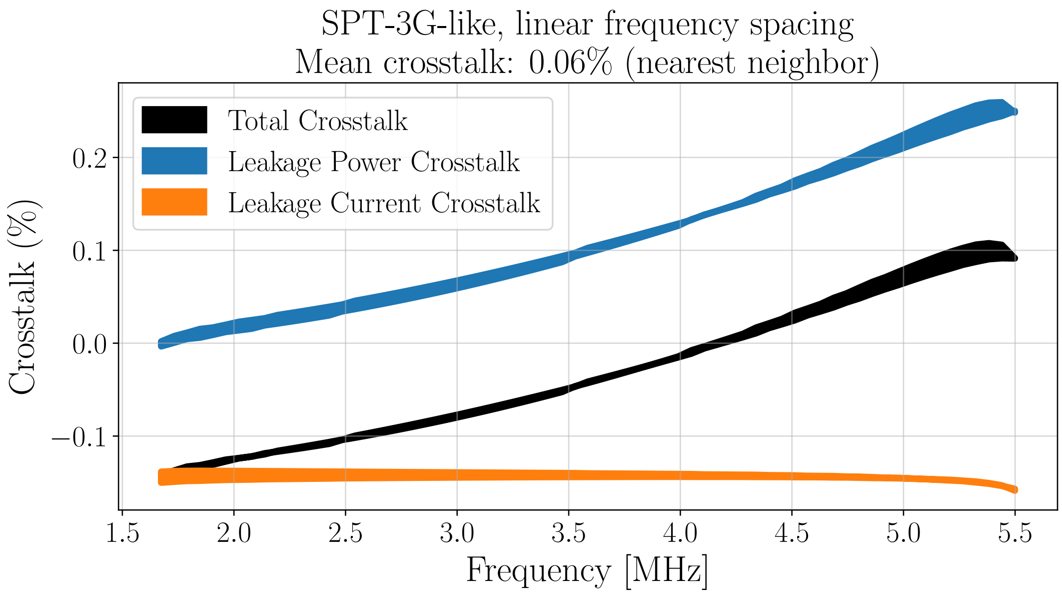

Figure 5.5: A linear frequency scheduling would more effectively leverage crosstalk cancellation and result in a better overall crosstalk performance.

pursued for LiteBIRD that use mK SQUIDs it will be important to explicitly add some Z_{com} to facilitate crosstalk cancellation.

The most effective set of parameters for mitigating crosstalk with a system that looks largely like SPT-3G (in terms of multiplexing factor and bandwidth) would be a reduction in detector normal resistance from R_n=2 Ω to R_n=1 Ω, and only a modest decrease in L_{stray} to ∼30 nH (Figure 5.7).

5.8 CROSSTALK REMOVAL

The crosstalk processes described above are linear in the small signal limit, and should be stable over time.[5] A complete crosstalk matrix can be constructed by varying deposited power on each detector individually, and measuring the response in neighboring TES channels. Provided that process is linear and stable, an inversion of this matrix can be used to deconvolve crosstalk from the data entirely. This crosstalk removal step is applied directly to time-domain data, and reduces the effective crosstalk to the measurement uncertainty in the crosstalk matrix. This process was performed on SPTpol [44], and measurements similar to those required to build such a template were performed for SPT-3G [13]. The SPT-3G crosstalk

5 Verified recently, [2020, *SPT-3G Instrument* [in preparation]].

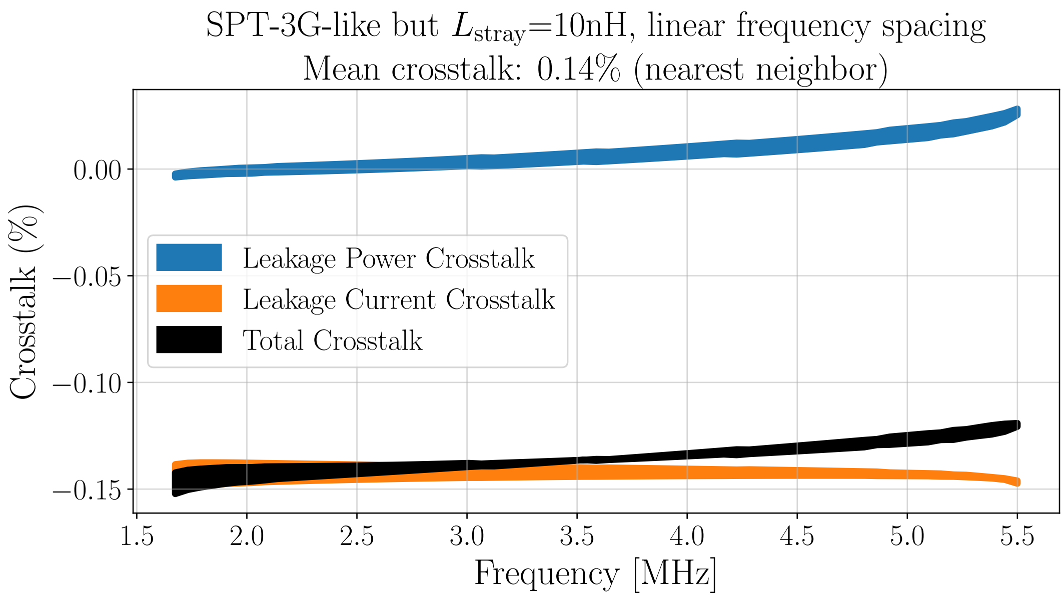

Figure 5.6: Recent efforts to reduce L_{stray} to as low as 10 nH, such as demonstrated in Lowitz et al., 2020 [62], result in worse crosstalk performance, as it dramatically improves leakage power crosstalk without affecting leakage current crosstalk, and in so doing spoils the existing crosstalk cancellation. The configuration here doubles the projected mean nearest neighbor crosstalk compared to a simple linear spacing of the existing SPT-3G system (where $L_{\text{stray}} \approx$45 nH).

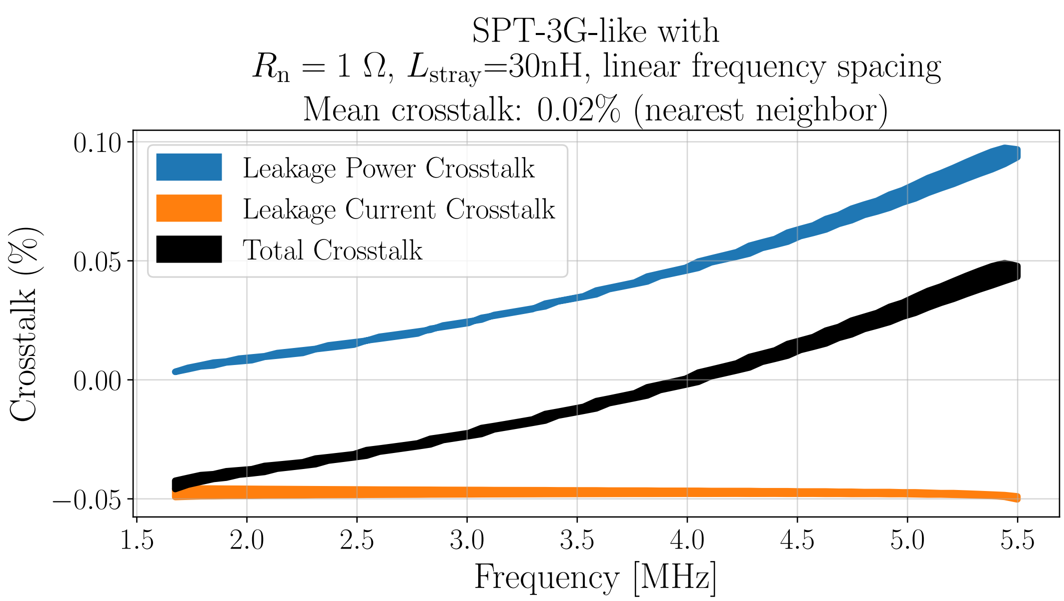

Figure 5.7: An example configuration that capitalizes on crosstalk cancellation to minimize the mean nearest neighbor crosstalk would have lower detector operating resistance, and only a modestly lower L_{stray} than SPT-3G (though, larger than currently planned for mK SQUID configurations). Such an optimization reduces crosstalk by about a factor of 3.

performance will be explored more in Chapter 6. Unlike SPTpol, the intrinsic crosstalk performance of SPT-3G seems sufficient without performing any crosstalk removal.

5.9 CROSSTALK SENSITIVITY TO LC FREQUENCY SCATTER

Crosstalk performance is very sensitive to statistical scatter in LC resonance frequencies, which can vary the frequency separations and channel isolation. This couples crosstalk performance with the fabrication precision of LC resonances, especially at higher multiplexing factors, where channel spacing becomes narrower. A linear frequency schedule ensures an approximately uniform distribution of crosstalk outliers across the bandwidth, while a logarithmic frequency schedule results in a much higher risk of crosstalk at low frequencies, and vanishingly small risk at high frequencies. Figure 5.8 demonstrates this for SPT-3G-like configurations, over a statistical LC resonance scatter ranging from σF=2.5 kHz to σF=10 kHz.

A caveat to this simulation is that it models LC frequency scatter as uniform across the resonators, but the actual phenomenology of that scatter in SPT-3G is more complicated, and covered in detail in Chapter 6. The range of LC resonator scatter presented here is representative though, with a median value near 5 kHz. In general, achieving higher multiplexing factors or a smaller total bandwidth will require precise control over the LC resonator scatter.

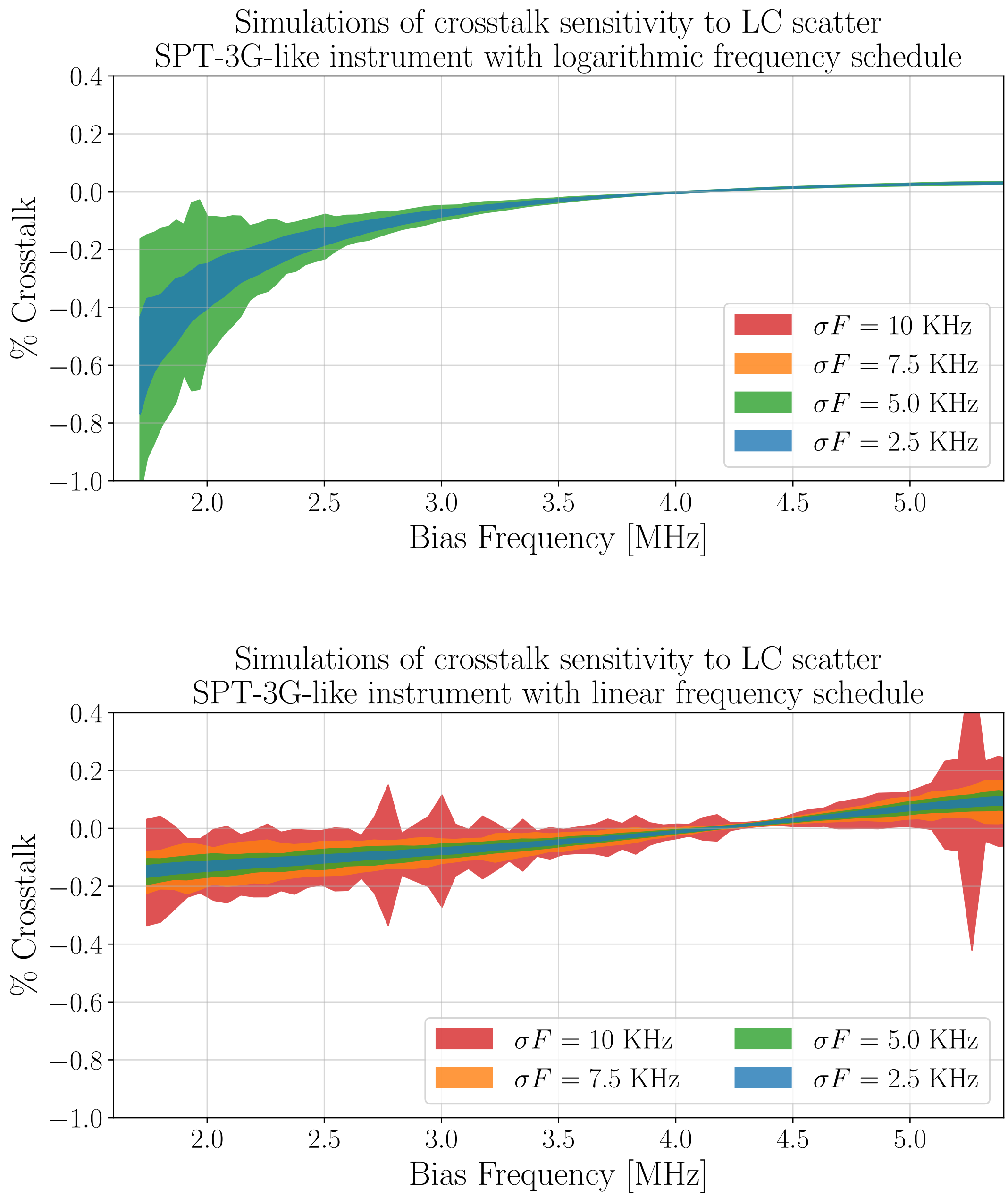

Figure 5.8: Shown above are the $\pm 1\sigma$ intervals for 100 crosstalk realizations using SPT-3G-like parameters. This is performed with a variety of LC frequency scatter scenarios (for SPT-3G, $\sigma F \sim 5\,$kHz), for both a logarithmic and linear frequency scheduling. The logarithmic spacing case (top) is more much sensitive to LC resonance scatter at the low frequencies, where spacing is narrowest. Both leakage current and leakage power crosstalk are asymmetrically nonlinear functions of frequency spacing, which is why for the same σF the crosstalk distributions are widest where the cancellation is the worst. As the cancellation improves, the sensitivity to ΔF declines, similar to how small signal regimes of non-linear processes can result in linear outputs. It is not possible (without a much more complicated architecture) to ensure perfect crosstalk cancellation across the entire bandwidth, so controlling LC frequency scatter will be important for higher-density multiplexing factors. Finally, in these simulations the LC scatter is assumed to be uniform across all bias frequencies, which is not the case for built devices (see Chapter 6), but illustrates the effect well.

6 SPT-3G PARAMETER CHARACTERIZATION

The SPT-3G instrument performance can be understood through the individual properties of the built hardware and the physical relationships that link them. In the sections that follow, I describe the measured parameters of SQUIDs, LC filters, and TES detectors that are most relevant to instrument stability, crosstalk, and noise performance. I also demonstrate how statistical lithography defects are directly implicated in the LC resonance scatter and parasitic series resistance that determine crosstalk performance, TES stability, and TES responsivity; and provide a set of design rules to minimize the effect of these defects in future experiments. The chapter concludes by evaluating the instrument stability and crosstalk performance using the analytic models in Chapter 4.

6.1 BUILT SQUID PROPERTIES

The SA13 SQUIDs used in the SPT-3G receiver were originally designed for a different application: second-stage SQUIDs for a two-stage TDM readout. Despite this, they suit our purposes because they have (relatively) low input coil inductance (70 nH, a factor of five lower than previously deployed SQUID designs[1]) and typically high transimpedance (700 Ω, up to a factor-of-two increase over previously-deployed SQUID designs for fMUX).

SQUID transimpedance plays a role in determining the total instrument noise, but because the relevant readout noise contributions add in quadrature there is a threshold above which improvements in transimpedance do not significantly improve the readout noise. For SPT-3G we initially targeted a threshold of 600 Ω for deployed SQUIDs, but had to make up a deficit in available SQUIDs from a poorer performing batch. This can be seen in the bi-modal distribution of deployed SQUID transimpedances (Figure 6.1, left).

1 This number includes some parasitic inductance present in the wiring and PCB to which the SQUID is mounted [88].

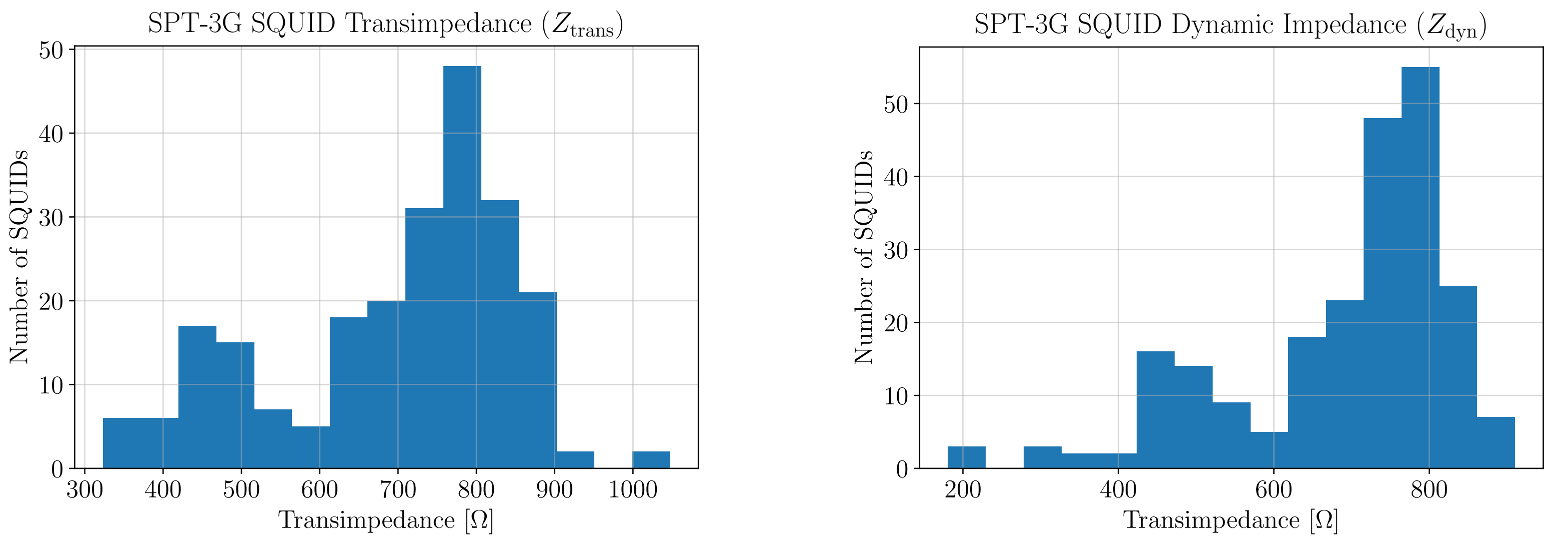

Figure 6.1: Left: SPT-3G deployed using two separate batches of SA13 SQUIDs. The first, and highest performing batch, has mean transimpedance of greater than 700 Ω, but the remainder of the receiver was filled using the best performing SQUIDs from a lower performing batch. This results in the bi-modal distribution seen here. The difference in transimpedance between the best and worst performing SQUIDs is significant, and has implications for the noise performance of the SPT-3G detectors. **Right:** For SA13 SQUIDs tuned to the high Z_{dyn} side of the $V(\phi)$ curves, Z_{dyn} is tightly coupled with Z_{trans}, resulting in a bi-modal distribution very similar to the figure on the left.

6.1.1 *SQUID dynamic impedance*

SQUID transimpedance has been covered in some detail in Section 4.4.1, but there is another property of SQUIDs that is important for noise performance when operating with the DfMUX warm electronics: *dynamic impedance* (Z_{dyn}). The dynamic impedance characterizes the relationship between the SQUID output voltage and junction current bias,

$$Z_{\mathrm{dyn}} = \frac{\delta V_{\mathrm{out}}}{\delta I_{\mathrm{bias}}} \,. \tag{6.1}$$

This impedance is not a relevant circuit element for any science signal, but it presents a mechanism to convert noise current that flows through the SQUID Josephson junctions into an apparent voltage noise that contaminates the signal at the output of the SQUID. A dynamic impedance of $\sim 300\,\Omega$ is optimal for noise performance of our readout system; as it grows larger it can impose noise penalties.[2]

SA13s have two potential operating points: one that exhibits a low dynamic impedance of $\sim 300\,\Omega$ and another that exhibits a much higher dynamic impedance that is well approximated by (and scales with) the transimpedance ($Z_{\mathrm{dyn}} \sim Z_{\mathrm{trans}}$, Figure 6.1, right). Unfortunately the low dynamic impedance operating point of the SA13 is prone to severe resonances internal to the SQUID arrays, which appear to occur at frequencies much higher than our readout band. In the most extreme examples this results in kinks of the $V(\phi)$ curve at that low dynamic impedance operating point (Figure 6.2).

This occurs due to a coupling mechanism between the SQUID output and the input coil, such that incident high frequency environmental noise resonates within the SQUID and suppresses the effective transimpedance. Without some way to dampen the high frequency signals, the resonances make operation of combs of bolometers nearly impossible at the low dynamic impedance tuning point. Consequently, with the exception of a few individual SQUIDs, SPT-3G operates instead at the high dynamic impedance tuning point. This solves the operational issues with the SA13 SQUIDs, but it exacerbates the readout noise.

During the deployment of SPT-3G and Polarbear-2 we had been treating these resonances on the low dynamic impedance operating point as a fundamental characteristic of the SA13 SQUIDs; however, this is incorrect. An output of my research has been to develop and validate a model that explains those resonances, and why they only affect the low

2 A more complete treatment of the mechanisms for this is given in Section 8.1.

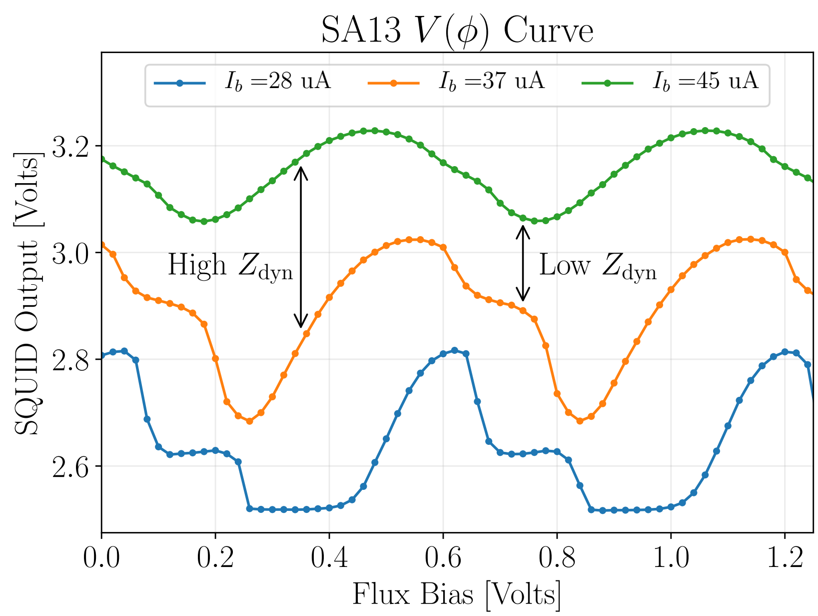

Figure 6.2: A set of $V(\phi)$ curves at different SQUID junction current biases (I_b) demonstrates the resonant features, which appear as a shoulder on one slope of the curve. Note how the change in output voltage (y-axis) as a function of SQUID junction current bias (coloured lines) is large on the high dynamic impedance slope of the $V(\phi)$, and low on the low dynamic impedance slope of the $V(\phi)$, where the problematic kinks appear.

dynamic impedance regime on the SQUID. Approximately 40 pF of parallel capacitance in the cryogenic feed-through wiring generates an RC low-pass filter with the SQUID dynamic impedance. At the high dynamic impedance operating point, this low-pass filter is strong enough to short out the high frequency resonances, but at the low dynamic impedance operating point the low-pass filter is much weaker. The TDM systems that employed these SQUIDs never encountered such resonances because of the much larger parallel capacitance built into their implementation [29]. This model has been experimentally verified in the laboratory by explicitly adding a low-pass filter at the SQUID output to resolve the resonance kinks.[3]

6.2 LITHOGRAPHIC FILTER PROPERTIES

The design and performance of the LC chips has been covered in much detail,[4] but these discussions haven't included a study of the scatter in the built LC resonance frequencies compared to the designed LC resonance frequencies, nor have they investigated the superconducting lithographic filters as a source of parasitic series impedance. LC resonance frequency scatter affects instrument performance through crosstalk and, to a lesser extent, detector stability. Parasitic series impedance with the TES degrades stability, increases responsivity, and can lead to greater crosstalk due to wider filter bandwidths. This section defines a model in which lithographic defects lead to physical processes that produce statistical LC resonance frequency variation and additional parasitic series impedance.

The fabrication of LC resonances has many steps, and this document will not cover all mechanisms by which errors can occur. A more detailed treatment of the lithograph process is available in [85]. However some broad terminology is helpful:

LITHOGRAPHY MASK: A mask is a plate used to project the lithography pattern, which is then focused onto a photolithographic target. Masks may be re-used many times. They are much larger than the resulting exposure, and so are comparatively easy to fabricate. This means errors in the mask are typically design errors, not fabrication errors.

LC WAFER: An LC wafer is the product of a single exposure of a mask. Each wafer produces 30 individual LC chips, which collectively are identified as a single batch.

3 The experimental verification of this model was carried out by Tucker Elleflot, without whom this would have remained theoretical.

4 For instance, Rotermund et al., 2016 [85] and Hattori et al., 2014 [41].

LC BATCH: The set of LC chips from the same LC wafer.

LC CHIP: An individually diced element of an LC wafer. Each LC chip is composed of 68 resonators, and defines the resonators of a single readout comb.

The current SPT-3G focal plane is made up primarily of aluminum LC chips from 3 different mask versions and a total of 13 different aluminum LC chip batches, each contributing between 3 and 20 individual LC chips.[5] An additional 35 LC chips are fabricated from niobium and were R&D chips that are not considered in this analysis.[6]

6.2.1 *Systematic LC frequency scatter*

Only scatter that changes the relative spacing of LC resonances *within* individual combs is significant for crosstalk. Systematic frequency shifts that affecting all resonant frequencies within an LC combs in the same way will maintain the relative frequency spacing *within* each comb; this type of scatter is not a significant concern from the perspective of crosstalk.

Systematic shifts in frequency can be produced by stray series inductance or capacitance in the cryogenic wiring, by non-uniform exposure of the mask, or variations by batch due to differences in material purity or processing. The largest contribution to the series inductance and capacitance come from the cryogenic wiring between the 4-Kelvin stage and the sub-Kelvin stage. This wiring is made up of broadside-coupled striplines of superconducting niobium, and is designed to be very low inductance [6]. The striplines vary in length across the focal plane, resulting in inductance ranging from $\sim$30 nH to $\sim$45 nH. Systematic shifts in frequency between combs of different stripline lengths is linear as a function of frequency. These shifts are not significant in terms of instrument performance because they result in smooth increases in frequency spacing between channels.[7]

6.2.2 *Statistical LC frequency scatter*

5 One of these batches is is known to have a specific material defect and is disregarded in the following analysis.
6 Niobium is harder to work with and did not exhibit significantly better performance.
7 They are also quite small. For a 25nH difference (an extreme example) the frequency shift varies from $\sim$0.4 kHz to $\sim$1.2 kHz.

Statistical scatter affects individual resonators within combs, shifting the frequency spacing between neighboring channels with respect to the design. Unlike systematic variations, this form of LC resonance scatter is important for understanding the instrument crosstalk performance. That variation can be produced by:

LC DEFECTS: Physical or geometric defects in the lithographed components, such as torn or ragged features in the traces, dimples and divots from contaminants, or damage during any stage of the lithography or handling of the resonator chips. Examples of some of these features can be found in Figure 6.3.

TES WAFER TRACE LENGTHS: Variations in series inductance *on the TES wafer* due to different path lengths of the traces connecting resonators to detectors can generate scatter in the frequency spacing. The SPT-3G readout design minimizes this by enforcing a mapping between each resonator frequency and detector such that frequency neighbors maintain similar wiring lengths.

DESIGN ERRORS: Discrete design errors in the mask can propagate to every resonator fabricated using this design. The v3 mask design for SPT-3G contained an error for one resonator that made the capacitor legs susceptible to shorts. This resulted in a significant number of these channels appearing at a frequency much higher than our intended bandwidth.

It is possible to measure statistical scatter independently of systematic shifts in resonator frequencies. I do this below by separately considering groups of LC resonances according to LC batch and stripline cabling lengths. The statistical scatter is then captured by calculating the *pooled standard deviation* of the separate distributions.[8] This works by assuming that the mechanism responsible for the variance is common across LC wafers, despite the fact that the central value of those frequencies is offset. The result of this measurement is shown in Figure 6.4. Each data point is the pooled standard deviation of that resonator frequency, from 28 populations separated by mask, batch, and stripline length. From the over 11,000 channels with mappings between observed frequency and LC resonator only 97 were excluded as outliers, likely due to bookkeeping errors in the mapping to LC resonator. The populations are shown by mask version and batch in Figure 6.5.

8 This is the square root of the more common “pooled variance,” or “unbiased least squares estimate of variance.”

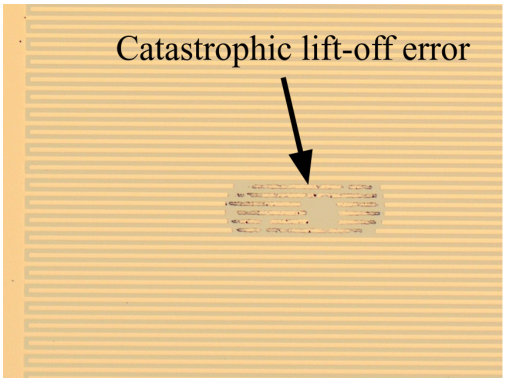

(a) A catastrophic lift-off error in a capacitor that would result in an apparent missing frequency.

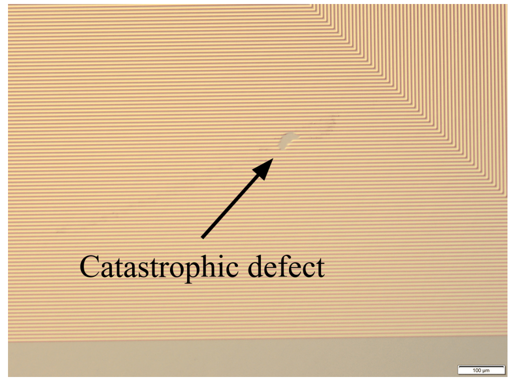

(b) A catastrophic defect in an inductor that would result in a missing frequency.

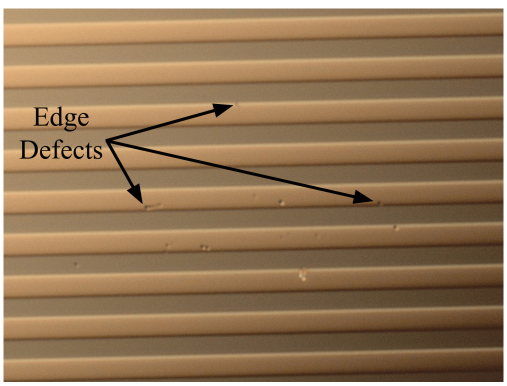

(c) An array of divots in a capacitor trace that may distort the field lines.

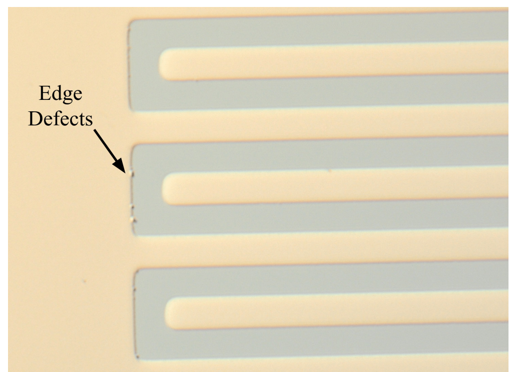

(d) Defects on the edges of a capacitor trace that may distort the field lines.

Figure 6.3: A selection of examples of defects in the production of lithographed inductors and capacitors are shown above (see Figure 4.3 for the intended structures of these elements). In each case above the trace widths are 4 μm. The top two panels show catastrophic defects that would result in missing resonances either due to an open circuit, as in **(b)**, or due to a significant enough change in capacitance that the resonant frequency is moved outside our observable bandwidth, as in **(a)**. These are extreme examples, but defects that result in missing frequencies are responsible for a ∼5-10% yield loss in SPT-3G resonances. The lower two panels show examples of defects that are more typical. These distort the field lines, and may be the features described by Equation 6.3 that cause scatter in our observed resonances. Photos by Amy Bender.

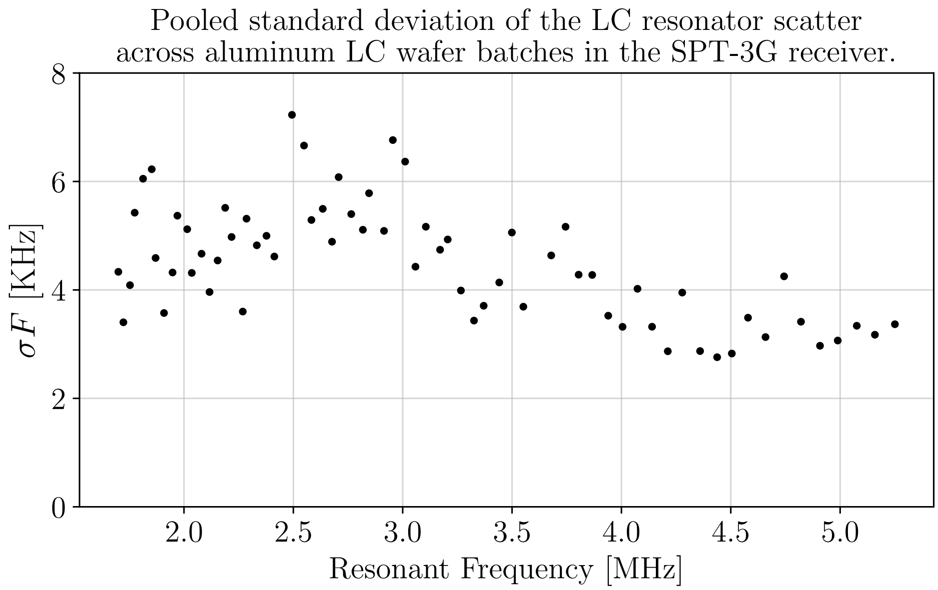

Figure 6.4: The scatter in resonator frequencies is estimated from the pooled standard deviation of many distributions of resonant frequencies. These distributions are defined by LC batch and stripline cable length and shown here binned by intended resonant frequency. This estimate of the scatter is largely insensitive to systematic differences between LC batches, stripline length, and wiring on the TES wafer. The remaining scatter plotted above is a good proxy for the scatter that is relevant to crosstalk performance. That this is non-uniform as a function of resonant frequency in such a clearly structured way is surprising. The source of this structure is described in Section 6.2.3, and attributed to edge-effects due to discrete defects in the lithography.

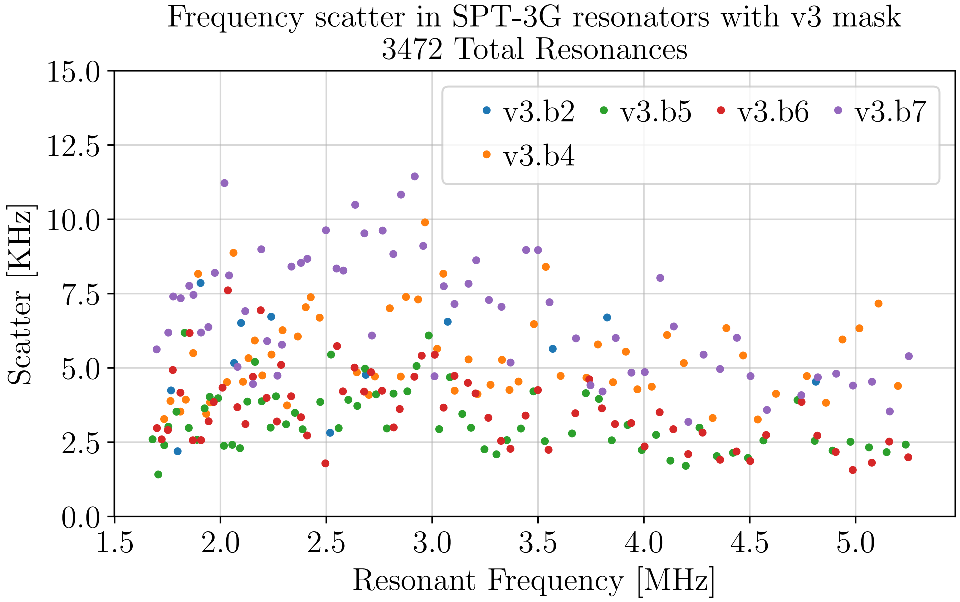

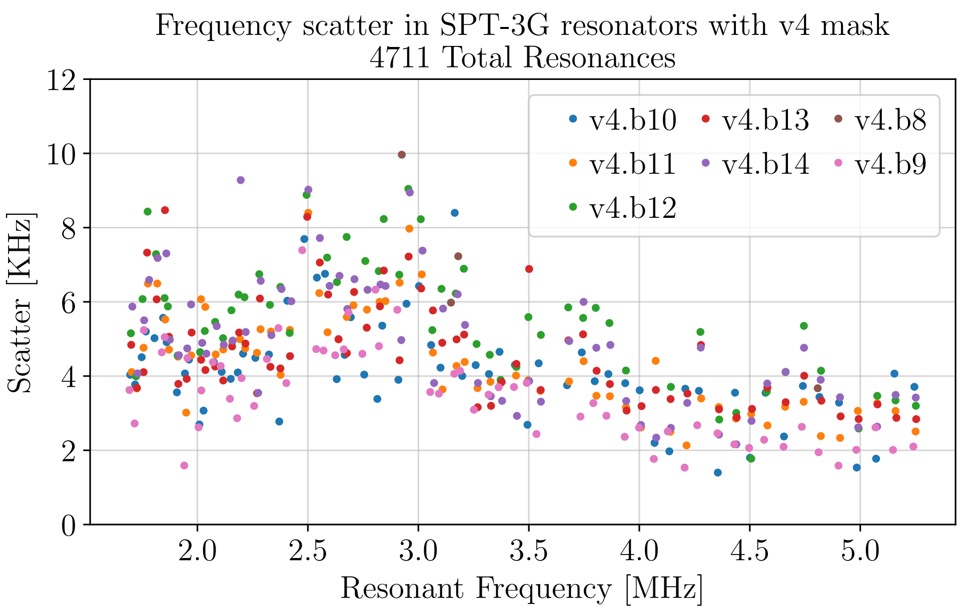

Figure 6.5: Statistical scatter in the SPT-3G LC resonances are shown here separated by mask version and batches. Each batch does have some distinctive features, and some are systematically worse in a scaled way, possibly indicating a contamination issue. The dominant frequency dependence remains common throughout all masks and versions. Note: only batches with at least five individual LC chips in the receiver are plotted here.

6.2.3 *Geometric susceptibility of LC resonators to defects*

The dominant source of statistical scatter in the LC resonant frequencies appears to come from physical defects in the lithography of individual capacitors and inductors (see Figure 6.3 for examples). Here I focus on statistical scatter due to defects on the capacitor: all LC resonators share the same inductor design – consequently inductor defects may contribute to resonant frequency variation, but cannot contribute to a frequency dependence in that variation. This can be surprisingly well described through simple unit analysis and geometric heuristics:

ASSUMPTION 1: Defects that modify the electric field lines enough to affect the capacitance do so by distorting the edges of the traces, or breaking the traces entirely. Defects fully enclosed by conductor or insulator will have minimal effect on the electrical properties.

ASSUMPTION 2: Defects are randomly distributed across the wafer. Additionally it appears true that the distribution of defect sizes are such that the majority are smaller than, or on the order of, the trace width.

HEURISTIC 1: The probability that any defect will cause an edge distortion is given by χ: the ratio of the area where a defect will intersect an edge to the total capacitor area. If we approximate defects as circular, for our capacitor geometries this is given by

$$\chi = \left(\frac{\text{Capacitor Perimeter} \cdot 2 \cdot \text{Defect Diameter}}{\text{Capacitor Area}} \right) , \tag{6.2}$$

shown in Figure 6.7a.

HEURISTIC 2: Each edge distortion imparts a fractional change in resonant frequency $\left(\frac{\Delta F}{F} \text{ per Edge Distortion} \right)$, such that that total fractional distortion in resonant frequency is given by $\left(\frac{\Delta F}{F} \text{ per Edge Distortion} \right) \cdot (\text{Number of Defects} \cdot \chi)$. Therefore, the expected scatter in frequency for a given resonator is:

$$\Delta F = F \left(\frac{\Delta F}{F} \text{ per Edge Distortion} \right) \cdot (\text{Number of Defects} \cdot \chi) \ . \tag{6.3}$$

The geometric components of Equation 6.3 are calculated using the LC lithography design, and shown in Figure 6.6. Equation 6.3 can be expressed in terms of the known properties (F and $\frac{\chi}{\text{Defect Diameter}}$) and an unknown but frequency-independent scalar (ρ):

$$\Delta F = F\left(\frac{\chi}{\text{Defect Diameter}}\right) \cdot \rho\,, \tag{6.4}$$

such that

$$\rho = \left(\frac{\Delta F}{F} \text{ per Edge Distortion}\right) \cdot \text{Number of Defects} \cdot \text{Defect Diameter}\,. \tag{6.5}$$

The quantities $\left(\frac{\chi}{\text{Defect Diameter}}\right)$ and $\left(\frac{\Delta F}{\rho}\right)$ can be calculated based on the lithography design, and are shown in Figures 6.7a and 6.7b. ρ is calibrated empirically by scaling $\left(\frac{\Delta F}{\rho}\right)$ to the mean of the pooled standard deviation of SPT-3G resonances. The agreement in Figure 6.7c between the calculated and observed frequency scatter suggests that, despite its simplicity, this model can explain the mechanism and phenomenology of LC resonant frequency scatter.

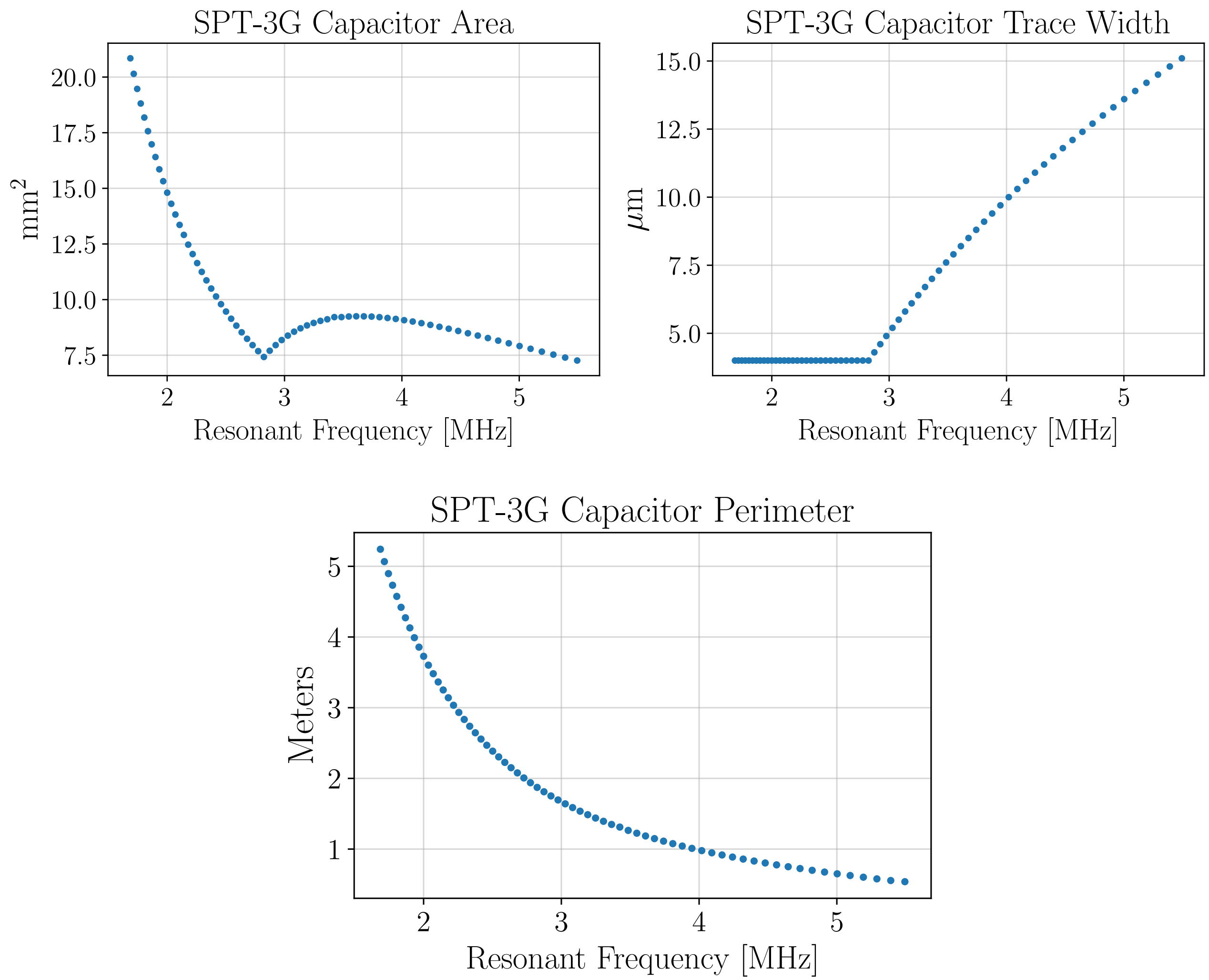

Figure 6.6: The geometries of each capacitor used in the SPT-3G LC chip vary in area, trace width, and perimeter, as shown above. These choices were made to minimize the required surface area of the LC chip. Large LC chips are more difficult to fabricate and adhere to a PCB without cracking under thermal contraction. Consequently, the lowest frequencies, which require the largest capacitors, are built using the narrowest trace widths. This choice trades some degree of yield risk. which comes with using narrow traces, for smaller overall chip sizes. An unintentional consequence of this trade was a substantial increase in LC resonant frequency scatter.

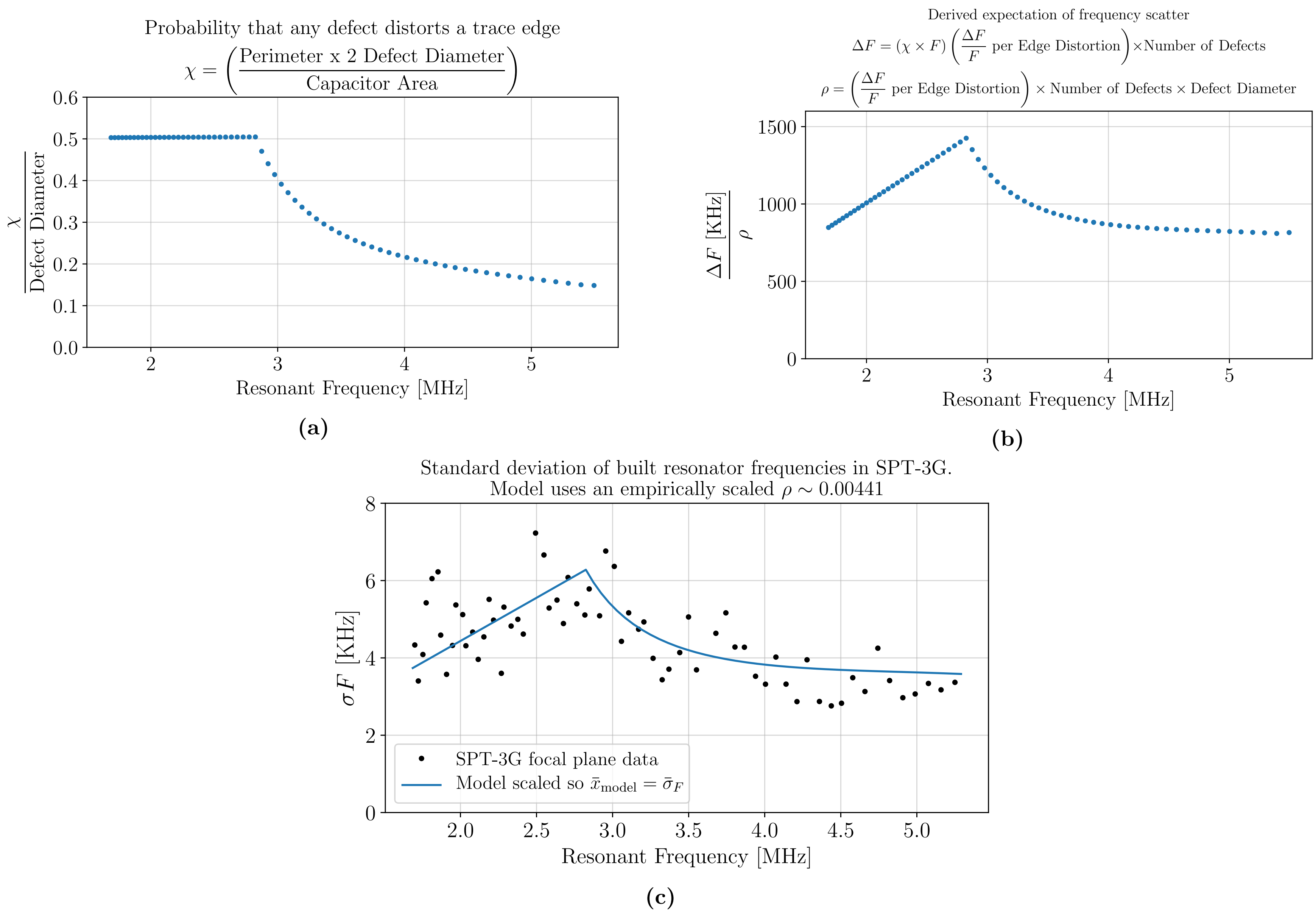

Figure 6.7: **(a)** Equation 6.2, calculated for SPT-3G design parameters. **(b)** The quantity $\left(\frac{\Delta F}{\rho}\right)$, a measurement of the frequency scatter up to a scaling factor. **(c)** Equation 6.3 with ρ empirically calibrated such that the mean model value matches the mean of the measured scatter. The resulting plot is not a fit to the data, just a linearly scaled version of (b), calculated entirely through the designed geometry.

The simple model for frequency scatter given in Equation 6.3 provides a compelling explanation for the frequency dependence observed in LC resonator scatter. It also suggests that substantial improvements in the LC resonator scatter can be achieved using existing technologies, but with slightly different design geometries, such as avoiding the smallest line widths, and establishing minimum area footprints.

6.2.4 *Missing frequencies in SPT-3G*

Large defects that sever one or more more of the traces in a capacitor (such as those in Figure 6.3a) result in sufficiently large shifts in frequency that these peaks will appear to be "missing." Similarly, a short across any capacitor, or break in the trace for an inductor will result in an open circuit for that filter, and also appear to be missing.[9] Finally, open circuits on the TES wafer will also generate missing peaks at the intended resonant frequency. These opens on the TES wafer are responsible for approximately half of all missing peaks, and are randomly distributed with respect to the LC resonances associated with those detectors.

Together this means that the distribution of missing channels will have a weaker frequency dependence than the distribution of frequency scatter, but will still reflect the same general shape as Figure 6.7c. Figure 6.8 shows the distribution of missing frequencies as a function of bias frequency, which is consistent with the above expectation.

6.2.5 *Parasitic impedance of lithographic filters*

The parasitic impedance of the cryogenic circuit is shown in Figure 6.9. This exhibits the same frequency-dependent structure as χ (the probability of defects that cause edge distortions), which was shown Figure 6.7a:

$$\begin{aligned} z_{\text{lcr}} &= \text{Impedance per Edge Distortion} \cdot \text{Number of Defects} \cdot \chi \\ z_{\text{lcr}} &= \beta \cdot \left(\frac{\chi}{\text{Defect Diameter}}\right) . \end{aligned} \tag{6.6}$$

9 The trace length for each inductor is ~1.5 meters. The trace lengths of capacitors vary between ~0.9 meters and ~2.6 meters. The inductors all use the most narrow 4 µm traces. So in general we expect frequency shifts from defects in the inductor to be similar in magnitude to those on the capacitor, but for them to be somewhat more susceptible to missing peaks.

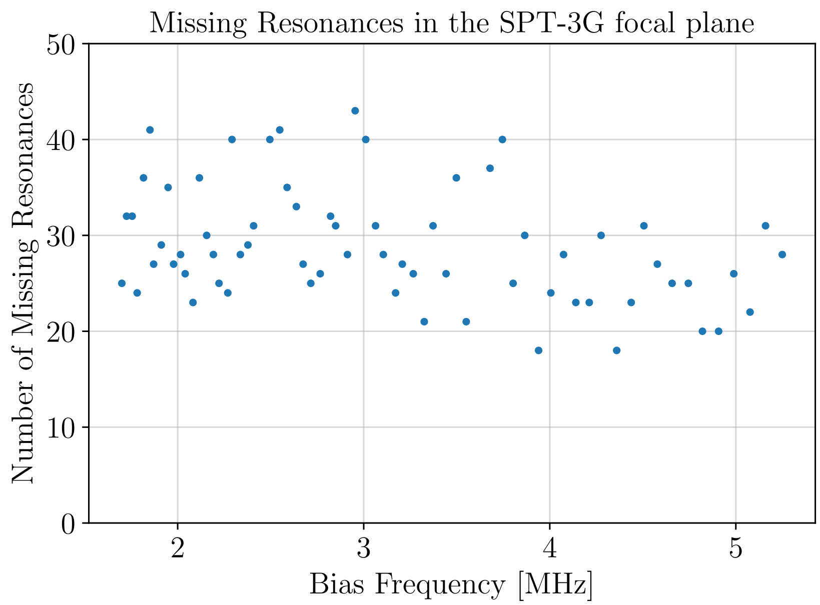

Figure 6.8: The above figure shows missing LC resonances as a function of frequency in SPT-3G. Missing resonances are the product of the same sort of defects that cause scatter in LC resonant frequencies, but at a larger scale. Because the inductors are series elements they cannot tolerate any interruption of the thin conductive traces, and so are more susceptible to defects that result in missing resonances. Because the inductor designs are identical at all frequencies you expect a largely frequency-independent distribution of missing resonances, with perhaps a slight contribution from the same frequency dependence exhibited by the capacitor defects in Figure 6.7c.

Where, similarly to Equation 6.4, we've separated the model into a term calculated from the geometric design of the capacitor ($\frac{\chi}{\text{Defect Diameter}}$) and a frequency-independent scalar (β).

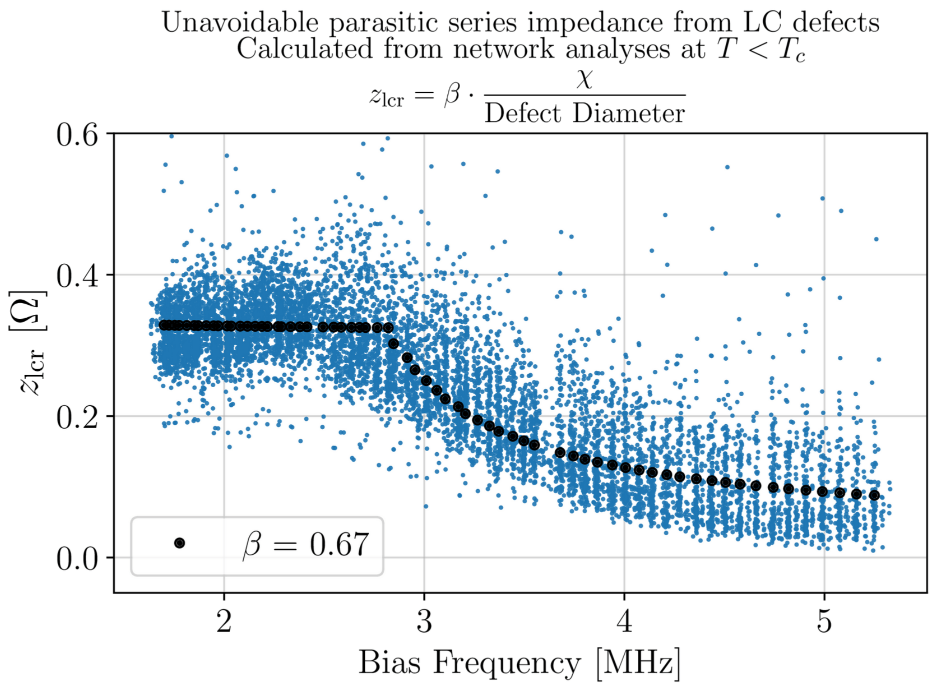

Figure 6.9: The fundamental parasitic series impedance with the TES is measured at the TES bias frequencies using a network analyses performed when the TES is fully superconducting. The resulting distribution of z_{lcr} across the instrument is well described by linearly scaling $\frac{\chi}{\text{Defect Diameter}}$, given in Equation 6.2 and shown in Figure 6.7a.

A complete model for how physical defects can modulate apparent parasitic impedance in a 2D surface is not available. One speculation is that defects decrease the *thickness* of the conductor, which in turn constrains the transport of Cooper pairs. Alternatively the defects could be the result of deposition of non-superconducting material into the conductor, or penetration of the conductor by lithography substrate, either of which may locally proximitize the superconductor.[10] What we can take from this is that the lithographic LCs contribute non-trivially to the destabilizing series impedance seen by the TES, and the same design rules that optimize for low scatter in resonant frequency also minimize this contribution.

10 One hint may be that, unlike frequency shifts, this effect appears confined to the capacitor: the difference in observed impedance has a minimum close to zero. Since any effect due to the inductor would be constant across the bandwidth that limits the magnitude of any contribution from the inductor.

6.3 built tes detector properties

For the purposes of evaluating the stability and noise of the SPT-3G instrument, the relevant detector properties are the TES normal resistance (R_n), the TES operating resistance (R_{TES}), and the effective TES time-constant (τ_{eff}). Authoritative measurements of detector R_n can be made with DC 4-wire measurements of individual TES test samples from each detector batch. In situ measurements of R_n are more challenging due to the transfer functions involved, but are in agreement with the expectations from 4-wire measurements. Detector time constant measurements must be performed in situ with an end-to-end optical system, but are less dependent on the transfer functions involved due to the nature of the measurement, which uses relative signal amplitudes rather than absolute calibrations.

Detector normal resistance (R_n)

DC 4-wire measurements of TES test samples made independently of the DfMUX system suggest that TES resistance is one of the best controlled, and uniform, detector parameters: normal resistances in a TES wafer are typically within 10% percent of the mean. The target R_n for SPT-3G detectors is $2\,\Omega$, which is met to within the uncertainty specified above for 7 out of the 10 detector wafers in the focal plane. Two of the remaining wafers have systematically higher normal resistances ($2.5\,\Omega$), and a third experimental wafer made from a different material has systematically lower TES normal resistances of $1.7\,\Omega$ [31].

In situ measurements of TES resistance requires knowledge of the transfer functions for both the warm and cryogenic electronics. The cryogenic circuit can be measured individually using network analyses, but the warm component transfer function can only be measured absolutely using an external reference. Rather than calibrate each readout model in the warm electronics individually, we construct a template transfer function based on a subset of measured readout modules and use that template for quality control during the fabrication and acceptance of subsequent electronics, we then require that newly manufactured modules agree with the template. This process guarantees a warm transfer function uncertainty within $\pm 10\%$ of the template.

This sets an upper limit on the accuracy of any resistances derived from in situ measurements.[11] After accounting for the known parasitic impedance (Figure 6.9) the resulting normal resistances are in agreement with the 4-wire measurements (Figure 6.10). The transfer functions used to perform these calculations are described in Section 7.2.[12]

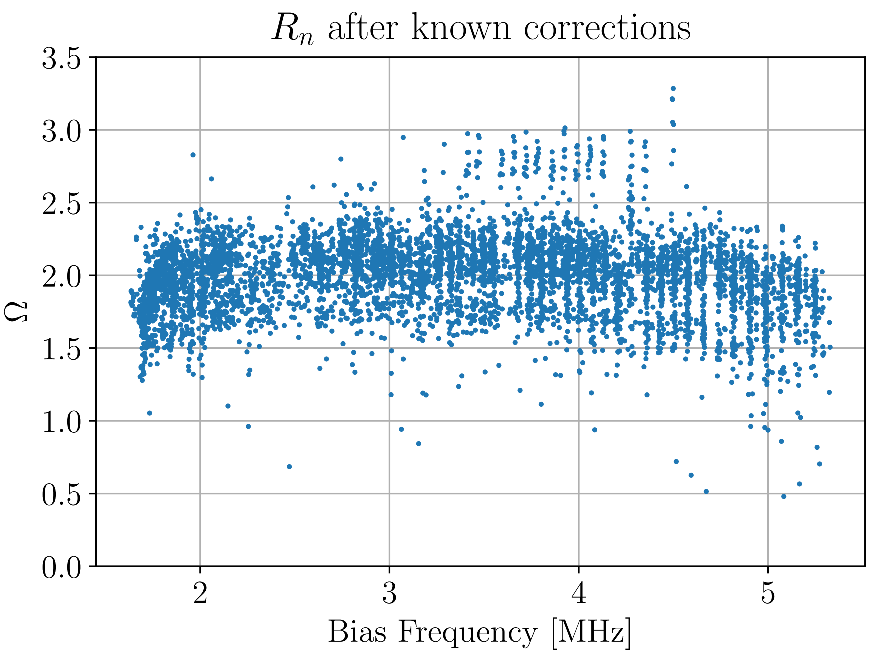

Figure 6.10: In situ measurements of R_n are difficult because they rely on semi-analytic transfer functions with some fundamental limitations in accuracy. Nevertheless, the final result is largely in agreement with trusted 4-wire measurements, though there does appear to be some frequency dependence at the lowest and highest frequencies that is not being perfectly captured by the transfer functions. For this plot I have excluded the three TES wafers with known systematic offsets of in R_n.

11 Science data is not limited by this tolerance, as it is not calibrated using these transfer functions. Instead the it is calibrated end-to-end directly using known optical sources.

12 This application of the transfer functions is much more challenging than what is required for an analysis of the noise, because the carrier transfer function for noise doesn't need to distinguish between the various different sources of impedance within the cryogenic comb. Uncertainty in measurements of R_n are also compounded by any uncertainty in the measurement of z_{lcr}. As we will see in Section 7.3, noise sources that depend on the carrier transfer function are so subdominant that variations of several tens of percent are negligible.

Effective TES time constants (τ_{eff})

Recall from Section 4.3, Equation 3.6 that the *effective time constant* (τ_{eff}) of the TES is given by

$$\tau_{\text{eff}} = \frac{\tau_0}{\mathcal{L}\frac{R_{\text{TES}}-|z_0|}{R_{\text{TES}}+|z_0|} + 1}\,, \tag{6.7}$$

where τ_0 is the thermal time constant of the TES and $\mathcal{L}$ is the detector loopgain. τ_{eff} can be measured directly using a chopped optical signal that ramps in frequency, and then fitting for the roll-off in response to the pulses. Chopped optical signals are used on SPT-3G to measure time constants, relative gains, and as a metric for the array sensitivity. An analysis of the SPT-3G time constants was performed by Zhaodi Pan, the output of which I used for a stability analysis of the array. A histogram of Pan's data for τ_{eff} is shown in Figure 6.11.

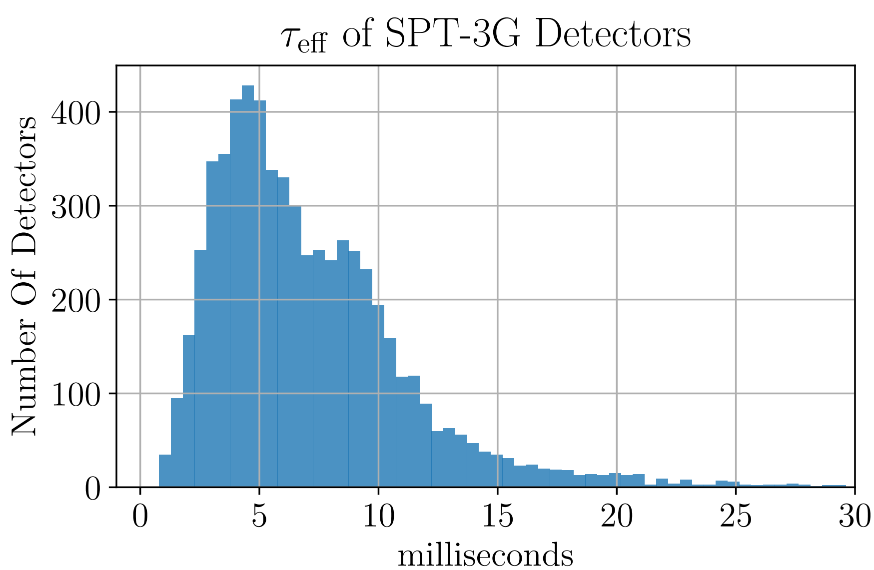

Figure 6.11: Effective time constants of SPT-3G detectors are measured using a chopped optical source and observing how the response attenuates as a function of the chopper frequency. That analysis was performed by Zhaodi Pan and appears in Dutcher et al., 2018 [31]. The distribution shown here is notable for how extended it is, which reflects the difficulty in controlling the time constants due to how many features of the TES are relevant. The 2017 engineering run of SPT-3G suffered from instabilities due to detectors that were too fast. The subsequent focal plane was built using much more conservative parameters for the target time constant, seen here.

The difference in the variance of the distributions of R_n ($\mathcal{O}$(10%)) and τ_{eff} (factors of several) demonstrates the relative difficulty in achieving target time constants in fabrication compared with target normal resistances. This is consistent with the fact that many more fabrication parameters are involved in determining τ_{eff} than R_n.

6.4 SPT-3G STABILITY

The DC and dynamic stability criteria for TES operation were derived in Section 3.3. While the detector and LC filter design and fabrication safety factors were chosen with these criteria in mind, we did so with an incomplete model for the parasitics and scatter in the distributions of built parameters. During the engineering run of SPT-3G in 2017 the focal plane suffered from serious instability due to violation of the dynamic stability criteria. We subsequently deployed a new focal plane for the 2018 season with significantly slower detectors. Slower detectors successfully addressed the yield issues during the engineering run, and in the current SPT-3G focal plane we are not limited by detector stability in any typical operating regime.

6.4.1 *DC stability*

The DC stability criterion (Section 3.3) is used to evaluate the relationship between stray series impedance and TES resistance. When this criterion is met, a change in TES resistance results in an opposing change in dissipated electrical bias power. The most strict formulation of this criterion is that the series impedance with the TES must be less than the operating resistance of the TES. While Section 6.2.5 calculated the z_{lcr} in series with the TES *within each LC filter leg*, the series impedance relevant here is the equivalent series impedance that the TES experiences from the circuit as a whole (z_s, or Thévenin equivalent series impedance). z_s includes effects such as leakage current and reactances from series inductances (Figure 6.12).

The magnitude of the stray series impedance ($|z_s|$) is much lower than the operating impedances of the $2\,\Omega$ SPT-3G detectors (Figure 6.13), and so we have significant margin in DC stability. This is more intuitively expressed as a difference between the operating R_{frac} and minimum DC stable R_{frac}, shown in Figure 6.16.

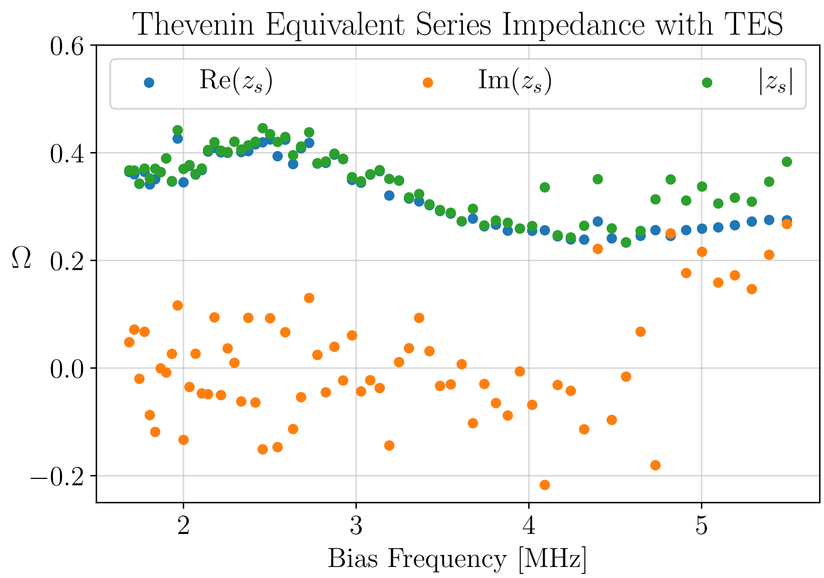

Figure 6.12: The median Thévenin equivalent series impedance for detectors in the SPT-3G receiver, binned by LC channel. This is dominated by the z_{lcr} from the lithographic chips, but additionally has contribution from the residual reactance from L_{stray} and the parallel network legs.

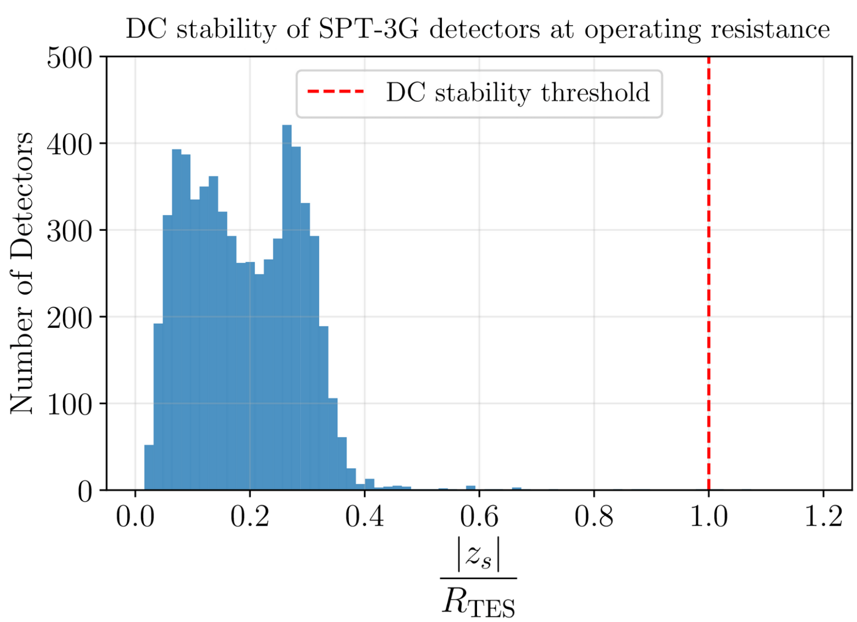

Figure 6.13: The DC stability criterion is violated when $R_{\mathrm{TES}} = |z_s|$. SPT-3G has sufficiently low parasitic impedance that this is not a problem.

6.4.2 *Dynamic stability*

The dynamic stability criterion (Equation 4.4, Section 4.3) gives the condition for which the detector impulse response is critically damped:

$$\begin{aligned}\frac{\tau_0}{\mathcal{L}\frac{R_{\mathrm{TES}}-|z_s|}{R_{\mathrm{TES}}+|z_s|}+1} &= \left(3+2\sqrt{2}\right)\left(\frac{2L}{|z_s|+R_{\mathrm{TES}}}\right)\\ \tau_{\mathrm{eff}} &= \left(3+2\sqrt{2}\right)\left(\frac{2L}{|z_s|+R_{\mathrm{TES}}}\right),\end{aligned} \tag{6.8}$$

where z_s is the Thévenin equivalent series impedance to the TES. The SPT-3G array demonstrates no violation of the dynamic stability criterion (Figure 6.14, top).

A closer look at the distribution nearest the critically damped threshold (Figure 6.14, bottom) makes it appear that the array is marginal with respect to this criterion. While it is likely that SPT-3G suffers a small yield penalty for detectors whose parameters scatter towards this threshold, this is misleading. Figure 6.15 shows the electrical term of the stability criterion equation without subtracting it from the underlying time constants. Unlike the time constant distribution (Figure 6.11), this distribution does not have significant outliers, and the mean value is a tenth of the mean τ_{eff} with which it is compared. This indicates that the small margin in Figure 6.14 (lower) comes from detectors that scatter to very fast time constants. This interpretation is consistent with the notion that detector time constants drive stability, and that electrical parameters are relatively well controlled by comparison.

Calculations of the minimum dynamically-stable R_{frac} given our measured τ_{eff} and SPT-3G detector properties demonstrate that the instrument stability is not meaningfully jeopardized by the detector time constants or violations of the dynamic stability criterion (Figure 6.16). This indicates that our interpretation of the instability experienced in 2017 was correct, and that the measures taken to improve stability in the 2018 deployment have been successful. It also indicates that we have the flexibility to operate deeper in the detector superconducting transition to improve responsivity and noise performance, without compromising the detector stability.

One of the limitations of FDM relative to TDM is the requirement of relatively slow detectors. We see here that the SPT-3G build is conservative in this respect, and limited not by the fundamentals of FDM, but by fabrication control over a TES detector property. The SPT-3G detectors could have been fabricated with time constants several times faster

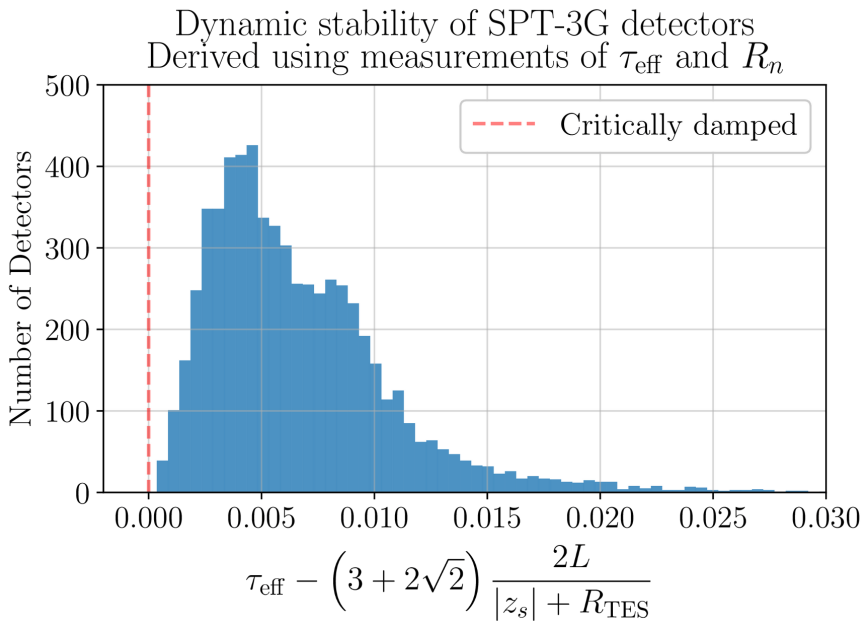

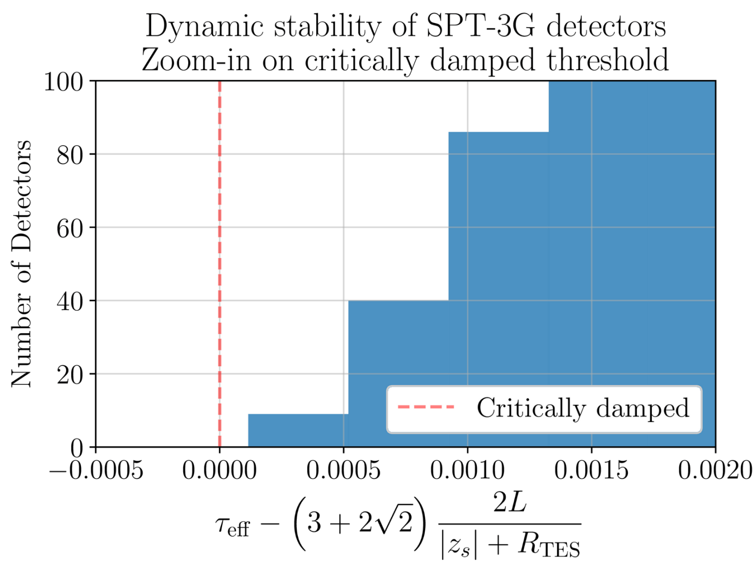

Figure 6.14: The SPT-3G focal plane operates entirely in the over-damped regime, and therefore meets the requirements for dynamic stability. The proximity of the extremum of the distribution to the critically damped threshold is shown in the lower plot, and is likely indicating that a small number of detectors in the array are inoperable in part because they violate this stability criterion. Detectors at this extremum of the distribution are the result of outliers in τ_{eff}. None of these detectors will exhibit under-damped behavior at any typical operating R_{frac} (Figure 6.16).

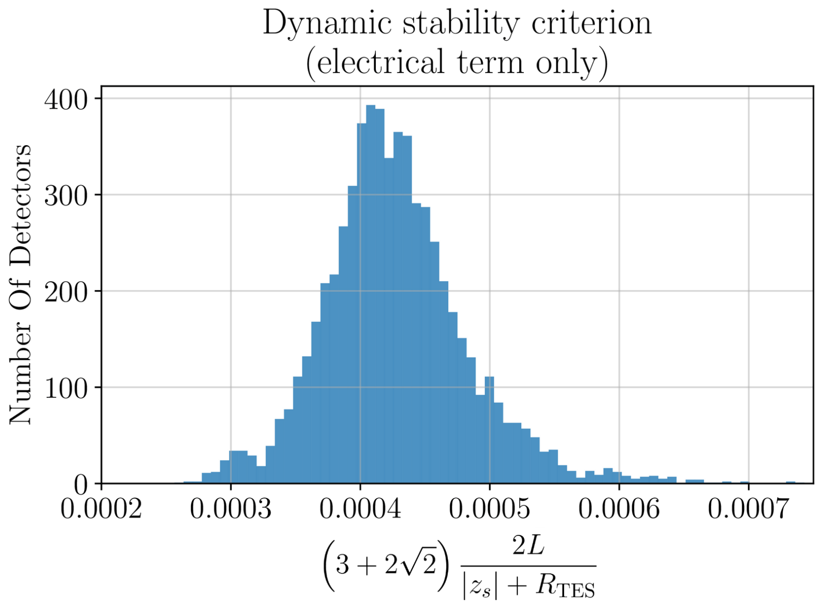

Figure 6.15: The dynamic stability criterion balances the effective detector time constant (τ_{eff}) with the dynamic properties of the electrical filter. Of these, τ_{eff} is significantly larger than the electrical stability term, and so the distribution of stability is strongly coupled to the underlying detector time constants, and not very sensitive to the choice of operating resistance (Figure 6.16).

than the median value (Figure 6.17). The primary barrier for faster detectors in an fMUX system is not presently the additional fMUX electrical stability constraints. Rather, it is control in the spread of the detector thermal time constants (τ_0) and loopgain ($\mathcal{L}$) in the fabrication process, and the series resistance in the cryogenic electronics (z_s) that modifies τ_0. In the case of SPT-3G, variations in z_s account for $\sim 50\%$ of the variation in τ_{eff}, while the underlying τ_0 varies by factors of several across the focal plane. Improved control over τ_{eff} could yield detectors as fast as a millisecond, which still remain stably-operable in an SPT-3G-like instrument (Figure 6.18).

6.5 SPT-3G CROSSTALK PERFORMANCE

In Section 5 I presented a new model for crosstalk in DfMUX systems. This built on previous work in Dobbs et al., 2012 [26], but is extended to include crosstalk cancellation and account for parasitic impedances intrinsic to the DfMUX system. These effects are substantial, in large part because of the higher operating frequencies of modern DfMUX.

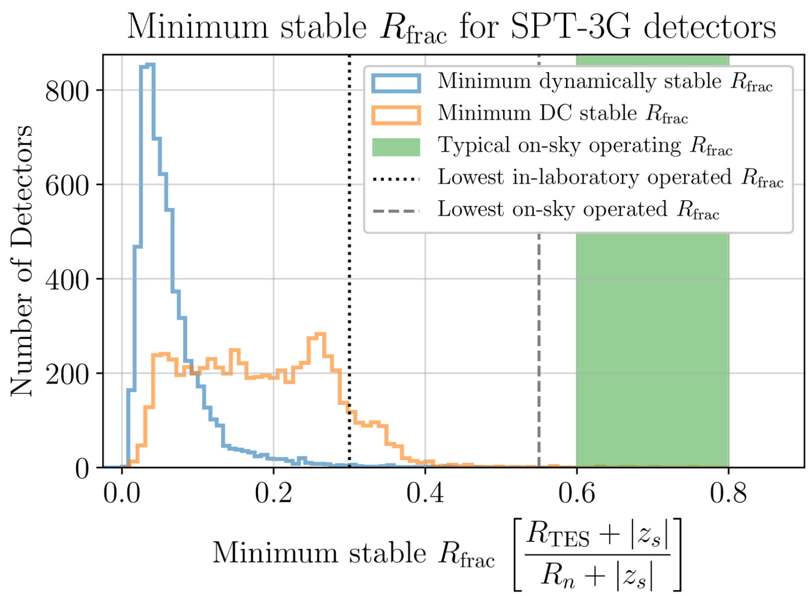

Figure 6.16: We typically prefer to operate at higher R_{frac} to avoid the instability issues experienced earlier during the 2017 engineering run. The actual operating point can vary by up to 10% with changes in radiative loading over the course of an observation. Operating points therefore must have a significant margin with respect to the minimum stable R_{frac}. The above shows the typical operating regime, together with the minimum stable regimes for both the dynamic and DC stability criteria. The SPT-3G detectors have been built with parameters that allow them to be operated well into the stable regime for both criteria.

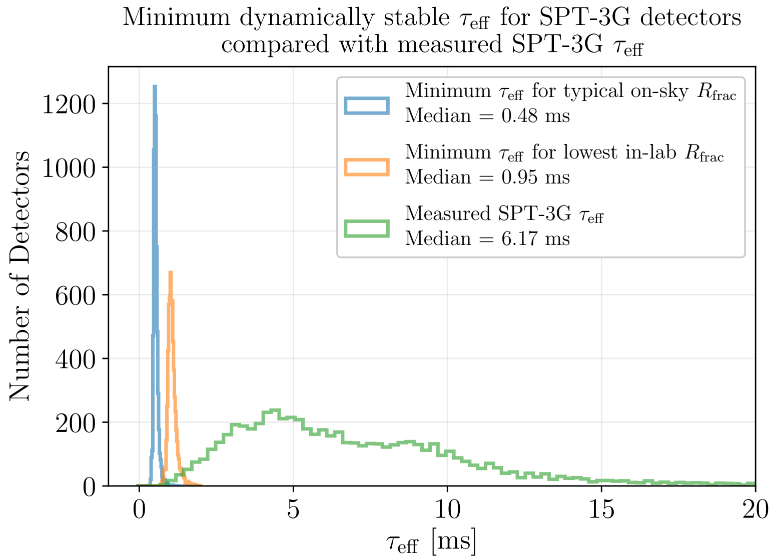

Figure 6.17: The above distributions show the minimum stable τ_{eff}, calculated for different operating points of the SPT-3G detectors, alongside the actual measured τ_{eff} for typical operation. Some detector time constants scatter quite close to the under-damped regime but the vast majority of the focal plane is well within the over-damped regime. The SPT-3G focal plane could therefore tolerate detectors several times faster before encountering dynamic stability issues. The minimum stable effective time constant becomes larger as the operating resistance is reduced; this is a particular challenge for low-resistance detectors.

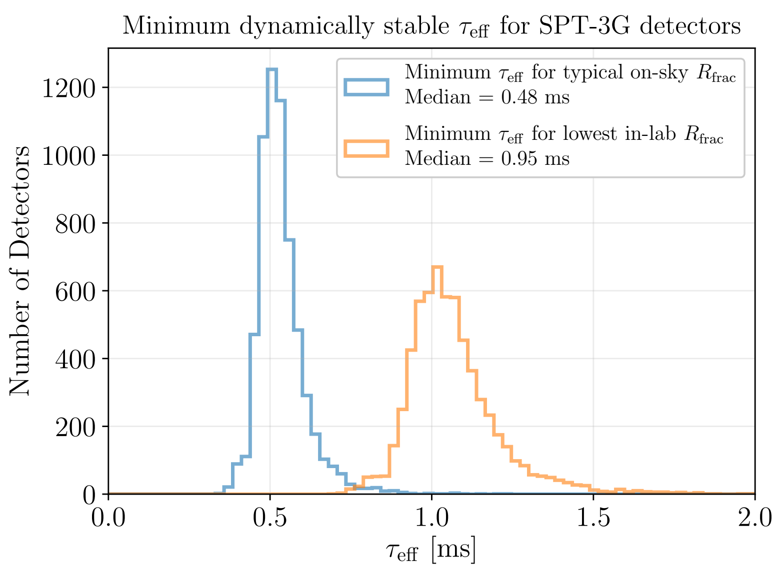

Figure 6.18: The SPT-3G instrument could in principal operate with detectors as fast as τ_{eff} ~1 ms and no other changes. This is currently challenging due to the difficulty in controlling τ_{eff} in detector and cryogenic filter fabrication.

This model can be validated against in situ measurements of crosstalk using observations of bright sky sources with the SPT-3G instrument.[13] Some caveats to this comparison are:

- Measurements of crosstalk derived from observations of the sky include additional sources (such as optical crosstalk due to reflections such as between filters or mirrors in the optics) not captured in the electrical crosstalk model.
- These measurements of crosstalk come with their own systematic uncertainties and limitations. Individual measurement accuracy is limited ($\sigma \sim$0.67%).
- The model relies on the individual measurements of R_n, $|z_0|$, bias frequency, and calculations of additional capacitances to ground within the LC chips for each crosstalk pair. The techniques in Section 6.3 and Section 6.2.5 build up this information, but also carry over their uncertainties.

Despite these limitations, it is a useful comparison to validate that the model can successfully predict end-to-end instrument performance. In Figure 6.19, 17,600 individual measurements of optical crosstalk between detector pairs, and corresponding pairs of simulated crosstalk for the same detectors, are binned by equal weight and plotted with error bars that represent statistical contributions to the errors only. At frequency separations that are much larger than the designed minimum spacing (the low crosstalk regime) the error bars are likely an underestimate. This is because systematic uncertainties (such as noise bias) in the optical measurements likely exist at the $< 0.1\%$ level. The most constraining comes from the low frequency separation region, but is hampered by a limited data set, as these are made up entirely of low frequency channels that scattered away from the designed schedule to a narrower spacing. Nevertheless, the agreement between the data and model suggest that the system crosstalk is dominated by electrical crosstalk within the cryogenic electronics, and that the analytic model is a good predictor of crosstalk performance with the precision that we typically care about.[14]

13 These optical measurements were performed by Jessica Avva, and the methodology is covered in detail in [12].

14 The SPT-3G target was for median detector crosstalk below 0.5%. We achieve this with a mean measured array crosstalk of ∼0.1% between nearest frequency neighbors.

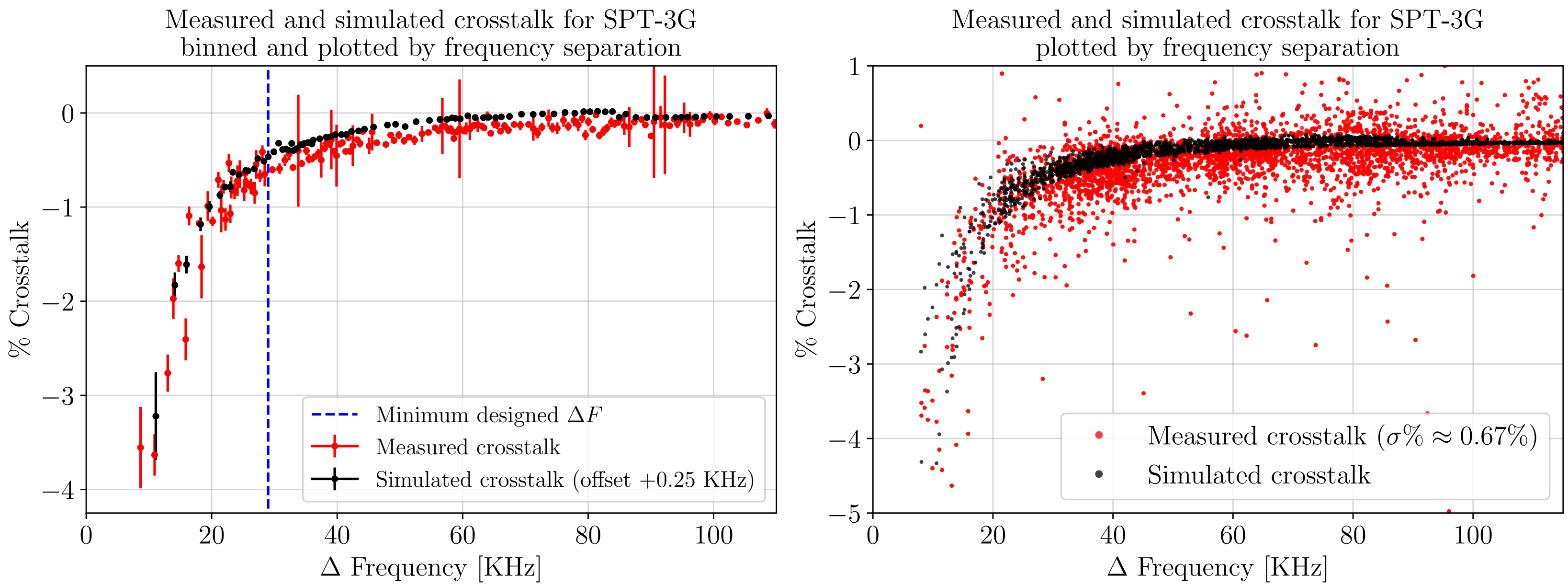

Figure 6.19: Shown above are two comparisons of measured and simulated crosstalk between individual detector pairs. The uncertainty on individual measured points is quite high ($\pm 0.67\%$), and the methods for measuring this optical crosstalk suffer from some systematic biases. For this reason the most constraining regime is the high-crosstalk region with low frequency separations. The binned data (left) uses bins of equal weight, with smaller bins below the designed minimum frequency spacing where there are fewer points. The raw points (right) show a clear bimodal distribution at low frequency spacing that is traced by the simulated crosstalk. In both cases the model correctly follows the main features in the array crosstalk.

Crosstalk is one of the most constrained performance metrics for future instruments targeting detection of primordial B-modes, such as the LiteBIRD satellite experiment. The result of this analysis suggests that we have a reasonable crosstalk model for DfMUX designs at higher multiplexing factors and ∼10 MHz of bandwidth. As demonstrated in Section 5, it is possible to dramatically improve crosstalk performance, even before utilizing crosstalk removal techniques, through the usage of lower resistance detectors, linear frequency scheduling, modest improvements in crosstalk scatter, and slightly lower series inductance to optimize crosstalk cancellation.

6.6 CROSSTALK AND STABILITY PERFORMANCE SUMMARY

Currently the most significant factors that determine the limits of instrument stability and crosstalk performance are control over the detector thermal time constant (τ_0), the series resistance to the TES (z_s), and scatter in the LC resonance frequencies (σF). In the above sections I introduced a model that explains the observed dominant source of z_s and σF through physical defects on the cryogenic lithographic filters. This model describes the phenomenology of both measured parameters, as well as indicates simple design changes to existing technology that would significantly mitigate these (such as increased trace widths in the lithographic etch, and a linear frequency scheduling). I additionally show that although the SPT-3G detector time constants are extremely conservative, an improvement in this without compromising stability will require more precise fabrication methods.

7 SPT-3G NOISE

An expectation value for DfMUX readout noise can be calculated by identifying uncorrelated broadband white noise contributions throughout the signal chain, referring them all back to a specific point in the system, and calculating their quadrature sum. In radio telescopes the system noise is commonly expressed as a Noise Equivalent Temperature ("NET," typically in units of $\mu K\sqrt{s}$ [1]), such that the point of reference chosen for the individual noise contributions is the temperature of a black-body emitter that would produce the equivalent signal power. This metric is also useful for TES-based CMB instruments when characterizing the telescope noise as a whole, but it is less useful for evaluating the readout-specific noise. This is because the readout noise is independent of detector responsivity, which parameterizes how a change in deposited power on the TES is converted to a change in current through the readout. A noise specification given in NET, or even as an electrical Noise Equivalent Power incident on the TES ("NEP," typically expressed in $\frac{\mathrm{aW}}{\sqrt{\mathrm{Hz}}}$), is insufficiently constraining to evaluate readout noise performance, because it is largely determined by the detector responsivity. Instead we choose to refer noise to a current at the SQUID summing junction ("NEI," Noise Equivalent Current, typically expressed in $\frac{\mathrm{pA}}{\sqrt{\mathrm{Hz}}}$); and contextualize this in terms of the *fractional increase in total noise* due to the readout electronics,

$$\text{Fractional Noise Increase} = \frac{\mathrm{NEI}_{\mathrm{total}}}{\mathrm{NEI}_{\mathrm{non\ readout}}}\,. \tag{7.1}$$

NEI at the SQUID summing junction assesses readout system noise independent of detector or telescope parameters, and the fractional noise increase is a metric for the overall readout performance in the context of the instrument. As we shall see, for the same NEI there are detector and cryogenic architectural choices that can result in dramatically worse overall noise performance.

In Section 7.1 I catalog the individual readout noise contributions at their source. Each of these is modified by an interaction with the cryogenic circuit, Digital Active Nulling (DAN), the sinusoidal voltage bias, or a combination of the three. These transfer functions must

1 Equivalent to a noise power per unit bandwidth, the convention to use $\sqrt{s}$ rather than $\frac{1}{\sqrt{\mathrm{Hz}}}$ is more utilitarian for astronomers, who often want to determine the total noise noise as a function of observing time.

be accounted for in order to refer each noise source to an NEI at the SQUID summing junction. In Section 7.2 and Section 7.3 I describe these transfer functions, validate them using SPT-3G data, and construct a complete noise and circuit model. In Section 7.4 that model is compared against measured instrument noise. In Section 7.5, Section 7.6, and Section 7.7, I present an interpretation of the results, including the interaction with detector responsivity and the overall readout performance.

7.1 INDIVIDUAL READOUT NOISE SOURCES

Processes that generate uncorrelated broadband noise[2] in the DfMUX system include:

- Thermal Johnson-Nyquist noise from ohmic components ("Johnson noise" hereafter).
- Intrinsic voltage and current noise from operational- or instrumentational- amplifiers used in the non-cryogenic electronics.
- Intrinsic Digital-to-Analog Converter (DAC) output noise or Analog-to-Digital Converter (ADC) input noise.
- Quantization (Digitization) noise as a result of the finite number of bits used in the ADC (DAC).
- Intrinsic SQUID noise (related to Johnson noise from ohmic components internal to the SQUID).

Individual sources are categorized, according to their location in the signal path, as *carrier-chain* sources (Table 7.1), *nuller-chain* sources (Table 7.2), *demodulator-chain* sources (Table 7.3), or sources from cryogenic elements (Table 7.4).

7.2 TRANSFER FUNCTIONS

Each noise source is referred to an NEI at the SQUID summing junction using the appropriate transfer function. All transfer functions can be derived from an analytic circuit model, and

2 Broadband noise sources are the biggest concern. Narrow-band noise such as RFI contamination can be mitigated. A discussion of narrow-band noise lines, RFI, and the steps employed to mitigate them, are given in Appendix C.

Individual Carrier Chain Noise Sources

Source	Notes	Location	Noise at location	Noise at reference [(a)]
DAC	Intrinsic [(b)]	DAC output	50 $\frac{\text{pA}}{\sqrt{\text{Hz}}}$	1.1 $\frac{\text{pA}}{\sqrt{\text{Hz}}}$
Amplifiers	Combined total [(c)]	DAC output	34 $\frac{\text{pA}}{\sqrt{\text{Hz}}}$	0.8 $\frac{\text{pA}}{\sqrt{\text{Hz}}}$
Quantization	Calculated [(d)]	DAC output	14 $\frac{\text{pA}}{\sqrt{\text{Hz}}}$	0.3 $\frac{\text{pA}}{\sqrt{\text{Hz}}}$
Johnson	When $R_{\text{bias}} << R_{\text{TES}}$ [(e)]	Across comb	0.3 $\frac{\text{pV}}{\sqrt{\text{Hz}}}$	0.2 $\frac{\text{pA}}{\sqrt{\text{Hz}}}$

(a) Average value during operation when referred to the SQUID summing junction using SPT-3G transfer functions. This is covered in more detail in Section 7.2.

(b) LTC1668IG (Linear Technology Corporation, Datasheet 666/7/8 G05) .

(c) In the design used on SPT-3G there are two amplification stages following the DAC:

1st **Stage**: 2x LT6231CS8 (Linear Technology Corporation, Datasheet 623012fc)

Configured with as a differential transimpedance amplifier with transimpedance $R_{\text{f,1st}}$=300 Ω

Noise from the datasheet: $e_{\text{amp,1st}} = 1.1 \frac{\text{nV}}{\sqrt{\text{Hz}}}$ and $i_{\text{amp,1st}} = 2.2 \frac{\text{pA}}{\sqrt{\text{Hz}}}$.

Total output voltage noise:

$$e_{\text{out,1st}} = \sqrt{2} \cdot \sqrt{e^2_{\text{amp,1st}} + (i_{\text{amp,1st}} \cdot R_{\text{f,1st}})^2 + 4k_b \cdot 300\,\text{K} \cdot R_{\text{f,1st}}} = 3.6 \ \frac{\text{nV}}{\sqrt{\text{Hz}}}$$

Referred to the DAC output:

$$i_{\text{DAC,1st}} = \frac{e_{\text{out,1st}}}{R_{\text{f,1st}}} = 12.1 \frac{\text{pA}}{\sqrt{\text{Hz}}}$$

2nd **Stage**: THS4131IDGNR (Texas Instruments, Datasheet SLOS318I, Revised August 2015)

Gain is set by $R_{\text{f,2nd}}$=200 Ω and R_g=300 Ω, and there is an input resistance of R_{in}=250 Ω.

Therefore,this differential amplifier is configured with a gain of 2/3:

Noise from the datasheet: $e_{\text{amp,2nd}} = 1.3 \frac{\text{nV}}{\sqrt{\text{Hz}}}$ and $i_{\text{amp,2nd}} = 1 \frac{\text{pA}}{\sqrt{\text{Hz}}}$.

Johnson noise at the output:

$$e_{\text{Johnson,2nd}} = 5.8 \ \frac{\text{nV}}{\sqrt{\text{Hz}}}$$

Voltage noise at the output due to amplifier voltage noise:

$$e_{\text{amp voltage,2nd}} = e_{\text{amp,2nd}} \frac{R_{\text{f,2nd}} + R_g}{R_g} = 2.2 \ \frac{\text{nV}}{\sqrt{\text{Hz}}}$$

Voltage noise at the output due to amplifier current noise:

$$e_{\text{amp current,2nd}} = i_{\text{amp,1st}} \cdot \sqrt{2}(R_{\text{f,2nd}} + R_{\text{in}} + \frac{R_{\text{f,2nd}} R_{\text{in}}}{R_g}) = 0.87 \ \frac{\text{nV}}{\sqrt{\text{Hz}}}$$

Total output voltage noise:

$$e_{\text{out,2nd}} = \sqrt{e^2_{\text{Johnson,2nd}} + e^2_{\text{amp voltage,2nd}} + e^2_{\text{amp current,2nd}}} = 6.3 \ \frac{\text{nV}}{\sqrt{\text{Hz}}}$$

Referred to the DAC output:

$$i_{\text{DAC,2nd}} = \frac{e_{\text{out,2nd}}}{R_{f,1} \frac{R_{f,2}}{R_g}} = \frac{e_{\text{out,2nd}}}{200} = 31.3 \frac{\text{pA}}{\sqrt{\text{Hz}}}$$

Total amplifier noise at the DAC output = $\sqrt{i^2_{\text{DAC,1st}} + i^2_{\text{DAC,2nd}}} = 34 \frac{\text{pA}}{\sqrt{\text{Hz}}}$

(d) The DAC uses 16 bits, has 10 mA peak-to-peak output, over 10 MHz of bandwidth:

Quantization Noise = $\frac{1}{\sqrt{12}} \frac{\text{LSB}_{\text{p-p}}}{\sqrt{\text{BW}}}$ [5].

(e) For SPT-3G, $R_{\text{bias}} = 30\,\text{m}\Omega$ and $R_{\text{n}} = 2\,\Omega$.

Table 7.1: Individual broadband readout noise contributions within the carrier chain signal path. Table 7.5 shows how to convert these to expected NEI at the SQUID summing junction.

Individual Nuller Chain Noise Sources

Source	Notes	Location	Noise at location	Noise at reference [a]
DAC	Intrinsic [b]	DAC output	50 $\frac{\text{pA}}{\sqrt{\text{Hz}}}$	2.3 $\frac{\text{pA}}{\sqrt{\text{Hz}}}$
Amplifiers	Combined total [c]	DAC output	34 $\frac{\text{pA}}{\sqrt{\text{Hz}}}$	1.6 $\frac{\text{pA}}{\sqrt{\text{Hz}}}$
Quantization	Calculated [d]	DAC output	14 $\frac{\text{pA}}{\sqrt{\text{Hz}}}$	0.7 $\frac{\text{pA}}{\sqrt{\text{Hz}}}$
Current Stiffening Johnson	$\sqrt{\frac{4k_b \cdot 300\,\text{K}}{3\,\text{k}\Omega}}$ [e]	Summing junction	2.35 $\frac{\text{pA}}{\sqrt{\text{Hz}}}$	3.3 $\frac{\text{pA}}{\sqrt{\text{Hz}}}$
SQUID Flux Bias Johnson	$\sqrt{\frac{4k_b \cdot 300\,\text{K}}{20\,\text{k}\Omega}}$	Summing junction	0.9 $\frac{\text{pA}}{\sqrt{\text{Hz}}}$	1.3 $\frac{\text{pA}}{\sqrt{\text{Hz}}}$
Low Frequency Feedback Johnson	$\sqrt{\frac{4k_b \cdot 300\,\text{K}}{20\,\text{k}\Omega}}$	Summing junction	0.9 $\frac{\text{pA}}{\sqrt{\text{Hz}}}$	1.3 $\frac{\text{pA}}{\sqrt{\text{Hz}}}$
Signal Path Johnson	Total combined	Summing junction	0.6 $\frac{\text{pA}}{\sqrt{\text{Hz}}}$	0.9 $\frac{\text{pA}}{\sqrt{\text{Hz}}}$

[a] Average value during operation when referred to the SQUID summing junction using SPT-3G transfer functions. This is covered in more detail in Section 7.2.

[b] See note in Table 7.1.

[c] See note in Table 7.1.

[d] See note in Table 7.1.

[e] Notice the outsized contribution here. These are output resistors used to stiffen the nuller current. They are a good candidate to move to the 4 Kelvin stage to improve noise performance.

Table 7.2: Individual broadband readout noise contributions within the nuller chain signal path. These share many of the same elements as the carrier-chain path (Table 7.1), but with additional Johnson noise due to large resistances used to stiffen current signals going into the cryostat (either for DAN, to provide the SQUID flux bias, or as low frequency feedback to that flux bias). Table 7.6 shows how to convert these to expected NEI at the SQUID summing junction.

Individual Demodulation Chain Noise Sources

Source	Notes	Location	Noise at location	Noise at reference [(a)]
SQUID I_{bias} Johnson	$4.22\,\text{k}\Omega$	SQUID I_{bias} input	$8.36\ \frac{\text{nV}}{\sqrt{\text{Hz}}}$	$4.9\ \frac{\text{pA}}{\sqrt{\text{Hz}}}$
1st Stage Amplifier (Current)	From datasheet [(b)]	SQCB input	$2.2\ \frac{\text{pA}}{\sqrt{\text{Hz}}}$	$5.5\ \frac{\text{pA}}{\sqrt{\text{Hz}}}$
1st Stage Amplifier (Voltage)	From datasheet [(b)]	SQCB input	$1.1\ \frac{\text{nV}}{\sqrt{\text{Hz}}}$	$5.1\ \frac{\text{pA}}{\sqrt{\text{Hz}}}$
Signal path Johnson	Combined total	SQCB input	$0.36\ \frac{\text{nV}}{\sqrt{\text{Hz}}}$	$1.7\ \frac{\text{pA}}{\sqrt{\text{Hz}}}$
ADC	From datasheet [(c)]	SQCB input	$0.23\ \frac{\text{nV}}{\sqrt{\text{Hz}}}$	$1.1\ \frac{\text{pA}}{\sqrt{\text{Hz}}}$
2nd Stage Amplification	Combined total [(d)]	SQCB input	$0.14\ \frac{\text{nV}}{\sqrt{\text{Hz}}}$	$0.7\ \frac{\text{pA}}{\sqrt{\text{Hz}}}$

[(a)] Average value during operation when referred to the SQUID summing junction using SPT-3G transfer functions. This is covered in more detail in Section 7.2.

[(b)] LT6200-5 (Linear Technology Corporation, Datasheet 62001ff) .
This is a low-noise differential amplifier configured with a gain of 17.5.

[(c)] LTC2192 (Linear Technology Corporation, Datasheet 219210f) .
The datasheet quotes a 77dB SNR, with 90dB of spur-free dynamic range.
This includes both digitization noise and input noise.
We use 2 V peak-to-peak input and 10 MHz of bandwidth:

$$e_{\text{ADC}} = \frac{2\,\text{V}}{2\sqrt{2}}\left(10^{\frac{77}{20}}\sqrt{10\,\text{MHz}}\right)^{-1} = 32.2\ \frac{\text{nV}}{\sqrt{\text{Hz}}}$$

There is a gain of 140 between the 1$^{\text{st}}$ Stage Amplifier and the ADC:

$$e_{\text{SQCB input}} = \frac{e_{\text{ADC}}}{140} = 0.23\ \frac{\text{nV}}{\sqrt{\text{Hz}}}$$

[(d)] THS4131ID (Texas Instruments, Datasheet SLOS318I, Revised August 2015) .
This is a fully differential amplifier with $R_{\text{f,2nd}}$=400 Ω, $R_{\text{g,2nd}}$=100 Ω (a gain of 4).
From the datasheet: $e_{\text{amp voltage,2nd}} = 1.3\frac{\text{nV}}{\sqrt{\text{Hz}}}$ and $i_{\text{amp,2nd}} = 1\frac{\text{pA}}{\sqrt{\text{Hz}}}$.
Voltage noise at the input from amplifier current noise):

$$e_{\text{amp current,2nd}} = i_{\text{amp,2nd}}\ \sqrt{\text{Hz}}\cdot\sqrt{2}R_{\text{f,2nd}}) = 0.57\ \frac{\text{nV}}{\sqrt{\text{Hz}}}.$$

Johnson noise from $R_{\text{f,2nd}}$ and $R_{\text{g,2nd}}$:

$$e_{\text{Johnson,2nd}} = \sqrt{2(4k_b\cdot 300\,\text{K}\cdot 100\,\Omega) + 2(4k_b\cdot 300\,\text{K}\cdot \frac{400\,\Omega}{16})} = 2\ \frac{\text{nV}}{\sqrt{\text{Hz}}}.$$

Total 2$^{\text{nd}}$ Stage noise at the 2$^{\text{nd}}$ Stage input:

$$e_{\text{total,2nd}} = \sqrt{e^2_{\text{amp voltage,2nd}} + e^2_{\text{amp current,2nd}} + e^2_{\text{Johnson,2nd}}} = 2.5\ \frac{\text{nV}}{\sqrt{\text{Hz}}}.$$

Total 2$^{\text{nd}}$ Stage noise at the 1$^{\text{st}}$ Stage input:

$$\frac{e_{\text{total,2nd}}}{17.5} = 0.14\ \frac{\text{nV}}{\sqrt{\text{Hz}}}.$$

Table 7.3: Individual broadband readout noise contributions within the demodulation chain signal path. A large SQUID dynamic impedance will drive the 1st Stage Amplifier Current noise to dominate these contributions. Table 7.7 shows how to convert these to expected NEI at the SQUID summing junction.

Individual Cryogenic Readout Noise Sources

Source	Notes	Location	Noise at location	Noise at reference [(a)]
SQUID	Estimated [(b)]	Summing junction	$3\ \frac{\mathrm{pA}}{\sqrt{\mathrm{Hz}}}$	$8.2\frac{\mathrm{pA}}{\sqrt{\mathrm{Hz}}}$
TES Johnson [(c)]	$\sqrt{\frac{4k_b \cdot 450\,\mathrm{mK}}{R_{\mathrm{TES}}}}$	Summing junction	$\frac{5}{\sqrt{R_{\mathrm{TES}}}}\frac{\mathrm{pA}}{\sqrt{\mathrm{Hz}}}$	$4.7\ \frac{\mathrm{pA}}{\sqrt{\mathrm{Hz}}}$
Damping Resistor [(d)]	$\approx \sqrt{\frac{4k_b \cdot 350\,\mathrm{mK}}{20\,\Omega}}$	Summing junction	$0.98\ \frac{\mathrm{pA}}{\sqrt{\mathrm{Hz}}}$	$1.4\ \frac{\mathrm{pA}}{\sqrt{\mathrm{Hz}}}$
Wire Harness Resistance [(e)]	$\approx \sqrt{4k_b \cdot 300\,\mathrm{K} \cdot 10\,\Omega}$	SQCB input	$0.4\ \frac{\mathrm{nV}}{\sqrt{\mathrm{Hz}}}$	$1.9\ \frac{\mathrm{pA}}{\sqrt{\mathrm{Hz}}}$
Bias Resistor Johnson	$\sqrt{4k_b \cdot 4\,\mathrm{K} \cdot 30\,\mathrm{m}\Omega}$	Across comb	$2.6\ \frac{\mathrm{nV}}{\sqrt{\mathrm{Hz}}}$	$1.7\ \frac{\mathrm{pA}}{\sqrt{\mathrm{Hz}}}$

(a) Average value during operation when referred to the SQUID summing junction using SPT-3G transfer functions. This is covered in more detail in Section 7.2.
(b) The expected SQUID noise is poorly constrained, but fits to measured noise data agree with this estimate, originally provided from NIST.
(c) This is only relevant when evaluating overbiased or unbiased noise. When the TES is in the transition the TES Johnson noise is suppressed by electro-thermal feedback.[26]
(d) This is a resistor in parallel with the comb to stabilize the SQUID (similar to the action of the low-pass filter described in Section 6.1.1).
(e) The extremely thin wires that provide a thermally isolated connection between the 300K and 4K electronics incur some series resistance.

Table 7.4: Individual broadband readout noise contributions within the cryogenic portion of the readout chain. Table 7.8 shows how to convert these to expected NEI at the SQUID summing junction.

a subset of these can also be measured directly for each individual readout channel. The analytic model captures all relevant electrical properties of the system, and is based on explicit measurements of, or calculations for, each parameter. The model is validated using comparisons with the quantities that can be directly measured, and with the end-to-end measured noise. Although the parameters shown in Figure 7.1 reflect the SPT-3G instrument, the model itself is general and can be deployed to forecast performance of future readout designs, as in Chapter 8 for the LiteBIRD instrument. The full circuit model is shown in Figure 7.1.

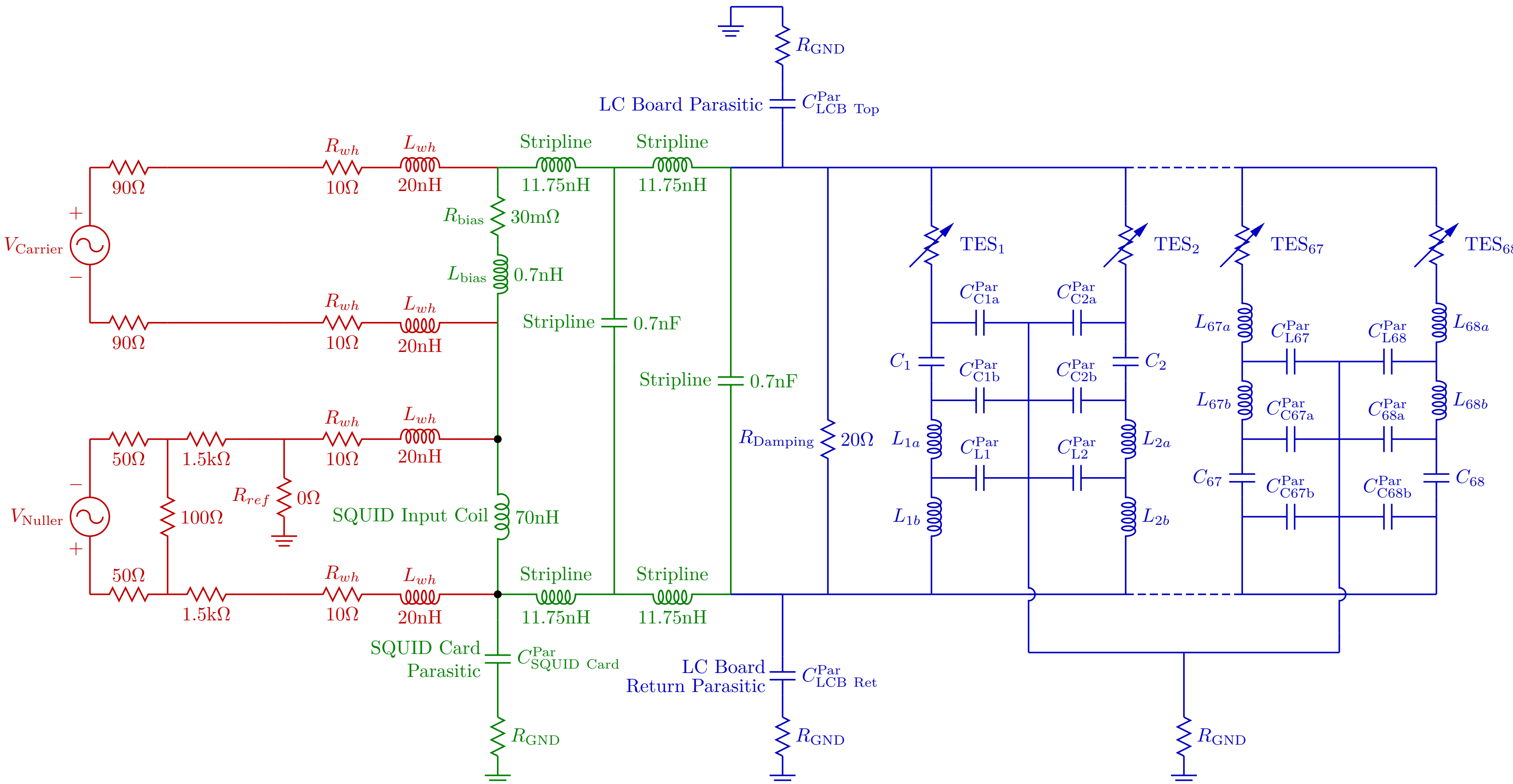

Figure 7.1: Above is the electrical model of the signal chain used in simulating the transfer functions. Red corresponds to electronics at room temperature through to the wire-harness. Green corresponds to electronics at the 4K stage through to the striplines, and blue indicates electronics at the sub-Kelvin stage. This above representation does not include the initial amplification or filtering common to both the carrier and nuller DAC outputs, which is applied separately. The C^{par} values are calculated from the lithography geometries, and the resonator values come from Sonnet simulations of the resonator designs. The additional parasitics to ground are constrained by measurement only at the $\sim$0.5 nF level and come from combinations of measurements and calculations based on the PCB geometries. R_{GND} is typically low impedance. Channels 1 & 2 demonstrate the LCR configuration, while Channels 67 & 68 demonstrate the CLR configuration.

7.2.1 *Cryogenic capacitances to ground*

Until now we've considered the lithographic filters as simple lumped-element components, but this overlooks a significant complexity: the 2D lithographic filter elements have sufficient area to act as parallel plate capacitors to a ground plane beneath the LC chip. This capacitance is calculated as a simple parallel plate capacitor:

$$C_{\text{par}} = \frac{k\epsilon_0 A}{D}\,, \tag{7.2}$$

where ϵ_0 is the permittivity of free space; $k = 11.68$ is the relative permittivity of the silicon wafer between the lithographic structure and ground plane; A is the surface area of the metalized portions of the 2D structures; and D=675 µm, the thickness of the silicon wafer between the lithographic component and ground plane. The inductor footprint and resulting ∼1.28 pF capacitance is constant for every resonator; but the capacitor geometry changes substantially, yielding a resonator-frequency dependent capacitance to ground as shown in Figure 7.2. These capacitances add additional current paths that can bypass the TES and/or

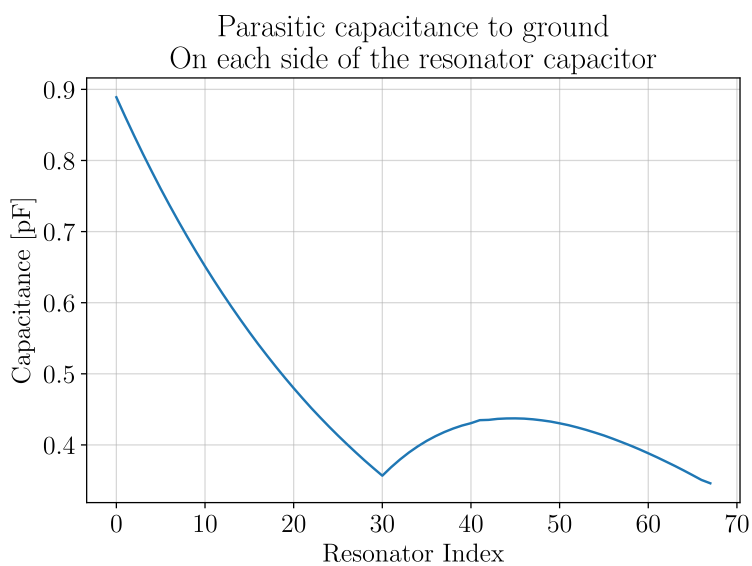

Figure 7.2: Capacitance to ground due to the solid surface area on each side of the inter-digitated capacitor footprints. This includes bond-pads but not the trace lengths from the chip edges to the resonators. The geometry of the lithographic inductors doesn't change as a function of resonator, so the associated parasitic capacitance to ground from those elements is a constant ∼1.28 pF.

SQUID, and modify the filter resonances. This is significant in two ways:

1. Voltage applied across the cryogenic network at the resonance frequency is divided down by the capacitive reactance to ground, rather than being applied across the TES directly.

2. Some of the current through the TES is not accounted for in the measured current at the SQUID summing junction.

This effect is compounded by the relative ordering of the filter components. SPT-3G uses a design that alternates the ordering of the inductor-capacitor pairs, such that some cryogenic network legs are ordered in series, TES-Inductor-Capacitor-SQUID, and others are TES-Capacitor-Inductor-SQUID. This is done to minimize the total LC chip size, while maintaining a checkerboard pattern to prevent inductive coupling between inductor structures. The resulting design can be seen in the chip layout in Figure 7.3. The schematic diagram of both configurations is shown in the full circuit model in Figure 7.1.

These capacitances alter the circuit in such a significant way that the component ordering is readily identifiable within SPT-3G data (Figure 7.16).[3] Figure 7.4 shows two simulations of the cryogenic readout circuit admittance with, and without, these calculated parasitic capacitances. The discontinuous changes in admittance follow the CL/LC ordering changes in the filter design. Note how variable the impedance of the network appears depending on these configurations, despite the fact that each leg is simulated here with exactly $2\,\Omega$ of real resistance.

7.2.2 *Demodulation chain transfer function*

The demodulation chain transfer function converts between a voltage at the ADC and current at the input of the SQUID coil. Following the diagram in Figure 7.5, this can be broken down further into:

3 This effect was first noted by Daniel Dutcher, and described in Dutcher et al., 2018 [31]. Daniel's work showed that empirically scaled capacitances within the filter elements could explain the variation between in situ measurements of the TES resistance, and independent 4-wire measurements of TES samples. My contribution to this work is in *deriving* these capacitances, and other previously undescribed parasitic elements, and assembling this with existing measured data to create a complete readout circuit model and set of transfer functions. Daniel's original memo, and the corresponding code he shared, was invaluable in doing this.

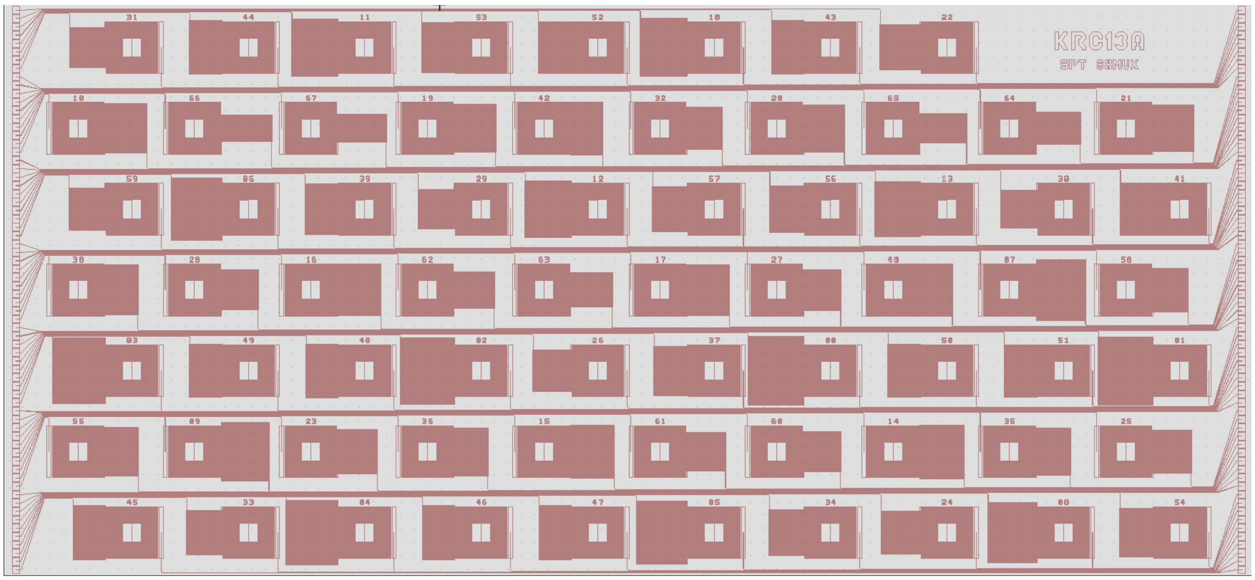

(a) The 2D layout geometry for a single 68x LC Chip is shown above.

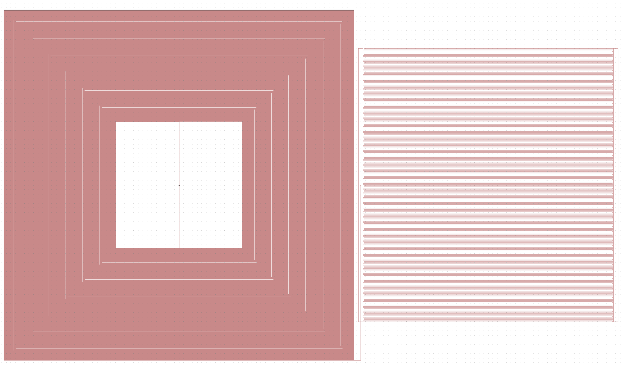

(b) A single resonance of an LC Chip: spiral inductor on the left and interdigitated capacitor on the right.

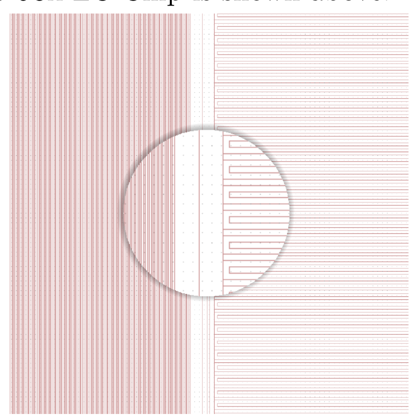

(c) Zoom-in of the element in (b) with the inductor (left) and capacitor (right).

Figure 7.3: The 2D layout of one LC Chip design used in the SPT-3G receiver. Parasitic capacitance forms between the surface of these elements and the ground plane below as well as the grounded shield above the lithographic elements. Layout file used to generate these images by Gavin Noble.

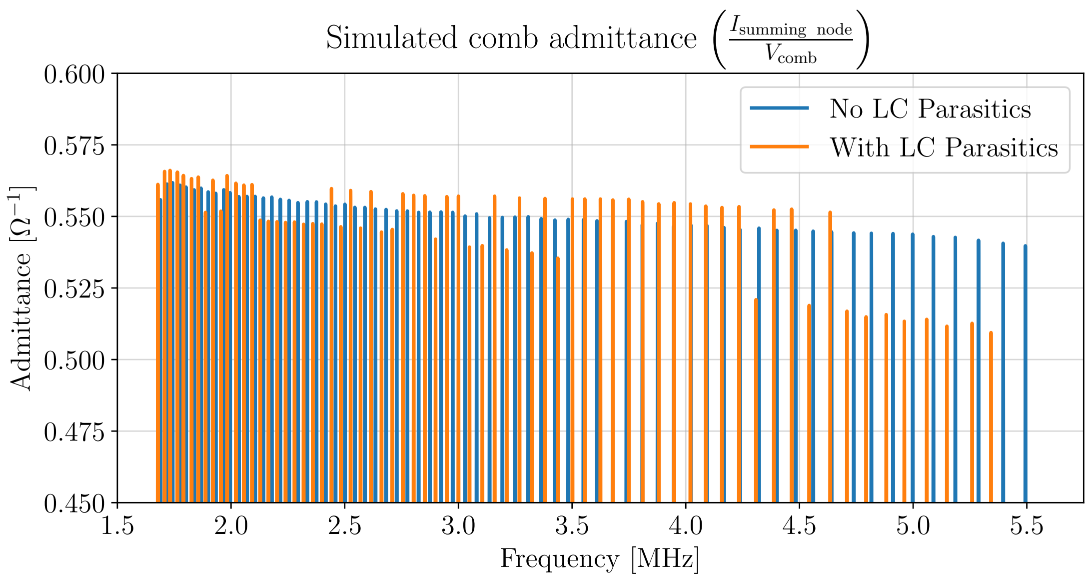

Figure 7.4: Above are simulations of the admittance of the cryogenic portion of the circuit with and without the parasitic capacitances. The steps up and down in network impedance reflect alternations in LCR and CLR ordering (also evident in Figure 7.16). These simulations use $2\,\Omega$ detectors for every channel, and the admittances greater than 0.5 everywhere reflect the fact that the parallel paths through the network legs lower the overall impedance of the network.

1. $H_{\text{adc}} = \dfrac{V_{\text{adc}}}{V_{\text{amp}}}$, a warm segment that converts between the 1st stage amplifier input voltage and a voltage at the ADC. This consists of a gain of 140 and slight RF filtering with a 3dB point at 10 MHz. This conversion has already been applied in the demodulation chain noise sources in Table 7.3.

2. $Z_{\text{trans}} = \dfrac{i_{in}}{V_{\text{SQUID}}}$, the SQUID transimpedance, measured in situ as detailed in Section 4.4.1.

3. $\chi_{\text{output}} = \dfrac{V_{\text{Amp}}}{V_{\text{SQUID}}}$, a low-pass filter within the wire-harness that attenuates V_{Amp} relative to V_{SQUID}. This is generated by the interaction between the SQUID dynamic impedance (Z_{dyn}) and a parallel capacitance within the wire-harness (C_{wh}), and has a cutoff frequency given by $f_c \sim \dfrac{1}{2\pi Z_{\text{dyn}} C_{\text{wh}}}$.

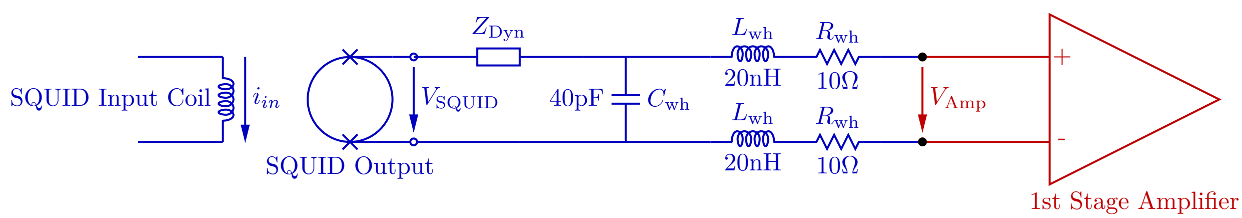

Figure 7.5: The cryogenic portion of the demodulation signal path is shown here in blue. An important interaction is between C_{wh} and Z_{dyn}, which form a low-pass filter that shorts out high frequency voltages before they can be recorded by the 1st stage amplifier input.

χ_{output} becomes a weaker filter if the SQUID dynamic impedance is low, as demonstrated in Figure 7.6. Noise sources in the demodulation signal chain are referred to an NEI at the SQUID input coil by dividing by χ_{output}, which is the primary reason why we see a noise improvement when operating SQUIDs at lower Z_{dyn}. Figure 7.7 shows χ_{output} across the entire SPT-3G receiver.

7.2.3 *Carrier transfer function*

The relevant carrier transfer functions are:

1. $H_c^{\text{Vcomb}} = \frac{V_{\text{comb}}}{I_{\text{DAC, carrier}}}$, the conversion between carrier DAC output current and a voltage across the cryogenic filter network.

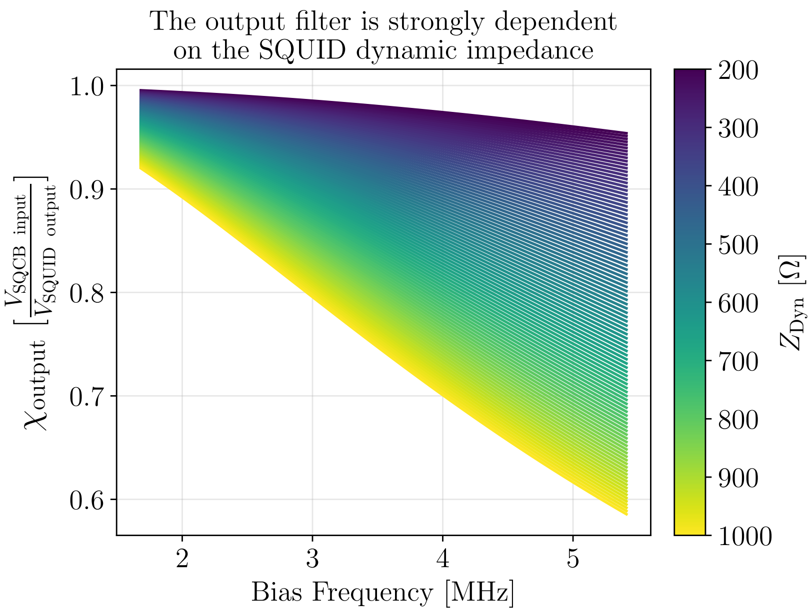

Figure 7.6: An analytic calculation of the output filter (χ_{output}) as a function of SQUID dynamic impedance (Z_{dyn}). Noise sources in the demodulation signal chain are referred to an NEI at the SQUID input coil by dividing by χ_{output}, and therefore appear *amplified* by this filter when referred to an NEI at the SQUID summing junction. This is the primary reason why a lower dynamic impedance improves the system noise.

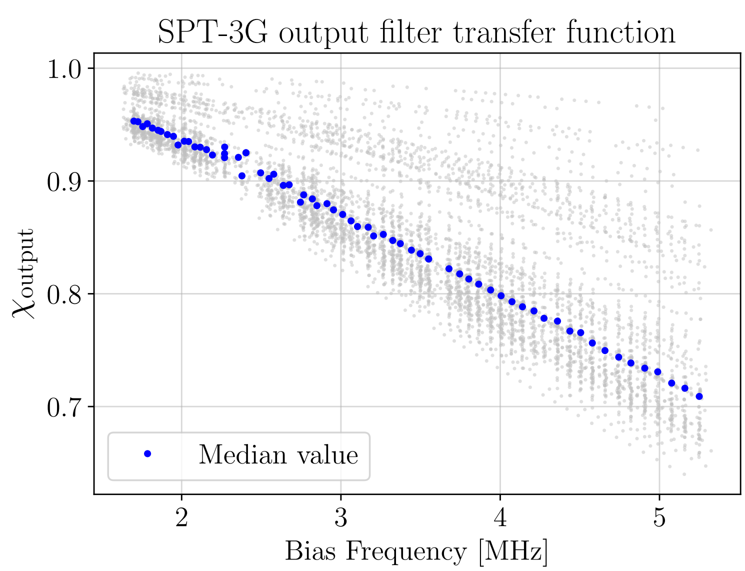

Figure 7.7: Shown here are measurements of χ_{output} for every channel in the SPT-3G receiver, and a synthesized median comb in blue with a dynamic impedance of 743 Ω. Although there are 6 SQUIDs in the SPT-3G receiver operated at low dynamic impedance, the vast majority of the SPT-3G SQUIDs have high dynamic impedance, and thus suffer from increased noise and a strong output filter.

2. $H_c^{\text{Vtes}} = \frac{V_{\text{tes}}}{I_{\text{DAC, carrier}}}$, the conversion between carrier DAC current to voltage across *the individual TES.*

3. $H_c^{\text{I}} = \frac{I_{\text{SQUID Summing Node}}}{H_c^{\text{Vcomb}}}$, the conversion between voltage across the comb and an induced current at the SQUID summing junction.

The model-derived transfer functions for each of these are shown in Figures 7.8, and 7.9.

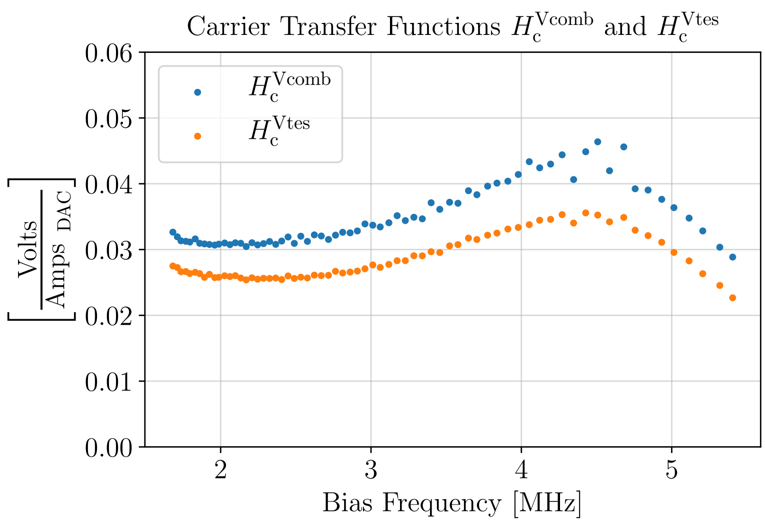

Figure 7.8: The dominant feature in the carrier transfer functions comes from an anti-imaging filtering at the output of the DAC. This filter is required to roll off steeply to shield the subsequent amplifiers from high frequency image tones, which would exceed the slew rate limitations of the amplifiers and generate non-linearities. The chosen filter architecture produces a frequency dependent structure with a peak near 4.5 MHz.

7.2.4 *Nuller transfer function*

The nuller transfer function converts a current at the DAC output to a current at the SQUID summing junction ($H_n = \frac{I_{\text{SQUID Summing Junction}}}{I_{\text{DAC, nuller}}}$). This is the simplest of the transfer functions, and is determined entirely by non-cryogenic elements: the 3 kΩ “stiffening resistors” seen in Figure 7.1 prevent impedances in the cryogenic circuit from effecting the total delivered current at the summing junction.

When DAN is operating, any modulation of current through the TES (including sky signal or noise) produces a current at the SQUID summing junction, which DAN cancels with an

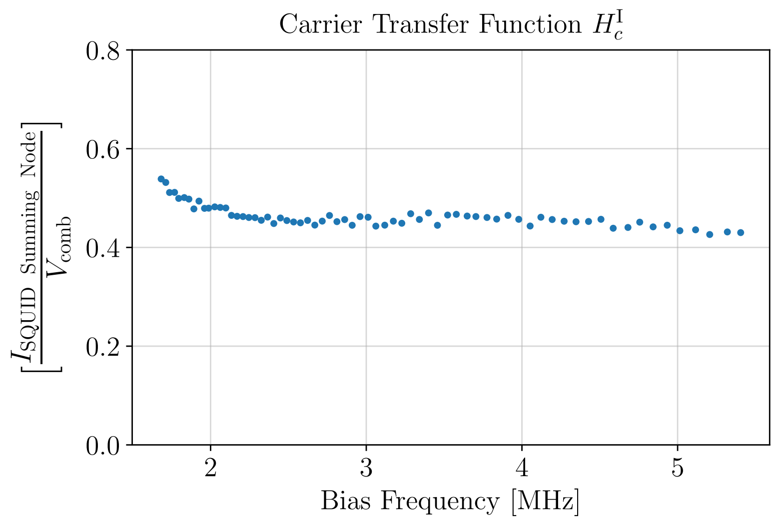

Figure 7.9: The transfer function that converts from voltage across the comb at the detector bias frequencies to a current at the SQUID input coil is required to generate noise expectations. This is calculated above for $R_{\text{TES}} = R_n$, and is nearly just a division by $R_{\text{TES}} + R_s$, but has some frequency dependence owing to the tighter frequency resonance spacing at low frequencies (where the comb appears lower impedance in due to the parallel paths), and the parasitic capacitances.

inverse copy. In this way, the waveform produced by DAN is a measurement of the current *at the summing junction,* and H_n is sufficient to recover that value. This is a strength of the DfMUX design – the transfer function required to understand the data is also the simplest to compute and the least variable. H_n is shown in Figure 7.10, and the frequency-dependent structure is primarily result of the anti-imaging and RF filtering (identical to those used in the carrier signal path).[4] Note that the current *at the SQUID summing junction* is distinct from *current through the SQUID input coil* because there are several paths through which current may flow across the junction. The transfer function for the latter is more complicated, and is detailed in Section 7.2.5.

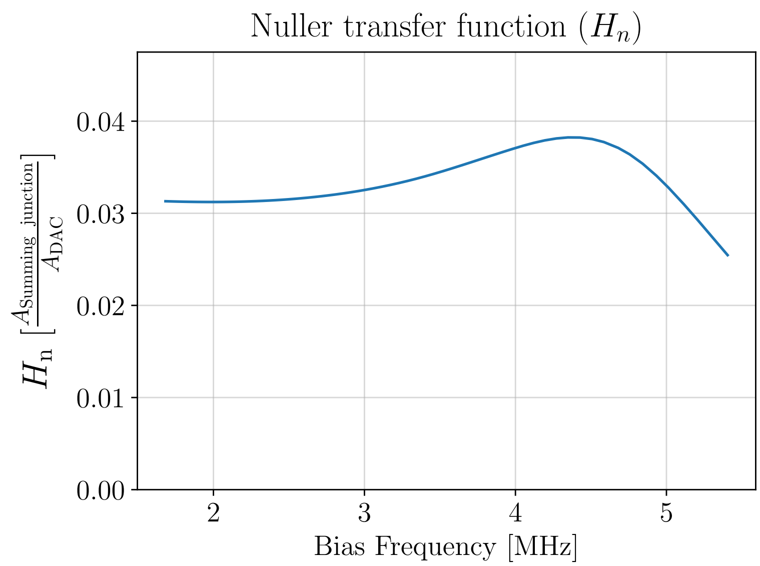

Figure 7.10: The nuller transfer function converts current at the DAC output to a current at the summing junction of the SQUID. This transfer function is invariant to the cryogenic electronics. Like the carrier transfer function, the peak at 4.5 MHz is a consequence of the anti-image filtering at the DAC output.

4 A quality control procedure applied to all fielded readout electronics guarantees this particular transfer function to within ±10%, which is useful for readout characterization and real-time operation and tuning of the detectors. The offline analysis of science products are not calibrated using this transfer function, and instead use on-sky measurements with each detector before each observation.

7.2.5 *Current sharing transfer function*

Aside from the nuller input, the SQUID summing junction (shown in Figure 7.1) has three distinct parallel legs, only one of which is the SQUID input coil. The other two are:

1. Through the comb, $R_{\text{TES},i} + R_s \approx Z_{\text{net}}(\omega_i) + Z_{\text{com}}(\omega_i)$ (following the approximation from Equation 5.4).

2. Through parasitic capacitances to ground within the cryogenic circuit (with a current return via R_{ref}). Although there are several of these paths, I'll refer to them collectively with with an impedance $Z_{\text{parasitic}}$.

DAN nulls most signals by *canceling* currents at the summing junction, such that no current flows through the SQUID input coil or parallel paths listed above. However, sources of noise in the demodulation signal chain (Table 7.3) occur *after* the summing junction, between the SQUID output and the ADC. Although the resulting noise may be referred to a current through the SQUID input coil, none is actually present. To null these sources, DAN drives an inverse copy of that referred current *through the SQUID input coil*. Because this current is now flowing through the summing junction, it is subject to a division ("sharing") between the SQUID input coil and the other parallel legs of the circuit. The different legs of this path are illustrated in Figure 7.11. This division is more pronounced at higher frequencies, where the reactance of the SQUID input coil grows relative to the impedance of the other current paths.

This process, known as "current sharing," results in an *effective amplification of noise sources in the demodulation chain*, as DAN compensates for the division by generating larger copies of these noise signals. It is parameterized by the transfer function

$$\begin{aligned}\chi_{\text{cs}} &= \frac{I_{\text{SQUID input coil}}}{I_{\text{SQUID Summing Junction}}} \\ &\approx \left| \frac{(R_{\text{TES}} + R_s + R_{\text{wh}}) \parallel (Z_{\text{parasitic}} + R_{ref})}{(j\omega_i L_{(\text{SQUID input coil})} + R_{\text{wh}}) + ((R_{\text{TES}} + R_s + R_{\text{wh}}) \parallel (Z_{\text{parasitic}} + R_{ref}))} \right|,\end{aligned} \tag{7.3}$$

where $\frac{1}{\chi_{\text{cs}}}$ is the *current sharing factor*. χ_{cs} can be calculated from the output of a nuller network analysis:

$$\frac{I_{\text{ADC}}}{I_{(\text{DAC, nuller})}} = \frac{H_n}{\chi_{\text{cs}}} \cdot (Z_{\text{trans}} \cdot \chi_{\text{output}} \cdot H_{\text{adc}}) \,. \tag{7.4}$$

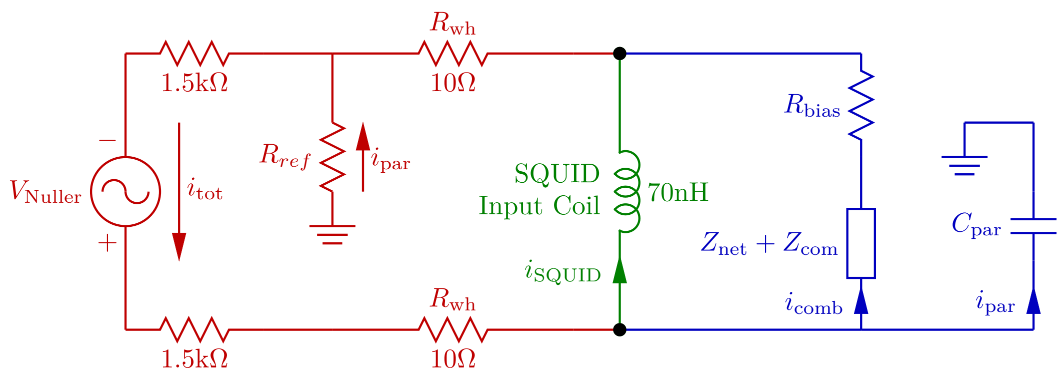

$$\text{Current Sharing Factor: } \frac{i_{\text{tot}}}{i_{\text{SQUID}}} = \frac{i_{\text{SQUID}} + i_{\text{comb}} + i_{\text{par}}}{i_{\text{SQUID}}}$$

Figure 7.11: A simplified diagram based on Figure 7.1, which specifically highlights the different parallel current paths for the nuller input. For signals which DAN can cancel at the summing junction, the voltage between the black nodes is zero, and so the division of current through these legs does not occur. Signals that DAN must drive a current through the SQUID input coil in order to cancel *will* be subject to this division, as that current is split between these three paths. The current sharing factor defines the magnitude of this division effect. Colors are coded according to temperature stages, with red at room temperature, green at the 4 Kelvin stage, and blue at sub-Kelvin.

It can also be derived analytically using the circuit model. Figure 7.12 compares median measured current sharing in the SPT-3G receiver with derived values from the circuit model.

The results show that some of our largest noise sources, such as the 1st stage amplifier voltage and current noise, are subject to enhancements due to current sharing of >2.5x. Moreover, by separating the relative importance of the different current paths in simulation (Figure 7.13), it is clear that in the SPT-3G system this effect is dominated by the "parasitic" current path to ground.

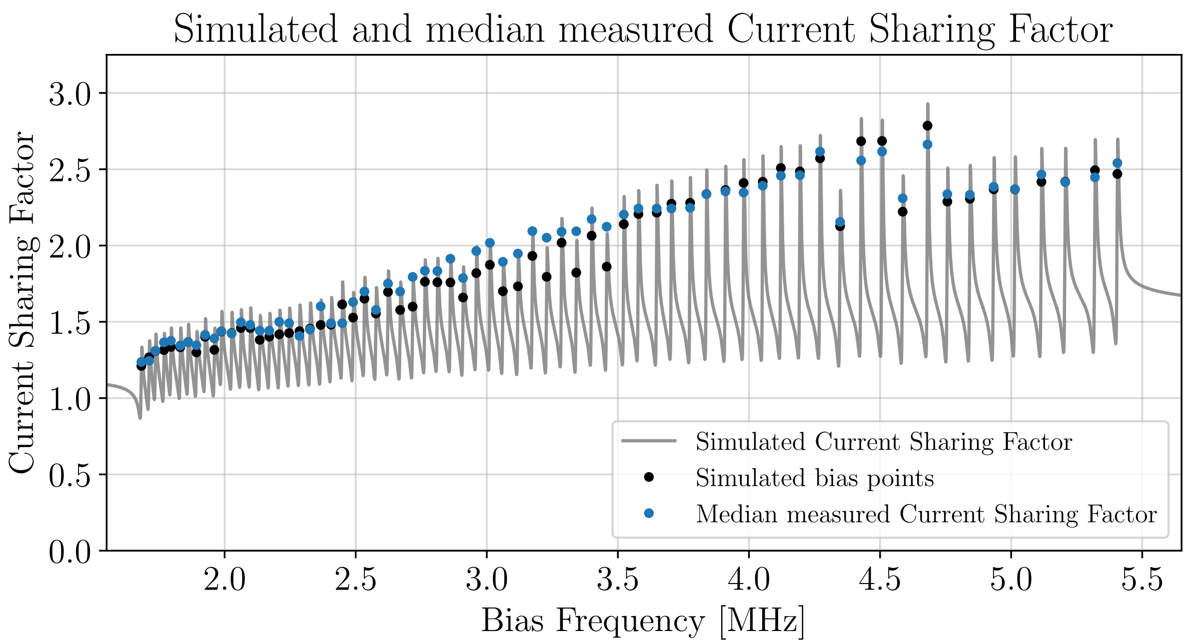

Figure 7.12: The current sharing factor $\left(\frac{1}{\chi_{\mathrm{cs}}}\right)$ can be measured using nuller network analysis data and simulated from an electrical model. The plot above compares measured values from SPT-3G with fully simulated values using the circuit model in Figure 7.1. There are two things to note in the result – the first is that the largest disagreement between the simulated and measured values occurs in the region of high LC scatter (Figure 6.4) and close resonance spacing. In this region resonances are more likely to deviate meaningfully from the circuit model and have overlapping filters. This scatter results in a lower total comb impedance at those frequencies, and therefore a higher total current sharing factor. The filter overlap due to large LC scatter is apparent in Figure 7.16. The second thing to notice is that choice of bias frequency matters. Off-resonance bias frequencies will include additional reactance from the filter that mitigates current sharing. Our bias frequencies are calculated from superconducting network analyses, and so they are not perfectly on-resonance when the detectors are operating.

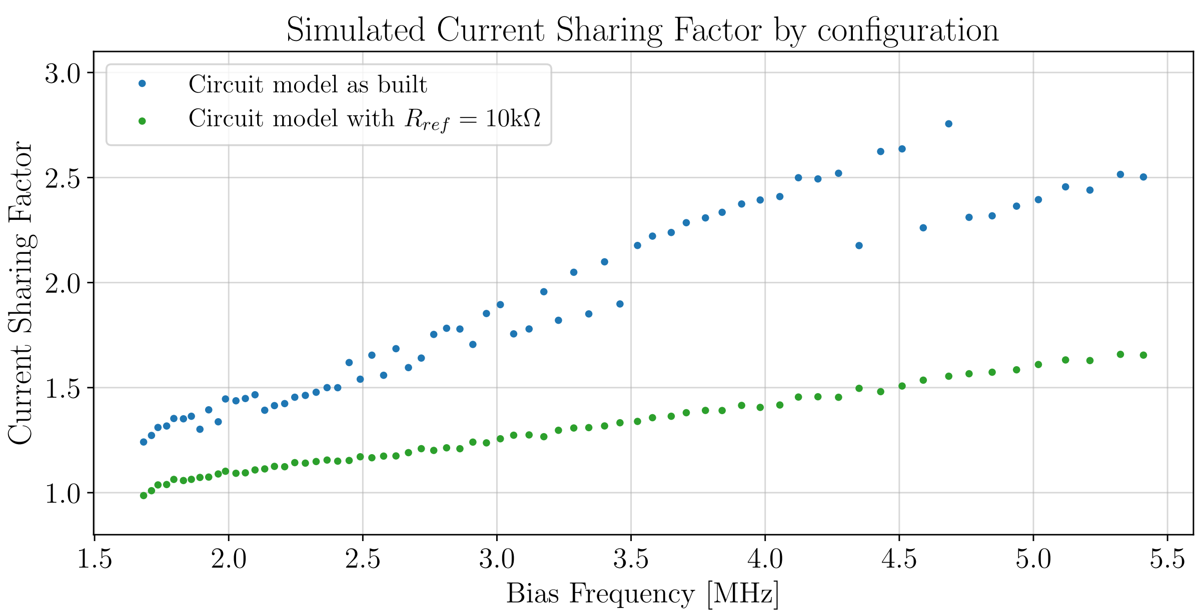

Figure 7.13: The capacitances to ground in the LC Board and SQUID Card enable parallel current paths relevant for current sharing. This is demonstrated by the green points, for which R_{ref} (which provides the low impedance current return path, and is shown in Figure 7.1) is increased to $10\,\text{k}\Omega$. This functionally disables the current path through the parasitic capacitances, leaving only the effect of the relative impedance of the SQUID input inductor and cryogenic network. R_{ref} is required to provide a current return for the SQUID flux bias, but this can be satisfied even through a large impedance.

We had assumed that improving noise performance within this modality required lower inductance SQUIDs, but these have proven difficult to fabricate and operate. This study suggests a means to dramatically improve the readout noise performance, especially at high frequency: increase the impedance of the current return path for the "parasitic" parallel leg. In the case of currently deployed systems this amounts to changing a single resistor per SQUID channel in the warm electronics.[5] Experimental verification of this is ongoing, but preliminary tests show a promising reduction in current sharing associated with this change, and this modification is being considered as an intervention for the SPT-3G receiver during the next summer season.

7.2.6 *Modulation penalty*

The use of a sinusoidal signal modulation in DfMUX systems incurs a noise penalty, which manifests as an enhancement of all broadband white noise sources within the readout by $\sqrt{2}$. This is described in detail in Dobbs et al., 2012 [26], but is often misunderstood. The modulation penalty does not translate into a *signal-to-noise* penalty, because the sinusoidal bias is also responsible for a $\sqrt{2}$ increase in detector responsivity (Equation 3.13), which offsets this effect. However, it does generate a noise enhancement when evaluating the system independent of a TES. This is a fundamental consequence of the modulation of the TES with a carrier tone.

Consider a TES with a time constant such that it has an effective bandwidth of f_τ Hz. We will calculate the output for the following sources:

1. An incident sky signal that is a precise deposition of power on the TES at f_0 Hz, P_{sig} [aW].

2. Incident noise (photon or phonon noise), which is broadband white noise power with a power spectral density of $P_{\text{ph}} \left[\frac{\text{aW}}{\sqrt{\text{Hz}}}\right]$. Integrated over f_τ Hz of bandwidth, the total noise power is $\sqrt{f_\tau} P_{\text{ph}}$ [aW].

5 The choice to robustly ground the nuller return line (and lower the impedance of the "parasitic" leg) with R_{ref}=0 Ω was intended to reduce susceptibility to RFI pickup, but failed to understand the parasitic path for current sharing. A ground reference is required for the SQUID flux bias, but that bias can easily accommodate 10 kΩ of additional impedance.

3. A broadband readout source that is a current noise at the SQUID summing junction, with an amplitude spectral density $i_{\text{readout}}\ \left[\frac{\text{pA}}{\sqrt{\text{Hz}}}\right]$.

Scenario I: DC Bias

In a DC biased TES, sources (1) and (2) are converted to a current at the SQUID summing junction via the DC-biased detector responsivity, $S_{\text{DC}}\left[\frac{\text{pA}}{\text{aW}}\right]$:

1. The incident f_0 Hz sky signal is converted to a current $i_{\text{sig}} = P_{\text{sig}}S_{DC}$ [pA].
2. The incident photon or phonon noise is converted to a current $i_{\text{ph}} = P_{\text{ph}}S_{DC}\left[\frac{\text{pA}}{\sqrt{\text{Hz}}}\right]$, over f_τ Hz of total the bandwidth in the interval $[0,\ f_\tau]$. The total noise current is therefore $\sqrt{f_\tau}i_{\text{ph}}$ [pA].
3. Readout noise, with an amplitude spectral density of $i_{\text{readout}}\left[\frac{\text{pA}}{\sqrt{\text{Hz}}}\right]$, contaminates the interval $[0,\ f_\tau]$ containing (1) and (2), for an integrated readout noise current of $\sqrt{f_\tau}i_{\text{readout}}$ [pA].

The total signal, noise, and signal-to-noise ratio is therefore

$$\text{Signal}_{\text{DC}} = i_{\text{sig}} = P_{\text{sig}}S_{DC} \tag{7.5}$$

$$\text{Noise}_{\text{DC}} = \sqrt{(\sqrt{f_\tau}i_{\text{ph}})^2 + (\sqrt{f_\tau}i_{\text{readout}})^2} \tag{7.6}$$

$$= \sqrt{(\sqrt{f_\tau}P_{\text{ph}}S_{DC})^2 + (\sqrt{f_\tau}i_{\text{readout}})^2} \tag{7.7}$$

$$\text{SNR}_{\text{DC}} = \frac{P_{sig}S_{DC}}{\sqrt{(\sqrt{f_\tau}P_{\text{ph}}S_{DC})^2 + (\sqrt{f_\tau}i_{\text{readout}})^2}} \tag{7.8}$$

Scenario II: Sinusoidal Bias Modulation

For a TES biased with a sinusoidal voltage tone, the incident power sources (1) and (2) are converted to a current via the AC-biased detector responsivity, S_{AC}, *and mixed with the carrier bias sinusoid* f_c. This modulation with the carrier tone splits the resulting current between modulation products in the upper and lower side-bands, $[f_c - f_\tau,\ f_c + f_\tau]$. The result is that:

1. The incident f_0 Hz sky signal is converted to currents

$$i_{(\text{sig},f_c \pm f_0)} = \frac{1}{2} P_{\text{sig}} S_{AC} \text{ [pA]} \,. \tag{7.9}$$

2. The incident photon or phonon noise is converted to currents

$$i_{(\text{ph},[f_c \pm f_\tau])} = \frac{1}{2} P_{\text{ph}} S_{AC} \left[\frac{\text{pA}}{\sqrt{\text{Hz}}}\right] , \tag{7.10}$$

   such that the total integrated noise current from (2) is

$$\sqrt{2 f_\tau}\; i_{(\text{ph},\ [f_c - f_\tau,\ f_c + f_\tau])} \text{ [pA]} = \sqrt{f_\tau} P_{\text{ph}} S_{AC} \text{ [pA]} \,. \tag{7.11}$$

   This is, notably, the same as the DC-biased case despite the larger bandwidth.

3. In the case of the readout noise, the signals are now spread out over double the bandwidth, $[f_c - f_\tau,\ f_c + f_\tau]$, and *each side-band is separately contaminated by the readout noise*. This noise is added at the SQUID summing junction, after modulation has occurred. The integrated total readout noise current in this case is $\sqrt{2 f_\tau}\; i_{\text{readout}}$ [pA], a factor of $\sqrt{2}$ higher than in the DC-biased case.

The total signal, noise, and signal-to-noise ratio is therefore,

$$\begin{aligned} \text{Signal}_{\text{AC}} &= i_{(\text{sig},\ f_c - f_0)} + i_{(\text{sig},\ f_c + f_0)} \qquad (7.12)\\ &= P_{\text{sig}} S_{AC} \\ \text{Noise}_{\text{AC}} &= \sqrt{(\sqrt{f_\tau} i_{(\text{ph},\ [f_c - f_\tau,\ f_c + f_\tau])})^2 + (\sqrt{2 f_\tau} i_{\text{readout}})^2} \qquad (7.13)\\ &= \sqrt{(\sqrt{f_\tau} P_{\text{ph}} S_{AC})^2 + (\sqrt{f_\tau} i_{\text{readout}})^2} \\ \text{SNR}_{\text{AC}} &= \frac{P_{\text{sig}} S_{AC}}{\sqrt{(\sqrt{f_\tau} P_{\text{ph}} S_{AC})^2 + (\sqrt{2 f_\tau} i_{\text{readout}})^2}} \,. \qquad (7.14) \end{aligned}$$

Notice that a measurement of only the readout noise in the sinusoidal-biased case (Equation 7.13, when $S_{AC} = 0$) yields a value $\sqrt{2}$ higher than the same measurement for the DC-biased case (Equation 7.7, when $S_{DC} = 0$). This modulation penalty is applied to all readout noise sources considered in our noise model, and is designated by $\chi_{\text{mod}} = \sqrt{2}$.

DC- vs AC- biased TES signal-to-noise ratio

Despite the fact that readout noise sources are enhanced in an fMUX system relative to a DC-biased system, the overall signal-to-noise ratio is the same. This is noted in Dobbs et al., 2012 [26], and covered later in Section 7.6, but relies on the fact that $S_{AC} \neq S_{DC}$. For an ideal TES under DC or sinusoidal bias with $V_{DC} = V_{(AC,\ \mathrm{rms})}$, the relationship between the two responsivities is $S_{AC} = \sqrt{2}S_{DC}$. The two expressions for signal-to-noise reduce to be equivalent:

$$\begin{aligned}
\mathrm{SNR_{AC}} &= \frac{P_{\mathrm{sig}} S_{AC}}{\sqrt{(\sqrt{f_\tau} P_{\mathrm{ph}} S_{AC})^2 + (\sqrt{2 f_\tau} i_{\mathrm{readout}})^2}} \\
&= \frac{P_{\mathrm{sig}} \sqrt{2} S_{DC}}{\sqrt{(\sqrt{2 f_\tau} P_{\mathrm{ph}} S_{DC})^2 + (\sqrt{2 f_\tau} i_{\mathrm{readout}})^2}} \\
&= \frac{P_{\mathrm{sig}} S_{DC}}{\sqrt{(\sqrt{f_\tau} P_{\mathrm{ph}} S_{DC})^2 + (\sqrt{f_\tau} i_{\mathrm{readout}})^2}} \\
&= \mathrm{SNR_{DC}}
\end{aligned} \tag{7.15}$$

Quadrature demodulation

The DfMUX system acquires the data contained in the side-bands of each carrier tone through quadrature ("complex") demodulation of every carrier frequency. This operation preserves the full information content in the spectrum $[f_c - f_\tau,\ f_c + f_\tau]$, and can be understood as a direct shift of the complex frequency interval down to [-f_τ, +f_τ]. The output of a quadrature demodulation is a decomposition of that frequency interval into the orthogonal basis that is "in-phase" (I) or "in-quadrature" (Q), where these are related by a 90° phase rotation.

When the phase of the complex demodulator is aligned with the phase of the carrier tone, the I-component contains all symmetric signals around the carrier tone. Any signal that modulates the carrier tone, such as deposited power on the TES, will generate symmetric side-bands (Equation 7.9). Therefore, with the proper relative phase of the demodulator, all of the TES signal (and deposited photon or phonon noise) will be contained in the I-component projection of the output data; while the Q-component is a 'null' for modulated signals, and contains just additive readout noise. For this reason we rotate the output basis to maximize signal in the I-component, and discard the rest.

This process is often incorrectly seen as a means to recover the modulation noise penalty, but that is not the case. The modulation penalty above is fundamental, and is not separable by a change of basis. It is a consequence of the statistical properties of the sum of a sine wave (or sine-wave-modulated signal) and band-pass limited Gaussian noise. These properties were derived in the 1948 by Steven Rice in his paper, "Statistical Properties of a Sine-wave Plus Random Noise" [83]. The *Rice Representation* is used to decompose a real random noise source (such as our readout noise) into in-phase (I) and quadrature (Q) components. He demonstrates that for processes such as our readout noise sources, the variance in each component is equal to the variance of the source. There is no linear combination of our I-Q basis that will reduce the variance due to the additive white noise, but there is a combination that will contain the full amplitude of our modulated signals.[6]

7.3 FULL SPT-3G READOUT NOISE MODEL IN NEI

In Tables 7.5, 7.6, 7.7, and 7.8, the appropriate transfer functions are applied to each noise source to arrive at an NEI at the SQUID summing junction, shown in the tables at two bias frequencies with the lowest and highest total NEI. The calculations assume the mean SPT-3G values of 700 Ω for both SQUID dynamic impedance (Z_{dyn}) and SQUID transimpedance (Z_{trans}). They are calculated for a system that is radiatively saturated, such that the detectors are at $R_{\text{tes}} = R_n$, and the TES johnson noise is not being suppressed by electrothermal feedback. This is the most convenient configuration to assess readout noise because the TES detectors can be treated as unresponsive resistors, and so the result isn't convolved with photon or phonon noise. It is also reasonably representative of the readout noise when operating TES detectors in the transition because the TES Johnson noise is a negligible contribution to the full noise.[7]

The entire frequency-dependent breakdown of each noise source is shown in Figure 7.14, and grouped by signal-chain in Figure 7.15. The overwhelmingly dominant noise sources are those to which the current sharing factor is applied – particularly the SQUID noise, but also the 1st stage amplifier current and voltage noise.

6 A corollary to this is that taking the magnitude of the complex output ($\sqrt{I^2+Q^2}$) would impose a *second* $\sqrt{2}$ noise penalty.

7 The difference between saturated and in-transition noise is quantified in Section 7.4.2.

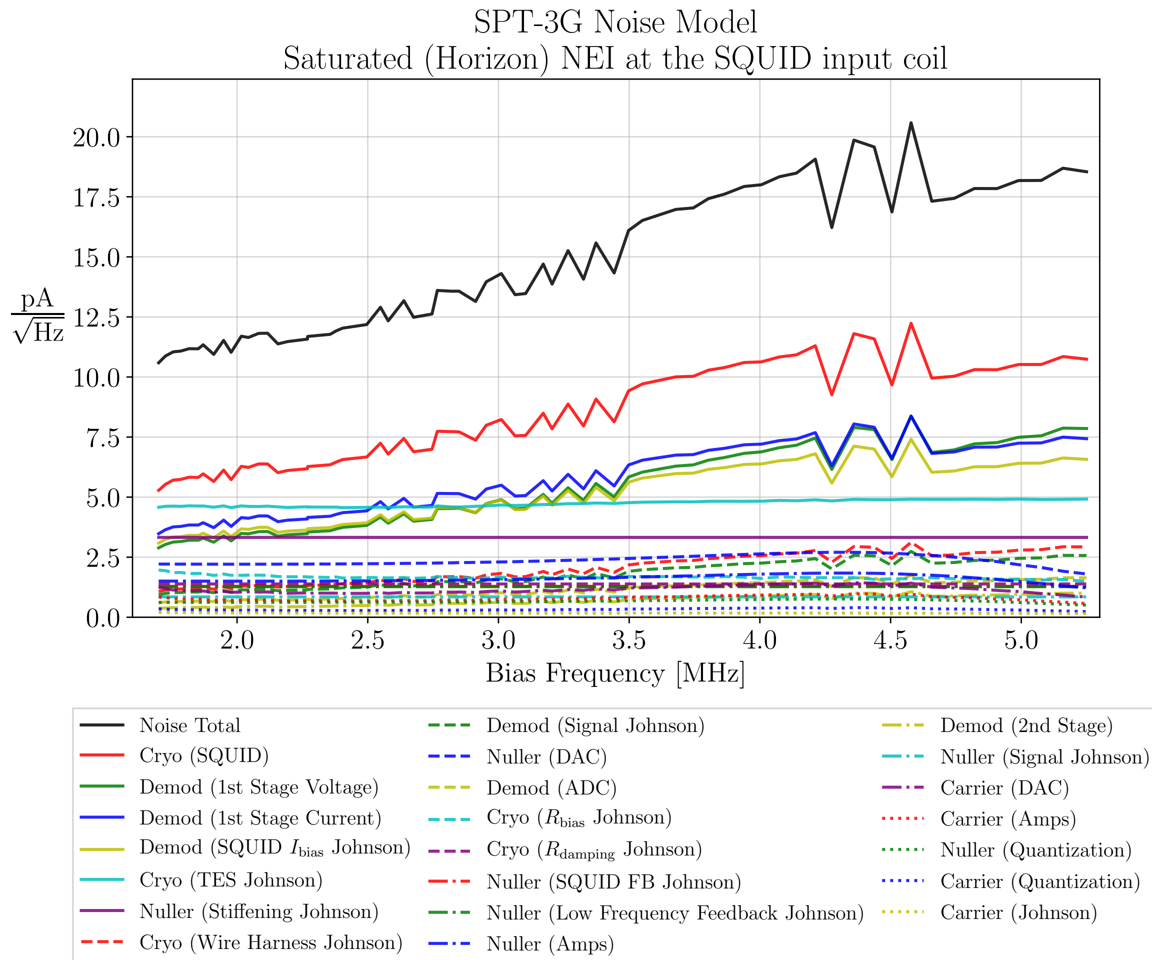

Figure 7.14: Shown above is the complete SPT-3G noise model, with the sources listed in the legend in descending order of amplitude at the highest frequency. This assumes SQUID transimpedance and SQUID dynamic impedance are both $700\,\Omega$. Values here assume the detectors are radiatively saturated ($R_{\text{TES}} = R_n$) as they are when SPT-3G intentionally observes the horizon.

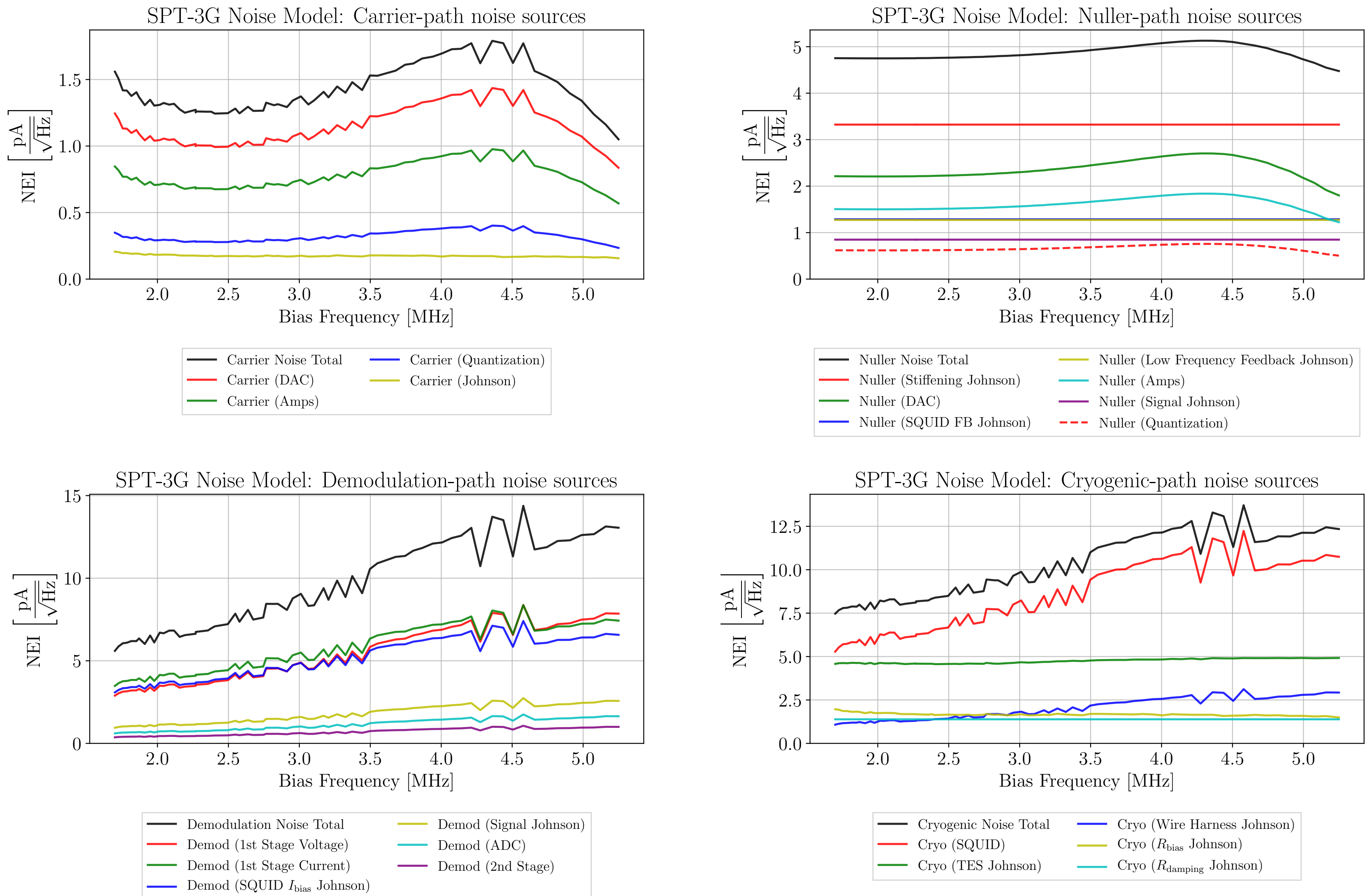

Figure 7.15: Shown above are the SPT-3G noise expectations for each signal path independently. Note that the carrier and nuller signal path components are far subdominant to the demodulation path and cryogenic sources. The biggest noise improvements would come from a reduction in the current sharing transfer function and the SQUID noise. Values here assume the detectors are radiatively saturated ($R_{\mathrm{TES}} = R_n$) as they are when SPT-3G intentionally observes the horizon.

Carrier-chain Noise Equivalent Current at the SQUID input coil

Source	Value	Location	Conversion	NEI (∼1.7 MHz)	NEI (∼4.57 MHz)
DAC	$50 \frac{\mathrm{pA}}{\sqrt{\mathrm{Hz}}}$	DAC	$\chi_{\mathrm{mod}} \cdot H_c^{\mathrm{Vcomb}} \cdot H_c^{\mathrm{I}}$	$1.3 \frac{\mathrm{pA}}{\sqrt{\mathrm{Hz}}}$	$1.4 \frac{\mathrm{pA}}{\sqrt{\mathrm{Hz}}}$
Quantization	$14 \frac{\mathrm{pA}}{\sqrt{\mathrm{Hz}}}$	DAC	$\chi_{\mathrm{mod}} \cdot H_c^{\mathrm{Vcomb}} \cdot H_c^{\mathrm{I}}$	$0.4 \frac{\mathrm{pA}}{\sqrt{\mathrm{Hz}}}$	$0.4 \frac{\mathrm{pA}}{\sqrt{\mathrm{Hz}}}$
Amplifiers	$34 \frac{\mathrm{pA}}{\sqrt{\mathrm{Hz}}}$	DAC	$\chi_{\mathrm{mod}} \cdot H_c^{\mathrm{Vcomb}} \cdot H_c^{\mathrm{I}}$	$0.9 \frac{\mathrm{pA}}{\sqrt{\mathrm{Hz}}}$	$1.0 \frac{\mathrm{pA}}{\sqrt{\mathrm{Hz}}}$
Johnson	$0.27 \frac{\mathrm{pV}}{\sqrt{\mathrm{Hz}}}$	Across comb	$\chi_{\mathrm{mod}} \cdot H_c^{\mathrm{I}}$	$0.2 \frac{\mathrm{pA}}{\sqrt{\mathrm{Hz}}}$	$0.2 \frac{\mathrm{pA}}{\sqrt{\mathrm{Hz}}}$
Total				$\mathbf{1.6} \frac{\mathrm{pA}}{\sqrt{\mathrm{Hz}}}$	$\mathbf{1.8} \frac{\mathrm{pA}}{\sqrt{\mathrm{Hz}}}$

Table 7.5: Carrier chain noise sources referred to NEI at the SQUID summing junction.

Nuller chain Noise Equivalent Current at the SQUID input coil

Source	Value	Location	Conversion	NEI ($\sim$1.7 MHz)	NEI ($\sim$4.57 MHz)
DAC	$50 \frac{\text{pA}}{\sqrt{\text{Hz}}}$	DAC	$\chi_{\text{mod}} \cdot H_n$	$2.2 \frac{\text{pA}}{\sqrt{\text{Hz}}}$	$2.6 \frac{\text{pA}}{\sqrt{\text{Hz}}}$
Quantization	$14 \frac{\text{pA}}{\sqrt{\text{Hz}}}$	DAC	$\chi_{\text{mod}} \cdot H_n$	$0.6 \frac{\text{pA}}{\sqrt{\text{Hz}}}$	$0.7 \frac{\text{pA}}{\sqrt{\text{Hz}}}$
Amplifiers	$34 \frac{\text{pA}}{\sqrt{\text{Hz}}}$	DAC	$\chi_{\text{mod}} \cdot H_n$	$1.5 \frac{\text{pA}}{\sqrt{\text{Hz}}}$	$1.8 \frac{\text{pA}}{\sqrt{\text{Hz}}}$
Signal Path Johnson	$0.6 \frac{\text{pA}}{\sqrt{\text{Hz}}}$	Summing junction	χ_{mod}	$0.9 \frac{\text{pA}}{\sqrt{\text{Hz}}}$	$0.9 \frac{\text{pA}}{\sqrt{\text{Hz}}}$
Current Stiffening Johnson	$2.35 \frac{\text{pA}}{\sqrt{\text{Hz}}}$	Summing junction	χ_{mod}	$3.3 \frac{\text{pA}}{\sqrt{\text{Hz}}}$	$3.3 \frac{\text{pA}}{\sqrt{\text{Hz}}}$
SQUID Flux Bias Johnson	$0.9 \frac{\text{pA}}{\sqrt{\text{Hz}}}$	Summing junction	χ_{mod}	$1.3 \frac{\text{pA}}{\sqrt{\text{Hz}}}$	$1.3 \frac{\text{pA}}{\sqrt{\text{Hz}}}$
Low Frequency Feedback Johnson	$0.9 \frac{\text{pA}}{\sqrt{\text{Hz}}}$	Summing junction	χ_{mod}	$1.3 \frac{\text{pA}}{\sqrt{\text{Hz}}}$	$1.3 \frac{\text{pA}}{\sqrt{\text{Hz}}}$
Total				$\mathbf{4.8} \frac{\text{pA}}{\sqrt{\text{Hz}}}$	$\mathbf{5.1} \frac{\text{pA}}{\sqrt{\text{Hz}}}$

Table 7.6: Nuller chain noise sources referred to an NEI at the SQUID summing junction.

Demodulation-chain Noise Equivalent Current at the SQUID input coil

Source	Value	Location	Conversion	NEI (~1.7 MHz)	NEI (~4.57 MHz)
ADC	$0.23 \frac{\mathrm{nV}}{\sqrt{\mathrm{Hz}}}$	SQCB input	$\frac{\chi_{\mathrm{mod}} \cdot \chi_{\mathrm{cs}}}{Z_{\mathrm{trans}} \cdot \chi_{\mathrm{output}}}$	$0.6 \frac{\mathrm{pA}}{\sqrt{\mathrm{Hz}}}$	$1.8 \frac{\mathrm{pA}}{\sqrt{\mathrm{Hz}}}$
2nd Stage Amplifier	$0.14 \frac{\mathrm{nV}}{\sqrt{\mathrm{Hz}}}$	SQCB input	$\frac{\chi_{\mathrm{mod}} \cdot \chi_{\mathrm{cs}}}{Z_{\mathrm{trans}} \cdot \chi_{\mathrm{output}}}$	$0.4 \frac{\mathrm{pA}}{\sqrt{\mathrm{Hz}}}$	$1.1 \frac{\mathrm{pA}}{\sqrt{\mathrm{Hz}}}$
1st Stage Amplifier (Current)	$2.2 \frac{\mathrm{pA}}{\sqrt{\mathrm{Hz}}}$	SQCB input	$R_{\mathrm{SQCB}} \left(\frac{\chi_{\mathrm{mod}} \cdot \chi_{\mathrm{cs}}}{Z_{\mathrm{trans}} \cdot \chi_{\mathrm{output}}} \right)$ (a)	$3.5 \frac{\mathrm{pA}}{\sqrt{\mathrm{Hz}}}$	$8.5 \frac{\mathrm{pA}}{\sqrt{\mathrm{Hz}}}$
1st Stage Amplifier (Voltage)	$1.1 \frac{\mathrm{nV}}{\sqrt{\mathrm{Hz}}}$	SQCB input	$\frac{\chi_{\mathrm{mod}} \cdot \chi_{\mathrm{cs}}}{Z_{\mathrm{trans}} \cdot \chi_{\mathrm{output}}}$	$2.9 \frac{\mathrm{pA}}{\sqrt{\mathrm{Hz}}}$	$8.5 \frac{\mathrm{pA}}{\sqrt{\mathrm{Hz}}}$
Signal path Johnson	$0.36 \frac{\mathrm{nV}}{\sqrt{\mathrm{Hz}}}$	SQCB input	$\frac{\chi_{\mathrm{mod}} \cdot \chi_{\mathrm{cs}}}{Z_{\mathrm{trans}} \cdot \chi_{\mathrm{output}}}$	$1 \frac{\mathrm{pA}}{\sqrt{\mathrm{Hz}}}$	$2.8 \frac{\mathrm{pA}}{\sqrt{\mathrm{Hz}}}$
SQUID junction I_{bias} Johnson	$8.36 \frac{\mathrm{nV}}{\sqrt{\mathrm{Hz}}}$	I_{bias} input	$\frac{R_{\mathrm{eq}}}{R_{\mathrm{eq}} + 4.22k} \left(\frac{\chi_{\mathrm{mod}} \cdot \chi_{\mathrm{cs}}}{Z_{\mathrm{trans}} \cdot \chi_{\mathrm{output}}} \right)$ (b)	$3.1 \frac{\mathrm{pA}}{\sqrt{\mathrm{Hz}}}$	$7.5 \frac{\mathrm{pA}}{\sqrt{\mathrm{Hz}}}$
Total				$\mathbf{5.6} \frac{\mathrm{pA}}{\sqrt{\mathrm{Hz}}}$	$\mathbf{14.4} \frac{\mathrm{pA}}{\sqrt{\mathrm{Hz}}}$

(a) R_{SQCB} is the total resistance seen between the input terminals of the 1st stage amplifier:

$$R_{\mathrm{SQCB}} = \left(\frac{1}{10\,\Omega} + \frac{1}{100\,\Omega} + \frac{1}{150\,\Omega} \right)^{-1} + \left(\frac{1}{4.22\,\mathrm{k}\Omega} + \frac{1}{R_{\mathrm{eq}}} \right)^{-1} .$$

(b) R_{eq} is the equivalent resistance of the wire of the SQUID dynamic impedance in parallel with the wire harness RC filter.

$$R_{\mathrm{eq}} = \left| ((j\omega C_{wh})^{-1} + Z_{\mathrm{dyn}}^{-1})^{-1} + 2R_{wh} + 2j\omega L_{wh} \right| .$$

Table 7.7: Demodulation chain noise sources referred to NEI at the SQUID summing junction.

Cryogenic-sourced Noise Equivalent Current at the SQUID input coil

Source	Value	Location	Conversion	NEI (∼1.7 MHz)	NEI (∼4.57 MHz)
TES Johnson [(a)]	$\frac{5}{\sqrt{R_{\mathrm{TES}}}} \frac{\mathrm{pA}}{\sqrt{\mathrm{Hz}}}$	Summing junction	χ_{mod}	$4.6 \frac{\mathrm{pA}}{\sqrt{\mathrm{Hz}}}$	$4.9 \frac{\mathrm{pA}}{\sqrt{\mathrm{Hz}}}$
Bias Resistor Johnson	$2.6 \frac{\mathrm{pV}}{\sqrt{\mathrm{Hz}}}$	Across comb	$\chi_{\mathrm{mod}} \cdot H_c^{\mathrm{I}}$	$2 \frac{\mathrm{pA}}{\sqrt{\mathrm{Hz}}}$	$1.6 \frac{\mathrm{pA}}{\sqrt{\mathrm{Hz}}}$
Damping Resistor	$0.98 \frac{\mathrm{pA}}{\sqrt{\mathrm{Hz}}}$	Summing junction	χ_{mod}	$1.4 \frac{\mathrm{pA}}{\sqrt{\mathrm{Hz}}}$	$1.4 \frac{\mathrm{pA}}{\sqrt{\mathrm{Hz}}}$
SQUID	$3 \frac{\mathrm{pA}}{\sqrt{\mathrm{Hz}}}$	Summing junction	$\chi_{\mathrm{mod}} \cdot \chi_{\mathrm{cs}}$	$5.3 \frac{\mathrm{pA}}{\sqrt{\mathrm{Hz}}}$	$12.2 \frac{\mathrm{pA}}{\sqrt{\mathrm{Hz}}}$
Wire Harness Resistance	$0.41 \frac{\mathrm{nV}}{\sqrt{\mathrm{Hz}}}$	SQCB input	$\frac{\chi_{\mathrm{demod}} \cdot \chi_{\mathrm{cs}}}{Z_{\mathrm{trans}} \cdot \chi_{\mathrm{output}}}$	$1.1 \frac{\mathrm{pA}}{\sqrt{\mathrm{Hz}}}$	$3.1 \frac{\mathrm{pA}}{\sqrt{\mathrm{Hz}}}$
Total				$\mathbf{7.5} \frac{\mathrm{pA}}{\sqrt{\mathrm{Hz}}}$	$\mathbf{13.7} \frac{\mathrm{pA}}{\sqrt{\mathrm{Hz}}}$

(a) The variation here is due to differences in series impedance (z_{lcr}).

Table 7.8: Noise sourced from cryogenic system components referred to NEI at the SQUID summing junction.

7.4 SPT-3G READOUT NEI

Direct measurements of SPT-3G readout noise are possible by biasing the array as if for observations, but then slewing to observe the horizon. The additional incident power from the atmospheric emission at the horizon is sufficient to saturate the detectors, disabling electrothermal feedback and rendering the TES elements simple resistors. This measurement matches the scenario simulated in the noise model above. Figure 7.16 shows this measurement for all operable bolometers in the SPT-3G receiver. In Figure 7.17 I compare that measurement with the expectations in the previous section, where each comb in the receiver has been separately simulated using the model described above, varying only the measured SQUID parameters (Z_{dyn} and Z_{trans}).

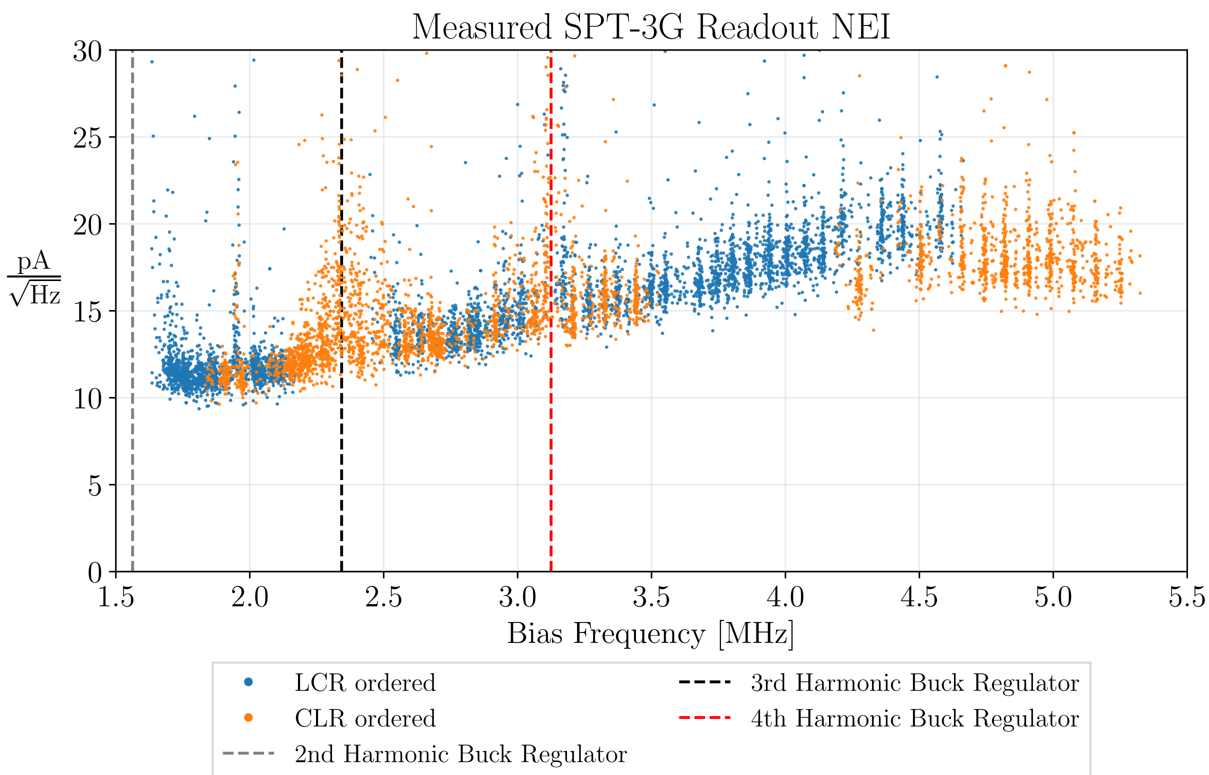

Figure 7.16: Measured SPT-3G readout noise in NEI – taken while the detectors are saturated while looking at the horizon. Notice the clear distinction between LCR and CLR ordered resonators, especially at high frequency. Noise features around the buck regulator switching frequency harmonics are a consequence of EMI pickup from the number of iceboards operating, described in detail in Appendix C. LC scatter is evident where overlapping colors are present, and is one reason for the disagreement between the simulated and measured current sharing factor presented in Figure 7.11, for which the measured points are binned by LC channel.

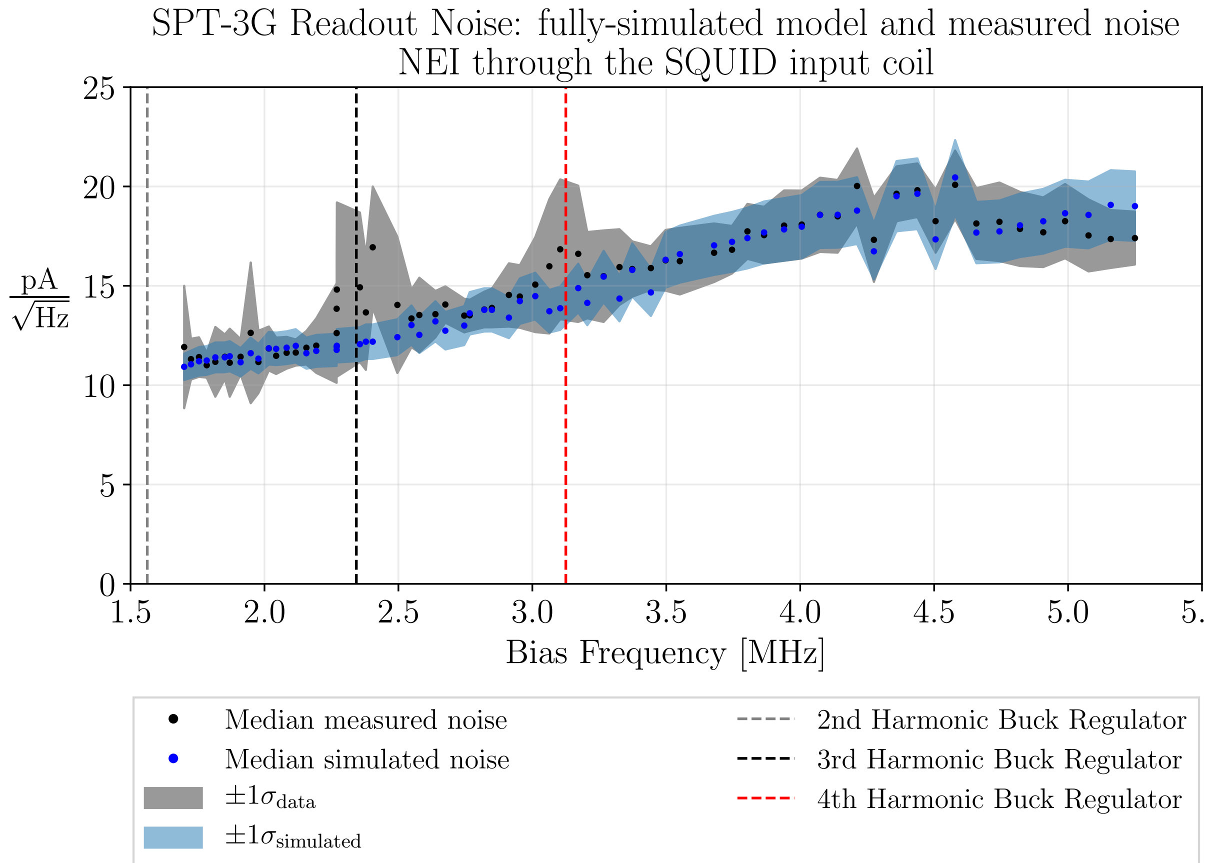

Figure 7.17: The SPT-3G instrument noise is plotted here with the calculated expectation of that noise based on the analytic model. Black points show the median measured noise binned by LC channel, with a gray 1-sigma envelope. The noise expectations are generated for each SQUID individually, using the measured SQUID parameters and a simulated frequency comb. The 1-sigma envelope for these points is shown in blue. There is some minor disagreement at high frequency, which is within the transfer function uncertainties. The success of the model is in correctly describing the rise in instrument noise as a function of frequency, and the sensitivity to capacitive paths to ground, as strongly suggested by the correlation with LC ordering. The primary readout noise drivers are current sharing noise, and the result of operating with SQUIDs exhibiting high dynamic impedance.

The strong agreement between the measurement and noise model indicates that the major noise mechanisms for the DfMUX system are well understood, and can be accurately modeled using an electrical description of the system. It also builds confidence in our ability to target specific changes for improving the noise performance of the system. The variance in the model is well matched to the variance in the data, indicating that scatter in the SQUID parameters is the primary source of variation in noise between combs; as expected in a system so sensitive to SQUID performance.

The model does overestimate readout noise at the highest frequencies by <9%, where the actual readout noise appears to roll-off slightly. This is within the uncertainty of the warm electronics transfer function measurement, and could simply be indicating a weaker roll-off of the RF filtering than is accounted for in H_n. An uncertainty of this magnitude, especially at the highest frequencies, is not indicating a substantive misunderstanding of the noise mechanisms. For this reason, I leave it as an minor caveat to the noise modeling.[8]

7.4.1 *Low dynamic impedance operation*

As discussed in Section 6.1.1, it is possible to operate the SA13 SQUIDs at a different flux bias, such that they exhibit a $Z_{\mathrm{dyn}} \sim 300\ \Omega$ rather than $Z_{\mathrm{dyn}} \sim 700\ \Omega$. There are currently six SQUIDs operating on SPT-3G in this manner, where it appears the $20\,\Omega$ damping resistor (Figure 7.1) is sufficient to mitigate the resonances internal to the SQUID that usually prevent low dynamic impedance operation. The resulting noise performance of the associated detectors, shown in Figure 7.18, agrees with the expected $\sim 10\%$ noise improvement derived from noise model.[9]

8 Nevertheless, some potential explanations include an additional parasitic that is not captured by the electrical model; perhaps due to capacitance in the routing traces on the lithographic chips. The fraction of area in these traces is highest at high frequencies where the lithographic capacitor elements are small. Alternatively, it may be the case we operate the high frequency detectors somewhat more off-resonance than predicted by this model, lowering the relative current sharing at those frequencies. This isn't a bad guess, comparison between the model current sharing and the measured current sharing shows good agreement, but relies on network analysis data taken when the detectors are kept above the superconducting transition with thermal, rather than electrical power. There are several processes by which such temperature changes to the sub-Kelvin cryogenic stage could systematically alter the higher frequency resonance locations.

9 An effort to operate the entire receiver in this configuration is planned for the upcoming austral summer, when we normally reserve some telescope time for tests and optimizations.

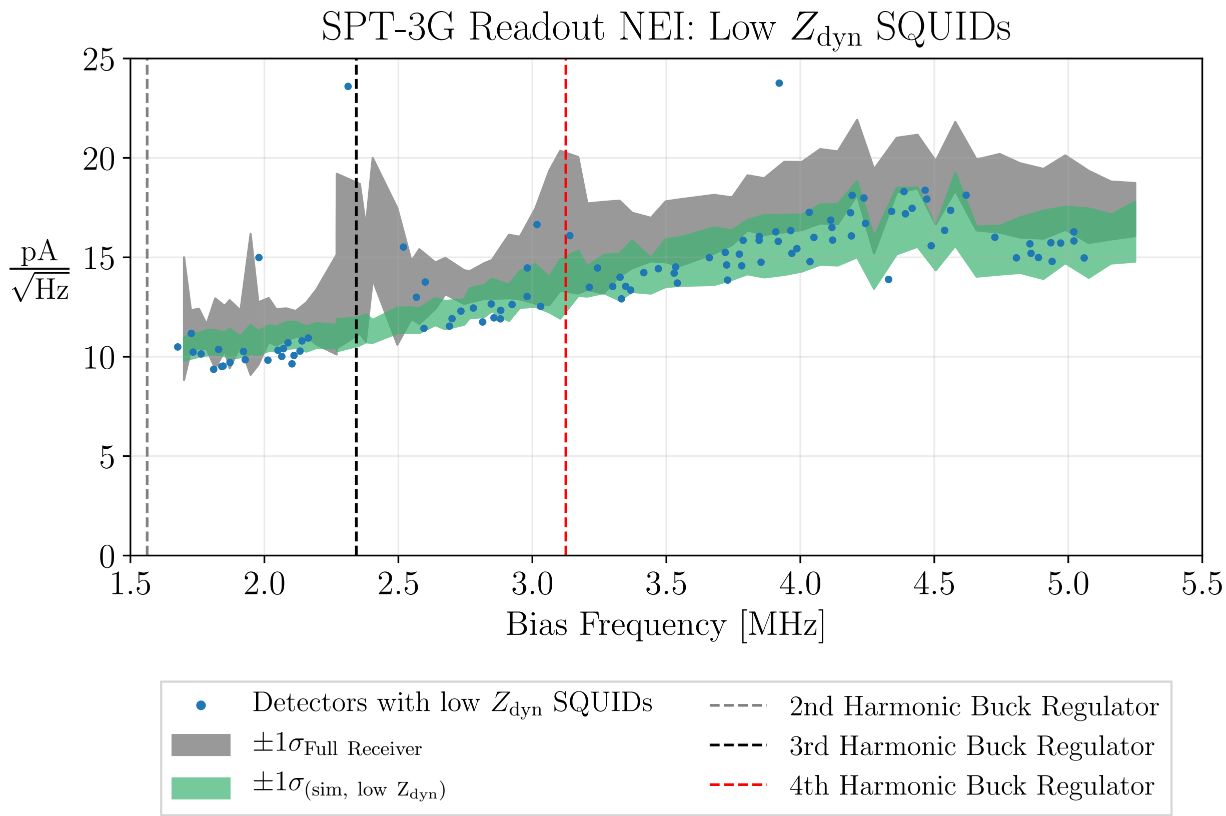

Figure 7.18: Measured readout noise in detectors operated with SQUIDs tuned to a lower dynamic impedance (blue points above) is systematically lower than the rest of the receiver. This difference is consistent with the expectation from the noise model, which predicts a $\sim 10\%$ noise improvement at high frequency from lower dynamic impedance SQUIDs. This model is shown in green, where low Z_{dyn} operation of the entire receiver is simulated. There are currently 6 SQUIDs on SPT-3G operated at low Z_{dyn}, but we may be able to operate the entire instrument in this configuration.

7.4.2 *SPT-3G readout NEI when observing*

Horizon (saturated) noise data, as above, is useful to validate the readout noise model, but the true readout noise when observing is slightly different: the detector resistances in the transition are lower than when saturated, increasing the current sharing factor slightly; and TES Johnson noise is suppressed by electrothermal feedback. The result is a $\sim 10\%$ increase in NEI, shown in Figure 7.19.

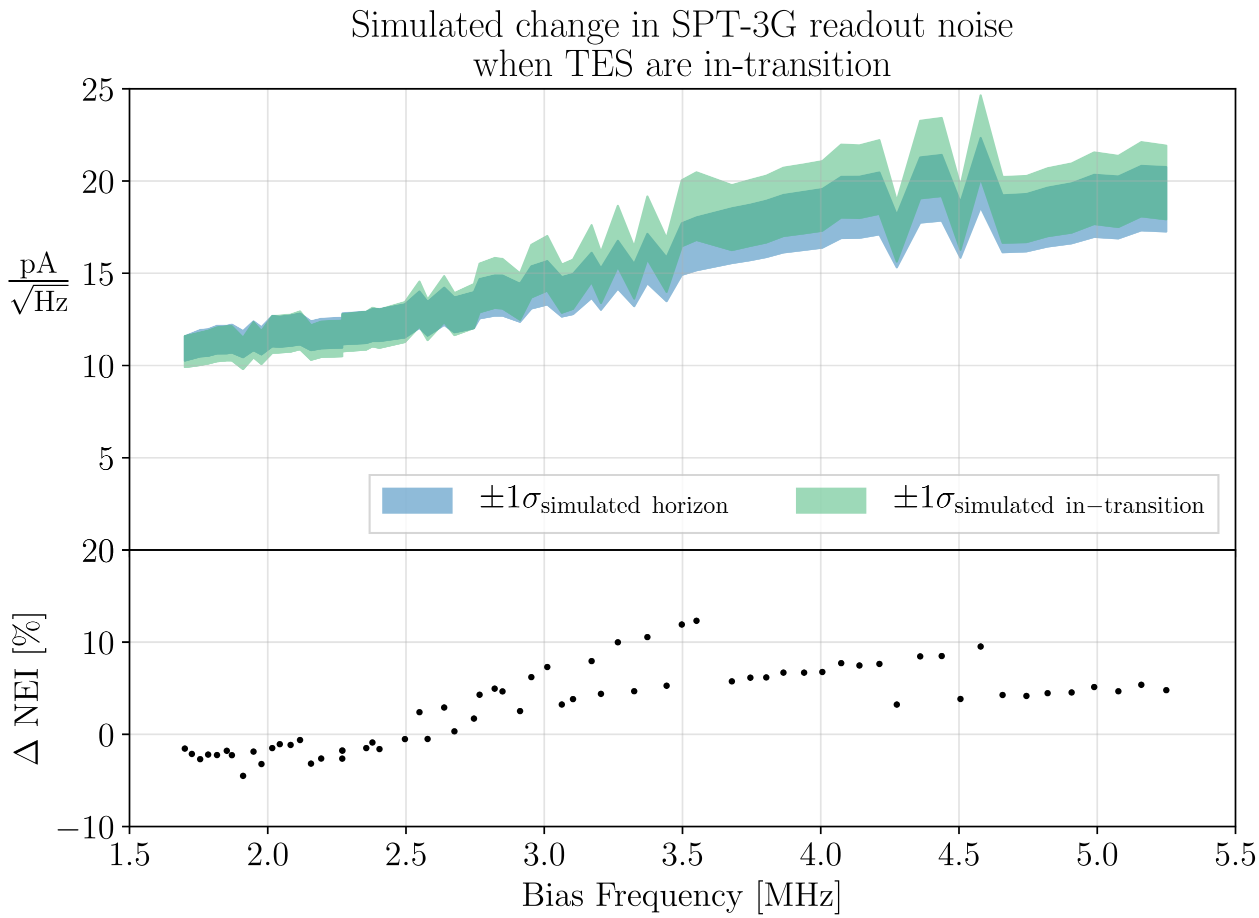

Figure 7.19: When the detectors are in their superconducting transition the TES resistance is lower than R_n, and so readout noise increases as the current sharing factor (χ_{cs}) grows. This is offset slightly by the reduction in TES Johnson noise, but does result in a $\sim 10\%$ correction to the noise model forecasts when observing, as shown above.

7.5 INTERPRETING NEI IN DFMUX SYSTEMS

In “background limited” instruments we expect the readout NEI to be subdominant to other sources of NEI, and small relative to the total noise of the system. A comparison between the readout NEI and the NEI of the full system while observing is given in Figure 7.20, and requires some care to to interpret.

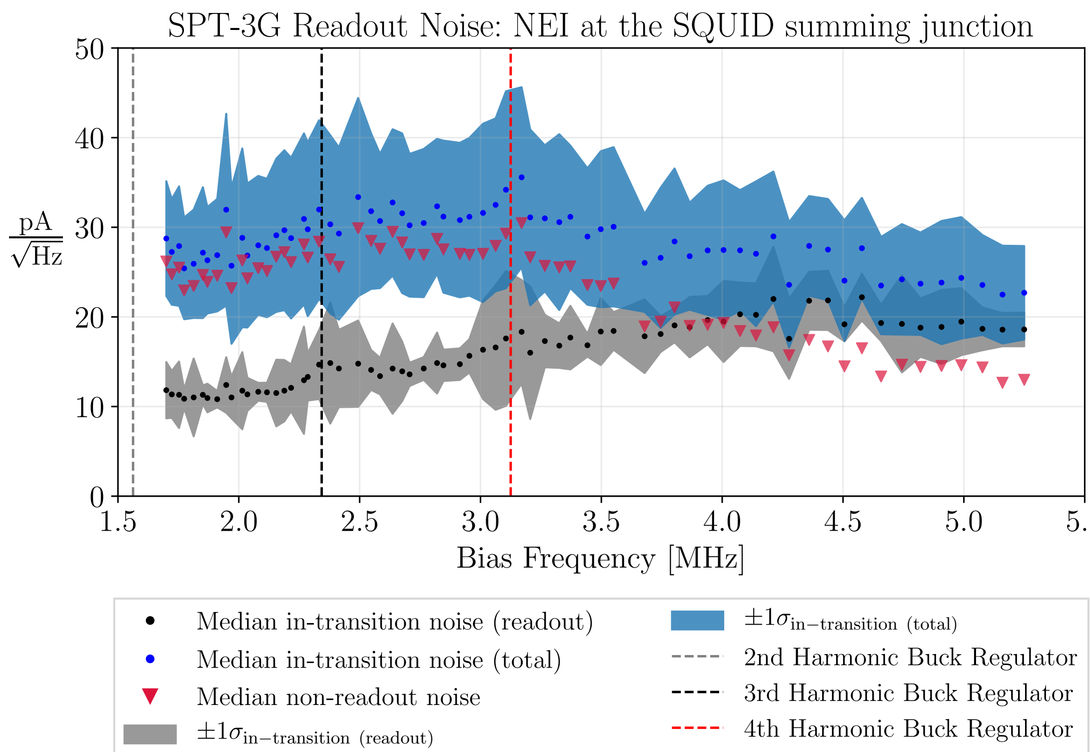

Figure 7.20: The above plot compares total in-transition measured noise with the readout-only noise. The readout noise is taken from horizon NEI measurements, modified by the factor in Figure 7.19 to account for operating in the transition. Included is also the derived non-readout noise calculated as the quadrature subtraction of the total in-transition noise from the readout-only noise.

The total NEI at high bias frequencies show an overall falling system noise, despite a rise in readout noise contributions. This is counter-intuitive, and indicates that the dominant noise contribution (non-readout noise) is **decreasing** as a function of bias frequency. The non-readout noise contributions all act by depositing power on the TES, either through phonon noise (NEP_g, Equation 3.15), or photon noise (NEP_γ, Equation 3.18). This deposited noise power is independent of readout parameters such as bias frequency. However, like all incident power, it is converted to a current through detector responsivity ($S = \frac{\delta I_{\text{Summing Junction}}}{\delta P_{\text{TES}}}$), which is sensitive to the readout parameters.

In this case the decrease in observed NEI is indicating a decline in detector responsivity, and with it a degradation in overall system noise performance. As introduced in the beginning of the chapter with Equation 7.1, we parameterize the overall system noise performance by the fractional noise increase due to readout, computed as

$$\text{Fractional Noise Increase} = \frac{\text{NEI}_{\text{total}}}{\sqrt{\text{NEI}^2_{\text{total}} - \text{NEI}^2_{\text{readout}}}} \,. \tag{7.16}$$

The result, given in Figure 7.21, clearly illustrates the worsening of total instrument performance at high bias frequencies, despite lower overall NEI.

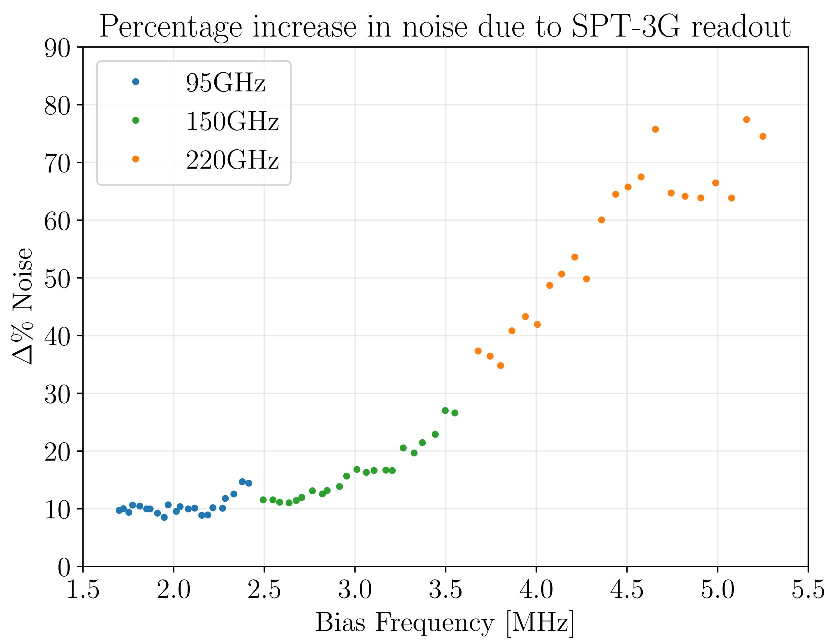

Figure 7.21: This metric parameterizes the percent increase in total noise over a hypothetical instrument with a noiseless readout. A typical target for the next generation of CMB instruments is $\lesssim 10\%$.

Typical targets for noise increase due to readout in the next generation of CMB instruments are between <10% (LiteBIRD) and <5% (CMB-S4). We can see here that SPT-3G achieves ∼10% noise increase due to readout in the lowest bias frequencies, and remains within a factor of two of that for the 150 GHz detectors, but is readout-noise dominated in the 220 GHz band. Understanding the performance of the SPT-3G 220 GHz detectors is essential for the success of future instruments such as the LiteBIRD satellite.

7.6 EXCESS RESPONSIVITY

The loss of detector responsivity at high bias frequencies is due to the manner in which detector responsivity is modified by the readout circuit. Recall from Section 3.4, Equation 3.13, that detector responsivity is given by

$$S = \left(\frac{-\sqrt{2}}{V_{(\text{TES bias, rms})}}\right) \frac{\mathcal{L}R_{\text{TES}}}{R_{\text{TES}} + z_s + \mathcal{L}(R_{\text{TES}} - z_s)}, \tag{7.17}$$

and that for our parameters only the real component of the Thévenin equivalent series resistance with the TES ($R_s = \text{Re}(z_s)$) has much of an impact on responsivity. The fractional change in responsivity due to variations in R_s is given by $\Delta\%\ S\ \left[\frac{S}{S_{(R_s=0)}}\right]$, and is strongly correlated with the change in non-readout NEI (Figure 7.22) as a function of bias frequency. This is a relatively crude comparison because it assumes a fixed loopgain, underestimating the coupled effect of changing R_s. However, it is sufficient to implicate the reduction of R_s in the loss of 220 GHz detector responsivity.

7.7 SPT-3G READOUT NOISE PERFORMANCE SUMMARY

By means of this analysis I find that the 220 GHz detectors on SPT-3G are readout noise dominated, and that this is caused by an unfortunate combination of two unrelated effects: higher than expected readout noise at high bias frequency, and a falling bias-frequency dependent responsivity. The former is a consequence of the current sharing factor, and the latter is a consequence of the geometric design used for the lithographic elements.

The readout noise is primarily determined by the following two previously unknown effects, described in detail for the first time in this analysis:

1. Current sharing (χ_{cs}), specifically the additional current sharing due to parallel paths through capacitances to ground in the cryogenic electronics (Section 7.2.5).[10]

10 The current sharing mechanism with the SQUID was first recognized collaboratively during the SPT-3G engineering run, and motivated the change to lower input inductance SQUIDs in the 2018

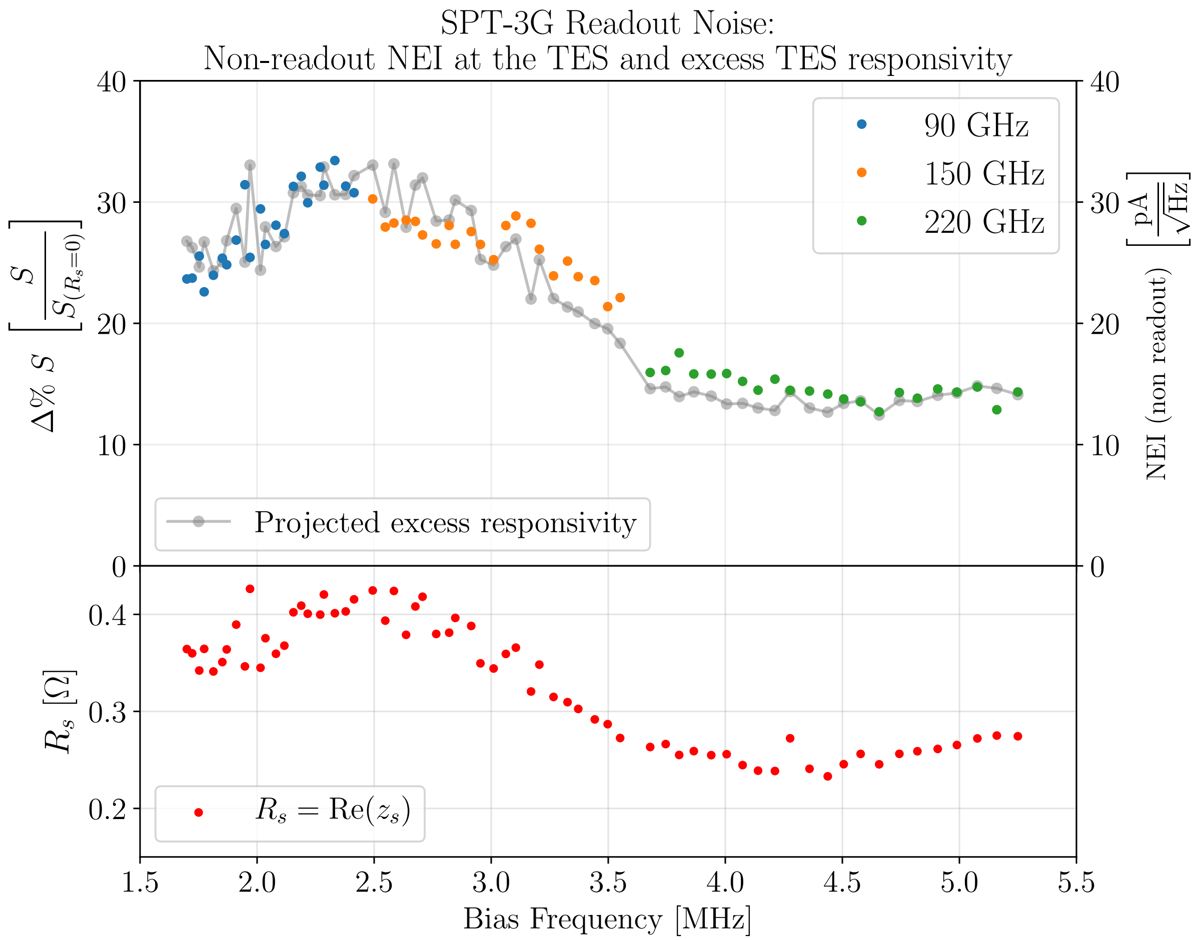

Figure 7.22: The plot above compares the expected excess responsivity, due to series resistance with the TES, against the inferred non-readout NEI at the TES. This crude comparison keeps loopgain fixed, but strongly suggests that the loss of additional series resistance with the TES is the reason for lower responsivity in the 220 GHz detectors. Astute readers may have noticed the slight difference between the non-readout NEI shown here, and that shown in Figure 7.20. This includes an additional transfer function to convert from a current at the SQUID summing junction to a current through the TES (ie, it accounts for leakage current). The latter is useful for evaluating relative responsivity, the former is the important metric for overall noise performance.

2. Noise penalties for operating SQUIDs with high Z_{dyn}. This is partially due to the 1st stage amplifier current noise, but primarily because of the resulting output filter χ_{output}, formed with the parallel capacitance in the wire-harness (Section 7.2.2). This has motivated attempts to operate the SA13 SQUIDs in a low dynamic impedance configuration on existing experiments, and has set new requirements on the next generation of SQUIDs being designed for LiteBIRD.

SPT-3G detector responsivity is a sensitive function of bias frequency, because the series resistance with the TES (R_s) varies with bias frequency. Excess responsivity $\left(\frac{S}{S_{(R_s=0)}}\right)$ from larger R_s contributes to improved performance in the 90 GHz and 150 GHz detectors. This is despite the fact that SPT-3G was not designed to require excess responsivity in this way. In fact, we attempted to optimize for *minimal* R_s to avoid degrading stability or linearity. In this respect we have been somewhat fortunate – had we more successfully minimized the series resistance, all but the detectors biased at the very lowest carrier frequencies would have been readout-noise co-dominated.

There are opportunities for improvement to SPT-3G without major hardware rework.

1. A minor modification to the warm electronics, mentioned in Section 7.2.5, would improve the current sharing noise by mitigating the "parasitic" current paths. This is being experimentally validated in laboratory test-beds and may be performed during the summer (2020-2021) maintenance period.

2. Deliberately biasing detectors off-resonance, to add some series reactance from the filter, may also successfully mitigate current sharing noise.

3. Operating SA13 SQUIDs in their lower dynamic impedance configuration would mitigate the output filter effect and minimize noise due to the first stage amplifier. Six SQUIDs are already operated in the SPT-3G receiver in this configuration, and the associated detectors are among our lowest noise detectors on the instrument. With some experimentation we may be able to implement a similar tuning configuration across the entire instrument. This experimentation will have to wait until the summer season at the South Pole, to avoid interrupting observations during the winter.

season. This work identifies the dominant source of this effect now as capacitances unrelated to the SQUID input coil.

7.8 TOWARDS A HIGHER-PERFORMING SYSTEM

The analysis of SPT-3G readout noise presented in this chapter provides the basis on which to both forecast LiteBIRD readout performance, and to direct development efforts most productively. It was evident that the noise models that had been successful for the Legacy DfMUX systems were not sufficient over these higher bandwidths and dense multiplexing factors, and so regaining confidence in the DfMUX noise model has been essential for proceeding with the LiteBIRD readout design. In addition to building up the specific tools and methodology here that will be applied to LiteBIRD modeling, I've shown that two most important design elements for readout noise performance are (1), mitigation of the parasitic current sharing path and (2), control over the responsivity-boosting series resistance (rather than outright minimization of it). This analysis additionally provides guidelines for other elements of the system, such as the minimization of parallel capacitance in the long wiring that generates χ_{output}, and quantitatively modeling the importance of Z_{dyn}. In Chapter 8 I apply these models to define several possible LiteBIRD readout configurations and assess the resulting readout noise performance.

8

LITEBIRD NOISE FORECASTING

Atmospheric emission makes up a large fraction of the incident power detected by ground-based CMB instruments. This contributes to the system noise directly (via increased photon noise, Equation 3.18), and indirectly (due to increased phonon noise from the higher thermal conductivity required, Equation 3.15). A space-based instrument, such as the proposed LiteBIRD satellite, has an intrinsic noise advantage by avoiding atmospheric emission. For this reason, achieving background-limited noise performance in space poses a greater challenge for the readout design.[1] The LiteBIRD science target is the detection of primordial B-modes within the CMB – the imprint of inflationary gravity waves – and a measurement of the tensor-to-scalar ratio with precision $\sigma_r < 0.001$ [43]. In order to produce the required high-fidelity multi-wavelength maps within the mission lifetime, the instrument must have a sufficient total sensitivity. This sensitivity may be tuned with a variety of parameters, such as focal plane size and quality of the optical elements, but those design decisions (and their success) are predicated on a confident assessment of the projected readout noise.

The present design target for the LiteBIRD readout is <10% increase in total noise due to readout within each observing band. This chapter uses the understanding of DfMUX noise from SPT-3G to assess whether that is achievable, and if so, under what conditions. I also present several scenarios for which the noise target can be met. All successful scenarios must address the most significant noise mechanisms identified in the study of SPT-3G, and in particular must mitigate excess current sharing. It will also be essential to strategically deploy a real series resistance with the TES (R_s) to boost detector responsivity. The use of R_s to boost responsivity isn't a departure from the currently fielded instruments on SPT-3G or Polarbear-2, but in this case the implementation will have to be intentional and well controlled. To do so will require a lithographic circuit design that accounts for the effects noted in Section 6.2.5.

I propose a baseline readout and detector configuration that meets the noise target and requires no speculative technology development, though the margin of error would be low (within a few percent) for the most constrained readout bands. Improvements to the

1 This is commonly thought to be offset by a reduction in overall required voltage bias, and associated increase in responsivity. As will be shown in Section 8.4, this only provides a limited benefit.

SQUID design and implementation currently in development would improve this margin considerably, and I include projections for several of these efforts. The detector configuration I propose to meet this noise target is R_{TES}=0.6 Ω, with R_{s}=0.3 Ω. This choice is an appropriate compromise between boosted responsivity and similarity to existing (high technology readiness level) systems, and is within the operational envelope already deployed successfully on the POLARBEAR-2 instrument [34].[2] The dynamic stability criterion associated with this configuration ($\tau_{eff} \gtrapprox 0.8$ ms) is compatible with the target LITEBIRD TES time constant ($\tau_{eff} \approx 3$ ms) by a more than 300% margin: a large safety factor that addresses the difficulty in controlling this detector parameter.

In Section 8.1 I define a baseline LITEBIRD readout configuration. The NEI for this configuration, and three others that include speculative SQUID hardware, are forecast in Section 8.2. Those forecasts are shown as a function of detector properties in Section 8.3. In Section 8.4 the expected detector responsivity is calculated from LITEBIRD instrument specifications. That responsivity is used in Section 8.5 to calculate fractional noise increases for each scenario as a function of detector parameter choice. Finally, in Section 8.6 the resulting readout performance is shown for each LITEBIRD observing band.

8.1 BASELINE LITEBIRD DFMUX CONFIGURATION

There are a number of relatively minor changes to the DfMUX readout that together can yield ∼25% improvement in NEI over the baseline SPT-3G-like configuration. These improvements are small relative to what is gained by a mitigation of the additional current sharing exhibited in the SPT-3G readout, which is the product of current paths through parasitic capacitances to ground in the cryogenic electronics. A comparison between the NEI with and without this current sharing mitigation is shown in Figure 8.2. Each of the modifications that make up the proposed LITEBIRD baseline configuration have been demonstrated in the laboratory or on the sky to some degree. They are as follows:

REDUCED DYNAMIC RANGE REQUIREMENTS: The baseline LITEBIRD multiplexing factor is not much different than SPT-3G, but the required electrical bias power (P_J) is about an order of magnitude lower. This is primarily because the reduced radiative

2 In POLARBEAR-2 the typical detector operating resistance is 700 mΩ and the typical series resistance is (like SPT-3G) 150 mΩ to 350 mΩ. The distribution in these parameters encompasses the proposed values.

loading from space allows lower detector saturation powers (~1 pW vs ~7 pW). The total change in required P_J allows stronger attenuation of noise sources in the carrier and nuller signal chains. In these projections I've assumed a conservative factor of 3 reduction in required carrier and nuller dynamic range compared to SPT-3G. This is still far more dynamic range than will likely be necessary, but is sufficient to make the nuller and carrier DAC and amplifier noise contributions negligible.

4K NULLER CURRENT STIFFENING RESISTORS: Recall in Table 7.6 that the Johnson noise from the 3 kΩ current stiffening resistors contributes $3.3\frac{\mathrm{pA}}{\sqrt{\mathrm{Hz}}}$ in NEI at the SQUID. This can be improved by moving those resistors from the 300K electronics to the 4K electronics, lowering the Johnson noise to $0.38\frac{\mathrm{pA}}{\sqrt{\mathrm{Hz}}}$.[3]

INDUCTIVE BIASING: We presently convert the carrier current into a voltage bias using a 30 mΩ bias resistor at 4K. This incurs a $\sim 2\frac{\mathrm{pA}}{\sqrt{\mathrm{Hz}}}$ Johnson noise noise penalty (Table 7.8). The same thing can be accomplished using purely reactive impedances in the form of an inductive voltage divider (Figure 8.1). This incurs no Johnson noise penalty, and has been demonstrated in Haan et al., 2019 [38], with a new generation under development and testing by Tucker Elleflot. This eliminates the full $\sim 2\frac{\mathrm{pA}}{\sqrt{\mathrm{Hz}}}$ contribution to readout noise.

LOWER DYNAMIC IMPEDANCE SQUID OPERATION: As discussed in Section 7.4.1, it is possible to operate the SA13 SQUIDs at a $Z_{\mathrm{dyn}} \sim 300\ \Omega$ bias, rather than $Z_{\mathrm{dyn}} \sim 700\ \Omega$. This has been demonstrated on SPT-3G (with a limited number of SQUIDs, as discussed in Section 7.4.1), and in the lab using explicit stabilizing filters. This improves overall readout noise by $\sim 10\%$.

CURRENT SHARING MITIGATION: The parasitic current paths that generate additional current sharing in SPT-3G had not been optimized for in the electronics design, and so there is reason to believe they can be mitigated through simple design changes, such as increasing the impedance of any stray current return path (eg R_{ref}, from 7.2.5), or decreasing the capacitive coupling to a ground plane in the lithographic filters.[4] Recent

3 This change requires care to implement without generating an unwanted RC filter in the wiring harness, similar to χ_{output}. A termination resistor at the 4K-side of the wire-harness should be sufficient.

4 Though this must be balanced against the possibility of increased magnetic coupling between LC elements, which the ground planes mitigate.

laboratory results demonstrate promising improvements but this is an area that will require development resources, and cannot simply clone existing SPT-3G-like designs. Even if this mitigation is maximally successful, there remains the fundamental current sharing between the SQUID input inductance and the comb impedance, which becomes the dominant noise mechanism.

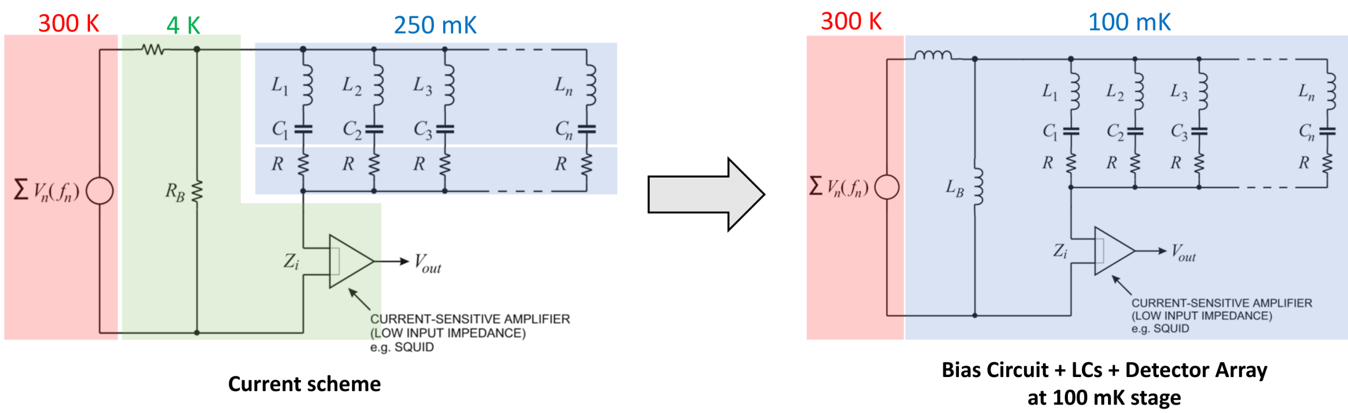

Figure 8.1: A comparison between the traditional bias circuit (left) and an inductive bias design (right). The inductive divider would deliver a voltage bias that is frequency independent like the bias resistor, but without any Ohmic noise or power dissipation. Such a design would use L_B ∼4 nH for the dividing inductor, and 6 µH for the series inductance. Image provided by Aritoki Suzuki, from de Haan et al., 2018 [23].

8.2 NEI PERFORMANCE FORECASTING

For the results in this forecasting I present four readout design scenarios:

BASELINE LITEBIRD CONFIGURATION: The baseline LiteBIRD readout configuration requires no additional SQUID development; it assumes SQUIDs that exhibit the same noise, transimpedance, and dynamic impedance, as the SA13 squids on SPT-3G. It does require several design modifications to the cryogenic readout circuit, described in Section 8.1. Of these, the most important is a mitigation of the additional current sharing.[5] Figure 8.3 breaks down the individual noise components in this baseline scenario.

5 This mitigation I assume to be equivalent to the change of R_{ref} =10 kΩ in the electronic noise model presented in Figure 7.13.

MK SQUID NOISE: The LiteBIRD design places the SQUIDs at sub-Kelvin, rather than at the 4 Kelvin stage as in SPT-3G. SQUID noise scales as the $\sqrt{\text{Temperature}}$ [30], but early tests indicate it may be a challenge to prevent them from self-heating. This scenario assumes it is possible to cool the SQUID Josephson junctions to 500 mK, and scales the projected SQUID noise appropriately from the SA13 values at 4 Kelvin.[6] Figure 8.4 breaks down the individual noise components in such a scenario.

30 nH INPUT INDUCTANCE SQUIDS: A lower input inductance reduces the current sharing factor and dramatically improves readout noise performance. This assumes a modest reduction in SQUID input inductance from 70 nH to 30 nH, with no change in the other parameters ($Z_{\text{trans}} = 700\ \Omega$, $Z_{\text{dyn}} = 300\ \Omega$). Figure 8.5 breaks down the individual noise components in such a scenario. This is a more advantageous configuration than the mK SQUID noise scenario, despite the fact that the mK SQUID configuration exhibits a lower minimum noise.

10 nH INPUT INDUCTANCE SQUIDS: This scenario assumes a SQUID design with a 10 nH input inductance, similar to ones that had previously been investigated for use on Polarbear-2. Those SQUIDs were unsuitable due to stability issues and prohibitively high dynamic impedance. This speculative item assumes those issues are solved. Figure 8.6 breaks down the individual noise components in such a scenario.

An overview of the readout NEI improvements in each of these scenarios is shown in Figure 8.2.

8.3 NEI VS DETECTOR PARAMETERS

The NEI of the system is coupled to the choice of detector operating resistance through the current sharing mechanism (Equation 7.3). This is particularly acute for readout configurations with large SQUID input coil inductance and low detector resistances. Figure 8.7 shows the relationship between total NEI and the quantity ($R_{\text{TES}} + R_s$) for each readout configuration.

6 In general, as described in Drung, 2016 [30], there is reason to be skeptical that simply cooling SQUIDs designed for 4K will be sufficient to benefit from the improved noise potentiality of operating at lower temperature; however there is promising development in new commercial SQUIDs that do achieve predicted sub-Kelvin noise. This scenario simply assumes a SQUID that benefits from the sub-Kelvin operation, but not necessarily from any lower input inductance redesign.

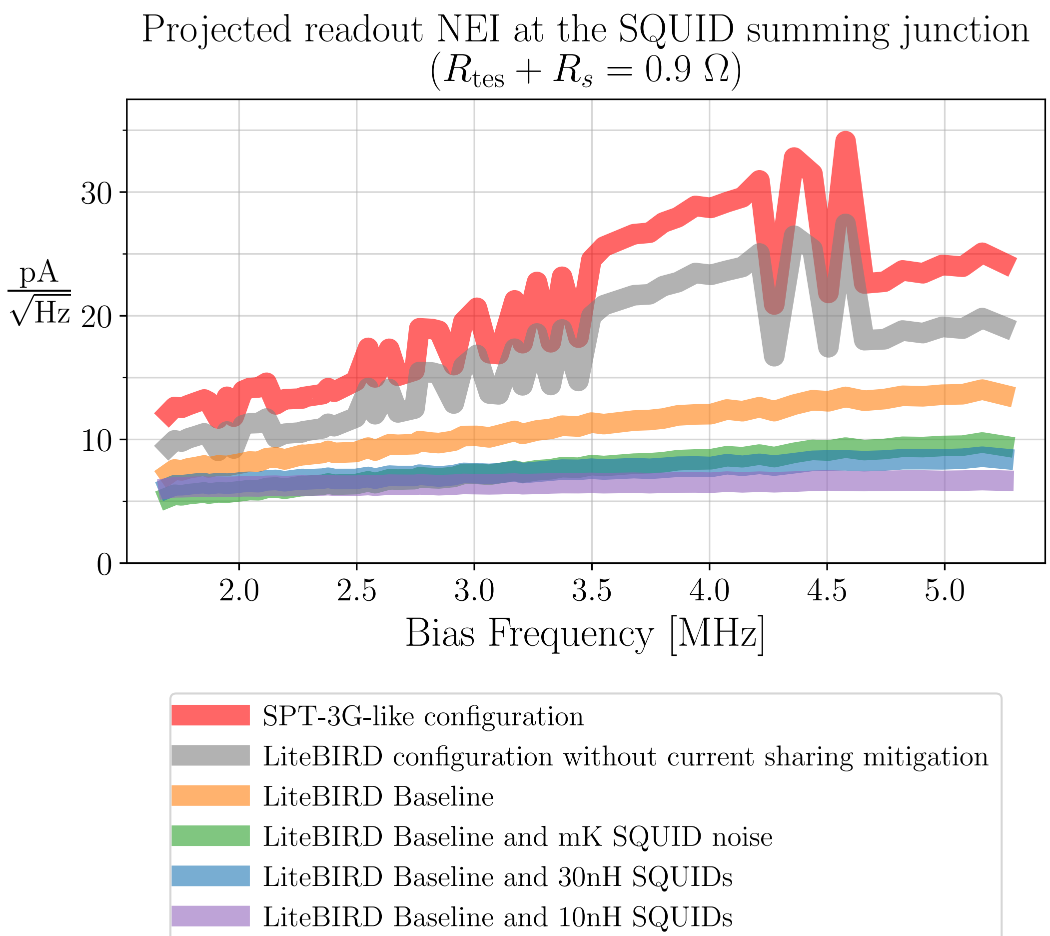

Figure 8.2: An overview is given above for the expected NEI in each of the scenarios considered. These are forecast using $R_{\mathrm{TES}} + R_s$=0.9 Ω, implied from the proposed target detector parameters. Mitigation of the additional current sharing noise is the single biggest possible improvement, and will be a requisite to meet the LiteBIRD readout noise target. The SPT-3G-like configuration exhibits a higher projected NEI than seen on SPT-3G (Figure 7.20) because of the lower TES operating resistance.

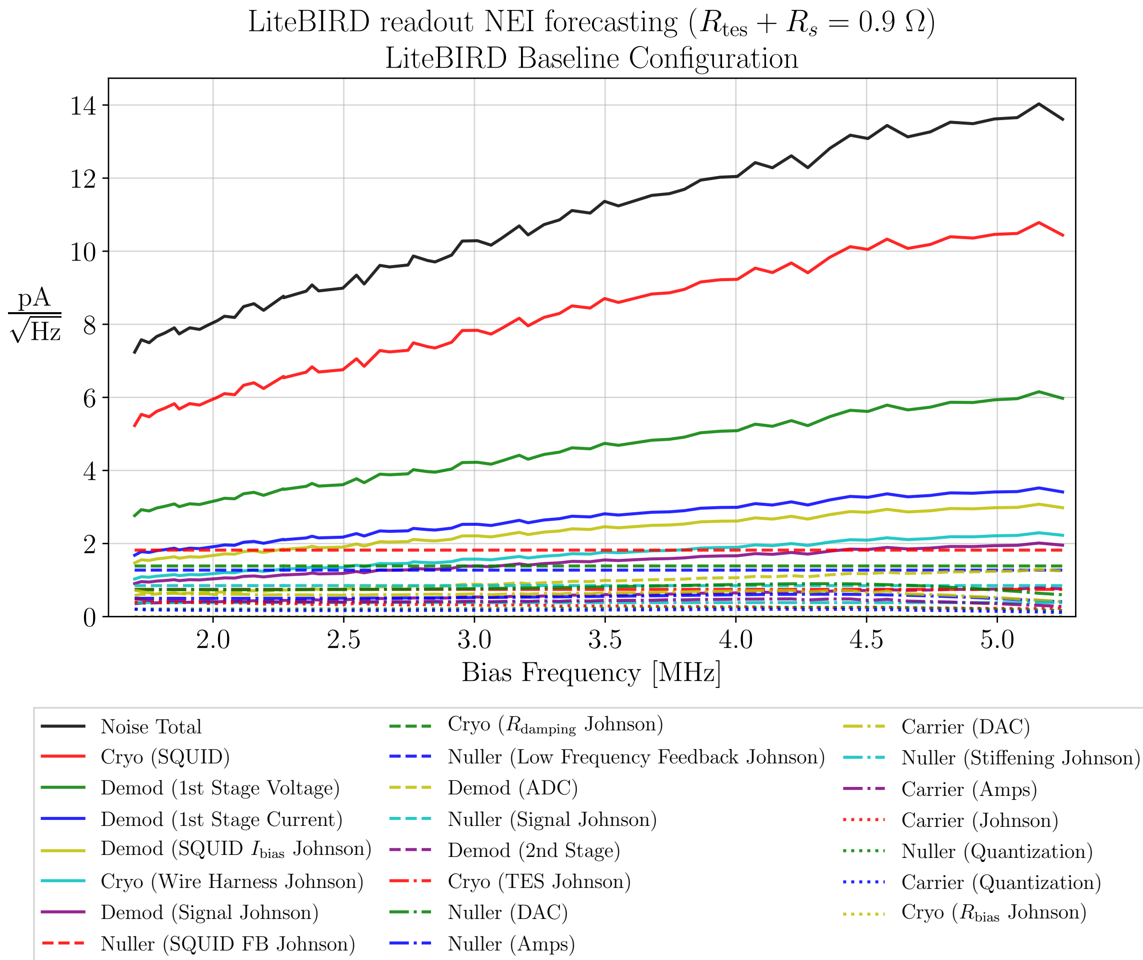

Figure 8.3: The above figure shows a full breakdown of the associated noise components for the scenario in which the suggested baseline LiteBIRD improvements are made, but no additional SQUID development occurs. Each noise source that appears in the legend is defined in Section 7.1.

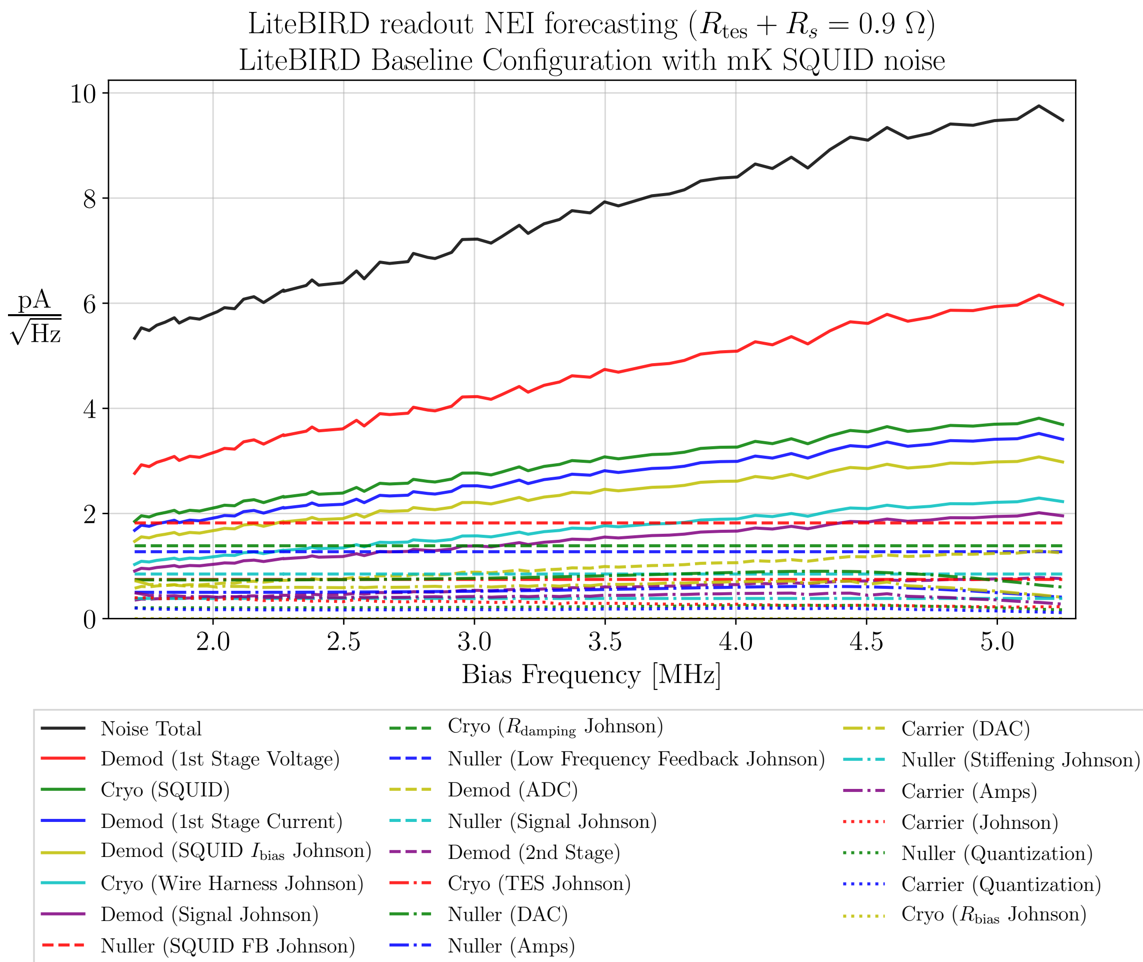

Figure 8.4: The above figure shows a full breakdown of the associated noise components for the scenario in which the suggested baseline LiteBIRD improvements are made, and additionally the SQUID Josephson junctions are cooled to 500 mK. Each noise source that appears in the legend is defined in Section 7.1.

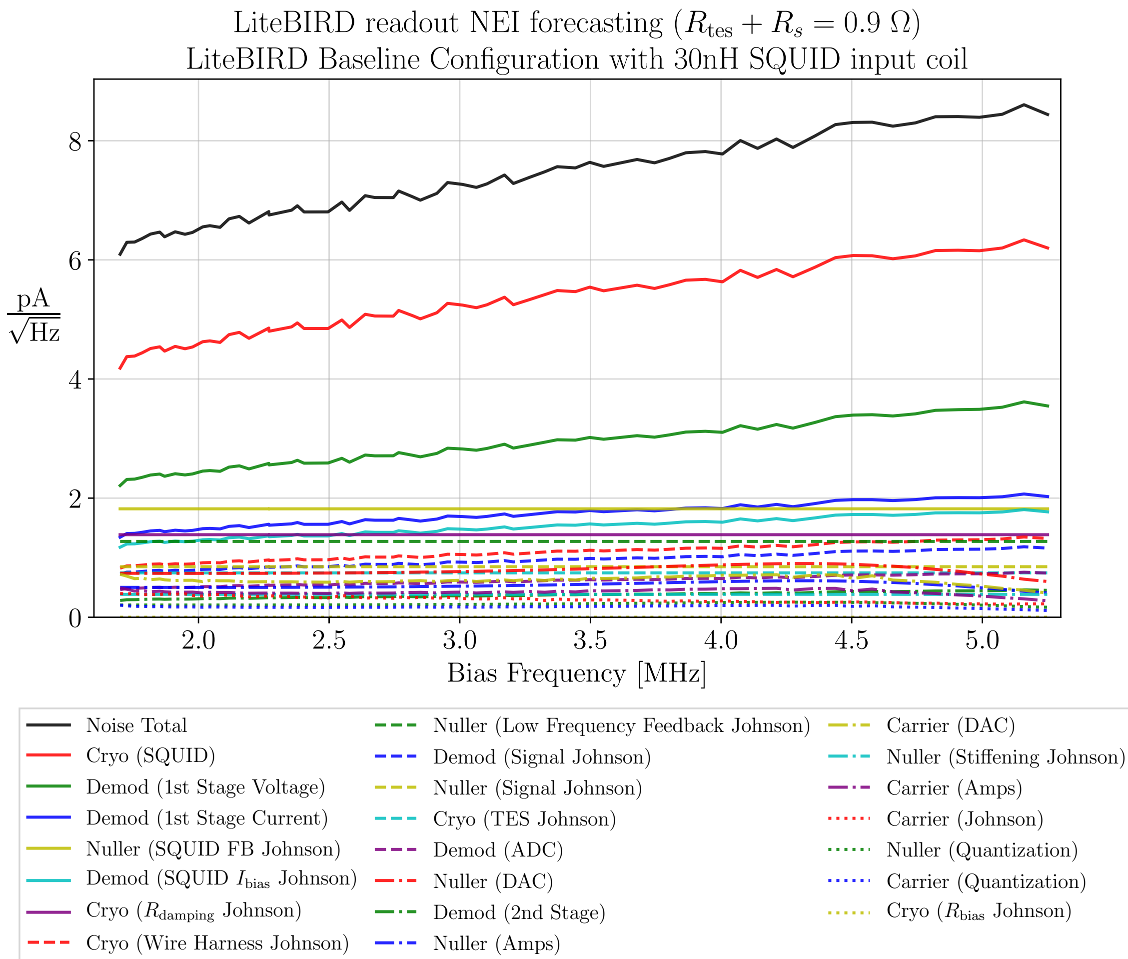

Figure 8.5: The above figure shows a full breakdown of the associated noise components for the scenario in which the suggested baseline LiteBIRD improvements are made, and additional SQUID development enables 30 nH input inductance and Z_{dyn}=300 Ω, with equivalent Z_{trans}. Each noise source that appears in the legend is defined in Section 7.1.

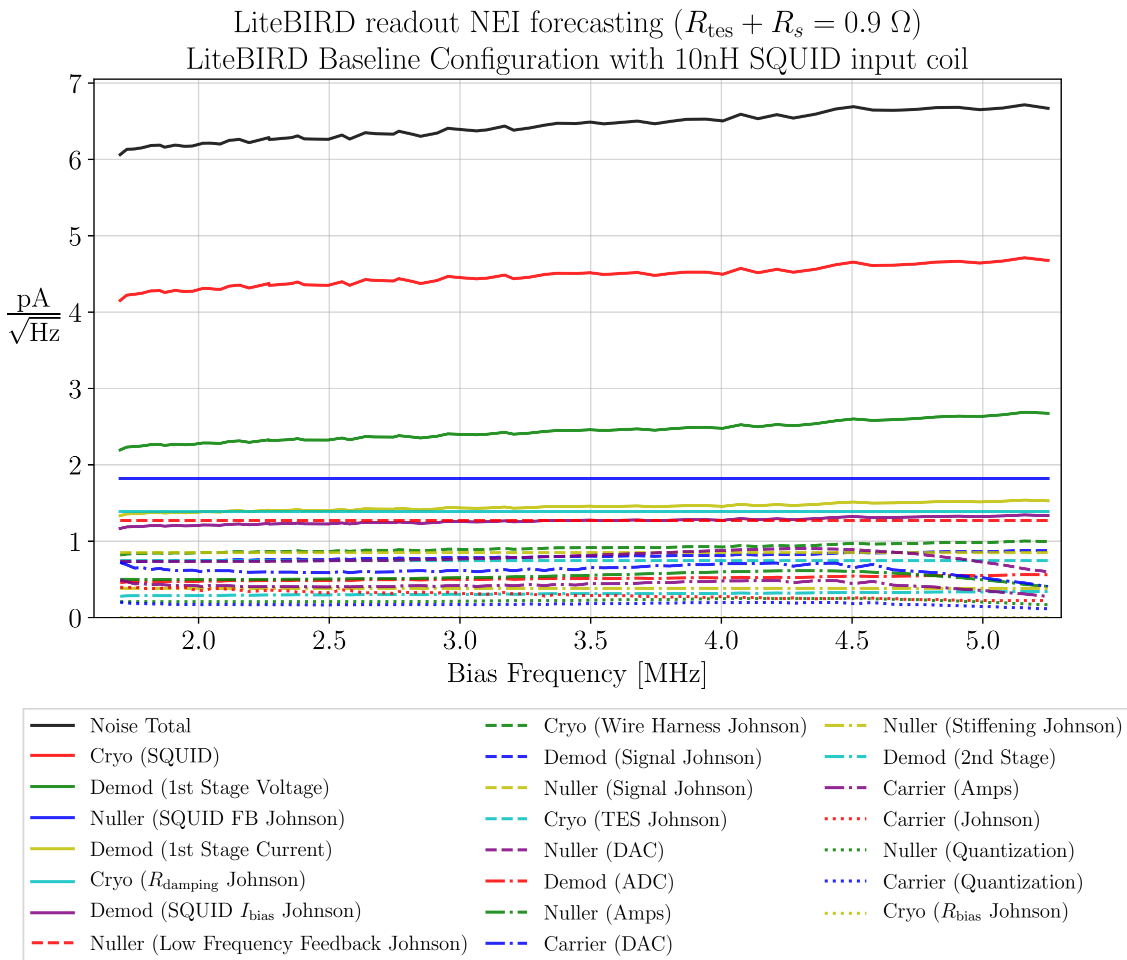

Figure 8.6: The above figure shows a full breakdown of the associated noise components in the scenario in which the suggested baseline LiteBIRD improvements are made, and additional SQUID development enables 10 nH input inductance and Z_{dyn}=300 Ω, with equivalent Z_{trans}. Each noise source that appears in the legend is defined in Section 7.1.

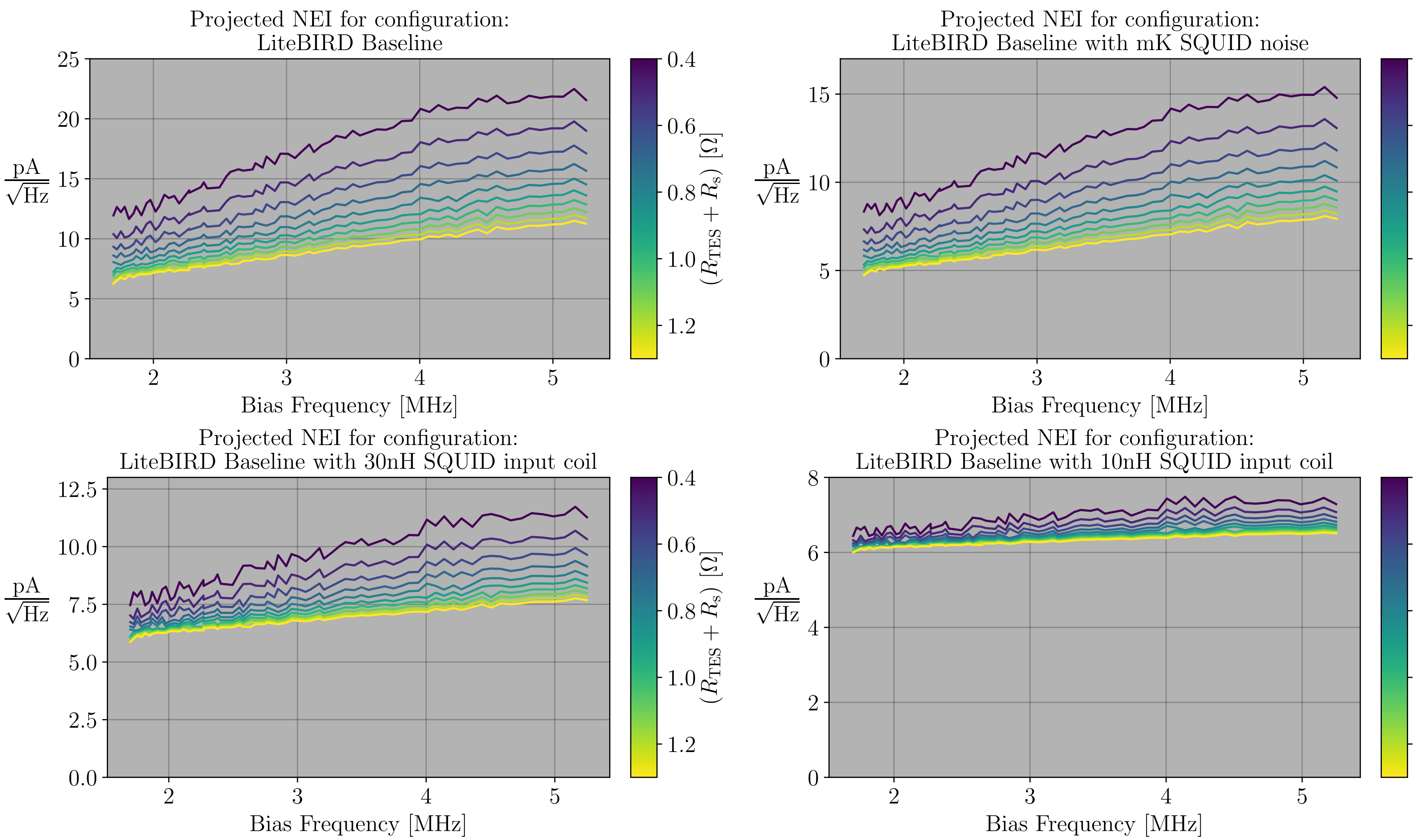

Figure 8.7: Shown above are the NEI projections as a function of $(R_{\text{TES}} + R_s)$ for the four LiteBIRD configurations investigated. In the top two configurations, where the SQUID input inductance remains 70 nH, the NEI is a strong function of $(R_{\text{TES}} + R_s)$. Ordinarily, lower detector resistances lead to better instrument performance because of the associated increase in responsivity. In the two top configurations this is countered by a steep rise in NEI, which disfavours configurations with very low detector resistance. As the SQUID inductance is reduced, so too is the sensitivity of NEI to $(R_{\text{TES}} + R_s)$, allowing more flexibility in the choice of operating conditions.

8.4 FORECASTING RESPONSIVITY

A useful formulation of the equation for DfMUX detector responsivity (Equation 3.13) takes advantage of the following equality, which relates detector voltage bias to detector saturation power (P_{sat}) and incident optical power (P_{opt}),

$$\sqrt{V_{(\text{TES bias, rms})}} = \sqrt{P_{\text{elec}}\ R_{\text{TES}}} = \sqrt{(P_{\text{sat}} - P_{\text{rad}})R_{\text{TES}}}\,. \tag{8.1}$$

A rule of thumb is to design for a safety margin such that $P_{\text{sat}} = 2.5P_{\text{rad}}$, and therefore $P_{\text{elec}} = 1.5P_{\text{rad}}$, ensuring that most of the power applied to the detector is electrical, and can accommodate changing loading conditions.[7] The full responsivity expression then becomes

$$S = \frac{-\sqrt{2}}{\sqrt{1.5P_{\text{rad}}\ R_{\text{tes}}}}\left(\frac{R_{\text{tes}}\mathcal{L}}{R_{\text{tes}} + z_s + \mathcal{L}(R_{\text{tes}} - z_s)}\right)\,. \tag{8.2}$$

LiteBIRD design documents already include calculations for P_{rad} at every observing band, and therefore the associated responsivity may be calculated for our various readout configuration scenarios.[8]

The 40 GHz band, the lowest observing frequency on the instrument, will be the most challenging from the perspective of readout noise. That band is expected to receive relatively large incident radiative power (which degrades responsivity), but will have low intrinsic photon noise (due to the low observing frequency, Equation 3.18). These qualities conspire to require a much lower readout NEI to achieve the same fractional noise increase compared with higher frequency observing bands. The relationship between R_{TES}, R_s, and S is shown visually for the 40 GHz band in Figure 8.8.

The increased responsivity that comes from real series resistance with the TES plays an enormous role in the potential instrument performance. Consider that the most optimistic of the proposed NEI configurations (10 nH SQUIDs) provides a factor of approximately 2 improvement in maximum NEI. The same overall improvement to instrument noise could be gained at $R_{\text{TES}} = 0.6\ \Omega$ in the difference between $R_s = 0\ \Omega$ and $R_s = 0.35\ \Omega$. This is a

7 Ground-based systems typically use a safety factor of $P_{\text{elect}} = 2.5P_{\text{rad}}$, which ensures the detectors won't saturate during poor weather or warm days. Space-based systems require a smaller safety factor, which is primarily insurance on the fabrication control of the saturation power, as well as to accommodate different temperatures of the optical elements or cryogenic base temperatures.

8 The expected P_{rad} is calculated based on expected source emission, cryogenic bath temperatures, the emissivity of various optical elements, and the total optical efficiency.

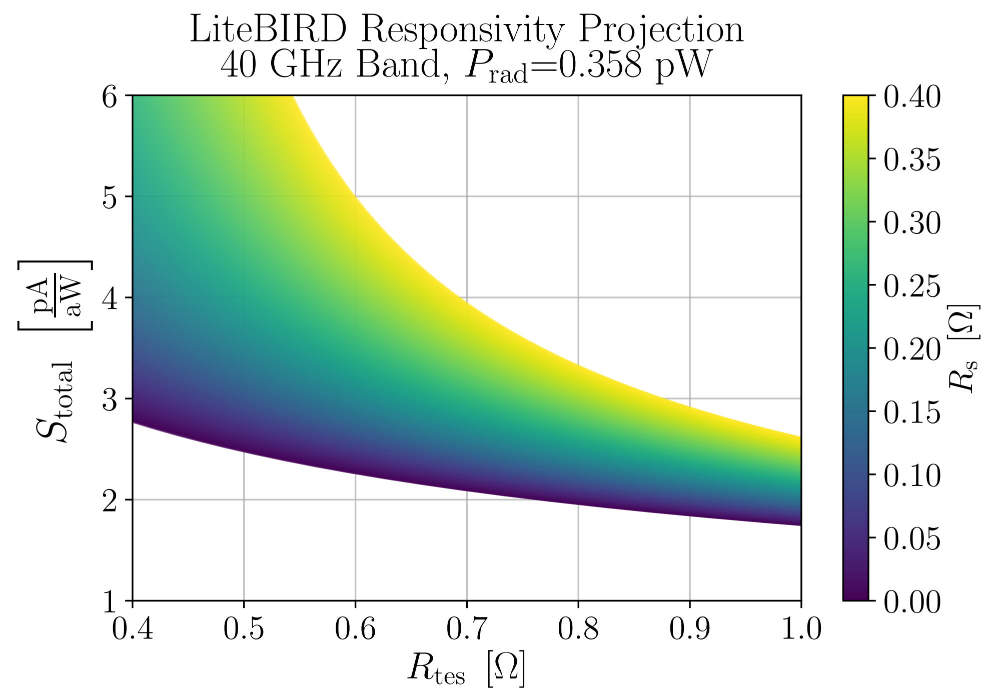

Figure 8.8: Projected responsivity as a function of R_{TES} and R_s in the most noise-constrained LiteBIRD observing band. Notice how non-linearly the responsivity increases as a function of additional R_s. The range in R_s plotted here matches the range of Thévenin equivalent series resistance with the TES seen in SPT-3G and Polarbear-2 instruments. The difference in responsivity between those extrema can be a factor of 2 or more.

strong motivator to intentionally target responsivity-boosting series resistances – and also a warning for the potential consequences of failing to control those values.

8.5 LITEBIRD NOISE PERFORMANCE VS DETECTOR PARAMETERS

Lower detector operating resistances with high series resistance will maximize detector responsivity, but too radical a departure from the operating regimes with which we are familiar may invite unknown issues. Detector linearity will degrade if the responsivity becomes a strong function of R_{TES},[9] and previously hidden parasitic impedances may become important once the comb is operating at very low impedance.

Relying too heavily on boosted responsivity from R_s also shrinks our margin of error in the fabrication parameters that regulate R_s. The best means to control this is probably to minimize the series resistance within the lithography, and then supplement it with precision resistive elements. Based on the work presented in Section 6.2.3, an R_s of $0.3\,\Omega$ would meet the requirements. This is sufficiently high that lithography contributions should never exceed it, and also equivalent to values fielded in SPT-3G and POLARBEAR-2.

Figure 8.9 (top) shows the calculated noise increase in the 40 GHz band for each configuration, using the proposed target parameters. It is possible to meet the requirement in every proposed configuration, although the baseline configuration would benefit from strategic allocation of lower bias frequencies to detectors from highly constrained readout bands. Less constrained observing bands, such as the 402 GHz band, easily meet the target noise requirement across all configurations (Figure 8.9, right).

The full ($R_{\text{TES}},\ R_s$) parameter space for each scenario using the LITEBIRD 40 GHz band is given in Figure 8.10. The most striking aspect of this parameter space is how critical R_s is in every readout configuration.

9 CMB experiments have a greater tolerance with respect to detector linearity than other experiments using TES detectors. This is because the instantaneous signal-to-noise is typically ≤ 1, and so the detector dynamic range doesn't need to be as large as required to accurately image bright sources. Still, there are limits to this tolerance. For LITEBIRD those limits may be related to changes in radiative power due to a rotating half-wave plate in front of the topics.

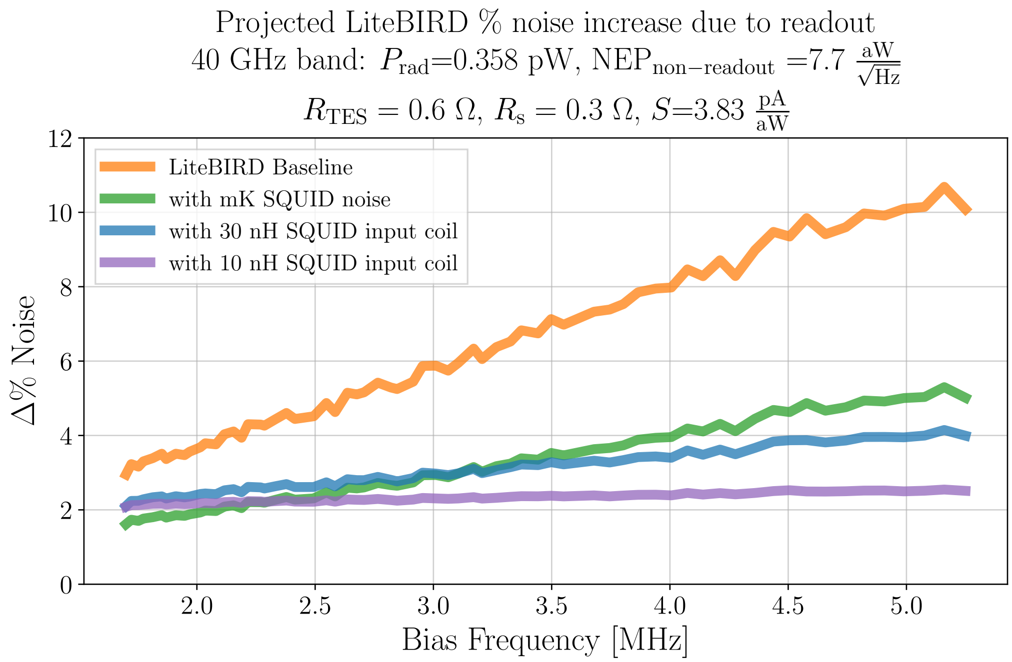

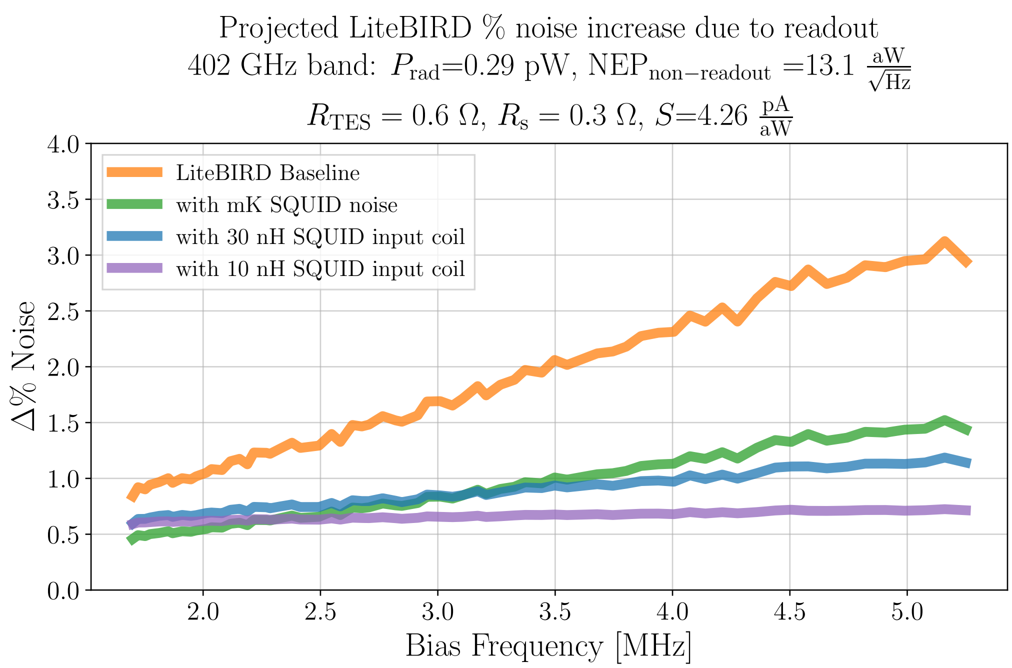

Figure 8.9: The above figures show the system noise increase due to readout as a function of bias frequency for the proposed target parameters in the most constrained (top, 40 GHz) and least constrained (bottom, 402 GHz) LiteBIRD bands. For the 40 GHz band the baseline configuration only exceeds the target of <10% increase at the highest bias frequencies. There will be very few of these detectors aboard LiteBIRD (<60), and for reliability reasons they will be spread out over several SQUID modules, and therefore could be allocated only the lowest bias frequencies. Detectors at higher observing frequencies comfortably achieve the target noise increase for all potential configurations. This is shown for all bands in Table 8.1.

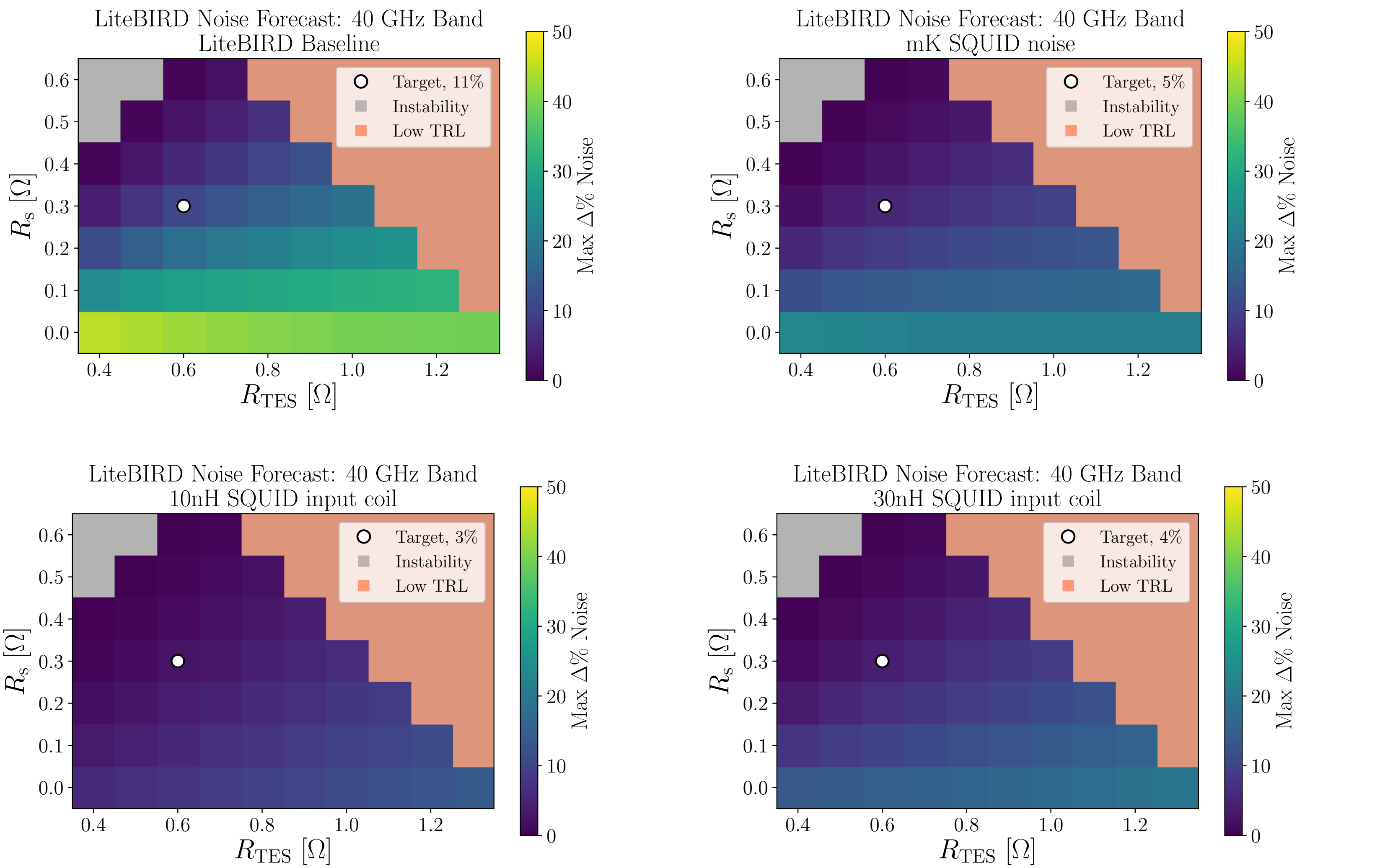

Figure 8.10: The maximum $\Delta\%$ noise increase across the bias frequencies for the 40 GHz LiteBIRD band is shown above, for each configuration and choice of R_{TES} and R_s. The white dots indicate the proposed target R_{TES} and R_s parameters, and the achieved maximum percent noise increase; the gray regions indicate parameters that violate the DC stability criteria; and the salmon-colored region is considered lower TRL due to the relatively high total $R_{\mathrm{TES}} + R_s$ (roughly equivalent to the mean SPT-3G parameters), which may require larger inductance filters to satisfactorily mitigate crosstalk. The 11% noise increase for proposed parameters in the baseline configuration (top left) assumes a worst-case scenario with no strategic allocation of the most sensitive bands to low bias frequencies. In all scenarios it is impossible to reach a $< 10\%$ NEI increase target without some designed-for non-zero R_s.

8.6 LITEBIRD NOISE PERFORMANCE FORECAST BY BAND

Table 8.1 contains noise projection parameters for my proposed readout configuration ($R_{\text{TES}} = 0.6\ \Omega$ and $R_s = 0.3\ \Omega$) in each LiteBIRD band. The results indicate that it will be possible to meet a target of $< 10\%$ noise increase due to readout across the bands if the following conditions are met:

1. The additional current sharing, due to current paths through parasitic capacitances, is mitigated within the cryogenic electronics design (as described in Section 7.2.5).

2. Strategic use of a real series resistance with the TES (R_s) is employed to boost the detector responsivity. As in SPT-3G, this is a parameter that the overall instrument noise performance will remain very sensitive to in all readout configurations. A failure to design for sufficient R_s will incur substantial noise penalties. Table 8.2 calculates the noise projections for an R_s=200 mΩ configuration, which nearly doubles the noise increase due to readout, especially in the most marginal observing bands. Despite this sensitivity to $\mathcal{O}(100\,\text{m}\Omega)$ variations, it should be possible to precisely control R_s with the appropriate lithography geometries.

Meeting each of these conditions will require close coordination between the detector fabrication, SQUID development, cryogenic lithography fabrication, and end-to-end testing teams. This effort would benefit from the success of any of the on-going SQUID development projects, the most effective of which would be a reduction in the SQUID input inductance. The Polarbear-2 collaboration has characterized SQUIDs with only 10 nH input inductance, including operating them end-to-end with detectors [38, 45]. However, they have suffered from stability issues and relatively high dynamic impedance, which will have to be solved.

LiteBIRD Noise Forecast

Target: <10% noise increase, R_{TES}=600 mΩ, R_s=300 mΩ

				Baseline only	mK SQUID noise	30 nH SQUIDs	10nH SQUIDs
Band GHz	$\boldsymbol{P}_{\mathbf{rad}}$ pW	$\boldsymbol{S}$ $\frac{\mathrm{pA}}{\mathrm{aW}}$	$\mathbf{NEP}_{\mathbf{ext}}$ $\frac{\mathrm{aW}}{\sqrt{\mathrm{Hz}}}$	$\mathbf{NEP}_{\mathbf{readout}}$ ($\mathbf{NEP}_{\mathbf{tot}}$) $\frac{\mathrm{aW}}{\sqrt{\mathrm{Hz}}}$ $\left(\frac{\mathrm{aW}}{\sqrt{\mathrm{Hz}}}\right)$ [+Δ%]	$\mathbf{NEP}_{\mathbf{readout}}$ ($\mathbf{NEP}_{\mathbf{tot}}$) $\frac{\mathrm{aW}}{\sqrt{\mathrm{Hz}}}$ $\left(\frac{\mathrm{aW}}{\sqrt{\mathrm{Hz}}}\right)$ [+Δ%]	$\mathbf{NEP}_{\mathbf{readout}}$ ($\mathbf{NEP}_{\mathbf{tot}}$) $\frac{\mathrm{aW}}{\sqrt{\mathrm{Hz}}}$ $\left(\frac{\mathrm{aW}}{\sqrt{\mathrm{Hz}}}\right)$ [+Δ%]	$\mathbf{NEP}_{\mathbf{readout}}$ ($\mathbf{NEP}_{\mathbf{tot}}$) $\frac{\mathrm{aW}}{\sqrt{\mathrm{Hz}}}$ $\left(\frac{\mathrm{aW}}{\sqrt{\mathrm{Hz}}}\right)$ [+Δ%]
40	0.358	3.83	7.7	3.7 (8.5) [11%]	2.5 (8.1) [5%]	2.2 (8.0) [4%]	1.8 (7.9) [3%]
50	0.386	3.69	8.1	3.8 (9.0) [10%]	2.6 (8.5) [5%]	2.3 (8.4) [4%]	1.8 (8.3) [2%]
60	0.3	4.19	7.3	3.4 (8.0) [10%]	2.3 (7.6) [5%]	2.1 (7.6) [4%]	1.6 (7.4) [2%]
68	0.367	3.79	8.4	3.7 (9.1) [9%]	2.6 (8.7) [5%]	2.3 (8.7) [4%]	1.8 (8.5) [2%]
78	0.367	3.79	8.5	3.7 (9.3) [9%]	2.6 (8.9) [4%]	2.3 (8.8) [3%]	1.8 (8.7) [2%]
89	0.363	3.81	8.7	3.7 (9.4) [9%]	2.6 (9.0) [4%]	2.3 (8.9) [3%]	1.8 (8.8) [2%]
100	0.356	3.84	8.8	3.7 (9.5) [8%]	2.5 (9.1) [4%]	2.2 (9.1) [3%]	1.7 (9.0) [2%]
119	0.449	3.42	10.3	4.1 (11.1) [8%]	2.8 (10.7) [4%]	2.5 (10.6) [3%]	2.0 (10.5) [2%]
140	0.44	3.46	10.7	4.1 (11.4) [7%]	2.8 (11.0) [3%]	2.5 (11.0) [3%]	1.9 (10.8) [2%]
166	0.416	3.56	10.9	3.9 (11.6) [6%]	2.7 (11.3) [3%]	2.4 (11.2) [2%]	1.9 (11.1) [1%]
195	0.386	3.69	11.2	3.8 (11.8) [6%]	2.6 (11.5) [3%]	2.3 (11.4) [2%]	1.8 (11.3) [1%]
235	0.603	2.95	15.1	4.8 (15.8) [5%]	3.3 (15.5) [2%]	2.9 (15.4) [2%]	2.3 (15.3) [1%]
280	0.486	3.29	14.5	4.3 (15.1) [4%]	3.0 (14.8) [2%]	2.6 (14.7) [2%]	2.0 (14.6) [1%]
337	0.384	3.70	13.9	3.8 (14.4) [4%]	2.6 (14.1) [2%]	2.3 (14.1) [1%]	1.8 (14.0) [1%]
402	0.29	4.26	13.1	3.3 (13.5) [3%]	2.3 (13.3) [2%]	2.0 (13.2) [1%]	1.6 (13.2) [1%]

Table 8.1: The above table shows the relevant parameterization of the LiteBIRD readout noise performance under the recommended detector parameters, for each observing band and each readout configuration. Calculations are performed for the bias frequency at which the readout noise increase is maximum, and so represent an upper limit: in all bands and all configurations the noise target is achieved for bias frequencies below approximately 4.5 MHz (Figure 8.9). Items in red indicate a maximum noise increase greater than 10%. The $\mathrm{NEP}_{\mathrm{ext}}$ column combines the expected photon and phonon noise for detectors in that observing band, but this is dominated by photon noise. All LiteBIRD detectors have phonon noise between 4 and 5.6 $\frac{\mathrm{aW}}{\sqrt{\mathrm{Hz}}}$, proportional to P_{rad}.

LiteBIRD Noise Forecast

Target: <10% noise increase due to readout, R_{TES}=600 mΩ, R_s=200 mΩ

				Baseline only	mK SQUID noise	30 nH SQUIDs	10nH SQUIDs
Band GHz	$\boldsymbol{P}_{\textbf{rad}}$ pW	$\boldsymbol{S}$ $\frac{\text{pA}}{\text{aW}}$	$\textbf{NEP}_{\textbf{ext}}$ $\frac{\text{aW}}{\sqrt{\text{Hz}}}$	$\textbf{NEP}_{\textbf{readout}}$ $(\textbf{NEP}_{\textbf{tot}})$ $\frac{\text{aW}}{\sqrt{\text{Hz}}}$ $\left(\frac{\text{aW}}{\sqrt{\text{Hz}}}\right)$ [+Δ%]	$\textbf{NEP}_{\textbf{readout}}$ $(\textbf{NEP}_{\textbf{tot}})$ $\frac{\text{aW}}{\sqrt{\text{Hz}}}$ $\left(\frac{\text{aW}}{\sqrt{\text{Hz}}}\right)$ [+Δ%]	$\textbf{NEP}_{\textbf{readout}}$ $(\textbf{NEP}_{\textbf{tot}})$ $\frac{\text{aW}}{\sqrt{\text{Hz}}}$ $\left(\frac{\text{aW}}{\sqrt{\text{Hz}}}\right)$ [+Δ%]	$\textbf{NEP}_{\textbf{readout}}$ $(\textbf{NEP}_{\textbf{tot}})$ $\frac{\text{aW}}{\sqrt{\text{Hz}}}$ $\left(\frac{\text{aW}}{\sqrt{\text{Hz}}}\right)$ [+Δ%]
40	0.358	3.11	7.7	4.8 (9.1) [18%]	3.3 (8.4) [9%]	2.9 (8.2) [7%]	2.2 (8.0) [4%]
50	0.386	3.00	8.1	5.0 (9.5) [17%]	3.5 (8.8) [9%]	3.0 (8.7) [7%]	2.3 (8.4) [4%]
60	0.3	3.40	7.3	4.4 (8.5) [17%]	3.1 (7.9) [8%]	2.6 (7.7) [6%]	2.0 (7.5) [4%]
68	0.367	3.08	8.4	4.9 (9.7) [16%]	3.4 (9.0) [8%]	2.9 (8.9) [6%]	2.2 (8.6) [3%]
78	0.367	3.08	8.5	4.9 (9.8) [15%]	3.4 (9.2) [8%]	2.9 (9.0) [6%]	2.2 (8.8) [3%]
89	0.363	3.09	8.7	4.9 (9.9) [15%]	3.4 (9.3) [7%]	2.9 (9.1) [5%]	2.2 (8.9) [3%]
100	0.356	3.12	8.8	4.8 (10.0) [14%]	3.3 (9.4) [7%]	2.9 (9.2) [5%]	2.2 (9.0) [3%]
119	0.449	2.78	10.3	5.4 (11.6) [13%]	3.7 (10.9) [6%]	3.2 (10.8) [5%]	2.4 (10.6) [3%]
140	0.44	2.81	10.7	5.3 (11.9) [12%]	3.7 (11.3) [6%]	3.2 (11.1) [4%]	2.4 (10.9) [3%]
166	0.416	2.89	10.9	5.2 (12.1) [11%]	3.6 (11.5) [5%]	3.1 (11.4) [4%]	2.4 (11.2) [2%]
195	0.386	3.00	11.2	5.0 (12.2) [10%]	3.5 (11.7) [5%]	3.0 (11.6) [4%]	2.3 (11.4) [2%]
235	0.603	2.40	15.1	6.3 (16.4) [8%]	4.3 (15.7) [4%]	3.7 (15.6) [3%]	2.8 (15.4) [2%]
280	0.486	2.67	14.5	5.6 (15.5) [7%]	3.9 (15.0) [4%]	3.3 (14.9) [3%]	2.5 (14.7) [2%]
337	0.384	3.01	13.9	5.0 (14.8) [6%]	3.5 (14.3) [3%]	3.0 (14.2) [2%]	2.3 (14.1) [1%]
402	0.29	3.46	13.1	4.3 (13.8) [5%]	3.0 (13.4) [3%]	2.6 (13.3) [2%]	2.0 (13.2) [1%]

Table 8.2: The above table shows the relevant parameterization of the maximum LiteBIRD readout noise performance, in each band and configuration, in a scenario in which R_{TES}=600 mΩ as targeted but R_s is only 200 mΩ, rather than the target of 300 mΩ. This demonstrates the precision needed in the fabrication of R_s. In practice we have some flexibility in being able to precisely choose R_{TES} in situ, but this won't help if R_s is sufficiently under target. Items in red indicate a maximum noise increase greater than 10%, and represent upper limits, as they take the worst achieved value across all bias frequencies. All configurations meet the noise requirement below 3 MHz. The NEP_{ext} column combines the expected photon and phonon noise for detectors in that observing band, but this is dominated by photon noise. All LiteBIRD detectors have phonon noise between 4 and 5.6 $\frac{\text{aW}}{\sqrt{\text{Hz}}}$, proportional to P_{rad}.

8.7 SPECULATIVE OPTIMIZATION: BANDWIDTH COMPRESSION

There are a number of further optimizations that are possible that haven't been modeled in detail here. The most straight-forward of these is a compression and shifting of the readout bandwidth to approximately 1 MHz to 3 MHz, rather than the current range of approximately 1.6 MHz to 5.5 MHz. This would require an increase in lithographic capacitor area and overall LC chip size, but should still be achievable. In SPT-3G, such a compression would result in a large increase in crosstalk, but the LiteBIRD design has intrinsically much lower crosstalk, owing to lower detector operating resistances and a move to a linear frequency scheduling. Such a projection for a LiteBIRD-like configuration was shown in Figure 5.7, and achieved mean nearest-neighbor crosstalk of approximately 0.02%. Figure 8.11 simulates the expected crosstalk for a bandwidth-compressed LiteBIRD design. The resulting projected crosstalk is lower than experienced with SPT-3G, even if we assume LC frequency scatter that is the highest median value measured in SPT-3G (Figure 6.7c). A modest improvement in the scatter of LC resonator frequencies to $\sigma F < 3$ kHz should be achievable using a lithography design that minimizes the parameters described in Section 6.2.3, and would further minimize crosstalk.

Such a change would sidestep the problem of current sharing noise without resolving it, by only populating detectors in the lower NEI regime. There is no reason why the LiteBIRD cryogenic filter design should occupy as high a bandwidth as SPT-3G, given the improved crosstalk performance by design, and the clear benefits to operating at lower bias frequencies. A bandwidth change similar to the one above would enable the readout noise requirement to be met in all four configurations, at each observing band, with considerably relaxed margins of error in the detector and readout parameters (specifically R_s, which could then fluctuate down to 200 mΩ without violating the noise requirement at any frequency).

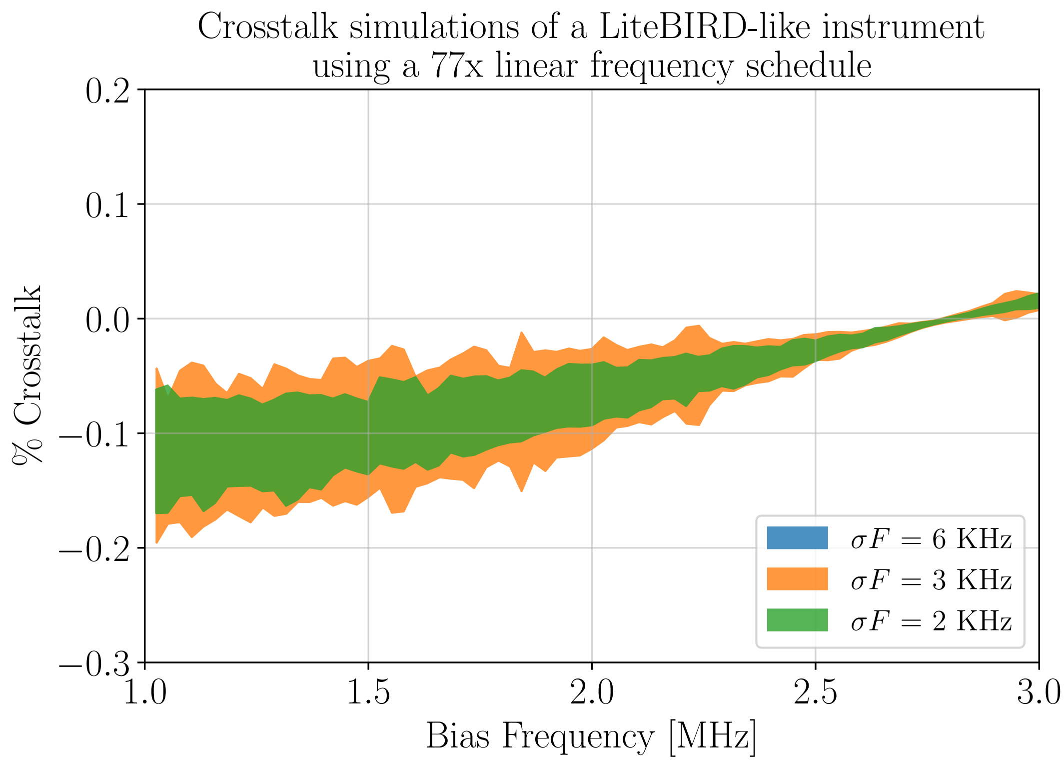

Figure 8.11: Projected crosstalk in a LiteBIRD-like instrument with a compressed bandwidth of 1 MHz to 3 MHz. In such a configuration the target LC resonance spacing would be ∼26 kHz, only 3 kHz narrower than the most narrow SPT-3G spacing. Even with no improvement to scatter in the LC resonator frequencies, the resulting crosstalk would be lower than observed in SPT-3G. Such a strategy would mitigate the largest contribution to readout NEI due to current sharing at high bias frequencies.

9 CONCLUDING REMARKS

A measurement or meaningful non-detection of primordial inflationary gravity waves will require at least an order of magnitude increase in sensitivity from the current best measurements. Such increases in sensitivity are dictated primarily by the number of background limited detectors on-sky. The planned LiteBIRD satellite telescope is designed for this measurement, and will have a focal plane with over *two orders of magnitude* more background limited detectors than the previous space-based CMB platform, Planck. Many of the primary challenges to increasing focal plane density and sensitivity come from limitations in readout.

The performance of the SPT-3G readout demonstrates that DfMUX multiplexing architecture succeeds in achieving the low-noise, high-density, and high-multiplexing required for the next generation of CMB measurements, and LiteBIRD, to succeed. More importantly, through a re-analysis of the theoretical framework for DfMUX we are able to update and complete the readout model for stability, crosstalk, and noise, in this higher-bandwidth and higher-multiplexing regime. This demonstrates a key building block that makes LiteBIRD technologically feasible.

9.1 DIGITAL ACTIVE NULLING

A cornerstone of the DfMUX readout system is the use of active feedback (DAN), which nulls signals at the SQUID summing junction in order to linearize the SQUID, and mitigate the series reactance of the input coil. DAN has been used on DfMUX readout systems for nearly a decade, but the newest version extends the capability to higher multiplexing (128x), lower power consumption (by approximately a factor of 2), and utilizes FPGA resources much more efficiently than previous implementations. All three of these technological advancements are required to enable the LiteBIRD satellite. However, the cost of these developments is digital latency, which is approximately three times worse than previous DAN implementations. The additional latency complicates the stability of the feedback loop, and required a new formalism to describe that stability, calculate stable parameters, and implement those parameters in real-time. This was described in Chapter 4, and enables the use of this system on future telescopes, such as LiteBIRD.

9.2 CROSSTALK

Chapter 5 derived a new crosstalk model for DfMUX systems. This model accurately accounts for complex impedance relevant at higher bandwidth. It also incorporates the way our data processing techniques are relevant to the observed crosstalk fraction. In Section 6.5 I validated this model and show that it describes the observed SPT-3G crosstalk phenomonology well. This comparison is given in Figure 6.19.

Some key lessons from this analysis come from a more complete understanding of cancellation effects between the two different crosstalk mechanisms. In particular, counter to what was previously assumed, a substantially lower series inductance with the cryogenic filter network (L_{stray}) will not necessarily improve crosstalk, and under some circumstances may make it worse by spoiling that cancellation. An ideal crosstalk-optimized design would reduce the TES resistance, implement a linear frequency scheduling, and tune the series impedance specifically to promote crosstalk cancellation. One example of this is given in Figure 5.7, which uses a LiteBIRD-like design ($1\,\Omega$ detectors, a linear frequency scheduling, and 30 nH stray series inductance), to achieve $\sim 0.02\%$ mean nearest neighbor crosstalk. That same design with a lower 10 nH stray series inductance would achieve no better crosstalk performance (on average) than the present SPT-3G design.

9.3 LITHOGRAPHY PERFORMANCE

The ability to precisely fabricate LC resonators, with the specified resonance frequency, is crucial for improving the multiplexing factor without ruining crosstalk performance. Chapter 6 introduced a model to explain the primary source of variability seen in the SPT-3G LC resonator scatter. This analysis suggests that edge defects to the lithography generate variation in the electrical properties of the filters, which source scatter in the resonant frequencies and generate parasitic series resistance.

The resulting scatter in LC resonance frequency, and amount of series resistance, can be predicted through geometric analysis of the 2D lithographic mask. The best way to improve both of these properties is to use larger lithography trace widths, and compromise somewhat on the total size of the LC chips. Optimizing for the smallest total LC chip size drove us to use combinations of thin traces and low lithographic areas, which made the effects of individual defects much more pronounced at some bias frequencies. Controlling the LC parameters according to these recommended optimizations will minimize LC scatter and parasitic resistance in the LiteBIRD design; the former will allow detectors to be biased at frequencies with the best readout noise performance, while the latter will allow precise control over the boosted detector responsivity.

9.4 SPT-3G READOUT NOISE

Chapter 7 calculated all of the relevant sources of noise in the DfMUX system, as implemented on SPT-3G, as well as the transfer functions necessary to relate that noise to an NEI at the SQUID summing junction. This noise model is successful in two ways – it correctly describes the actual noise performance of the SPT-3G readout, and validates a completely analytic model for the system, which can be adapted for us in alternative designs. One of the most striking results of the noise analysis is the role played by parasitic capacitance between the lithographic elements and the ground planes, which were intended to minimize magnetic coupling between the resonators. These capacitances can be successfully calculated using a simple parallel plate capacitor model and the lithography design. The resulting capacitances produce a tertiary current path through the ground.

In Section 7.2.5 I showed the consequence of this tertiary current path, which increases the *current sharing* mechanism, and therefore readout noise, by approximately a factor of 2 at the highest bias frequencies. Ordinarily this current path wouldn't matter much, since it is relatively high impedance compared to the SQUID input coil and the detectors. However, that is spoiled by a ground reference at the output of the cryostat (R_{ref}), which provides a current return for that parasitic path that bypasses any series impedance in the wire-harness, making the parallel current path competitive with the traditional current paths through the SQUID input coil and comb.

A modification of that current path will mitigate most of this additional current sharing, and minimize the effect of the parasitic capacitances to ground. This is a design requirement for the LiteBIRD readout, and will likely be implemented on SPT-3G during an austral summer maintenance period.

A corollary to the importance of the parasitic capacitances to ground is the importance of parallel capacitances within the wire-harness itself. In Section 7.2.2 I showed how the SQUID dynamic impedance and a parallel capacitance in the wire-harness can generate a low-pass filter (χ_{output}), which has the effect of increasing readout noise at higher bias frequencies.

This is relevant for LiteBIRD, for which a much longer wire-harness is necessary, and puts strict requirements on the electrical characteristics of that wire-harness and the dynamic impedance of the SQUIDs.

9.5 RESPONSIVITY

The most troubling aspect of the SPT-3G performance has been the low sensitivity of the 220 GHz detectors. Both the current sharing effect and the output filter effect increase NEI at higher bias frequencies where these detectors are operated. However, that NEI increase alone isn't sufficient to explain the poor noise performance of the these detectors. Instead, in Section 7.6, I show that this is primarily due to a loss of detector *responsivity* at those bias frequencies, caused by a drop in the parasitic series resistance with the TES (R_s). This parasitic series resistance is often considered undesirable due to its potentially destabilizing effect on the TES, and design efforts have sought to minimize it. I find in the case of SPT-3G that the remaining R_s is essential to the readout noise performance of the 95 GHz and 150 GHz detectors. It provides a large increase in responsivity that makes the NEI contributions from readout noise negligible ($\lesssim$15% total noise increase due to readout). Unfortunately, that R_s is sourced by the LC lithography and it drops by a factor of two as the geometries of those resonators change at the higher bias frequencies. The resulting loss of responsivity magnifies the impact of already elevated readout NEI relative. Consequently, the 220 GHz detectors suffer from a fractional noise increase due to readout of up to 70% at the highest bias frequencies.

9.6 LITEBIRD FORECASTING

Chapter 8 used the models built up through the previous chapters to propose a baseline LiteBIRD readout configuration and assess the predicted readout performance. It also included several speculative configurations that take advantage of ongoing SQUID development. As currently defined, in order to achieve the targeted instrument sensitivity, the LiteBIRD readout requirement is <10% fractional noise increase in any observing band. I show that this is possible with a readout configuration that requires no additional speculative technology development. However, that result is predicated on two important requirements:

1. The additional current sharing path seen in SPT-3G is mitigated by design.
2. The intentional deployment of series resistance (R_s), in order to boost detector responsivity.

The second of these two will require the most development work. It will require that unintended sources of R_s (such as from the lithography) can be minimized, and intended sources of R_s can be implemented precisely.

I propose a target that is R_{tes}=0.6 Ω and R_s=0.3 Ω. These are already high-TRL parameters currently operated on POLARBEAR-2. They also maintain a sufficiently high total resistance that NEI is controlled, while also providing substantially boosted TES responsivity from the series resistance. Geometry changes to the lithography design should enable much lower series resistance from the resonators than currently exhibited in SPT-3G, which will allow the 0.3 Ω to be provided with an explicit resistive element, removing the major source of scatter in this parameter.

Any successful SQUID development that provides lower SQUID noise (such as from lower junction temperatures), or a reduction in input coil inductance (to mitigate the primary current sharing mechanism) will result in a comfortable readout noise margin below the target performance. Additionally, the intrinsically lower crosstalk design of LITEBIRD should be taken advantage of to adjust the bias frequency bandwidth lower. A change in bandwidth from between 1.6 MHz and 5.5 MHz to a lower frequency range of 1 MHz to 3 MHz would not result in significantly worse crosstalk performance, but would double the safety margin with respect to noise (or scatter in R_s).

9.7 THE PATH FORWARD

SPT-3G has several more years left in its planned survey, and can benefit directly from what has been learned in evaluating the first two years. With the help of collaborators who continue to perform laboratory tests, and those who travel to the South Pole for summer or winter seasons, I hope to implement a current sharing mitigation fix to improve the performance of the 220 GHz detectors.

Separately, the LITEBIRD readout is progressing at a rapid pace. We are currently completing the design of, and beginning to test, the flight-qualified versions of the readout electronics, and the work in this thesis is being used to define requirements for wire-harness procurement, detector design, and cryogenic circuit design. One of the lessons of SPT-3G is in how challenges in fabrication or procurement can slowly result in systematically different parameters than initially targeted. There are several places in the system where flexibility exists due to the way parameters interact, and it is possible to adapt to changes elsewhere. Other parameters have very little flexibility, and systematic shifts can greatly effect overall instrument performance. Continuous evaluation of any systematic change will be necessary to recognize where such change may be impinging on critical areas (such as the detector stability issues in the 2017 focal plane), or could simply benefit from some adaptation in the surrounding infrastructure (such as how a move to linear frequency scheduling would have benefited SPT-3G under the achieved detector parameters). Much of the challenge ahead will be in the close coordination necessary between collaboration members working across nearly half a dozen countries, but SPT-3G has provided an invaluable road-map for what comes next. Through an exhaustive study and modeling of SPT-3G, this research has established a clear, defensible, readout design for LiteBIRD, bringing this ambitious telescope one step closer to realization.

Appendix

A

COMPARISONS BETWEEN DOBBS2012 AND THE PRESENT CROSSTALK MODEL

The crosstalk model derived in Chapter 5 improves on the simple model first presented in Dobbs et al., 2012 [26]. In particular, the model in Chapter 5:

1. Allows calculation of crosstalk with realistic bias frequencies that are offset from the precise LC resonant frequencies, as is usually the case due to series parasitic impedance and the manner in which we calculate bias frequencies.

2. Preserves the complex signature of each crosstalk component, which have different phases with respect to the science signal and each other, allowing a vector addition representation of the crosstalk that accounts for crosstalk cancellation.

3. Incorporates the process used in DfMUX systems in which we select the phase of the output data that maximizes variations due to changes in radiative power on the focal plane. In particular, leakage power crosstalk is often out of phase with the data signal, and so the result of that crosstalk is strongly attenuated by the proper choice of basis.

4. Includes the contribution to leakage current crosstalk due to a common impedance in series with the full network (such as arising from stripline inductance, L_{stray}).

Here I briefly compare the results of the two models using early SPT-3G design parameters (from which we decided to use a logarithmic frequency scheduling, Figure A.1) and built SPT-3G parameters (Figure A.2). For early SPT-3G design parameters, even with a more accurate crosstalk model we may still have chosen to use a logarithmic frequency scheduling, though the differences between the two models can be substantial. In both cases the Dobbs2012 model overestimates crosstalk in a linear frequency scheduling (where the phase misalignment of leakage power crosstalk increases at high frequency), and underestimates it under a logarithmic frequency scheduling (due to the contribution of L_{stray} in leakage current crosstalk).

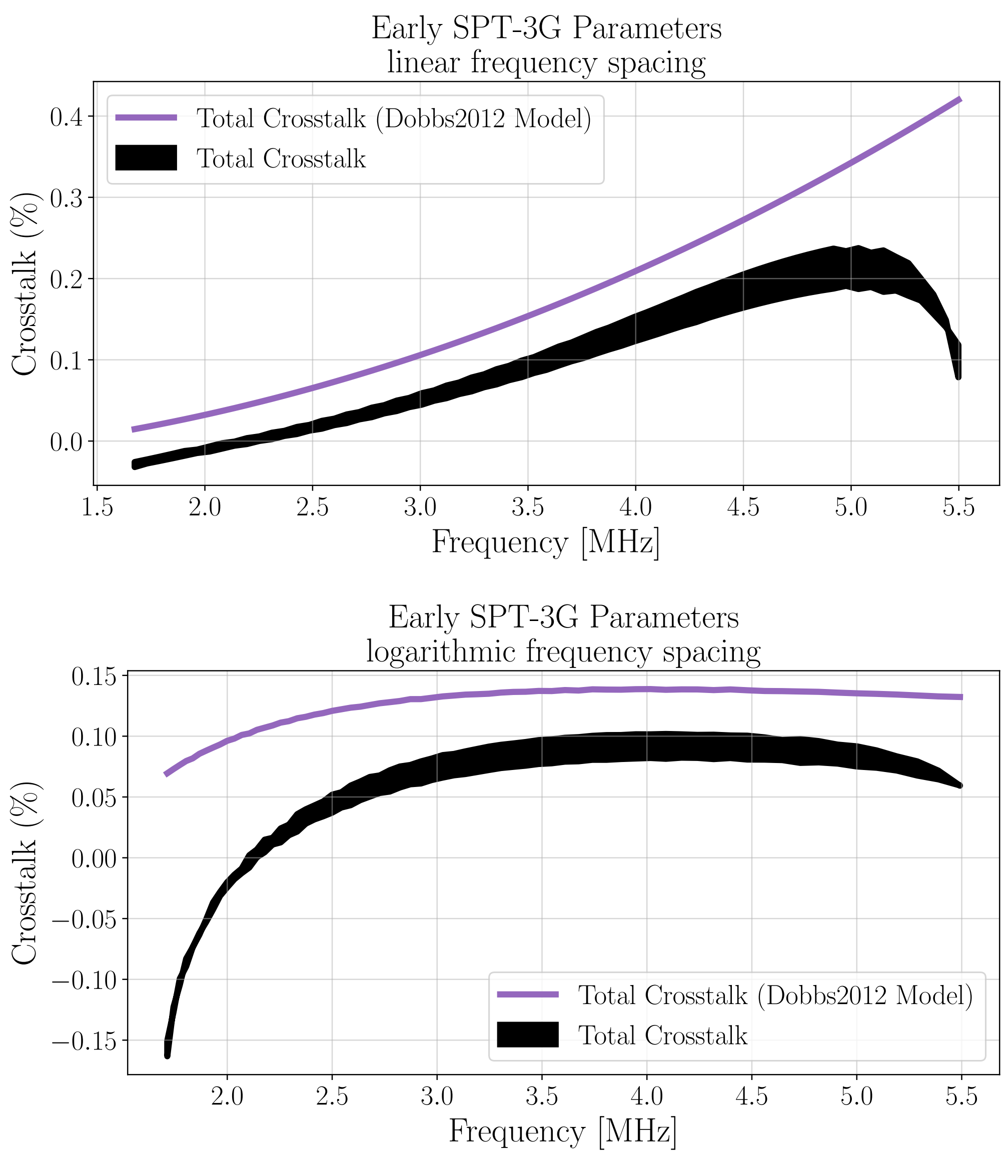

Figure A.1: A comparison between crosstalk projections made using the simple Dobbs2012 crosstalk model, and the detailed model derived in Chapter 5. Early SPT-3G design parameters assumed a series inductance of 60 nH from the striplines, and TES normal resistances of 1 Ω.

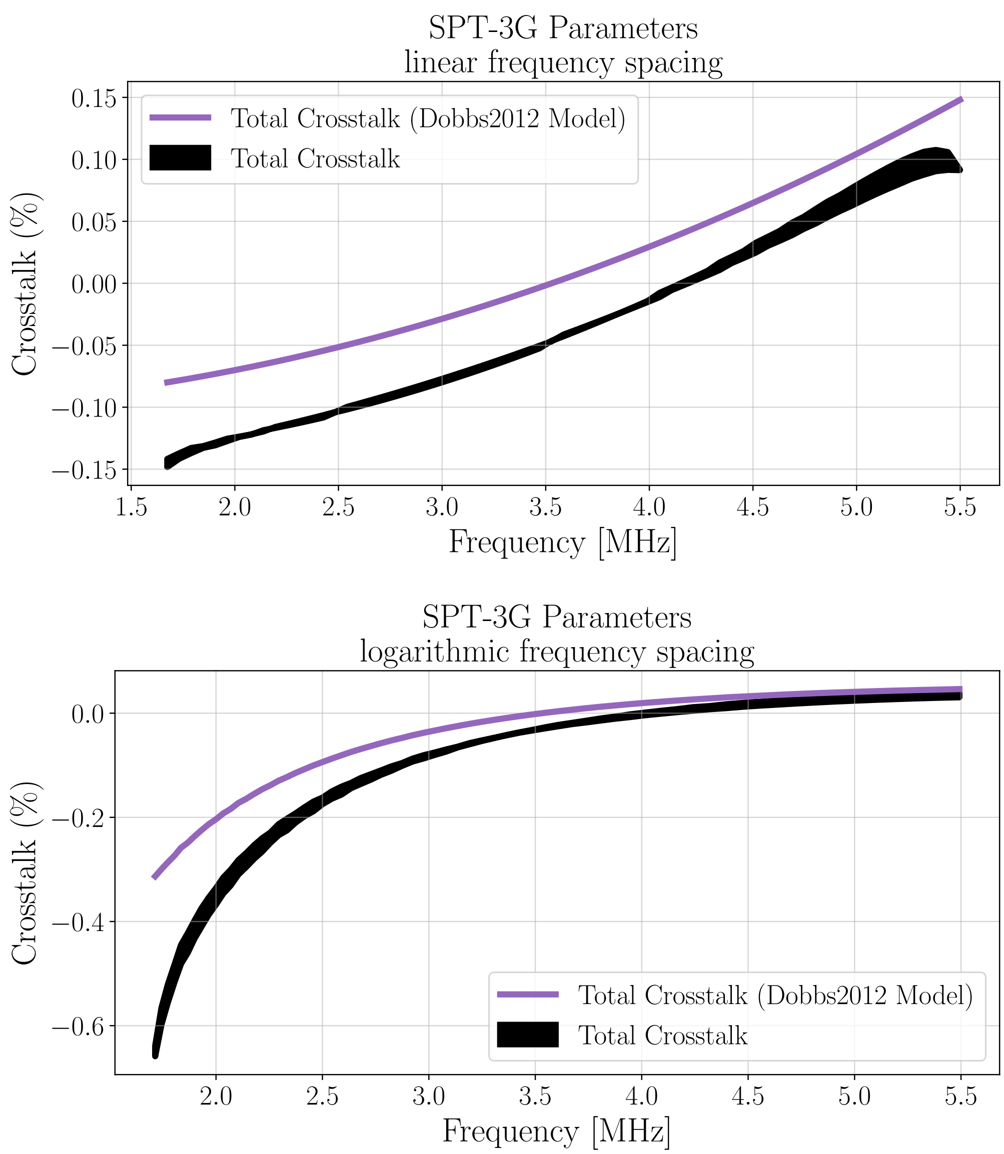

Figure A.2: A comparison between crosstalk projections made using the simple Dobbs2012 crosstalk model, and the detailed model derived in Chapter 5. Final SPT-3G had a lower series inductance than initially planned, 45 nH, and 2 Ω TES normal resistances.

B

DESIGNING FOR NON-LINEARITY

Narrow-band noise contamination is only problematic if it (A) it is substantial enough to flux burden the SQUID, or (B) the lines fall within the bandwidth that is read out around each carrier frequency containing the science signal (up to 65 Hz of bandwidth). The latter comprises such a small fraction of the total bandwidth that it is usually not a problem, except for the ways in which additional lines can be generated internally due to intermodulation distortion.

B.1 THIRD ORDER INTERMODULATION DISTORTION

Any non-linear system will generate tones at new frequencies due to the nonlinear mixing of tones that are injected into the system. With the intrinsically nonlinear TES detector and SQUID responses, some degree of non-linearity is unavoidable. As we add large signals (such as the carrier tones, clock tones, and buck-regulator switching frequencies) we will generate additional narrow lines that populate the bandwidth due to mixing. The amplitude of these mixing tones is a function of the total non-linearity of the system, and decreases with the harmonics involved in the mixing. The most problematic are the third order distortion products (IMD3). Even-ordered harmonic mixing will produce mixing products at frequencies either much larger than, or much smaller than, the fundamental tones involved in the mixing. Third order distortion products can still be relatively large, and can place mixing products among the primary tones. Three frequencies $f_a,\ f_b,\ f_c$ will generate IMD3 products at frequencies:

- $f_a + f_b - f_c$
- $f_a + f_c - f_b$
- $f_a + f_c - f_b$
- $f_b + f_c - f_a$
- $f_b + f_c - f_a$
- $2f_a - f_b$
- $2f_a - f_b$
- $2f_a - f_c$
- $2f_a - f_c$
- $2f_b - f_a$
- $2f_b - f_a$
- $2f_b - f_c$
- $2f_b - f_c$
- $2f_c - f_a$
- $2f_c - f_a$
- $2f_c - f_b$
- $2f_c - f_b$

A full comb of carrier tones, plus clock and buck regulator tones, will generate over ten thousand mixing products large enough to contaminate data. These can not be suppressed sufficiently for them to be irrelevant, and so the only way to proceed is to ensure the mixing products never interfere with the readout bandwidth.

B.2 BASE FREQUENCY

IMD3 products are generated through linear combinations of integer multiples of the primary tones, and so they share some properties with the fundamental tones. If all fundamental tones share a common multiple (the largest of which is known as a *base frequency*), then the IMD3 products will as well. By ensuring all fundamental tones (carrier frequencies, buck regulator switching frequencies, and clock frequency) share a base frequency that is larger than the readout bandwidth (in our case approximately 76 Hz, just at the extremum of the readout bandwidth), we guarantee that none of those mixing tones will land within the science bandwidth. This strategy is essential to the operation of DfMUX over such a large bandwidth.

C

BUCK REGULATOR NOISE

"Buck regulators" are power converters that generate the different voltages used by the readout electronics. These are switching power supplies, and so provide the required voltage and current by integrating over rapid oscillations. The switching frequencies of these regulators must be tightly controlled to respect the base frequency (Appendix B). This works well enough for small numbers of readout boards, but each buck regulator does wander in its synchronization frequency a small amount in response to changes in load.[1] The product of all buck regulator tones, each wandering very slightly with respect to one another (~ 180 total switching buck regulators) generates a non-trivial increase in readout noise near the switching frequency harmonics. This was an unexpected challenge in scaling up to the full SPT-3G instrument; we were able to mitigate it to some degree by modifying components in the electrical circuit that controls the buck switching feedback to enforce a narrower frequency switching span. Future implementations will avoid this with a different buck regulator design, more isolation between the analog signal paths and the power distribution, or the use of exclusively linear power supplies.

1 This is exacerbated by a particular design choice made for one mezzanine rail in the ICE system.

BIBLIOGRAPHY

[1] Kevork Abazajian et al. CMB-S4 Decadal Survey APC White Paper. *Bull. Am. Astron. Soc.*, 51(7):209, 2019. doi:10.2172/1556957.

[2] Z. Ahmed et al. BICEP3: a 95GHz refracting telescope for degree-scale CMB polarization. *Proc. SPIE Int. Soc. Opt. Eng.*, 9153:91531N, 2014. doi:10.1117/12.2057224.

[3] Andreas Albrecht and Paul J. Steinhardt. Cosmology for grand unified theories with radiatively induced symmetry breaking. *Physical Review Letters*, 48(17):1220–1223, April 1982. doi:10.1103/physrevlett.48.1220. URL `https://doi.org/10.1103/physrevlett.48.1220`.

[4] A. J. Anderson et al. SPT-3G: A Multichroic Receiver for the South Pole Telescope. *J. Low. Temp. Phys.*, 193(5-6):1057–1065, 2018. doi:10.1007/s10909-018-2007-z.

[5] François Aubin. *Detector readout electronics for EBEX: a balloon-borne cosmic microwave background polarimeter*. PhD thesis, McGill University, 2013.

[6] J. Avva, Peter Ade, Z. Ahmed, A. Anderson, J. Austermann, R. Thakur, D. Barron, A. Bender, B. Benson, J. Carlstrom, F. Carter, Thomas Cecil, Clarence Chang, Jean-Francois Cliche, A. Cukierman, E. Denison, T. Haan, Junjia Ding, M. Dobbs, and M. Young. Design and assembly of spt-3g cold readout hardware. *Journal of Low Temperature Physics*, 193, 05 2018. doi:10.1007/s10909-018-1965-5.

[7] Horace W. Babcock. The rotation of the Andromeda Nebula. *Lick Observatory Bulletin*, 498:41–51, January 1939. doi:10.5479/ADS/bib/1939LicOB.19.41B.

[8] K. Bandura, A. N. Bender, J. F. Cliche, T. de Haan, M. A. Dobbs, A. J. Gilbert, S. Griffin, G. Hsyu, D. Ittah, J. Mena Parra, J. Montgomery, T. Pinsonneault-Marotte, S. Siegel, G. Smecher, Q. Y. Tang, K. Vanderlinde, and N. Whitehorn. ICE: A Scalable, Low-Cost FPGA-Based Telescope Signal Processing and Networking System. *Journal of Astronomical Instrumentation*, 5(4):1641005, Dec 2016. doi:10.1142/S2251171716410051.

[9] K. Bandura, J. F. Cliche, M. A. Dobbs, A. J. Gilbert, D. Ittah, J. Mena Parra, and G. Smecher. Ice-based custom full-mesh network for the chime high bandwidth radio astronomy correlator. *Journal of Astronomical Instrumentation*, 05(04): 1641004, 2016. doi:10.1142/S225117171641004X. URL https://doi.org/10.1142/S225117171641004X.

[10] Kevin Bandura, Graeme E. Addison, Mandana Amiri, J. Richard Bond, Duncan Campbell-Wilson, Liam Connor, Jean-François Cliche, Greg Davis, Meiling Deng, Nolan Denman, Matt Dobbs, Mateus Fandino, Kenneth Gibbs, Adam Gilbert, Mark Halpern, David Hanna, Adam D. Hincks, Gary Hinshaw, Carolin Höfer, Peter Klages, Tom L. Landecker, Kiyoshi Masui, Juan Mena Parra, Laura B. Newburgh, Ue li Pen, Jeffrey B. Peterson, Andre Recnik, J. Richard Shaw, Kris Sigurdson, Mike Sitwell, Graeme Smecher, Rick Smegal, Keith Vanderlinde, and Don Wiebe. Canadian Hydrogen Intensity Mapping Experiment (CHIME) pathfinder. In Larry M. Stepp, Roberto Gilmozzi, and Helen J. Hall, editors, *Ground-based and Airborne Telescopes V*, volume 9145, pages 738 – 757. International Society for Optics and Photonics, SPIE, 2014. doi:10.1117/12.2054950. URL https://doi.org/10.1117/12.2054950.

[11] James M. Bardeen, Paul J. Steinhardt, and Michael S. Turner. Spontaneous creation of almost scale-free density perturbations in an inflationary universe. *Phys. Rev. D*, 28:679–693, Aug 1983. doi:10.1103/PhysRevD.28.679. URL https://link.aps.org/doi/10.1103/PhysRevD.28.679.

[12] A. Bender, A. Anderson, J. Avva, Peter Ade, Zyad Ahmed, Peter Barry, R. Thakur, B. Benson, L. Bryant, K. Byrum, J. Carlstrom, F. Carter, Thomas Cecil, Clarence Chang, Hee-mun Cho, Jean-Francois Cliche, A. Cukierman, T. Haan, E. Denison, and M. Young. On-sky performance of the spt-3g frequency-domain multiplexed readout. *Journal of Low Temperature Physics*, 199, 12 2019. doi:10.1007/s10909-019-02280-w.

[13] A. N. Bender, P. A. R. Ade, Z. Ahmed, A. J. Anderson, J. S. Avva, K. Aylor, P. S. Barry, R. Basu Thakur, B. A. Benson, L. S. Bleem, S. Bocquet, K. Byrum, J. E. Carlstrom, F. W. Carter, T. W. Cecil, C. L. Chang, H.-M. Cho, J. F. Cliche, T. M. Crawford, A. Cukierman, T. de Haan, E. V. Denison, J. Ding, M. A. Dobbs, S. Dodelson, D. Dutcher, W. Everett, A. Foster, J. Gallicchio, A. Gilbert, J. C. Groh, S. T. Guns, N. W. Halverson, A. H. Harke-Hosemann, N. L. Harrington, J. W. Henning, G. C. Hilton,

G. P. Holder, W. L. Holzapfel, N. Huang, K. D. Irwin, O. B. Jeong, M. Jonas, A. Jones, T. S. Khaire, L. Knox, A. M. Kofman, M. Korman, D. L. Kubik, S. Kuhlmann, C.-L. Kuo, A. T. Lee, E. M. Leitch, A. E. Lowitz, S. S. Meyer, D. Michalik, J. Montgomery, A. Nadolski, T. Natoli, H. Ngyuen, G. I. Noble, V. Novosad, S. Padin, Z. Pan, J. Pearson, C. M. Posada, W. Quan, S. Raghunathan, A. Rahlin, C. L. Reichardt, J. E. Ruhl, J. T. Sayre, E. Shirokoff, G. Smecher, J. A. Sobrin, A. A. Stark, K. T. Story, A. Suzuki, K. L. Thompson, C. Tucker, L. R. Vale, K. Vanderlinde, J. D. Vieira, G. Wang, N. Whitehorn, W. L. K. Wu, V. Yefremenko, K. W. Yoon, and M. R. Young. Year two instrument status of the SPT-3G cosmic microwave background receiver. In *Millimeter, Submillimeter, and Far-Infrared Detectors and Instrumentation for Astronomy IX*, volume 10708, pages 1 – 21. International Society for Optics and Photonics, SPIE, 2018. doi:10.1117/12.2312426. URL https://doi.org/10.1117/12.2312426.

[14] Amy N. Bender, Jean-François Cliche, Tijmen de Haan, Matt A. Dobbs, Adam J. Gilbert, Joshua Montgomery, Neil Rowlands, Graeme M. Smecher, Ken Smith, and Andrew Wilson. Digital frequency domain multiplexing readout electronics for the next generation of millimeter telescopes. *Millimeter, Submillimeter, and Far-Infrared Detectors and Instrumentation for Astronomy VII*, Jul 2014. doi:10.1117/12.2054949. URL http://dx.doi.org/10.1117/12.2054949.

[15] C. L. Bennett, D. Larson, J. L. Weiland, N. Jarosik, G. Hinshaw, N. Odegard, K. M. Smith, R. S. Hill, B. Gold, M. Halpern, E. Komatsu, M. R. Nolta, L. Page, D. N. Spergel, E. Wollack, J. Dunkley, A. Kogut, M. Limon, S. S. Meyer, G. S. Tucker, and E. L. Wright. Nine-year Wilkinson Microwave Anisotropy Probe (WMAP) Observations: Final Maps and Results. *The Astrophysical Journal*, 208(2):20, October 2013. doi:10.1088/0067-0049/208/2/20.

[16] B. A. Benson, P. A. R. Ade, Z. Ahmed, S. W. Allen, K. Arnold, J. E. Austermann, A. N. Bender, L. E. Bleem, J. E. Carlstrom, C. L. Chang, and et al. Spt-3g: a next-generation cosmic microwave background polarization experiment on the south pole telescope. *Millimeter, Submillimeter, and Far-Infrared Detectors and Instrumentation for Astronomy VII*, Jul 2014. doi:10.1117/12.2057305. URL http://dx.doi.org/10.1117/12.2057305.

[17] George R. Blumenthal, Heinz Pagels, and Joel R. Primack. Galaxy formation by dissipationless particles heavier than neutrinos. *Nature*, 299(5878):37–38, September 1982. doi:10.1038/299037a0. URL `https://doi.org/10.1038/299037a0`.

[18] J. R. Bond, A. S. Szalay, and M. S. Turner. Formation of galaxies in a gravitino-dominated universe. *Phys. Rev. Lett.*, 48:1636–1639, Jun 1982. doi:10.1103/PhysRevLett.48.1636. URL `https://link.aps.org/doi/10.1103/PhysRevLett.48.1636`.

[19] Steve K. Choi, Matthew Hasselfield, Shuay-Pwu Patty Ho, Brian Koopman, Marius Lungu, Maximilian H. Abitbol, Graeme E. Addison, Peter A. R. Ade, Simone Aiola, David Alonso, Mandana Amiri, Stefania Amodeo, Elio Angile, Jason E. Austermann, Taylor Baildon, Nick Battaglia, James A. Beall, Rachel Bean, Daniel T. Becker, J Richard Bond, Sarah Marie Bruno, Erminia Calabrese, Victoria Calafut, Luis E. Campusano, Felipe Carrero, Grace E. Chesmore, Hsiao mei Cho., Susan E. Clark, Nicholas F. Cothard, Devin Crichton, Kevin T. Crowley, Omar Darwish, Rahul Datta, Edward V. Denison, Mark J. Devlin, Cody J. Duell, Shannon M. Duff, Adriaan J. Duivenvoorden, Jo Dunkley, Rolando Dünner, Thomas Essinger-Hileman, Max Fankhanel, Simone Ferraro, Anna E. Fox, Brittany Fuzia, Patricio A. Gallardo, Vera Gluscevic, Joseph E. Golec, Emily Grace, Megan Gralla, Yilun Guan, Kirsten Hall, Mark Halpern, Dongwon Han, Peter Hargrave, Shawn Henderson, Brandon Hensley, J. Colin Hill, Gene C. Hilton, Matt Hilton, Adam D. Hincks, Renée Hložek, Johannes Hubmayr, Kevin M. Huffenberger, John P. Hughes, Leopoldo Infante, Kent Irwin, Rebecca Jackson, Jeff Klein, Kenda Knowles, Arthur Kosowsky, Vincent Lakey, Dale Li, Yaqiong Li, Zack Li, Martine Lokken, Thibaut Louis, Amanda MacInnis, Mathew Madhavacheril, Felipe Maldonado, Maya Mallaby-Kay, Danica Marsden, Loïc Maurin, Jeff McMahon, Felipe Menanteau, Kavilan Moodley, Tim Morton, Sigurd Naess, Toshiya Namikawa, Federico Nati, Laura Newburgh, John P. Nibarger, Andrina Nicola, Michael D. Niemack, Michael R. Nolta, John Orlowski-Sherer, Lyman A. Page, Christine G. Pappas, Bruce Partridge, Phumlani Phakathi, Heather Prince, Roberto Puddu, Frank J. Qu, Jesus Rivera, Naomi Robertson, Felipe Rojas, Maria Salatino, Emmanuel Schaan, Alessandro Schillaci, Benjamin L. Schmitt, Neelima Sehgal, Blake D. Sherwin, Carlos Sierra, Jon Sievers, Cristobal Sifon, Precious Sikhosana, Sara Simon, David N. Spergel, Suzanne T. Staggs, Jason Stevens, Emilie Storer, Dhaneshwar D. Sunder, Eric R. Switzer, Ben

Thorne, Robert Thornton, Hy Trac, Jesse Treu, Carole Tucker, Leila R. Vale, Alexander Van Engelen, Jeff Van Lanen, Eve M. Vavagiakis, Kasey Wagoner, Yuhan Wang, Jonathan T. Ward, Edward J. Wollack, Zhilei Xu, Fernando Zago, and Ningfeng Zhu. The atacama cosmology telescope: A measurement of the cosmic microwave background power spectra at 98 and 150 ghz. *arXiv e-prints*, 2020.

[20] P. de Bernardis, P. A. R. Ade, J. J. Bock, J. R. Bond, J. Borrill, A. Boscaleri, K. Coble, B. P. Crill, G. De Gasperis, P. C. Farese, P. G. Ferreira, K. Ganga, M. Giacometti, E. Hivon, V. V. Hristov, A. Iacoangeli, A. H. Jaffe, A. E. Lange, L. Martinis, S. Masi, P. V. Mason, P. D. Mauskopf, A. Melchiorri, L. Miglio, T. Montroy, C. B. Netterfield, E. Pascale, F. Piacentini, D. Pogosyan, S. Prunet, S. Rao, G. Romeo, J. E. Ruhl, F. Scaramuzzi, D. Sforna, and N. Vittorio. A flat universe from high-resolution maps of the cosmic microwave background radiation. *Nature*, 404(6781):955–959, April 2000. doi:10.1038/35010035. URL `https://doi.org/10.1038/35010035`.

[21] P. de Bernardis et al. BOOMERanG: Balloon Observations Of Millimetric Extragalactic Radiation And Geophysics. In *Microwave background anisotropies. Proceedings, 31st Rencontres de Moriond, 16th Moriond Astrophysics Meeting, Les Arcs, France, March 16-23, 1996*, pages 155–160, Gif-Sur-Yvette, 1997. Ed. Frontieres, Ed. Frontieres.

[22] Tijmen de Haan, Graeme Smecher, and Matt Dobbs. Improved performance of tes bolometers using digital feedback. *Proc SPIE*, 8452, 10 2012. doi:10.1117/12.925658.

[23] Tijmen de Haan, Darcy Barron, Ari Cukierman, Akito Kusaka, Leo Steinmetz, and Aritoki Suzuki. Towards the next generation of frequency-multipexed TES bolometer readout (Conference Presentation). In Jonas Zmuidzinas and Jian-Rong Gao, editors, *Millimeter, Submillimeter, and Far-Infrared Detectors and Instrumentation for Astronomy IX*, volume 10708. International Society for Optics and Photonics, SPIE, 2018. doi:10.1117/12.2313913. URL `https://doi.org/10.1117/12.2313913`.

[24] Piet A. J. de Korte, Joern Beyer, Steve Deiker, Gene C. Hilton, Kent D. Irwin, Mike MacIntosh, Sae Woo Nam, Carl D. Reintsema, Leila R. Vale, and Martin E. Huber. Time-division superconducting quantum interference device multiplexer for transition-edge sensors. *Review of Scientific Instruments*, 74(8):3807–3815, August 2003. doi:10.1063/1.1593809. URL `https://doi.org/10.1063/1.1593809`.

[25] Bascom S. Deaver and William M. Fairbank. Experimental evidence for quantized flux in superconducting cylinders. *Phys. Rev. Lett.*, 7:43–46, Jul 1961. doi:10.1103/PhysRevLett.7.43. URL https://link.aps.org/doi/10.1103/PhysRevLett.7.43.

[26] M A Dobbs, M Lueker, K A Aird, A N Bender, B A Benson, L E Bleem, J E Carlstrom, C L Chang, H M Cho, J Clarke, T M Crawford, A T Crites, D I Flanigan, T de Haan, E M George, N W Halverson, W L Holzapfel, J D Hrubes, B R Johnson, J Joseph, R Keisler, J Kennedy, Z Kermish, T M Lanting, A T Lee, E M Leitch, D Luong-Van, J J McMahon, J Mehl, S S Meyer, T E Montroy, S Padin, T Plagge, C Pryke, P L Richards, J E Ruhl, K K Schaffer, D Schwan, E Shirokoff, H G Spieler, Z Staniszewski, A A Stark, K Vanderlinde, J D Vieira, C Vu, B Westbrook, and R Williamson. Frequency multiplexed superconducting quantum interference device readout of large bolometer arrays for cosmic microwave background measurements. *Review of Scientific Instruments*, 83(7):3113, July 2012.

[27] Matt Dobbs, Eric Bissonnette, and Helmuth Spieler. Digital frequency domain multiplexer for millimeter-wavelength telescopes. *Nuclear Science, IEEE Transactions on*, 55:21 – 26, 03 2008. doi:10.1109/TNS.2007.911601.

[28] R. Doll and M. Näbauer. Experimental proof of magnetic flux quantization in a superconducting ring. *Phys. Rev. Lett.*, 7:51–52, Jul 1961. doi:10.1103/PhysRevLett.7.51. URL https://link.aps.org/doi/10.1103/PhysRevLett.7.51.

[29] W. B. Doriese, K. M. Morgan, D. A. Bennett, E. V. Denison, C. P. Fitzgerald, J. W. Fowler, J. D. Gard, J. P. Hays-Wehle, G. C. Hilton, K. D. Irwin, Y. I. Joe, J. A. B. Mates, G. C. O'Neil, C. D. Reintsema, N. O. Robbins, D. R. Schmidt, D. S. Swetz, H. Tatsuno, L. R. Vale, and J. N. Ullom. Developments in time-division multiplexing of x-ray transition-edge sensors. *Journal of Low Temperature Physics*, 184(1-2):389–395, December 2015. doi:10.1007/s10909-015-1373-z. URL https://doi.org/10.1007/s10909-015-1373-z.

[30] Dietmar Drung. Introduction to nb-based squid sensors. *IEEE/CSC & ESAS SUPERCONDUCTIVITY NEWS FORUM (global edition)*, Apr 2016. URL https://snf.ieeecsc.org/abstracts/cr70-introduction-nb-based-squid-sensors.

[31] D. Dutcher, P. A. R. Ade, Z. Ahmed, A. J. Anderson, J. S. Avva, R. Basu Thakur, A. N. Bender, B. A. Benson, J. E. Carlstrom, F. W. Carter, T. W. Cecil, C. L. Chang, J. F. Cliche, A. Cukierman, T. de Haan, J. Ding, M. A. Dobbs, W. Everett, A. Foster, J. Gallicchio, A. Gilbert, J. C. Groh, A. H. Harke-Hosemann, S. T. Guns, N. W. Halverson, N. L. Harrington, J. W. Henning, W. L. Holzapfel, N. Huang, K. D. Irwin, O. B. Jeong, M. Jonas, T. S. Khaire, A. M. Kofman, M. Korman, D. L. Kubik, S. Kuhlmann, C.-L. Kuo, A. E. Lowitz, A. T. Lee, S. S. Meyer, D. Michalik, J. Montgomery, A. Nadolski, T. Natoli, H. Nguyen, G. I. Noble, V. Novosad, S. Padin, Z. Pan, J. Pearson, C. M. Posada, W. Quan, A. Rahlin, J. E. Ruhl, J. T. Sayre, E. Shirokoff, G. Smecher, J. A. Sobrin, A. A. Stark, K. T. Story, A. Suzuki, K. L. Thompson, C. Tucker, K. Vanderlinde, J. D. Vieira, G. Wang, N. Whitehorn, V. Yefremenko, K. W. Yoon, and M. R. Young. Characterization and performance of the second-year SPT-3G focal plane. In Jonas Zmuidzinas and Jian-Rong Gao, editors, *Millimeter, Submillimeter, and Far-Infrared Detectors and Instrumentation for Astronomy IX*, volume 10708, pages 246 – 258. International Society for Optics and Photonics, SPIE, 2018. doi:10.1117/12.2312451. URL `https://doi.org/10.1117/12.2312451`.

[32] John Earman and Jesus Mosterin. A critical look at inflationary cosmology. *Philosophy of Science*, 66(1):1–49, 1999. ISSN 00318248, 1539767X. URL `http://www.jstor.org/stable/188736`.

[33] EBEX Collaboration, Maximilian Abitbol, Asad M. Aboobaker, Peter Ade, Derek Araujo, François Aubin, Carlo Baccigalupi, Chaoyun Bao, Daniel Chapman, Joy Didier, Matt Dobbs, Stephen M. Feeney, Christopher Geach, Will Grainger, Shaul Hanany, Kyle Helson, Seth Hillbrand, Gene Hilton, Johannes Hubmayr, Kent Irwin, Andrew Jaffe, Bradley Johnson, Terry Jones, Jeff Klein, Andrei Korotkov, Adrian Lee, Lorne Levinson, Michele Limon, Kevin MacDermid, Amber D. Miller, Michael Milligan, Kate Raach, Britt Reichborn-Kjennerud, Carl Reintsema, Ilan Sagiv, Graeme Smecher, Gregory S. Tucker, Benjamin Westbrook, Karl Young, and Kyle Zilic. The ebex balloon-borne experiment - detectors and readout. *The Astrophysical Journal*, 239(1):8, Nov 2018. doi:10.3847/1538-4365/aae436.

[34] Tucker Elleflot. *Measuring the Polarization of the Cosmic Microwave Background with POLARBEAR-1 and Developing the Next-Generation Experiment POLARBEAR-2*. PhD thesis, UC, San Diego, 2019.

[35] Claude-André Faucher-Giguère, Adam Lidz, and Lars Hernquist. Numerical simulations unravel the cosmic web. *Science*, 319(5859):52–55, 2008. ISSN 00368075, 10959203. URL http://www.jstor.org/stable/20051916.

[36] Alan H. Guth. Inflationary universe: A possible solution to the horizon and flatness problems. *Phys. Rev. D*, 23:347–356, Jan 1981. doi:10.1103/PhysRevD.23.347. URL http://link.aps.org/doi/10.1103/PhysRevD.23.347.

[37] Alan H. Guth and So-Young Pi. Fluctuations in the new inflationary universe. *Physical Review Letters*, 49(15):1110–1113, October 1982. doi:10.1103/physrevlett.49.1110. URL https://doi.org/10.1103/physrevlett.49.1110.

[38] T. Haan, A. Suzuki, S. Boyd, R. Cantor, A. Coerver, M. Dobbs, R. Hennings-Yeomans, W. Holzapfel, A. Lee, G. Noble, G. Smecher, and J. Zhou. Recent advances in frequency-multiplexed tes readout: Vastly reduced parasitics and an increase in multiplexing factor with sub-kelvin squids. *Journal of Low Temperature Physics*, 08 2019.

[39] D. Hanson, S. Hoover, A. Crites, P. A. R. Ade, K. A. Aird, J. E. Austermann, J. A. Beall, A. N. Bender, B. A. Benson, L. E. Bleem, J. J. Bock, J. E. Carlstrom, C. L. Chang, H. C. Chiang, H-M. Cho, A. Conley, T. M. Crawford, T. de Haan, M. A. Dobbs, W. Everett, J. Gallicchio, J. Gao, E. M. George, N. W. Halverson, N. Harrington, J. W. Henning, G. C. Hilton, G. P. Holder, W. L. Holzapfel, J. D. Hrubes, N. Huang, J. Hubmayr, K. D. Irwin, R. Keisler, L. Knox, A. T. Lee, E. Leitch, D. Li, C. Liang, D. Luong-Van, G. Marsden, J. J. McMahon, J. Mehl, S. S. Meyer, L. Mocanu, T. E. Montroy, T. Natoli, J. P. Nibarger, V. Novosad, S. Padin, C. Pryke, C. L. Reichardt, J. E. Ruhl, B. R. Saliwanchik, J. T. Sayre, K. K. Schaffer, B. Schulz, G. Smecher, A. A. Stark, K. T. Story, C. Tucker, K. Vanderlinde, J. D. Vieira, M. P. Viero, G. Wang, V. Yefremenko, O. Zahn, and M. Zemcov. Detection of b-mode polarization in the cosmic microwave background with data from the south pole telescope. *Phys. Rev. Lett.*, 111:141301, Sep 2013. doi:10.1103/PhysRevLett.111.141301. URL https://link.aps.org/doi/10.1103/PhysRevLett.111.141301.

[40] F.J. Harris, C. Dick, and M. Rice. Digital receivers and transmitters using polyphase filter banks for wireless communications. *Microwave Theory and Techniques, IEEE Transactions on*, 51(4):1395–1412, Apr 2003. ISSN 0018-9480. doi:10.1109/TMTT.2003.809176.

[41] Kaori Hattori, Yoshiki Akiba, Kam Arnold, Darcy Barron, Amy Bender, Matthew Adam Dobbs, Tijmen de Haan, Nicholas Harrington, Masaya Hasegawa, Masashi Hazumi, William Laird Holzapfel, Yasuto Hori, Brian G. Keating, Adrian T. Lee, Joshua Montgomery, Hideki Morii, Michael J. Myers, Kaja Rotermund, Ian Shirley, Graeme M. Smecher, Nathan Stebor, Aritoki Suzuki, and Takayuki Tomaru. Optimization of cold resonant filters for frequency domain multiplexed readout of POLARBEAR-2. In Wayne S. Holland and Jonas Zmuidzinas, editors, *Millimeter, Submillimeter, and Far-Infrared Detectors and Instrumentation for Astronomy VII*. SPIE, August 2014. doi:10.1117/12.2057045. URL https://doi.org/10.1117/12.2057045.

[42] S.W. Hawking. The development of irregularities in a single bubble inflationary universe. *Physics Letters B*, 115(4):295–297, September 1982. doi:10.1016/0370-2693(82)90373-2. URL https://doi.org/10.1016/0370-2693(82)90373-2.

[43] M. Hazumi et al. LiteBIRD: A Satellite for the Studies of B-Mode Polarization and Inflation from Cosmic Background Radiation Detection. *J. Low Temp. Phys.*, 194(5-6): 443–452, 2019. doi:10.1007/s10909-019-02150-5.

[44] J. W. Henning, J. T. Sayre, C. L. Reichardt, P. A. R. Ade, A. J. Anderson, J. E. Austermann, J. A. Beall, A. N. Bender, B. A. Benson, L. E. Bleem, and et al. Measurements of the temperature and e-mode polarization of the cmb from 500 square degrees of sptpol data. *The Astrophysical Journal*, 852(2):97, Jan 2018. ISSN 1538-4357. doi:10.3847/1538-4357/aa9ff4. URL http://dx.doi.org/10.3847/1538-4357/aa9ff4.

[45] Logan Alfred Howe. *The POLARBEAR-2 Cryogenic Receiver for Cosmic Microwave Background Polarization Science*. PhD thesis, University of California, San Diego, January 2019.

[46] Wayne Hu. Concepts in cmb anisotropy formation. In Enrique Martínez-González and Jose Luis Sanz, editors, *The Universe at High-z, Large-Scale Structure and the Cosmic Microwave Background*, pages 207–239, Berlin, Heidelberg, 1996. Springer Berlin Heidelberg. ISBN 978-3-540-68386-5.

[47] Wayne Hu and Martin White. A CMB polarization primer. *New Astronomy*, 2(4): 323–344, October 1997. doi:10.1016/s1384-1076(97)00022-5. URL https://doi.org/10.1016/s1384-1076(97)00022-5.

[48] J. D. Hunter. Matplotlib: A 2d graphics environment. *Computing in Science & Engineering*, 9(3):90–95, 2007. doi:10.1109/MCSE.2007.55.

[49] K. D. Irwin, G. C. Hilton, D. A. Wollman, and John M. Martinis. Thermal-response time of superconducting transition-edge microcalorimeters. *Journal of Applied Physics*, 83(8): 3978–3985, 1998. doi:10.1063/1.367153. URL https://doi.org/10.1063/1.367153.

[50] K.D. Irwin and G.C. Hilton. Transition-edge sensors. In *Topics in Applied Physics*, pages 63–150. Springer Berlin Heidelberg, July 2005. doi:10.1007/10933596_3. URL https://doi.org/10.1007/10933596_3.

[51] Ivan Akira. Illustration of amplitude modulation, 2010. URL https://upload.wikimedia.org/wikipedia/commons/8/8d/Illustration_of_Amplitude_Modulation.png. [Online; Distributed under a CC BY-SA 3.0 license].

[52] A. Braginski J. Clarke. *The SQUID Handbook: Fundamentals and Technology of SQUIDs and SQUID Systems*, volume 1. Wiley-VCH Verlag GmbH & Co. KGa, 2004.

[53] B. D. Josephson. Possible new effects in superconductive tunnelling. *Physics Letters*, 1: 251–253, July 1962. doi:10.1016/0031-9163(62)91369-0.

[54] Marc Kamionkowski and Ely D. Kovetz. The quest for b modes from inflationary gravitational waves. *Annual Review of Astronomy and Astrophysics*, 54(1):227–269, 2016. doi:10.1146/annurev-astro-081915-023433. URL https://doi.org/10.1146/annurev-astro-081915-023433.

[55] D. Kazanas. Dynamics of the universe and spontaneous symmetry breaking. *The Astrophysical Journal*, 241:L59, October 1980. doi:10.1086/183361. URL https://doi.org/10.1086/183361.

[56] R. Keisler, S. Hoover, N. Harrington, J. W. Henning, P. A. R. Ade, K. A. Aird, J. E. Austermann, J. A. Beall, A. N. Bender, B. A. Benson, and et al. Measurements of sub-degreeb-mode polarization in the cosmic microwave background from 100 square degrees of sptpol data. *The Astrophysical Journal*, 807(2):151, Jul 2015. ISSN 1538-4357. doi:10.1088/0004-637x/807/2/151. URL http://dx.doi.org/10.1088/0004-637X/807/2/151.

[57] A. Kogut, D. J. Fixsen, D. T. Chuss, J. Dotson, E. Dwek, M. Halpern, G. F. Hinshaw, S. M. Meyer, S. H. Moseley, M. D. Seiffert, D. N. Spergel, and E. J. Wollack. The Primordial Inflation Explorer (PIXIE): a nulling polarimeter for cosmic microwave background observations. *Journal of Cosmology and Astroparticle Physics*, 2011(7):025, Jul 2011. doi:10.1088/1475-7516/2011/07/025.

[58] J. M. Kovac, E. M. Leitch, C. Pryke, J. E. Carlstrom, N. W. Halverson, and W. L. Holzapfel. Detection of polarization in the cosmic microwave background using DASI. *Nature*, 420(6917):772–787, December 2002. doi:10.1038/nature01269. URL https://doi.org/10.1038/nature01269.

[59] A.D. Linde. A new inflationary universe scenario: A possible solution of the horizon, flatness, homogeneity, isotropy and primordial monopole problems. *Physics Letters B*, 108(6):389–393, February 1982. doi:10.1016/0370-2693(82)91219-9. URL https://doi.org/10.1016/0370-2693(82)91219-9.

[60] F. London. *Superfluids: Macroscopic theory of superconductivity*. Structure of matter series. John Wiley & Sons, 1950. URL https://books.google.ca/books?id=VNxEAAAAIAAJ.

[61] Thibaut Louis, Emily Grace, Matthew Hasselfield, Marius Lungu, Loïc Maurin, Graeme E. Addison, Peter A. R. Ade, Simone Aiola, Rupert Allison, Mandana Amiri, and et al. The atacama cosmology telescope: two-season actpol spectra and parameters. *Journal of Cosmology and Astroparticle Physics*, 2017(06):031–031, Jun 2017. ISSN 1475-7516. doi:10.1088/1475-7516/2017/06/031. URL http://dx.doi.org/10.1088/1475-7516/2017/06/031.

[62] Amy Lowitz, A. Bender, P. Barry, Thomas Cecil, Clarence Chang, R. Divan, M. Dobbs, Adam Gilbert, S. Kuhlmann, Marharyta Lisovenko, Jeannine Montgomery, V. Novosad, S. Padin, John Pearson, Guimei Wang, V. Yefremenko, and J. Zhang. Performance of a low-parasitic frequency-domain multiplexing readout. *Journal of Low Temperature Physics*, 199, 02 2020. doi:10.1007/s10909-020-02384-8.

[63] Martin Lueker. *Measurements of Secondary Cosmic Microwave Background Anisotropies with the South Pole Telescope*. PhD thesis, University of California, Berkeley, 2010.

[64] J. C. Mather, D. J. Fixsen, R. A. Shafer, C. Mosier, and D. T. Wilkinson. Calibrator design for theCOBEFar-infrared absolute spectrophotometer (FIRAS). *The Astrophysical Journal*, 512(2):511–520, February 1999. doi:10.1086/306805. URL https://doi.org/10.1086/306805.

[65] John C. Mather. Bolometer noise: nonequilibrium theory. *Appl. Opt.*, 21(6):1125–1129, Mar 1982. doi:10.1364/AO.21.001125. URL http://ao.osa.org/abstract.cfm?URI=ao-21-6-1125.

[66] Joshua Montgomery. Development of multiplexed bolometer readout electronics for mm-wave space astronomy. Master's thesis, McGill University, Canada, 2015.

[67] A. Nadolski, J. D. Vieira, J. A. Sobrin, A. M. Kofman, P. A. R. Ade, Z. Ahmed, A. J. Anderson, J. S. Avva, R. Basu Thakur, A. N. Bender, B. A. Benson, L. Bryant, J. E. Carlstrom, F. W. Carter, T. W. Cecil, C. L. Chang, J. R. Cheshire, G. E. Chesmore, J. F. Cliche, A. Cukierman, T. de Haan, M. Dierickx, J. Ding, D. Dutcher, W. Everett, J. Farwick, K. R. Ferguson, L. Florez, A. Foster, J. Fu, J. Gallicchio, A. E. Gambrel, R. W. Gardner, J. C. Groh, S. Guns, R. Guyser, N. W. Halverson, A. H. Harke-Hosemann, N. L. Harrington, R. J. Harris, J. W. Henning, W. L. Holzapfel, D. Howe, N. Huang, K. D. Irwin, O. Jeong, M. Jonas, A. Jones, M. Korman, J. Kovac, D. L. Kubik, S. Kuhlmann, C.-L. Kuo, A. T. Lee, A. E. Lowitz, J. McMahon, J. Meier, S. S. Meyer, D. Michalik, J. Montgomery, T. Natoli, H. Nguyen, G. I. Noble, V. Novosad, S. Padin, Z. Pan, P. Paschos, J. Pearson, C. M. Posada, W. Quan, A. Rahlin, D. Riebel, J. E. Ruhl, J. T. Sayre, E. Shirokoff, G. Smecher, A. A. Stark, J. Stephen, K. T. Story, A. Suzuki, C. Tandoi, K. L. Thompson, C. Tucker, K. Vanderlinde, G. Wang, N. Whitehorn, V. Yefremenko, K. W. Yoon, and M. R. Young. Broadband, millimeter-wave antireflection coatings for large-format, cryogenic aluminum oxide optics. *Appl. Opt.*, 59(10):3285–3295, Apr 2020. doi:10.1364/AO.383921. URL http://ao.osa.org/abstract.cfm?URI=ao-59-10-3285.

[68] Andrew Nadolski, Anna Kofman, Joaquin Vieira, Peter Ade, Zeeshan Ahmed, Adam Anderson, Jessica Avva, Ritoban Basu Thakur, Amy Bender, Bradford Benson, and et al. Broadband anti-reflective coatings for cosmic microwave background experiments. *Millimeter, Submillimeter, and Far-Infrared Detectors and Instrumentation for Astronomy IX*, Jul 2018. doi:10.1117/12.2315674. URL http://dx.doi.org/10.1117/12.2315674.

[69] P. J. E. Peebles. Large-scale background temperature and mass fluctuations due to scale-invariant primeval perturbations. *The Astrophysical Journal*, 263:L1–L5, December 1982. doi:10.1086/183911.

[70] F. Perez and B. E. Granger. Ipython: A system for interactive scientific computing. *Computing in Science Engineering*, 9(3):21–29, 2007.

[71] S. Perlmutter, G. Aldering, G. Goldhaber, R. A. Knop, P. Nugent, P. G. Castro, S. Deustua, S. Fabbro, A. Goobar, D. E. Groom, I. M. Hook, A. G. Kim, M. Y. Kim, J. C. Lee, N. J. Nunes, R. Pain, C. R. Pennypacker, R. Quimby, C. Lidman, R. S. Ellis, M. Irwin, R. G. McMahon, P. Ruiz-Lapuente, N. Walton, B. Schaefer, B. J. Boyle, A. V. Filippenko, T. Matheson, A. S. Fruchter, N. Panagia, H. J. M. Newberg, W. J. Couch, and The Supernova Cosmology Project. Measurements of Ω and Λ from 42 high-redshift supernovae. *The Astrophysical Journal*, 517(2):565–586, jun 1999. doi:10.1086/307221. URL https://doi.org/10.1086%2F307221.

[72] Pilbratt, G. L., Riedinger, J. R., Passvogel, T., Crone, G., Doyle, D., Gageur, U., Heras, A. M., Jewell, C., Metcalfe, L., Ott, S., and Schmidt, M. Herschel space observatory* - an esa facility for far-infrared and submillimetre astronomy. *A&A*, 518:L1, 2010. doi:10.1051/0004-6361/201014759. URL https://doi.org/10.1051/0004-6361/201014759.

[73] Planck Collaboration, P. A. R. Ade, N. Aghanim, C. Armitage-Caplan, M. Arnaud, M. Ashdown, F. Atrio-Barandela, J. Aumont, C. Baccigalupi, A. J. Banday, R. B. Barreiro, J. G. Bartlett, N. Bartolo, E. Battaner, R. Battye, K. Benabed, A. Benoît, A. Benoit-Lévy, J.-P. Bernard, M. Bersanelli, P. Bielewicz, J. Bobin, J. J. Bock, A. Bonaldi, L. Bonavera, J. R. Bond, J. Borrill, F. R. Bouchet, M. Bridges, M. Bucher, C. Burigana, R. C. Butler, J.-F. Cardoso, A. Catalano, A. Challinor, A. Chamballu, L.-Y Chiang, H. C. Chiang, P. R. Christensen, S. Church, D. L. Clements, S. Colombi, L. P. L. Colombo, F. Couchot, A. Coulais, B. P. Crill, A. Curto, F. Cuttaia, L. Danese, R. D. Davies, R. J. Davis, P. de Bernardis, A. de Rosa, G. de Zotti, J. Delabrouille, J.-M. Delouis, F.-X. Désert, J. M. Diego, H. Dole, S. Donzelli, O. Doré, M. Douspis, A. Ducout, J. Dunkley, X. Dupac, G. Efstathiou, T. A. Enßlin, H. K. Eriksen, J. Fergusson, F. Finelli, O. Forni, M. Frailis, E. Franceschi, S. Galeotta, K. Ganga, M. Giard, G. Giardino, Y. Giraud-Héraud, J. González-Nuevo, K. M. Górski, S. Gratton,

A. Gregorio, A. Gruppuso, F. K. Hansen, D. Hanson, D. Harrison, S. Henrot-Versillé, C. Hernández-Monteagudo, D. Herranz, S. R. Hildebrandt, E. Hivon, M. Hobson, W. A. Holmes, A. Hornstrup, W. Hovest, K. M. Huffenberger, T. R. Jaffe, A. H. Jaffe, W. C. Jones, M. Juvela, E. Keihänen, R. Keskitalo, T. S. Kisner, J. Knoche, L. Knox, M. Kunz, H. Kurki-Suonio, G. Lagache, A. Lähteenmäki, J.-M. Lamarre, A. Lasenby, R. J. Laureijs, C. R. Lawrence, J. P. Leahy, R. Leonardi, J. Lesgourgues, M. Liguori, P. B. Lilje, M. Linden-Vørnle, M. López-Caniego, P. M. Lubin, J. F. Macías-Pérez, B. Maffei, D. Maino, N. Mandolesi, M. Maris, D. J. Marshall, P. G. Martin, E. Martínez-González, S. Masi, S. Matarrese, F. Matthai, P. Mazzotta, J. D. McEwen, A. Melchiorri, L. Mendes, A. Mennella, M. Migliaccio, S. Mitra, M.-A. Miville-Deschênes, A. Moneti, L. Montier, G. Morgante, D. Mortlock, A. Moss, D. Munshi, P. Naselsky, P. Natoli, C. B. Netterfield, H. U. Nørgaard-Nielsen, F. Noviello, D. Novikov, I. Novikov, S. Osborne, C. A. Oxborrow, F. Paci, L. Pagano, F. Pajot, D. Paoletti, F. Pasian, G. Patanchon, H. V. Peiris, O. Perdereau, L. Perotto, F. Perrotta, F. Piacentini, M. Piat, E. Pierpaoli, D. Pietrobon, S. Plaszczynski, E. Pointecouteau, G. Polenta, N. Ponthieu, L. Popa, T. Poutanen, G. W. Pratt, G. Prézeau, S. Prunet, J.-L. Puget, J. P. Rachen, C. Räth, R. Rebolo, M. Remazeilles, C. Renault, S. Ricciardi, T. Riller, C. Ringeval, I. Ristorcelli, G. Rocha, C. Rosset, G. Roudier, M. Rowan-Robinson, B. Rusholme, M. Sandri, D. Santos, G. Savini, D. Scott, M. D. Seiffert, E. P. S. Shellard, L. D. Spencer, J.-L. Starck, V. Stolyarov, R. Stompor, R. Sudiwala, F. Sureau, D. Sutton, A.-S. Suur-Uski, J.-F. Sygnet, J. A. Tauber, D. Tavagnacco, L. Terenzi, L. Toffolatti, M. Tomasi, M. Tristram, M. Tucci, J. Tuovinen, L. Valenziano, J. Valiviita, B. Van Tent, J. Varis, P. Vielva, F. Villa, N. Vittorio, L. A. Wade, B. D. Wandelt, D. Yvon, A. Zacchei, and A. Zonca. Planck 2013 results. XXV. searches for cosmic strings and other topological defects. *Astronomy & Astrophysics*, 571:A25, October 2014. doi:10.1051/0004-6361/201321621. URL `https://doi.org/10.1051/0004-6361/201321621`.

[74] Planck Collaboration, P. A. R. Ade, N. Aghanim, C. Armitage-Caplan, M. Arnaud, M. Ashdown, F. Atrio-Barandela, J. Aumont, C. Baccigalupi, A. J. Banday, and et al. Planck2013 results. XV. CMB power spectra and likelihood. *Astronomy & Astrophysics*, 571:A15, Oct 2014. ISSN 1432-0746. doi:10.1051/0004-6361/201321573.

[75] Planck Collaboration, Adam, R., Ade, P. A. R., Aghanim, N., Alves, M. I. R., Arnaud, M., Ashdown, M., Aumont, J., Baccigalupi, C., Banday, A. J., Barreiro, R. B., Bartlett,

J. G., Bartolo, N., Battaner, E., Benabed, K., Benoît, A., Benoit-Lévy, A., Bernard, J.-P., Bersanelli, M., Bielewicz, P., Bock, J. J., Bonaldi, A., Bonavera, L., Bond, J. R., Borrill, J., Bouchet, F. R., Boulanger, F., Bucher, M., Burigana, C., Butler, R. C., Calabrese, E., Cardoso, J.-F., Catalano, A., Challinor, A., Chamballu, A., Chary, R.-R., Chiang, H. C., Christensen, P. R., Clements, D. L., Colombi, S., Colombo, L. P. L., Combet, C., Couchot, F., Coulais, A., Crill, B. P., Curto, A., Cuttaia, F., Danese, L., Davies, R. D., Davis, R. J., de Bernardis, P., de Rosa, A., de Zotti, G., Delabrouille, J., Désert, F.-X., Dickinson, C., Diego, J. M., Dole, H., Donzelli, S., Doré, O., Douspis, M., Ducout, A., Dupac, X., Efstathiou, G., Elsner, F., Enßlin, T. A., Eriksen, H. K., Falgarone, E., Fergusson, J., Finelli, F., Forni, O., Frailis, M., Fraisse, A. A., Franceschi, E., Frejsel, A., Galeotta, S., Galli, S., Ganga, K., Ghosh, T., Giard, M., Giraud-Héraud, Y., Gjerløw, E., González-Nuevo, J., Górski, K. M., Gratton, S., Gregorio, A., Gruppuso, A., Gudmundsson, J. E., Hansen, F. K., Hanson, D., Harrison, D. L., Helou, G., Henrot-Versillé, S., Hernández-Monteagudo, C., Herranz, D., Hildebrandt, S. R., Hivon, E., Hobson, M., Holmes, W. A., Hornstrup, A., Hovest, W., Huffenberger, K. M., Hurier, G., Jaffe, A. H., Jaffe, T. R., Jones, W. C., Juvela, M., Keihänen, E., Keskitalo, R., Kisner, T. S., Kneissl, R., Knoche, J., Kunz, M., Kurki-Suonio, H., Lagache, G., Lähteenmäki, A., Lamarre, J.-M., Lasenby, A., Lattanzi, M., Lawrence, C. R., Le Jeune, M., Leahy, J. P., Leonardi, R., Lesgourgues, J., Levrier, F., Liguori, M., Lilje, P. B., Linden-Vørnle, M., López-Caniego, M., Lubin, P. M., Macías-Pérez, J. F., Maggio, G., Maino, D., Mandolesi, N., Mangilli, A., Maris, M., Marshall, D. J., Martin, P. G., Martínez-González, E., Masi, S., Matarrese, S., McGehee, P., Meinhold, P. R., Melchiorri, A., Mendes, L., Mennella, A., Migliaccio, M., Mitra, S., Miville-Deschênes, M.-A., Moneti, A., Montier, L., Morgante, G., Mortlock, D., Moss, A., Munshi, D., Murphy, J. A., Naselsky, P., Nati, F., Natoli, P., Netterfield, C. B., Nørgaard-Nielsen, H. U., Noviello, F., Novikov, D., Novikov, I., Orlando, E., Oxborrow, C. A., Paci, F., Pagano, L., Pajot, F., Paladini, R., Paoletti, D., Partridge, B., Pasian, F., Patanchon, G., Pearson, T. J., Perdereau, O., Perotto, L., Perrotta, F., Pettorino, V., Piacentini, F., Piat, M., Pierpaoli, E., Pietrobon, D., Plaszczynski, S., Pointecouteau, E., Polenta, G., Pratt, G. W., Prézeau, G., Prunet, S., Puget, J.-L., Rachen, J. P., Reach, W. T., Rebolo, R., Reinecke, M., Remazeilles, M., Renault, C., Renzi, A., Ristorcelli, I., Rocha, G., Rosset, C., Rossetti, M., Roudier, G., Rubiño-Martín, J. A., Rusholme, B., Sandri, M., Santos, D., Savelainen, M., Savini, G., Scott, D., Seiffert, M. D., Shellard, E. P. S., Spencer, L.

D., Stolyarov, V., Stompor, R., Strong, A. W., Sudiwala, R., Sunyaev, R., Sutton, D., Suur-Uski, A.-S., Sygnet, J.-F., Tauber, J. A., Terenzi, L., Toffolatti, L., Tomasi, M., Tristram, M., Tucci, M., Tuovinen, J., Umana, G., Valenziano, L., Valiviita, J., Van Tent, F., Vielva, P., Villa, F., Wade, L. A., Wandelt, B. D., Wehus, I. K., Wilkinson, A., Yvon, D., Zacchei, A., and Zonca, A. Planck 2015 results - X. Diffuse component separation: Foreground maps. *A&A*, 594:A10, 2016. doi:10.1051/0004-6361/201525967. URL https://doi.org/10.1051/0004-6361/201525967.

[76] Planck Collaboration, N. Aghanim, Y. Akrami, M. Ashdown, J. Aumont, C. Baccigalupi, M. Ballardini, A. J. Banday, R. B. Barreiro, N. Bartolo, S. Basak, R. Battye, K. Benabed, J. P. Bernard, M. Bersanelli, P. Bielewicz, J. J. Bock, J. R. Bond, J. Borrill, F. R. Bouchet, F. Boulanger, M. Bucher, C. Burigana, R. C. Butler, E. Calabrese, J. F. Cardoso, J. Carron, A. Challinor, H. C. Chiang, J. Chluba, L. P. L. Colombo, C. Combet, D. Contreras, B. P. Crill, F. Cuttaia, P. de Bernardis, G. de Zotti, J. Delabrouille, J. M. Delouis, E. Di Valentino, J. M. Diego, O. Doré, M. Douspis, A. Ducout, X. Dupac, S. Dusini, G. Efstathiou, F. Elsner, T. A. Enßlin, H. K. Eriksen, Y. Fantaye, M. Farhang, J. Fergusson, R. Fernandez-Cobos, F. Finelli, F. Forastieri, M. Frailis, A. A. Fraisse, E. Franceschi, A. Frolov, S. Galeotta, S. Galli, K. Ganga, R. T. Génova-Santos, M. Gerbino, T. Ghosh, J. González-Nuevo, K. M. Górski, S. Gratton, A. Gruppuso, J. E. Gudmundsson, J. Hamann, W. Handley, F. K. Hansen, D. Herranz, S. R. Hildebrandt, E. Hivon, Z. Huang, A. H. Jaffe, W. C. Jones, A. Karakci, E. Keihänen, R. Keskitalo, K. Kiiveri, J. Kim, T. S. Kisner, L. Knox, N. Krachmalnicoff, M. Kunz, H. Kurki-Suonio, G. Lagache, J. M. Lamarre, A. Lasenby, M. Lattanzi, C. R. Lawrence, M. Le Jeune, P. Lemos, J. Lesgourgues, F. Levrier, A. Lewis, M. Liguori, P. B. Lilje, M. Lilley, V. Lindholm, M. López-Caniego, P. M. Lubin, Y. Z. Ma, J. F. Macías-Pérez, G. Maggio, D. Maino, N. Mandolesi, A. Mangilli, A. Marcos-Caballero, M. Maris, P. G. Martin, M. Martinelli, E. Martínez-González, S. Matarrese, N. Mauri, J. D. McEwen, P. R. Meinhold, A. Melchiorri, A. Mennella, M. Migliaccio, M. Millea, S. Mitra, M. A. Miville-Deschênes, D. Molinari, L. Montier, G. Morgante, A. Moss, P. Natoli, H. U. Nørgaard-Nielsen, L. Pagano, D. Paoletti, B. Partridge, G. Patanchon, H. V. Peiris, F. Perrotta, V. Pettorino, F. Piacentini, L. Polastri, G. Polenta, J. L. Puget, J. P. Rachen, M. Reinecke, M. Remazeilles, A. Renzi, G. Rocha, C. Rosset, G. Roudier, J. A. Rubiño-Martín, B. Ruiz-Granados, L. Salvati, M. Sandri, M. Savelainen, D. Scott, E. P. S. Shellard, C. Sirignano, G. Sirri, L. D. Spencer, R. Sunyaev, A. S. Suur-Uski, J. A.

Tauber, D. Tavagnacco, M. Tenti, L. Toffolatti, M. Tomasi, T. Trombetti, L. Valenziano, J. Valiviita, B. Van Tent, L. Vibert, P. Vielva, F. Villa, N. Vittorio, B. D. Wandelt, I. K. Wehus, M. White, S. D. M. White, A. Zacchei, and A. Zonca. Planck 2018 results. VI. Cosmological parameters. 2018.

[77] Planck Collaboration, Y. Akrami, F. Arroja, M. Ashdown, J. Aumont, C. Baccigalupi, M. Ballardini, A. J. Banday, R. B. Barreiro, N. Bartolo, S. Basak, R. Battye, K. Benabed, J.-P. Bernard, M. Bersanelli, P. Bielewicz, J. J. Bock, J. R. Bond, J. Borrill, F. R. Bouchet, F. Boulanger, M. Bucher, C. Burigana, R. C. Butler, E. Calabrese, J.-F. Cardoso, J. Carron, B. Casaponsa, A. Challinor, H. C. Chiang, L. P. L. Colombo, C. Combet, D. Contreras, B. P. Crill, F. Cuttaia, P. de Bernardis, G. de Zotti, J. Delabrouille, J.-M. Delouis, F.-X. Désert, E. Di Valentino, C. Dickinson, J. M. Diego, S. Donzelli, O. oré, M. Douspis, A. Ducout, X. Dupac, G. Efstathiou, F. Elsner, T. A. Enßlin, H. K. Eriksen, E. Falgarone, Y. Fantaye, J. Fergusson, R. Fernand ez Cobos, F. Finelli, F. Forastieri, M. Frailis, E. Franceschi, A. Frolov, S. Galeotta, S. Galli, K. Ganga, R. T. Génova-Santos, M. Gerbino, T. Ghosh, J. González-Nuevo, K. M. Górski, S. Gratton, A. Gruppuso, J. E. Gudmundsson, J. Hamann, W. Handley, F. K. Hansen, G. Helou, D. Herranz, E. Hivon, Z. Huang, A. H. Jaffe, W. C. Jones, A. Karakci, E. Keihänen, R. Keskitalo, K. Kiiveri, J. Kim, T. S. Kisner, L. Knox, N. Krachmalnicoff, M. Kunz, H. Kurki-Suonio, G. Lagache, J.-M. Lamarre, M. Langer, A. Lasenby, M. Lattanzi, C. R. Lawrence, M. Le Jeune, J. P. Leahy, J. Lesgourgues, F. Levrier, A. Lewis, M. Liguori, P. B. Lilje, M. Lilley, V. Lindholm, M. López-Caniego, P. M. Lubin, Y.-Z. Ma, J. F. acías Pérez, G. Maggio, D. Maino, N. Mandolesi, A. Mangilli, A. Marcos-Caballero, M. Maris, P. G. Martin, E. artínez González, S. Matarrese, N. Mauri, J. D. McEwen, P. D. Meerburg, P. R. Meinhold, A. Melchiorri, A. Mennella, M. Migliaccio, M. Millea, S. Mitra, M.-A. Miville-Deschênes, D. Molinari, A. Moneti, L. Montier, G. Morgante, A. Moss, S. Mottet, M. Münchmeyer, P. Natoli, H. U. Nørgaard-Nielsen, C. A. Oxborrow, L. Pagano, D. Paoletti, B. Partridge, G. Patanchon, T. J. Pearson, M. Peel, H. V. Peiris, F. Perrotta, V. Pettorino, F. Piacentini, L. Polastri, G. Polenta, J.-L. Puget, J. P. Rachen, M. Reinecke, M. Remazeilles, A. Renzi, G. Rocha, C. Rosset, G. Roudier, J. A. ubiño Martín, B. Ruiz-Granados, L. Salvati, M. Sandri, M. Savelainen, D. Scott, E. P. S. Shellard, M. Shiraishi, C. Sirignano, G. Sirri, L. D. Spencer, R. Sunyaev, A.-S. Suur-Uski, J. A. Tauber, D. Tavagnacco, M. Tenti, L. Terenzi, L. Toffolatti, M. Tomasi, T. Trombetti, J. Valiviita, B. Van Tent, L. Vibert, P. Vielva, F. Villa, N. Vittorio, B. D.

Wandelt, I. K. Wehus, M. White, S. D. M. White, A. Zacchei, and A. Zonca. Planck 2018 results. I. Overview and the cosmological legacy of Planck. *arXiv e-prints*, page arXiv:1807.06205, Jul 2018.

[78] Planck Collaboration, Y. Akrami, F. Arroja, M. Ashdown, J. Aumont, C. Baccigalupi, M. Ballardini, A. J. Banday, R. B. Barreiro, N. Bartolo, S. Basak, K. Benabed, J. P. Bernard, M. Bersanelli, P. Bielewicz, J. J. Bock, J. R. Bond, J. Borrill, F. R. Bouchet, F. Boulanger, M. Bucher, C. Burigana, R. C. Butler, E. Calabrese, J. F. Cardoso, J. Carron, A. Challinor, H. C. Chiang, L. P. L. Colombo, C. Combet, D. Contreras, B. P. Crill, F. Cuttaia, P. de Bernardis, G. de Zotti, J. Delabrouille, J. M. Delouis, E. Di Valentino, J. M. Diego, S. Donzelli, O. Doré, M. Douspis, A. Ducout, X. Dupac, S. Dusini, G. Efstathiou, F. Elsner, T. A. Enßlin, H. K. Eriksen, Y. Fantaye, J. Fergusson, R. Fernandez-Cobos, F. Finelli, F. Forastieri, M. Frailis, E. Franceschi, A. Frolov, S. Galeotta, S. Galli, K. Ganga, C. Gauthier, R. T. Génova-Santos, M. Gerbino, T. Ghosh, J. González-Nuevo, K. M. Górski, S. Gratton, A. Gruppuso, J. E. Gudmundsson, J. Hamann, W. Handley, F. K. Hansen, D. Herranz, E. Hivon, D. C. Hooper, Z. Huang, A. H. Jaffe, W. C. Jones, E. Keihänen, R. Keskitalo, K. Kiiveri, J. Kim, T. S. Kisner, N. Krachmalnicoff, M. Kunz, H. Kurki-Suonio, G. Lagache, J. M. Lamarre, A. Lasenby, M. Lattanzi, C. R. Lawrence, M. Le Jeune, J. Lesgourgues, F. Levrier, A. Lewis, M. Liguori, P. B. Lilje, V. Lindholm, M. Lpez-Caniego, P. M. Lubin, Y. Z. Ma, J. F. Macías-Pérez, G. Maggio, D. Maino, N. Mandolesi, A. Mangilli, A. Marcos-Caballero, M. Maris, P. G. Martin, E. Martínez-González, S. Matarrese, N. Mauri, J. D. McEwen, P. D. Meerburg, P. R. Meinhold, A. Melchiorri, A. Mennella, M. Migliaccio, S. Mitra, M. A. Miville-Deschênes, D. Molinari, A. Moneti, L. Montier, G. Morgante, A. Moss, M. Münchmeyer, P. Natoli, H. U. Nørgaard-Nielsen, L. Pagano, D. Paoletti, B. Partridge, G. Patanchon, H. V. Peiris, F. Perrotta, V. Pettorino, F. Piacentini, L. Polastri, G. Polenta, J. L. Puget, J. P. Rachen, M. Reinecke, M. Remazeilles, A. Renzi, G. Rocha, C. Rosset, G. Roudier, J. A. Rubiño-Martín, B. Ruiz-Granados, L. Salvati, M. Sandri, M. Savelainen, D. Scott, E. P. S. Shellard, M. Shiraishi, C. Sirignano, G. Sirri, L. D. Spencer, R. Sunyaev, A. S. Suur-Uski, J. A. Tauber, D. Tavagnacco, M. Tenti, L. Toffolatti, M. Tomasi, T. Trombetti, J. Valiviita, B. Van Tent, P. Vielva, F. Villa, N. Vittorio, B. D. Wandelt, I. K. Wehus, S. D. M. White, A. Zacchei, J. P. Zibin, and A. Zonca. Planck 2018 results. X. Constraints on inflation. *arXiv e-prints*, 2018.

[79] Planck Collaboration, Y. Akrami, M. Ashdown, J. Aumont, C. Baccigalupi, M. Ballardini, A. J. Band ay, R. B. Barreiro, N. Bartolo, S. Basak, K. Benabed, J. P. Bernard, M. Bersanelli, P. Bielewicz, J. R. Bond, J. Borrill, F. R. Bouchet, F. Boulanger, A. Bracco, M. Bucher, C. Burigana, E. Calabrese, J. F. Cardoso, J. Carron, H. C. Chiang, C. Combet, B. P. Crill, P. de Bernardis, G. de Zotti, J. Delabrouille, J. M. Delouis, E. Di Valentino, C. Dickinson, J. M. Diego, A. Ducout, X. Dupac, G. Efstathiou, F. Elsner, T. A. Enßlin, E. Falgarone, Y. Fantaye, K. Ferrière, F. Finelli, F. Forastieri, M. Frailis, A. A. Fraisse, E. Franceschi, A. Frolov, S. Galeotta, S. Galli, K. Ganga, R. T. Génova-Santos, T. Ghosh, J. González-Nuevo, K. M. Górski, A. Gruppuso, J. E. Gudmundsson, V. Guillet, W. Handley, F. K. Hansen, D. Herranz, Z. Huang, A. H. Jaffe, W. C. Jones, E. Keihänen, R. Keskitalo, K. Kiiveri, J. Kim, N. Krachmalnicoff, M. Kunz, H. Kurki-Suonio, J. M. Lamarre, A. Lasenby, M. Le Jeune, F. Levrier, M. Liguori, P. B. Lilje, V. Lindholm, M. López-Caniego, P. M. Lubin, Y. Z. Ma, J. F. Macías-Pérez, G. Maggio, D. Maino, N. Mandolesi, A. Mangilli, P. G. Martin, E. Martínez-González, S. Matarrese, J. D. McEwen, P. R. Meinhold, A. Melchiorri, M. Migliaccio, M. A. Miville-Deschênes, D. Molinari, A. Moneti, L. Montier, G. Morgante, P. Natoli, L. Pagano, D. Paoletti, V. Pettorino, F. Piacentini, G. Polenta, J. L. Puget, J. P. Rachen, M. Reinecke, M. Remazeilles, A. Renzi, G. Rocha, C. Rosset, G. Roudier, J. A. Rubiño-Martín, B. Ruiz-Granados, L. Salvati, M. Sandri, M. Savelainen, D. Scott, J. D. Soler, L. D. Spencer, J. A. Tauber, D. Tavagnacco, L. Toffolatti, M. Tomasi, T. Trombetti, J. Valiviita, F. Vansyngel, F. Van Tent, P. Vielva, F. Villa, N. Vittorio, I. K. Wehus, A. Zacchei, and A. Zonca. Planck 2018 results. XI. Polarized dust foregrounds. *arXiv e-prints*, art. arXiv:1801.04945, January 2018.

[80] Polarbear Collaboration, P. A. R. Ade, Y. Akiba, A. E. Anthony, K. Arnold, M. Atlas, D. Barron, D. Boettger, J. Borrill, S. Chapman, Y. Chinone, M. Dobbs, T. Elleflot, J. Errard, G. Fabbian, C. Feng, D. Flanigan, A. Gilbert, W. Grainger, N. W. Halverson, M. Hasegawa, K. Hattori, M. Hazumi, W. L. Holzapfel, Y. Hori, J. Howard, P. Hyland, Y. Inoue, G. C. Jaehnig, A. H. Jaffe, B. Keating, Z. Kermish, R. Keskitalo, T. Kisner, M. Le Jeune, A. T. Lee, E. M. Leitch, E. Linder, M. Lungu, F. Matsuda, T. Matsumura, X. Meng, N. J. Miller, H. Morii, S. Moyerman, M. J. Myers, M. Navaroli, H. Nishino, A. Orlando, H. Paar, J. Peloton, D. Poletti, E. Quealy, G. Rebeiz, C. L. Reichardt, P. L. Richards, C. Ross, I. Schanning, D. E. Schenck, B. D. Sherwin, A. Shimizu, C. Shimmin, M. Shimon, P. Siritanasak, G. Smecher, H. Spieler, N. Stebor, B. Steinbach, R. Stompor,

A. Suzuki, S. Takakura, T. Tomaru, B. Wilson, A. Yadav, and O. Zahn. A Measurement of the Cosmic Microwave Background B-mode Polarization Power Spectrum at Sub-degree Scales with POLARBEAR. *The Astrophysical Journal*, 794(2):171, October 2014. doi:10.1088/0004-637X/794/2/171.

[81] C M Posada, P A R Ade, Z Ahmed, K Arnold, J E Austermann, A N Bender, L E Bleem, B A Benson, K Byrum, J E Carlstrom, C L Chang, H M Cho, S T Ciocys, J F Cliche, T M Crawford, A Cukierman, D Czaplewski, J Ding, R Divan, T de Haan, M A Dobbs, D Dutcher, W Everett, A Gilbert, N W Halverson, N L Harrington, K Hattori, J W Henning, G C Hilton, W L Holzapfel, J Hubmayr, K D Irwin, O Jeong, R Keisler, D Kubik, C L Kuo, A T Lee, E M Leitch, S Lendinez, S S Meyer, C S Miller, J Montgomery, M Myers, A Nadolski, T Natoli, H Nguyen, V Novosad, S Padin, Z Pan, J Pearson, J E Ruhl, B R Saliwanchik, G Smecher, J T Sayre, E Shirokoff, L Stan, A A Stark, J Sobrin, K Story, A Suzuki, K L Thompson, C Tucker, K Vanderlinde, J D Vieira, G Wang, N Whitehorn, V Yefremenko, K W Yoon, and K E Ziegler. Fabrication of large dual-polarized multichroic TES bolometer arrays for CMB measurements with the SPT-3g camera. *Superconductor Science and Technology*, 28(9):094002, aug 2015. doi:10.1088/0953-2048/28/9/094002. URL `https://doi.org/10.1088%2F0953-2048%2F28%2F9%2F094002`.

[82] Alexandra Sasha Rahlin. *The First Flight of the SPIDER Balloon-Borne Telescope* . PhD thesis, Princeton University, 2016.

[83] S. O. Rice. Statistical properties of a sine wave plus random noise. *The Bell System Technical Journal*, 27(1):109–157, 1948.

[84] Adam G. Riess, Alexei V. Filippenko, Peter Challis, Alejandro Clocchiatti, Alan Diercks, Peter M. Garnavich, Ron L. Gilliland, Craig J. Hogan, Saurabh Jha, Robert P. Kirshner, B. Leibundgut, M. M. Phillips, David Reiss, Brian P. Schmidt, Robert A. Schommer, R. Chris Smith, J. Spyromilio, Christopher Stubbs, Nicholas B. Suntzeff, and John Tonry. Observational evidence from supernovae for an accelerating universe and a cosmological constant. *The Astronomical Journal*, 116(3):1009–1038, sep 1998. doi:10.1086/300499. URL `https://doi.org/10.1086%2F300499`.

[85] K. Rotermund, B. Barch, S. Chapman, K. Hattori, A. Lee, N. Palaio, I. Shirley, A. Suzuki, and C. Tran. Planar Lithographed Superconducting LC Resonators for

Frequency-Domain Multiplexed Readout Systems. *Journal of Low Temperature Physics*, 184(1-2):486–491, July 2016. doi:10.1007/s10909-016-1554-4.

[86] James Tomlinson Sayre. *Measuring Polarization of the Cosmic Microwave Background with the South Pole Telescope Polarization Experiment*. PhD thesis, Case Western Reserve University, 2014.

[87] Joseph Silk. Cosmic black-body radiation and galaxy formation. *The Astrophysical Journal*, 151:459, February 1968. doi:10.1086/149449. URL https://doi.org/10.1086/149449.

[88] Maximiliano Silva-Feaver, Kam Arnold, Darcy Barron, Edward V. Denison, Matt Dobbs, John Groh, Gene Hilton, Johannes Hubmayr, Kent Irwin, Adrian Lee, and Leila R. Vale. Comparison of NIST SA13a and SA4b SQUID array amplifiers. *Journal of Low Temperature Physics*, 193(3-4):600–610, September 2018. doi:10.1007/s10909-018-2052-7. URL https://doi.org/10.1007/s10909-018-2052-7.

[89] SPT-3G Collaboration. Spt-3g instrument paper. In preparation.

[90] A.A. Starobinsky. A new type of isotropic cosmological models without singularity. *Physics Letters B*, 91(1):99–102, March 1980. doi:10.1016/0370-2693(80)90670-x. URL https://doi.org/10.1016/0370-2693(80)90670-x.

[91] A.A. Starobinsky. Dynamics of phase transition in the new inflationary universe scenario and generation of perturbations. *Physics Letters B*, 117(3-4):175–178, November 1982. doi:10.1016/0370-2693(82)90541-x. URL https://doi.org/10.1016/0370-2693(82)90541-x.

[92] K. T. Story, C. L. Reichardt, Z. Hou, R. Keisler, K. A. Aird, B. A. Benson, L. E. Bleem, J. E. Carlstrom, C. L. Chang, H.-M. Cho, and et al. A measurement of the cosmic microwave background damping tail from the 2500-square-degree spt-sz survey. *The Astrophysical Journal*, 779(1):86, Nov 2013. ISSN 1538-4357. doi:10.1088/0004-637x/779/1/86. URL http://dx.doi.org/10.1088/0004-637X/779/1/86.

[93] R. A. Sunyaev and Ya. B. Zeldovich. The Observations of Relic Radiation as a Test of the Nature of X-Ray Radiation from the Clusters of Galaxies. *Comments on Astrophysics and Space Physics*, 4:173, November 1972.

[94] M. Tanabashi et al. Review of Particle Physics. *Phys. Rev. D*, 98(3):030001, 2018. doi:10.1103/PhysRevD.98.030001.

[95] Till Tantau. *The TikZ and PGF Packages*. URL `http://sourceforge.net/projects/pgf/`.

[96] The BICEP/Keck collaboration, P. A. R. Ade, Z. Ahmed, R. W. Aikin, K. D. Alexander, D. Barkats, S. J. Benton, C. A. Bischoff, J. J. Bock, R. Bowens-Rubin, J. A. Brevik, I. Buder, E. Bullock, V. Buza, J. Connors, B. P. Crill, L. Duband, C. Dvorkin, J. P. Filippini, S. Fliescher, J. Grayson, M. Halpern, S. Harrison, G. C. Hilton, H. Hui, K. D. Irwin, K. S. Karkare, E. Karpel, J. P. Kaufman, B. G. Keating, S. Kefeli, S. A. Kernasovskiy, J. M. Kovac, C. L. Kuo, E. M. Leitch, M. Lueker, K. G. Megerian, C. B. Netterfield, H. T. Nguyen, R. O'Brient, R. W. Ogburn, A. Orlando, C. Pryke, S. Richter, R. Schwarz, C. D. Sheehy, Z. K. Staniszewski, B. Steinbach, R. V. Sudiwala, G. P. Teply, K. L. Thompson, J. E. Tolan, C. Tucker, A. D. Turner, A. G. Vieregg, A. C. Weber, D. V. Wiebe, J. Willmert, C. L. Wong, W. L. K. Wu, and K. W. Yoon. Improved constraints on cosmology and foregrounds from bicep2 and keck array cosmic microwave background data with inclusion of 95 ghz band. *Phys. Rev. Lett.*, 116:031302, Jan 2016. doi:10.1103/PhysRevLett.116.031302. URL `https://link.aps.org/doi/10.1103/PhysRevLett.116.031302`.

[97] The BICEP/Keck collaboration, P.A.R. Ade, et al. Measurements of Degree-Scale B-mode Polarization with the BICEP/Keck Experiments at South Pole. In *53rd Rencontres de Moriond on Cosmology*, 7 2018.

[98] S. van der Walt, S. C. Colbert, and G. Varoquaux. The numpy array: A structure for efficient numerical computation. *Computing in Science Engineering*, 13(2):22–30, 2011.

[99] Pauli Virtanen, Ralf Gommers, Travis E. Oliphant, Matt Haberland, Tyler Reddy, David Cournapeau, Evgeni Burovski, Pearu Peterson, Warren Weckesser, Jonathan Bright, Stéfan J. van der Walt, Matthew Brett, Joshua Wilson, K. Jarrod Millman, Nikolay Mayorov, Andrew R. J. Nelson, Eric Jones, Robert Kern, Eric Larson, CJ Carey, İlhan Polat, Yu Feng, Eric W. Moore, Jake Vand erPlas, Denis Laxalde, Josef Perktold, Robert Cimrman, Ian Henriksen, E. A. Quintero, Charles R Harris, Anne M. Archibald, Antônio H. Ribeiro, Fabian Pedregosa, Paul van Mulbregt, and SciPy 1. 0 Contributors.

SciPy 1.0: Fundamental Algorithms for Scientific Computing in Python. *Nature Methods*, 17:261–272, 2020. doi:https://doi.org/10.1038/s41592-019-0686-2.

[100] Jonas Zmuidzinas. Thermal noise and correlations in photon detection. *Appl. Opt.*, 42 (25):4989–5008, Sep 2003. doi:10.1364/AO.42.004989. URL `http://ao.osa.org/abstract.cfm?URI=ao-42-25-4989`.